COLORIMETRIC SENSOR ARRAY FOR IDENTIFICATION OF FUNGI
&
ULTRASONIC SPRAY SYNTHESIS FOR SUPERCAPACITOR MATERIALS

BY

YINAN ZHANG

DISSERTATION

Submitted in partial fulfillment of requirements
for the degree of Doctor of Philosophy in Chemistry
in the Graduate College of the
University of Illinois at Urbana-Champaign, 2015

Urbana, Illinois

Doctoral Committee:

Professor Kenneth S. Suslick, Chair
Professor Jonathan V. Sweedler
Professor Peter Orlean
Professor Ryan C. Bailey

ABSTRACT

In this thesis, functional materials synthesis and fabrication is described within the two areas of (1) colorimetric sensor array for identification of fungi, and (2) ultrasonic spray synthesis for supercapacitor electrode materials.

Human fungal infections have attracted intense current interest, especially in the light of recent outbreaks from pharmaceutical contamination, but also due to infections of immunocompromised patients by opportunistic fungal strains. Fungi stink: that is to say, they produce distinctive volatile organic compounds. The profiles of these VOCs provide a potential diagnostic method that may be able to overcome current limitations in traditional fungal diagnostics. Previous methods for VOC profiling, however, are either costly, non-portable (*e.g.,* GC-MS) or insensitive and intolerant to humidity variation (*e.g.,* electronic noses).

In this project, an optoelectronic nose approach was used with our disposable colorimetric sensor array for rapid differentiation and identification of human pathogenic fungi based on their smell (*i.e.*, the volatiles that they produce). Twelve clinically relevant fungal strains gave unique sensor array responses and were correctly clustered using hierarchical cluster analysis within 3 hours, which is a clinically relevant time frame. Classification prediction accuracy was 94%, based on standard jackknifed linear discriminant analysis. We also introduce the application of a cutting-edge statistical method, tensor discriminant analysis, which takes advantage of the high dimensionality of our sensor array data, giving a prediction accuracy of 98.1%. Furthermore, we have shown that our sensor array has great potential for rapid screening the effects of anti-fungal drugs on particular fungal strains.

This is the first example of colorimetric volatile profiling for fungal strain identification. Compared to single-data-point analysis methods, this inexpensive technique (~$3 for each test kit using an ordinary flatbed scanner) allows for real-time identification of fungi in culture. We expect this is the first step in the development of a rapid, facile, and low-cost tool for diagnosis of fungal infections with potential additional applications for environmental monitoring (e.g., “sick-building syndrome”).

Conjugated polymers have been intensively investigated as electrode materials for supercapacitors because of their excellent electrochemical reversibility, fast switching between redox states, high conductivity in a doped state, mechanical flexibility, and low cost. Among them, poly(3,4-ethylenedioxythiophene) (PEDOT) is especially attractive due to its high stability and low toxicity. Prior PEDOT materials are generally synthesized with surfactants or template methods so as to achieve nano- or micro-structures with high surface area and to maximize capacitance at high charge and discharge rates. These synthesis methods, however, are generally cumbersome (multiple steps) or expensive (such as nano-structured sacrificial templates), and can easily introduce impurities that negatively affect the electrochemical properties of the PEDOT products.

In this project, we used ultrasonic spray polymerization (USPo) method for facile and continuous PEDOT microsphere synthesis without the addition of templates or surfactants. During this USPo process, PEDOT is synthesized by polymerization of the monomer 3,4-ethylenedioxythiophene in the precursor solution in micron-sized droplets that are generated during ultrasonic nebulization. Here, three types of morphologies (solid, porous, and hollow) are synthesized by simply controlling oxidants and precursor solvents. Supercapacitor behavior is characterized and determined to be as high as 160 F/g (Farad/gram), which is the highest of reported PEDOT microspheres. Moreover, taking advantage of the USPo setup, we also demonstrate an innovative spray coating method as a useful electrode fabrication process.

This is the first synthetic route to provide PEDOT microsphere production with controllable morphologies, and it does not require additional stabilizing agents or sacrificial templates. In addition, it also covers a little-investigated area of ultrasonic spray techniques for polymer microsphere synthesis. The potential impact of a facile, cost-effective, and scalable synthetic method for PEDOT supercapacitor materials makes our approach significant to the field of energy storage materials as well as more generalized microsphere materials synthesis.

The second example of using an ultrasonic spray technique is in the synthesis of manganese oxide (MnO_2) microspheres. In this case, a mixed solution of potassium permanganate and hydrochloric acid was nebulized into micro-sized droplets, which were

then carried by air flow through a furnace tube. Each micro-droplet serves as one micro-reactor and produces one microsphere. Upon heating, $KMnO_4$ was decomposed into MnO_2 microspheres; this synthetic process can easily be scaled up. Characterization of the MnO_2 microspheres by SEM, TEM, powder XRD, Raman Spectroscopy, and XPS is described. Different morphologies of MnO_2 microspheres could be controlled by tuning the precursor concentrations (and ratios) and furnace temperatures; for example, microspheres synthesized at 150 °C gave polycrystalline MnO_2 while synthesis at 500 °C yielded needle-shape α-MnO_2 crystals. The electrochemical properties investigated by cyclic voltammetry gave specific capacitance as high as 320 F/g, demonstrating promising properties as supercapacitors. In addition, these microspheres can be directly sprayed on conductive substrates, such as carbon fiber paper, and may have useful applications as a supercapacitor electrode coating. The supercapacitive properties of MnO_2 microspheres at higher charge and discharge rates can be improved by increasing the surface area coverage or coating them with a thin layer of conductive polymer.

ACKNOWLEDGMENTS

Well, I understand this segment of thesis will mention LOTs of names and I will do my best to express thankfulness to ALL of the people who gave me help and suggestions during my graduate school life (both with thesis research and life in general).

First, I want to thank my advisor Professor Kenneth Suslick. It was a big decision for me to switch from pharmaceutical science to chemistry, and then migrate from chemical biology to materials chemistry. And certainly it would be less smooth without support and help from Ken. I am glad to have an advisor like him, who taught me how to be a good researcher, how to generate new ideas, and how to adapt to western culture.

Second, I want to thank all the past and current Suslick group members, with special thanks to Dr. Jon Askim, and Dr. Jinrui Guo. I want to thank Jon for helping me with English (both writing and accent reduction in speaking), and I also enjoyed scientific discussions with him. I want to thank Jinrui for her support during graduate school for, not only in equipment training but also with graduate school life. Since we are going to be colleagues soon, I will save some words and express my thankfulness in person when we meet. I also want to mention all the people received help from and I had fun talking with (order is in alphabetical order of last name, which is in honor of Ken's famous saying): Prof. Shin-Ichi Hatanaka, Jordan Hinman, Dr. Howard Kim, Hyo Na Kim, Maria Lagasse, Zheng Li, Kimberly Lundberg, Yurun Miao, Nitin Neelakantan, Dr. John Overcash, Dr. Jackie Rankin, Dr. John Sander, Dr. Maryam Sayyah, Dr. Sizhu You, Dr. Zhi Su, Dr. Bradley Zeiger,

Third, I want to thank my collaborators, Prof. Peter Orlean, Prof. Wenxuan Zhong, and Dr. Laura Huff. Thank you all for kind help and creative input which made our projects possible. I really learned a lot and experienced so many interesting science and technologies – from microbiology, to statistics, to electrochemistry.

Next, I want to thank University of Illinois staff members all over the campus, including School of Chemical Sciences Micro Analysis Lab, Materials Research Laboratory, and School of Chemical Sciences Machine Shop. I appreciate their time for instrument training and help. Those members include (but not limited to) Rudiger Laufhutte, Tom Wilson, Elizabeth Eves, Jim Mabon, Wacek Swiech, Honghui Zhou,

Julio Soares, Lou Ann Miller, Fubo Rao, Tim Spila, Rich Haasch, Mauro Sardela, Changqiang Chen, and Matt Bresin, Hodge Harland, Brad Lutz, Robert Brown. Besides, I want to express thankfulness to administrative officers, Connie Knight, Beth Myler, Theresa Struss, Karen Neumann, Becky Duffield, and Lori Johnson, without there nice and efficient ladies, I could hardly make schedules and have paper work done. The Suslick group "mom", Nasrin Gahvari, I want to say thank you for your help with all the detailed things over the years, and I wish you well!

Now it is time to thank my friends outside the group. I want to thank Xiao Yang, Yang Song, Brian Trinh, and Ying Xiao. You guys gave me so much positive energy and great help. And I am sure our friendship will last beyond graduate school. Also, I want to mention Ellen Althaus for her encouragement and volunteer opportunities which built up my leadership skills, and Patricia Simpson for her suggestions on job hunting.

I was fortunate to have a great advisor who encouraged me to build up my professional experience outside graduate school. During 2015 summer I was a Materials Intern at TE Connectivity at Menlo Park, CA. This opportunity greatly broadened my research horizon and gave me a chance to apply what I have learned in an industrial research setting. Here I want to thank my supervisor Dr. Yiliang Wu, who helped to enhance my thinking and problem solving ability. I also want to thank Dr. Michael Oar, Dr. Len Radzilowski, Dr. Ting Gao, and Dr. Jibin Sun, for their mentorship.

Finally, I would like to thank my parents, who have always been there with their unconditional love and support. I also want to thank my late grandfather Jindong Zhang, who named me and always gave me big hug – with which I am able to be strong and confident. Also, thanks to late grandfather Guobin Cao, whose gene and smartness I am proud to carry on with. I also want to thank my relatives in the US. I definitely feel more welcomed in this land.

With that, I want to conclude I am glad I chose here to complete my graduate study in the Suslick group in chemistry at University of Illinois. This experience definitely enriched my life and will be of great treasure and help for the rest of my life.

TABLE OF CONTENTS

CHAPTER 1:

COLORIMETRIC SENSOR ARRAY FOR CHEMICAL AND BIO-SENSING…1

1.1 Optoelectronic Nose Introduction……..……..1

1.2 Types of Optoelectronic Noses……...…2

1.3 Colorimetric Sensor Arrays……5

1.4 Statistical Analysis and Modeling…….……...…15

1.5 Applications of Colorimetric Sensor Arrays ……20

1.6 Summary and Outlook ……..…30

1.7 References……...…31

CHAPTER 2:

DETECTION AND IDENTIFICATION OF FUNGI VIA

COLORIMETRIC SENSOR ARRAY……45

2.1 Introduction……...……45

2.2 Experimental Procedures…….……47

2.3 Results and Discussions……...……57

2.4 Conclusions……72

2.5 References……72

CHAPTER 3:

ULTRASONIC SPRAY TECHNIQUE FOR MATERIALS SYNTHESIS……77

3.1 Introduction……..……77

3.2 Spray Techniques ……77

3.3 Reaction Pathway and Commonly Used Methods for Morphology Control…..…82

3.4 Examples of Products Prepared by Ultrasonic Spray Technique…….87

3.5 Summary and Outlook……101

3.6 References……102

CHAPTER 4:

ULTRASONIC SPRAY SYNTHESIS FOR MNO_2 MICROSPHERES AS SUPERCAPACITOR ELECTRODE MATERIALS……..…...…110

4.1 Introduction to Supercapacitors…….……110

4.2 Electrochemical Double Layer Capacitors (EDLC) ……111

4.3 Pseudocapacitor (Redox-Based) Capacitors……...…114

4.4 Current MnO_2 Materials for Supercapacitors……..…116

4.5 Ultrasonic Spray Pyrolysis for MnO_2 Microspheres……116

4.6 Results and Discussion…….…..……123

4.7 Conclusions……146

4.8 References……147

CHAPTER 5:

ULTRASONIC SPRAY POLYMERIZATION FOR PEDOT MICROSPHERES AS SUPERCAPACITOR ELECTRODE MATERIALS……..…...…155

5.1 Introduction……155

5.2 Ultrasonic Spray Polymerization for PEDOT Microspheres……158

5.3 Results and Discussions……161

5.4 Conclusions……173

5.5 References……..……173

CHAPTER 1
COLORIMETRIC SENSOR ARRAY FOR CHEMICAL AND BIO-SENSING

1.1 **Optoelectronic Nose Introduction**

Ever since Persaud and Dodd[1] used semiconductor transducers to mimic olfactory sensing systems in 1982, there has been tremendous attention drawn to the use of artificial devices to discriminate among various volatile chemicals or their composite mixtures. Due to its potential use in everyday life such as applications for chemical workers, soldiers, and medical doctors, development of sensitive, facile, inexpensive, and portable sensors for the detection of a wide range of analytes (including toxic gas, explosives, and pathogenic contaminations) has attracted significant attention. So far, there have been numerous novel approaches to chemical sensing[2-11] with improved discriminatory powers that are essential to eliminate false positives for the monitoring of toxic gases at sub-ppm levels.[12]

Compared to electronic sensors, optical sensor arrays have proven to have better detection limits and better tolerance to the environment. In general, optical sensor arrays provide a facile, efficient, and sensitive approach for the rapid detection and identification of wide range of chemical substances based on colorimetric (or fluorescent) changes quantified by digital imaging.[5, 13-18] The major structure of the optical sensor array has an active center which interacts with analytes and a reporting chromophore or fluorophore that is coupled with the active center to give detectable signals.[12] If the coupled centers are arranged in an array fashion, a pattern of response can then be converted to multidimensional data that can then be used to discriminate or identify a specific chemical or a mixture of chemicals.

In this chapter, the key factors and applications of the colorimetric sensor array are described. Chemo-responsive colorants are arranged in an array manner and a pattern or optical fingerprint is then generated to analyze any odorant or gas mixtures.[3, 8, 19-21] Chemical sensor arrays take advantage of cross-responsive chemical interactions of the analyte and the arrayed probes, and these olfactory-like responses are converted into easily monitored optical outputs, thus acting as an optoelectronic nose.

1.2 Types of Optoelectronic Noses

A sensor is a device that converts an input signal from a stimulus into a readable output signal.[11, 22] The input signal can be any measurable characteristic such as quantity or physical variation, while the output is ultimately an electrical signal. Small and inexpensive sensors enable mass production and widespread application.[23] Disposable sensors are especially attractive in that they can take advantage of irreversible, fast chemical responses and avoid any potential problems with reusability (e.g., cross-contamination or sensor degradation).

Chemical sensors respond to the chemical environment (i.e., interactions with molecular species, such as reactivity, redox potential, acid-base interactions, etc.) rather than physical properties (e.g., temperature or pressure). By transduction methods, one can classify chemical sensors into three classes: (1) electrical and electrochemical, (2) thermometric, and (3) optical.

1.2.1 Electrical, Electrochemical and Thermometric Sensors

An electrical sensor is a resistive or capacitive measurement device that responds to analyte interactions with a receptor layer (electrical circuit) and a resistance, capacitance, current, or voltage as the monitored response.[11, 24, 25] Various electrical and electrochemical sensors have been explored as mimics to the olfactory system including metal oxide semiconductors (e.g. SnO_2)[26], metal oxide semiconductor field effect transistors (FET) (e.g. Ga_2O_3)[27-29], chemical field-effect transistors (ChemFET),[30, 31] conductive polymer sensors[32] of both intrinsically conductive (e.g. polythiophenes)[33] and composite types (e.g. carbon-black polymer composite),[10] and coated quartz vibrators or acoustic wave sensors.[34] In general, electrical sensors rely mostly on physical adsorption as the primary interaction between the chemical analyte and the electrically active surface. This reliance on physical adsorption, however, inevitably causes these sensors to be susceptible to humidity, which remains a practical problem in real life applications.[4, 6, 7, 11, 22] In addition, aging of electrical sensor surfaces can induce significant baseline drift.[4] Since these sensors rely on one primary dimensional factor – physical adsorption – selectivity remains problematic in chemical or biomedical applications.

In this area, tremendous efforts have been focused on nanostructured materials as "highly sensitive" sensor transducers.[35-43] Their high sensitivity comes from high surface

area to mass ratios, which maximizes the interaction between analyte and probe. Electrochemical sensors[44-47] have been diversely investigated for applications in environmental[48-52], clinical[53-55], bio-sensing[31, 47, 56-59], food[25, 60] and biohazard agent[61] analyses.

1.2.2 Thermometric Sensors

Thermometric sensors rely on the measurement of local heat change from specific chemical reactions or analyte adsorptions. These interactions happen in a catalytic sensing layer which is coupled with a thermometer. The temperature changes, induced by the interactions of the analytes, are then measured by temperature-dependent semiconductors.[62, 63] Thermometric sensors most commonly use enzymatic reactions with high enthalpy changes.[22, 64-66] A wide range of applications (e.g. detection of sucrose[67], glucose[68-71], uric acid[72], insulin[73], and lactate[74]) by suitable immobilized enzymes have been reported for such biosensors. Moreover, a multi-analyte determination method has been performed by thermal biosensors using microelectromechanical system thermopiles.[70, 75, 76]

1.2.3 Optical Sensors

Optical sensors use visible or ultraviolet light as source and output signal during sensing. In general, light from a source is transmitted to the material used to sense a given analyte, and then the light output is monitored by the detector. (**Figure 1.1**). Specific detectors depend on the sensing method (e.g. refractive index, scattering, diffraction, absorbance, reflectance, photoluminescence, chemiluminescence, etc.) and can monitor a variety of parameters, such as light intensity, lifetime, polarization, etc.[22, 77]

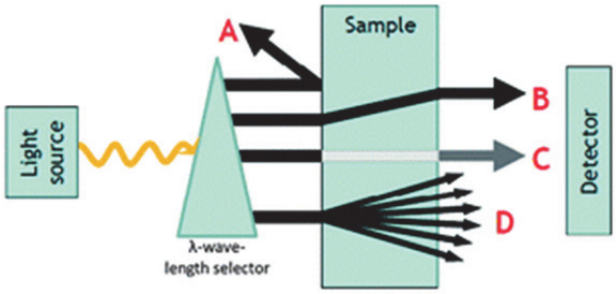

Figure 1.1 A general schematic diagram of spectroscopic measurement components: A: light reflection; B: light refraction; C: light absorption; D: fluorescent emission.[77]

Colorimetry (i.e., quantitative measurement of absorbance or reflectance spectra) is one of the oldest of analytical techniques, and colorimetric sensing is a simple and straightforward method.[78] Updated by modern digitization, one can use pattern recognition techniques (which allows simple three color imaging), hyperspectral imaging (i.e., more color channels), and full spectrophotometry (i.e., hundreds of color channels with nm resolution).[5, 20, 79-81]

Fluorometry (**Figure 1.2**)[82, 83] can provide excellent sensitivity (normally due to low background fluorescence) although the instrument is generally more expensive.[84] Fluorescence-based approaches and fluorescence parameters (e.g. Stokes shift, fluorescence intensity and anisotropy, emission and excitation spectra, and fluorescence lifetime) can provide substantial flexibility as an analytical approach.[85, 86] Fluorescence techniques can be divided into three main classes: intrinsic fluorescence[87-90], extrinsic fluorescence[85, 91, 92] and displacement or differential[93-97] probes.

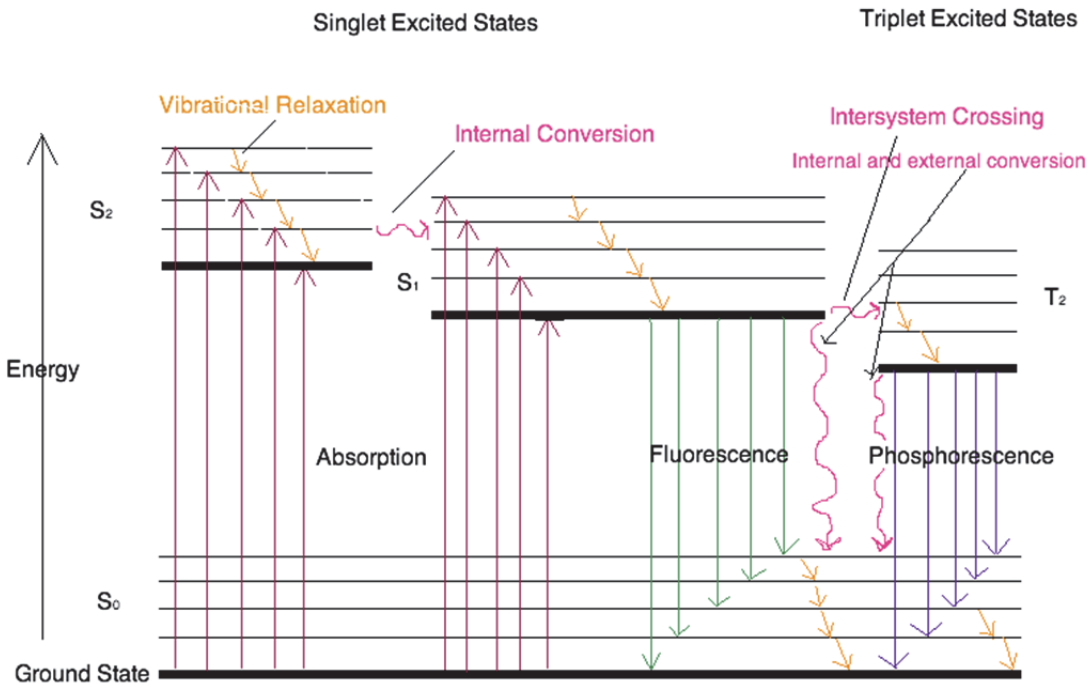

Figure 1.2 Partial Jablonski diagram for absorption, fluorescence, and phosphorescence.[98]

1.3. Colorimetric Sensor Arrays

1.3.1 Importance of Intermolecular Interactions

Intermolecular interactions are crucial to array-based chemical sensing that relies on cross-reactive pattern recognition.[99-101] **Figure 1.3** shows the classification and strengths of intermolecular interactions in continuum from the weakest of interactions (~0.1 kJ/mol) to the strongest (~100 kJ/mol). These interactions include bond formation and ligand coordination, electrostatic ion-ion and proton acid-base interactions, hydrogen-bonding, halogen bonding, charge-transfer and π-π molecular complexation, dipolar and multipolar interactions, and van der Waals interactions (e.g., physical adsorption).

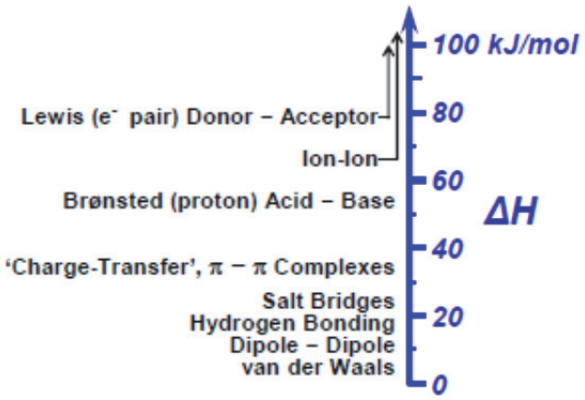

Figure 1.3 A schematic illustration of semi-quantitative energy scale, from weakest van der Waals interactions to strongest covalent/ ionic bonds.

As previously stated, electronic nose technology essentially relies on physical adsorption and van der Waals interactions, which are among the weakest interactions in the energy chart. Colorimetric sensor arrays rely on stronger interactions between analytes and the probes. This allows a higher sensitivity, better selectivity and chemical specificity. For example, ligation of Lewis base analytes (e.g. amines, thiols, etc.) gives bond enthalpies from ~40 to ~200 kJ/mol. The enthalpy for the physical adsorption of an analyte, however, is only around 10 kJ/mol. The effective equilibrium constant for

physical adsorption will typically be only about 5 x 10^{-5} as large as that for ligation to metal ions. More importantly, incorporating stronger interactions expands the chemical interaction space beyond simple physisorption, and consequently allows higher dimensionality to discriminate among very similar analytes or complex mixtures of analytes.

Based on the properties of the recognition elements, the sensors used in an array will span a range of molecular specificity. At one end, there are individual sensors that are almost completely promiscuous, i.e., highly cross-reactive; these include polymers and polymer blends with optical reporters embedded that adsorb analytes based primarily on hydrophobicity.[102, 103] Promiscuous sensors can contribute to the sum of an array's response, but are insufficient in and of themselves to provide the differential selectivity most desirable for chemical sensor arrays. At the other extreme, there are highly selective artificial receptors that are specific for one or perhaps one closely related class of analytes. While this class of sensors can produce high specificity for target analytes, they alone will not make a sensor array capable of dealing with a wide range of analytes and mixtures;[104] furthermore, the synthesis of such selective artificial receptors can be complex and problematic. The optimal optical sensor array will therefore incorporate a range of colorimetric or fluorometric sensors from the promiscuous to the monogamous.

1.3.2 Design Requirements for an Optical Sensor Array

There are two fundamental design requirements for a colorimetric (or fluorometric) sensor array: (1) the chemo-responsive dye (or fluorophore) must contain a center to interact with analytes, and (2) this interaction center must be strongly coupled to an intense chromophore or fluorophore. The first requirement implies that it would be highly advantageous for the interaction to be more than simple physical adsorption and involve other, stronger chemical interactions.

Based on the significant intermolecular interactions responsible for optical changes, one may divide chemoresponsive dyes into roughly five separate classes (with slight overlaps): (1) Lewis acid/base dyes (i.e., metal ion containing dyes), (2) Brønsted acidic or basic dyes (i.e., pH indicators), (3) dyes with large permanent dipoles (i.e., solvatochromic) for detection of local polarity and hydrogen bonding, (4) redox responsive dyes, and (5) chromogenic aggregative colorants (including simple ionic

sulfides and plasmonic nanoparticle precursors). An example of a 36 spot sensor array for use with gas phase analytes is shown in **Figure 1.4**.

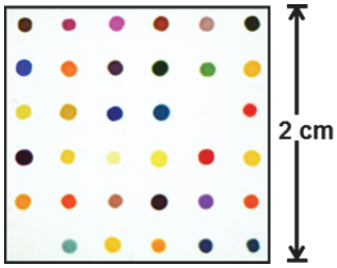

Figure 1.4 A photographic image of a 6 by 6 colorimetric sensor array.

For gas phase sensing, a colorimetric sensor array is simply digitally imaged before and during exposure to any volatile analyte, odorant, or complex mixture of odorants. The imaging is mostly commonly achieved with an ordinary flatbed scanner, but one may also use digital cameras, portable handheld readers, and even cell phones; where constancy of illumination is, of course, important.

From the digital images, a difference map (**Figure 1.5**) is easily generated by digital subtraction, pixel by pixel, of the image of the array before and after exposure: red value after exposure minus red value before, green minus green, blue minus blue. Averaging of the centers of the spots (typically ~200 pixels) avoids artifacts from non-uniformity of the dye spots, especially at their edges. The other advantage of using the change in RGB values is that it tends to cancel out discrepancies in printing because the difference in spot color are only a weak function of variation in dye concentration from array to array.[79] For display purposes, the absolute value of the color change in each spot is expanded to yield a pictorial representation of array response.

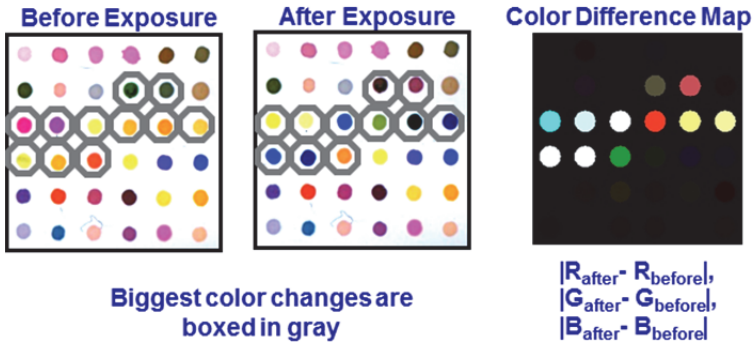

Figure 1.5 Representative image of a 36 spot colorimetric sensor array **(left)** before exposure and **(middle)** after exposure. **(right)** Subtraction of the two images yields a difference vector in 108 dimensions (i.e., 36 changes in red, green, and blue color values), which is visualized using a difference map (representing the absolute values of the color changes).

The resulting data is inherently digital (simply a vector of 3N dimensions where N=total number of spots) and all quantitative and statistically analysis is done directly from the digital difference vectors. The color difference maps are primarily useful for convenient visualization of color changes occurring in each spot; note that the colors shown in each difference map represents the absolute value of the ΔRGB values expanded from a range useful for visualization.

The choice of individual dyes used in an optical sensor array is governed empirically by its intended use. One must consider if this array is meant to detect and discriminate between a broad range of analytes or will it have a more specialized application.

1.3.3 Classes of Colorimetric and Fluorometric Sensors

1.3.3.1 Lewis Acid/Base Dyes

Most strongly odiferous compounds are Lewis bases: thiols, phosphines, amines, carboxylic acids. For these gaseous analytes, Lewis acids are the good solution. Among Lewis acid dyes, metalloporphyrins (with different metals and peripheral substituents) are a natural choice for the detection of metal-ligating vapors because of their open coordination sites for axial ligation, their large spectral shifts upon ligand binding, and their intense coloration. The difference in color of scarlet red arterial blood and the purple

of venous blood is an example of the colorimetric detection of dioxygen as it ligates to a metalloporphyrin (i.e., the iron heme of hemoglobin). In addition, it is well recognized that porphyrins show significant solvatochromic effects resulting in distinguishable colorimetric changes before and after interaction with a wide range of both ligating volatile organic compounds (VOCs) (e.g., amines, thiols, phosphines, phosphites, thiols, etc.) and even weakly-interacting vapors (e.g., arenes, halocarbons, or ketones).[20] Metalloporphyrins are therefore ideal for colorimetric[8, 12, 20, 105] detection of metal-ligating vapors.

1.3.3.2 Brønsted Acidic/Basic Dyes

Many organic chromophores (*e.g.* azo dyes, nitrophenols, phthaleins, sulfophthaleins, aniline-sulfophthaleins, triphenylmethane dyes, etc.) are used to measure the pH of aqueous solutions or as histological stains for biomedical applications.[106, 107] An example of color change vs. change in molecular structure is shown in **Figure 1.6**.

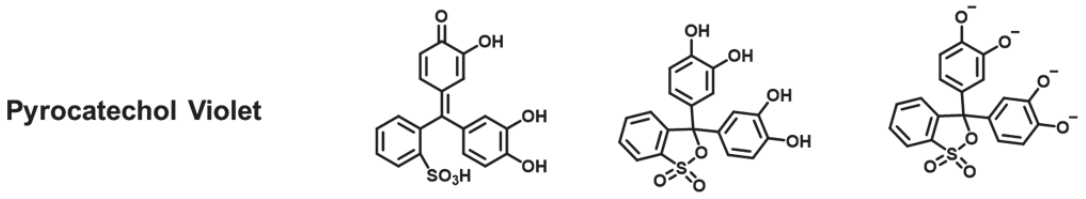

Figure 1.6 Illustration of color and pH change of Pyrocatachol Violet dye with change in structure. Color shows red at pH 0 (left), yellow at pH 2 (middle), and purple at pH 8 (right).

1.3.3.3 Solvatochromic Dyes

Dyes whose dipole moments are significantly different between their ground and excited states and show a color change depending upon the polarity of their environment are called solvatochromic. If the excited state has a larger dipole moment, it will be more stable relative to the ground state in a polar environment and vice versa. Nearly all dyes show some inherent solvatochromism. For "solvatochromic" dyes, these changes in dipole moment are very large, leading to impressive chromic or fluorescent changes that depend upon the polarity of the solvent in which the dye is dissolved.

A common feature of most solvatochromic dyes is that they are "push-pull" systems with a strong zwitterionic component to their electronic structure, i.e., a large conjugated π system with strong electron donor groups at one end and strong electron withdrawing groups at the other. An illustration of color change (either red shift or blue shift) is shown in **Figure 1.7**.

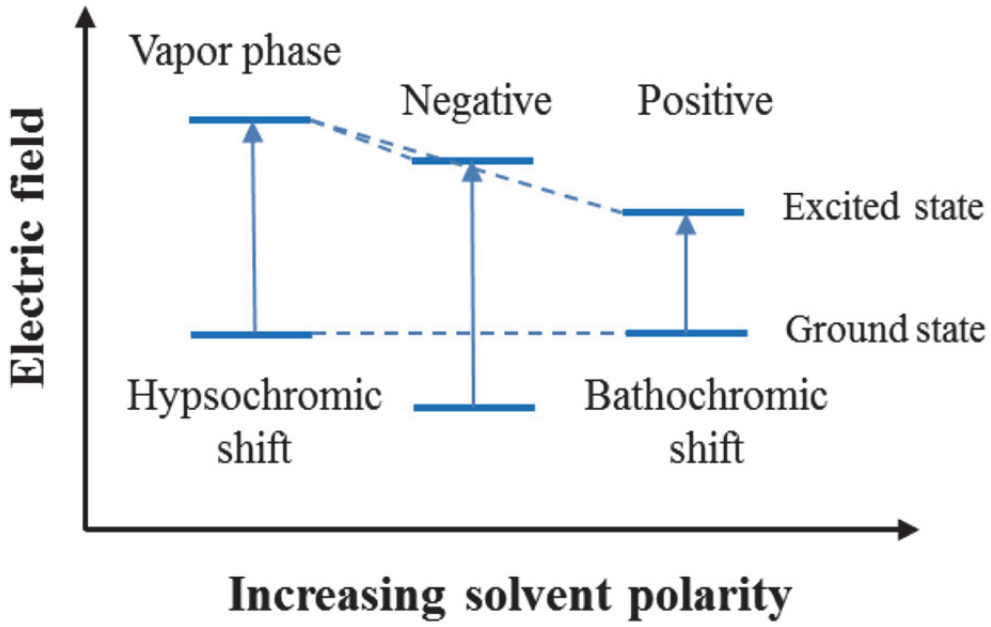

Figure 1.7 Schematic diagram of solvatochromism.[108]

Several solvent polarity scales[109] have been based on the wavelength shifts and optical transitions of solvatochromic dyes, including Kosower's and Brooker's early studies, Reichardt's E_T[109-113] and Taft's π*[114, 115] scales. Solvent polarity is very much a multi-parameter property, involving dipolar, quadrupolar, and multi-polar interactions, hydrogen bond donation and acceptor properties, Lewis acid-base interactions, etc. Thermodynamic and theoretical analyses of the origin and meaning of solvation, solvent polarity, and solvatochromism continue[116-119] and are especially useful for thorough comparisons among all multiparameter descriptions of solvent polarity.[109, 117, 120, 121]

1.3.3.4 Redox Indicator Dyes

Redox indicators are colorimetric reagents that show color change at specific redox potentials. Typical examples include anilinic acid, diphenylamine, methylene blue,

and Nile blue.[122-124] Since proton transfer sometimes happens during this process, redox dyes are generally divided into two classes based on whether the interaction is pH dependent or not.. A good example of using a redox dye for an optical sensor is in the detection of triacetone triperoxide (TATP) vapor (50 ppb - 10 ppm). The TATP vapor is first hydrolyzed to acetone and hydrogen peroxide, and then exposed to redox probes such as Lissamine Green B, o-dianisidine, diphenyl amine, N-phenyl-1,4-phenylenediamine and N,N'-diphenyl-1,4-diphenyldiamine (**Figure 1.8**). This array was capable of detecting concentrations of TATP vapor down to 2 ppb.[123]

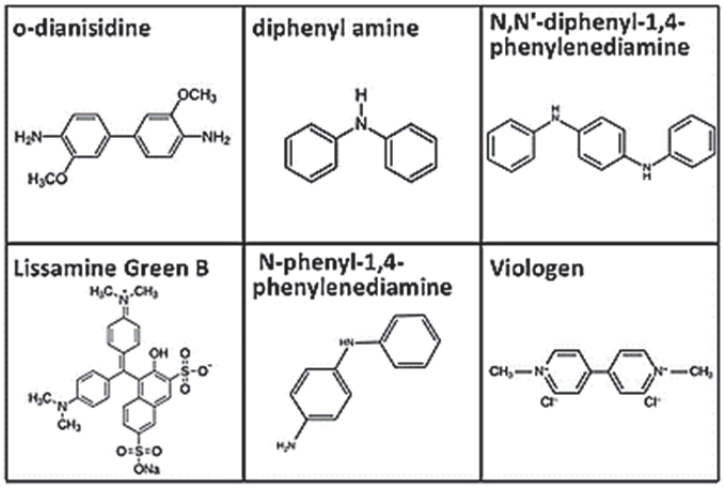

Figure 1.8 Representative structure of some common pH-independent redox dyes.[123]

1.3.4 Printing Method, Substrate, and Immobilization Matrix

While the choice of chemoresponsive dye will dominate the effectiveness of any optical sensor array, there are also some other factors that can affect a sensors function (i.e., sensitivity, shelf life, reliability, and robustness).

As for batch fabrication of an array, a simple method is to use contact printing. This process involves printing dye formulations on a surface where the whole process is controlled by a robotic printer. (**Figure 1.9**). Ink-jet printing and spin-coating are also reported, though with limited successful applications.[125]

Substrates for optical sensor arrays should be (1) inert to analytes and the environment, (2) have adequate surface area to allow for sufficient indicator loading and allow analyte permeation to immobilized probes, and (3) depending on the measurement

method, the substrate should be optically transparent or with high reflectivity. Some commonly used substrates include reverse phase silica gel plates, acid-free paper, or porous polymer membranes made out of a material such as cellulose acetate or polyvinylidene difluoride (PVDF).[19, 40, 77, 83, 126]

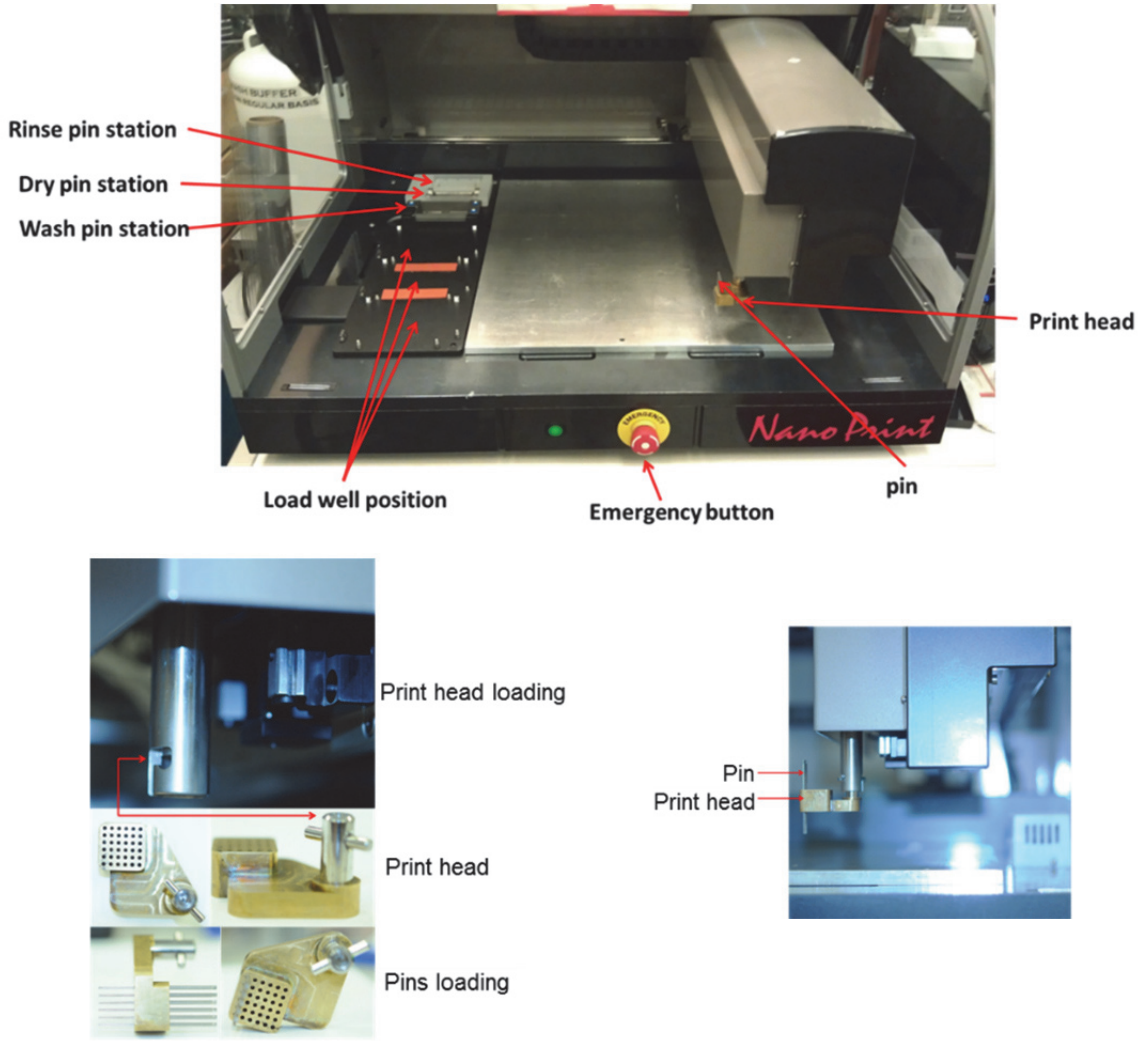

Figure 1.9 Images of **(left)** robotic contact pin printer with **(right panel)** print head and pins.

A major issue with chemical sensors (actually with any sensor) is its susceptibility to ambient humidity, which is in fact crucial to its real life applications.[4, 6] One way to overcome this shortcoming is to use hydrophobic materials (e.g., PVDF membranes) as colorimetric or fluorometric sensor array substrates. This approach can not only reduce

array response to humidity over a wide humidity range (10 to >95% relative humidity)[12, 20, 79, 127, 128] but can also permit their application for aqueous sensing.[129]

Ideally, for sensing applications, soluble, molecular dyes are deposited as a viscous film or on a high surface area substrate so analytes can gain access to the colorant with an acceptable response time. In contrast, pigments (insoluble colorants) are not generally permeable to analytes and therefore reactive only on their outermost surface, which dramatically reduces the desired response.[130] To solve this problem, porous sol–gel chemistry has been adopted to provide excellent matrices for chemically responsive colorants.[77, 83, 126, 131] Simply by adding chemoresponsive dyes to organically modified silicates (ormosils) prepared in advance (in low volatility solvents to provide sufficient working time)[19, 127, 130, 132, 133] an effective nanoporous pigment sensors can be prepared. With the help of advanced printing technologies, arrays of sensors can be made in a consistent fashion.[2] Moreover, the physical and chemical properties of the matrix (e.g., hydrophobicity, porosity) can be easily tailored by incorporating differently substituted silicate precursors which then allows good dispersion of pigments in the matrix. The use of these porous pigments has proven to improve sensitivity and shelf-life, and permits direct printing onto non-permeable polymer surfaces.[19, 130, 132, 134]

These nanoporous pigment films are typically ~3-4 μm thick with uniform silicon content throughout the spot The TEM image below clearly shows the internal pore structure of these ormosil films (**Figure 1.10** and **Figure 1.11**), which assist in mass-transport, and are responsible for the fast response times observed during sensing experiments (reaches 90% of equilibrium response in < 2 minutes).[130]

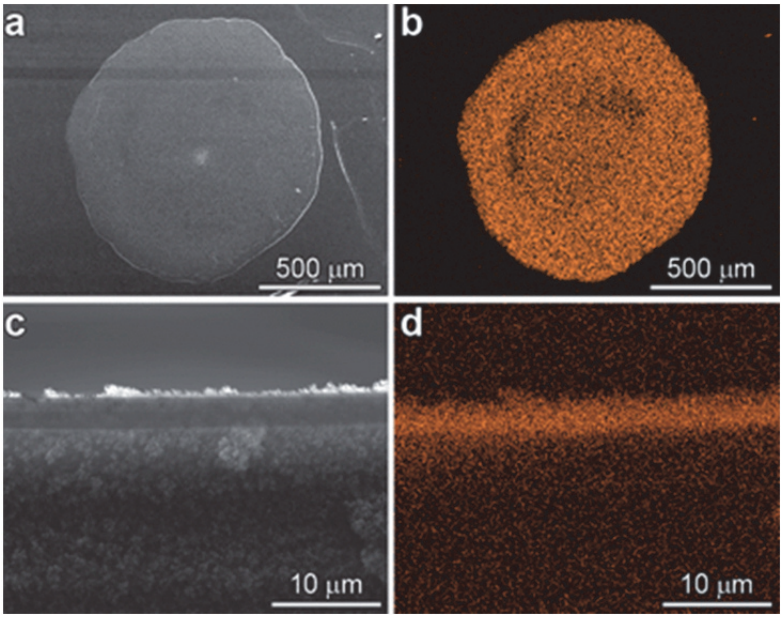

Figure 1.10 SEM micrographs of a 1 mm diameter spot of a porous ormosil pigment printed on PET film: (a) top surface and (b) energy dispersive spectroscopic (EDS) elemental mapping (Si Kα); (c) cross-section and (d) EDS elemental mapping (Si Kα).[130]

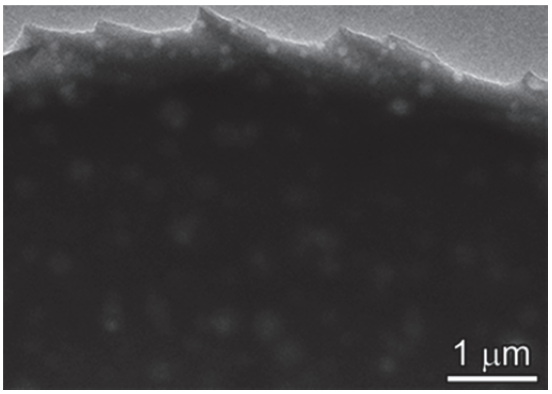

Figure 1.11 TEM micrograph of porous ormosil pigment showing the 50 to 200 nm pores created in these ormosil xerogels.[130]

The uniformity of dye distribution can also be demonstrated by digital image analysis of the printed nanoporous pigments. (**Figure 1.12**).[130] With excellent reproducibility of these printed spots, chemical sensing experiments are generally performed by measuring the averaged difference between before-exposure and during-exposure images, which further reduces errors in the pattern analysis.[79]

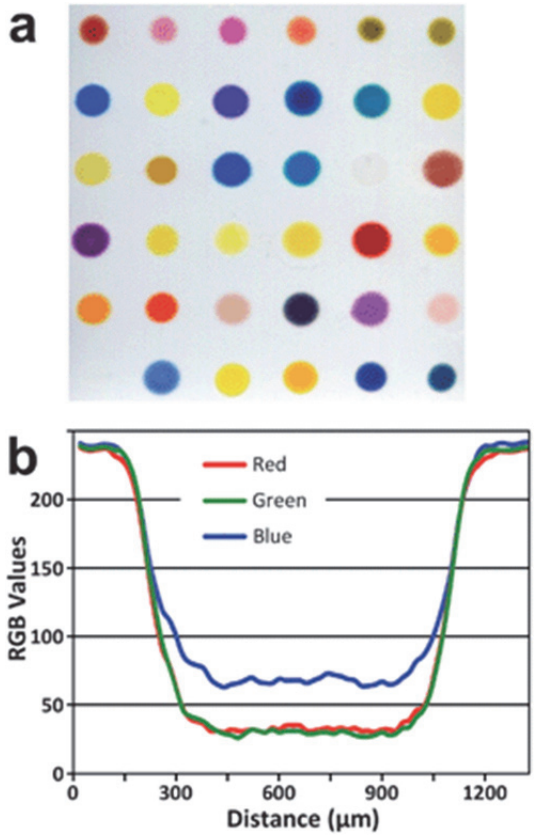

Figure 1.12 (a) Image of a printed array, 1.2.5 x 1.2.5 cm. (b) RGB values of a line scan across the center of a typical spot.[130]

1.4 Statistical Analysis and Modeling

The key to high sensitivity and selectivity of a chemical sensor array relies on its orthogonal detecting mechanism (e.g., Lewis acid/base, Brønsted acid/base, redox, electrophilicity, nucleophilicity, hydrogen bonding, polarity, etc.), which naturally provides high dimensionality for interaction with a variety of analytes. This is also the reason why sensors that rely merely on physical interactions (metal oxide electrical sensors or chemFETs, coated quartz microbalances, conductive or composite polymer sensors, etc.) lose their selectivity.[3, 6, 128] In these physical arrays, though a high number of probes can be used, there is usually one dominant dimension (typically hydrophobicity) that contains >90% of the total variance among analytes. As a result, most conventional electronic nose technologies are not able to distinguish among large libraries of similar complex mixtures.

In contrast, sensor arrays based on chemical interactions intrinsically have a much higher dimensionality. Having a high dimensionality has the advantage of much greater ability to differentiate among similar analytes. The greater dimensionality, however, also has the drawback of involving sophisticated statistics.[135]

There are some commonly used statistical methods to deal with high dimensional data.[136, 137] In the following paragraphs, hierarchical cluster analysis (HCA), principal component analysis (PCA), and linear discriminant analysis (LDA) will be briefly discussed as they will be used in the next chapter for data analysis.

In general, for chemometric data there are two distinct statistical approaches: clustering vs. classification.[136-138] Cluster analyses describe what resembles what; while classification analyses are used to predict which category a new dataset belongs to. Statistical methods can be unsupervised (e.g., HCA, in which case the class identities are unknown and the results provide a semi-quantitative idea of the quality of the overall data set), or supervised (e.g., LDA, that can give answers to future predictions based on the training set).

1.4.1 Hierarchical Cluster Analysis (HCA)

HCA is a clustering technique in which the Euclidean distance between the nearest-neighbor points are calculated and clustered further, rendering a final dendrogram tree that describes "what data set resembles what". A descriptive conversion from a 2-dimensional data set to a HCA dendrogram is shown in **Figure 1.13**[137, 138]

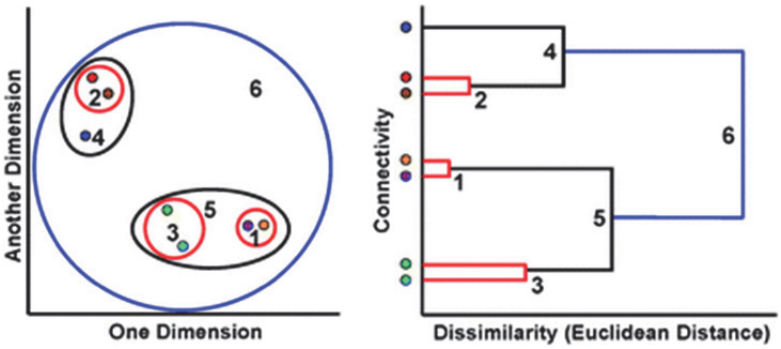

Figure 1.13 Schematic representation of a hierarchical cluster analysis (HCA) for multidimensional data (shown in two dimensions on the left) that forms a dendrogram based on clustering of those experimental measurements (right).[139]

Dendrograms from HCA provide a straightforward semi-quantitative description of the dataset. **Figure 1.14** shows an example of clustering for 100 VOCs in which similar chemical classes are clustered tightly together as a result of the chemical reactivity of a particular chemical sensor array.

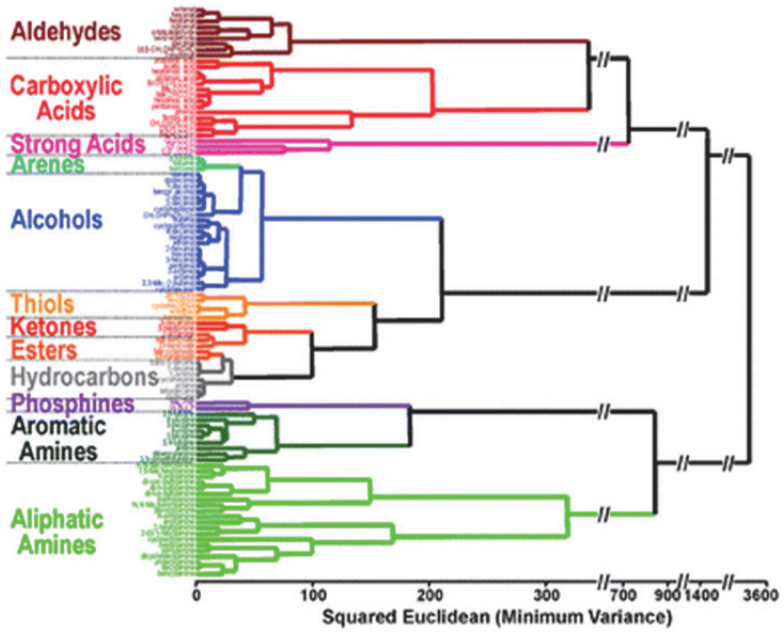

Figure 1.14 Dendrogram from HCA of the colorimetric array responses to 100 common organic compounds at full vapor pressure at 300 K.[20, 79]

1.4.2 Principal Component Analysis (PCA)

PCA is a dimensional reduction technique that condenses the variance among several possibly-correlated dimensions by creating a new orthogonal set of dimensions using linear combinations of the initial dimensions. Similar to HCA, PCA is an unsupervised method that is used for evaluation rather than for future prediction. These new dimensions (also called components) are ranked by the contribution of amount of data variance. Normally, a combination of data variance accumulates to be at least 95% of the totally variance.

As mentioned earlier, traditional electronic nose technologies only require two principle components to express up to 95% of the total variance. This is because they only rely on physical interactions between analytes and the sensor arrays. On the other

hand, a sensor array that takes advantage of cross-responsive chemical interaction is highly effective when dealing with a large amount of varied reactive species. In other words, PCA is a useful tool to evaluate the number and possibly identities of chemical interactions being probed by the sensor array. **Figure 1.15** shows the scree plot of the cumulative contributions of each principal component, providing a quantitative measure of the reactivity space from the array response.

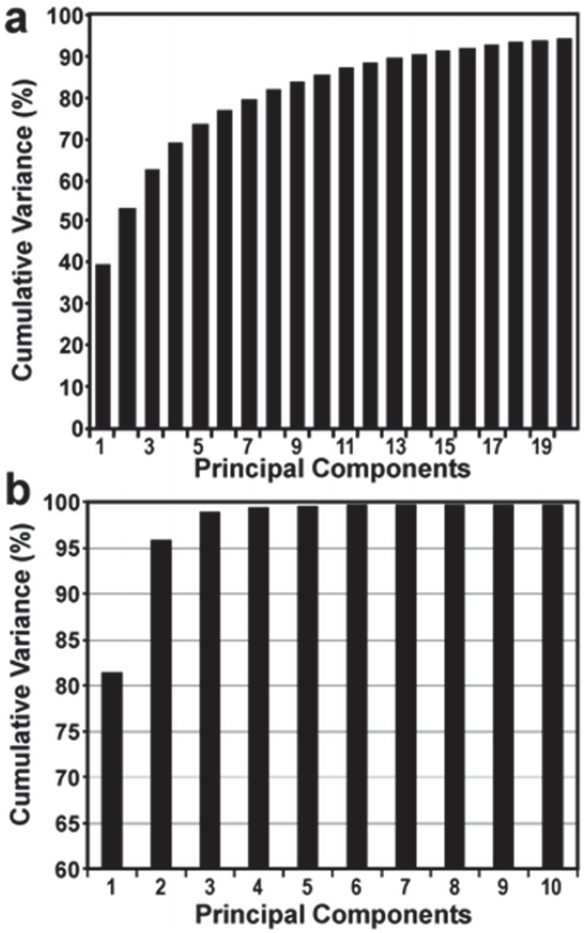

Figure 1.15 (a) A scree plot of data from a colorimetric sensor array tested with 100 VOCs, showing high dimensionality: 22 dimensions required for >95% total variance.[79] **(b)** A scree plot from a colorimetric sensor array tested with 14 natural and artificial sweeteners, showing low dimensionality: 2 dimensions required for >95% total variance. It can be inferred that the chemical reactivity space of the sensor array interacting with VOCs is large, while that used in the array for artificial sweeteners is small, with pH being a primary component.[140]

1.4.3 Linear Discriminant Analysis (LDA)

Linear discriminant analysis (LDA) seeks to find a set of dimensions that best separates data into already known classes. LDA is a biased method and each analyte needs to be labeled in the designated class. The linear combination is used to separate the data set in an effort to maximize the ratio of between-sample variance to within-sample variance. A general example of this separation is shown as **Figure 1.16**. After a linear combination description is determined with a training set, LDA can be used to predict the identity of unknown samples.

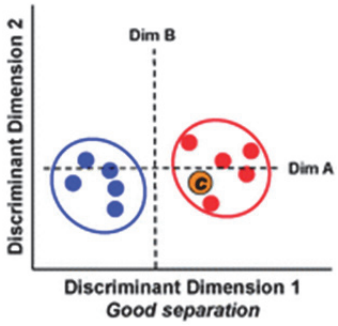

Figure 1.16 Score plots comparing data analyzed with LDA. Circled areas represent 95% confidence intervals. Clearly, group red and group blue is separated by (projecting on) Dim A while ambiguous with (projection on) Dim B. With this LDA description Dim A, orange circle C is clearly identified as part of red group.[139]

As an improvement to LDA, tensor discriminant analysis (TDA)[141-144] is an array generalization of LDA that takes advantage of high dimensionality. In other words, tensor discriminant analysis is used to classify multi-way measurements rather than one-way vector measurements.[141-143] For example, the data collected using colorimetric sensor arrays can be viewed as a 3-way tensor with the first way corresponding to choice of the dye, the second way corresponding to the effects of the color changes (i.e., ΔR, ΔG, ΔB), and the third way corresponding to time progression (for kinetic responses).[142, 143] The general strategy for tensor discriminant analysis is to find orthogonal linear classifiers of this three-way tensor to maximize the ratio of between-class variation to within-class variation. Tensor discriminant analysis can greatly improve the sensitivity, specificity, and computational efficiency of the discriminant analysis method because of the

dimensionality reduction. For example, if there are 36 dyes, then LDA would have to deal with 36*3=108 dimensions, whereas TDA would reduce that to 36+3=39 dimensions, thus eliminating 69 dimensions (i.e., 108-39) that contain primarily noise.[144]

1.5 Applications of Colorimetric Sensor Arrays

The following paragraphs are some examples of applications of optical sensors for single chemical detection and composite gas detection. The focus will be placed on the application of colorimetric sensors with some relevant fluorescent sensor arrays also discussed.

1.5.1 Discrimination of Volatile Organic Compounds and Pretreatment

The first colorimetric sensor array used various metalloporphyrins for the detection of different organic chemical families via ligation interaction. The sensor array was able to respond to a wide range of organic compounds such as alcohols, amines, ethers, phosphines, phosphites, thioethers, thiols, arenes, halocarbons and ketones. The sensitivity reached 1 ppm and the sensor array was immune to humidity.[20]

A later generation of the sensor array incorporated more dyes such as pH indicators, and solvatochromic dyes to a total of 24 probes[145] and greatly broadened the detection scope and improved the sensitivity. This array could selectively discriminate among very closely related amines (linear alkyl amines and even isomeric amines among them), with sub-ppm sensitivities (**Figure 1.17**).

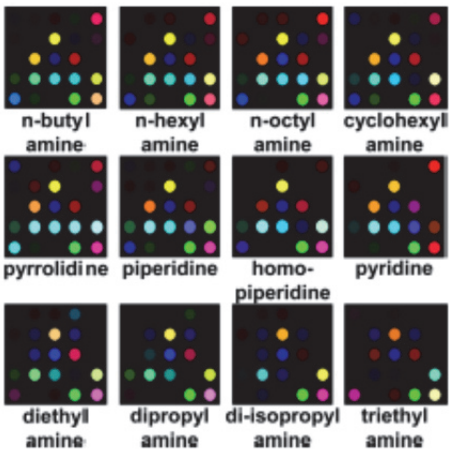

Figure 1.17 Color-difference maps for a family of 12 amines using a 24 spot colorimetric sensor array containing shape selective bis-pocket metalloporphyrins.[145]

With further expansion of the array to 36 probes that included dyes capable of Lewis acid-base, Brønsted acid-base, metal ion coordination, hydrogen bonding, and dipole interactions, the array could discriminate up to 100 different VOCs with no error (including chemicals with primary, secondary, tertiary, and aromatic substituents of amines, arenes, alcohols, aldehydes, carboxylic acids, esters, hydrocarbons, ketones, phosphines, and thiols). The high sensitivity is attributed to strong metal-analyte interactions, either by metal ligation (coordination) or by Brønsted acid-base interactions. Weakly coordinating vapors such as esters, ketones, alcohols, arenes, and hydrocarbons show a lower response due to weaker interactions. Again, with proper choice of dyes and substrate, the array shows no response to humidity. A selection of the difference maps for a representative subset of 24 VOCs is presented in **Figure 1.18.**

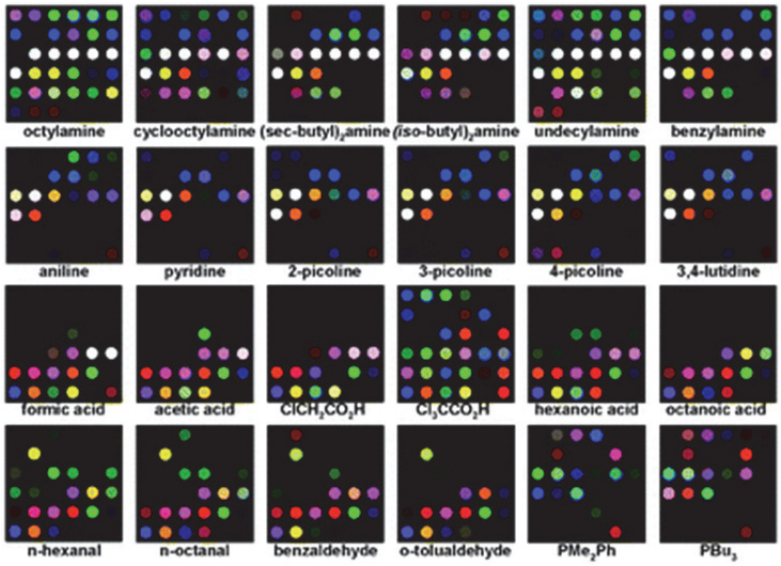

Figure 1.18 Colorimetric array response to VOCs visualized as color difference maps. Shown are 24 representative VOCs after equilibration at their saturated vapor pressure at 295 K.[79]

The PCA of this 100 VOC dataset shows a high level of dispersion of dimensionality, with 14 dimensions required to define 90% of the total variance, 22 dimensions for 95% of the total variance, and 40 dimensions for 99% (**Figure 1.15**). Moreover, HCA analysis shows a "family tree" type of clustering based on chemical

similarity, which is due to the chemical reactivity probing ability of the colorimetric sensor array (**Figure 1.14**).

Although these colorimetric sensor arrays succeed in targeting reactive chemical volatiles, they are not as sensitive to less reactive species such as aromatic hydrocarbons, chlorocarbons, or other organic solvents, which are important pollutants in indoor air. In order to solve this problem, a pre-oxidation technique was developed to convert these less-reactive chemicals into more responsive ones.[21] This peroxidation process typically involves passing the VOCs through an oxidation tube of chromic acid on silica and then let the product chemicals interact with the sensor array (**Figure 1.19**). This approach greatly improved the sensitivity (by ~300-fold with a better discrimination ability) for the detection of carboxylic acids, phenols, and aldehydes. With this pre-oxidation approach, common VOC pollutants in indoor air were studied at the level of immediately dangerous to life or health (IDLH) and at their permissible exposure limit (PEL) (**Figure 1.20**).[133]

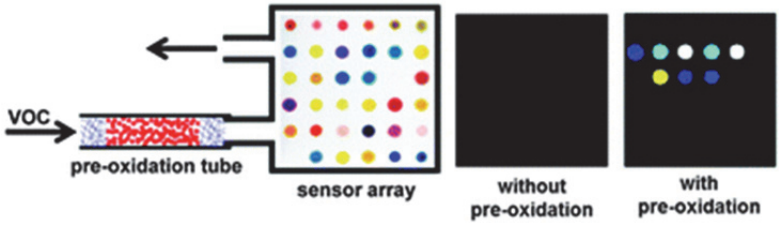

Figure 1.19 (left) Schematic illustration of the pre-oxidation technique. A Teflon tube is packed with chromic acid to pretreat the gas flow containing a VOC before it is passed over the colorimetric sensor array. As an illustration of improvement in array response capable with the pre-oxidation technique, difference maps showing array response to p-Xylene at IDLH concentration (middle) without and (right) with pre-oxidation treatment are shown above.[21]

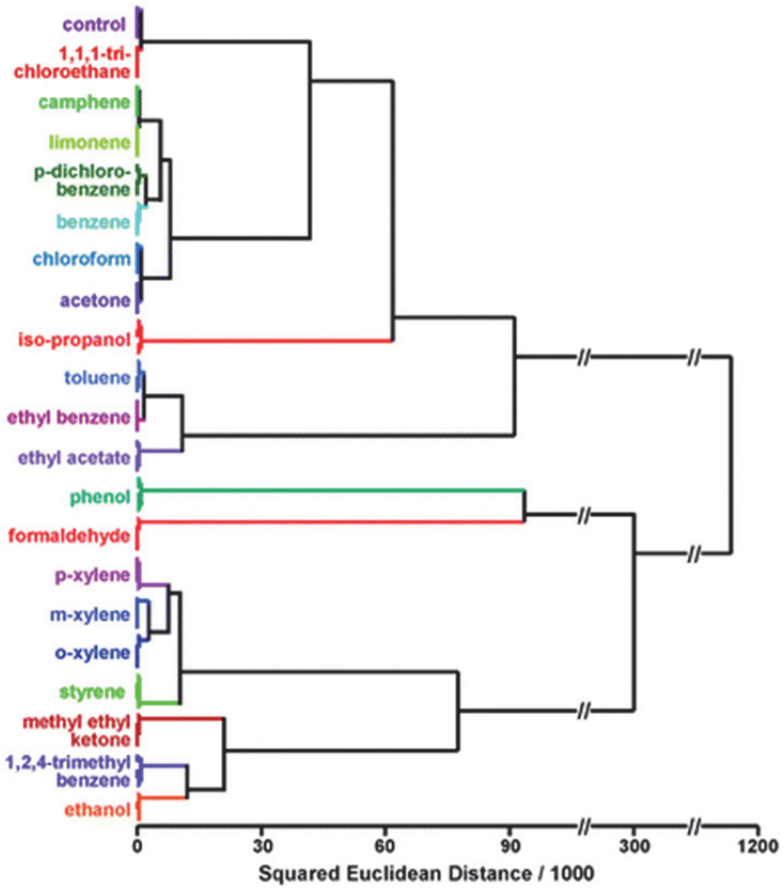

Figure 1.20 HCA dendrogram for 20 commonly found indoor pollutant VOCs at their IDLH concentrations and a control. All experiments were run in quintuplicate with 30 mg chromic acid on silica as the pre-oxidation reagent; no confusions or errors in classification were observed in 105 trials.[21]

1.5.2 Toxic Industrial Chemicals

Toxic industrial chemicals (TICs, such as HCl, HF, HCN etc.), are chemically reactive and are specifically harmful to living organisms, and thus a sensitive, cost-effective, and rapid detection method for field workers or soldiers is needed.[146]

Prior electronic nose technologies, as mentioned earlier, have their limitations due to reliance on physical analyte-sensor interactions, and thus have a limited ability to detect compounds at low concentrations (e.g., TICs at their IDLH or PEL concentrations). Colorimetric sensor arrays, on the other hand, are suitable for such detection in that they rely on strong and cross-responsive chemical interactions between the analytes and the array. Within less than 5 minutes of exposure, 20 TICs are detected and differentiated at

both IDLH and PEL levels,[19, 127, 132, 147]. HCA showed no mis-clustering errors and jackknifed LDA gave an error rate below 0.7% out of 147 trials (**Figure 1.21** and **Figure 1.22**). In addition, PCA analysis shows a high dimensionality with 17 PCA dimensions required to capture 95% of the variance.[127]

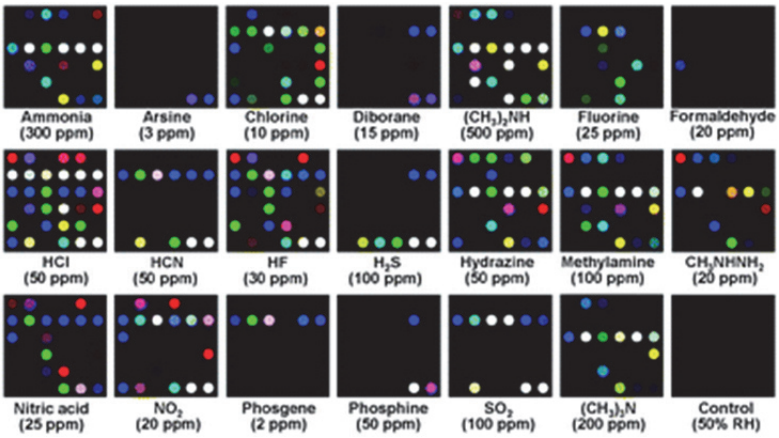

Figure 1.21 Color difference maps of 20 representative TICs at their IDLH.[147]

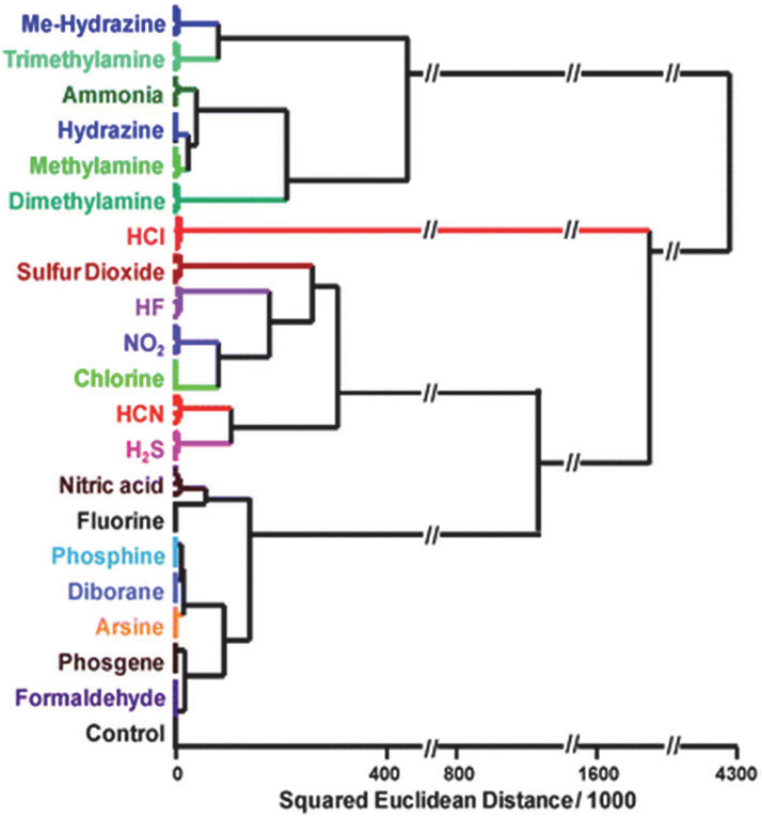

Figure 1.22 HCA dendrogram for 20 TICs at IDLH concentrations and a control. All experiments were performed in septuplicate; no confusions or errors in clustering were observed in 147 trials.[127]

1.5.3 Applications to Complex Mixtures

The analysis of complex mixtures presents a difficult challenge in the sensing field, and such complex mixtures include food, beverage, microbial culture, exhale from patients.

1.5.3.1 Foods and Beverages

Foods and beverages are characteristic in the complexity of their composition. A component by component analysis is generally too sophisticated to be practical, and often the overall quality of a complex mixture is necessary.

Coffee provides a readily available archetype of a diverse, multicomponent system. Depending on the fermentation process, VOCs in coffee can range from 300 to 1000 chemicals including carboxylic acids, alcohols, aldehydes, alkanes, alkenes, aromatics, esters, furans, ketones, lactones, oxazoles, phenols, pyridines, pyrazines, pyrroles, thiazoles, and thiophenes.[148-150] Moreover, the VOC aroma is also dependent on storage time and temperature. Thanks to the wide detection scope of TICs colorimetric sensor array, coffee aroma was successfully probed. [151] PCA revealed that the sensor array has as high as 18 dimensions required for 90% total variance and 25 for 95%. Furthermore, HCA shows no errors in classification of 55 trials (**Figure 1.23**).

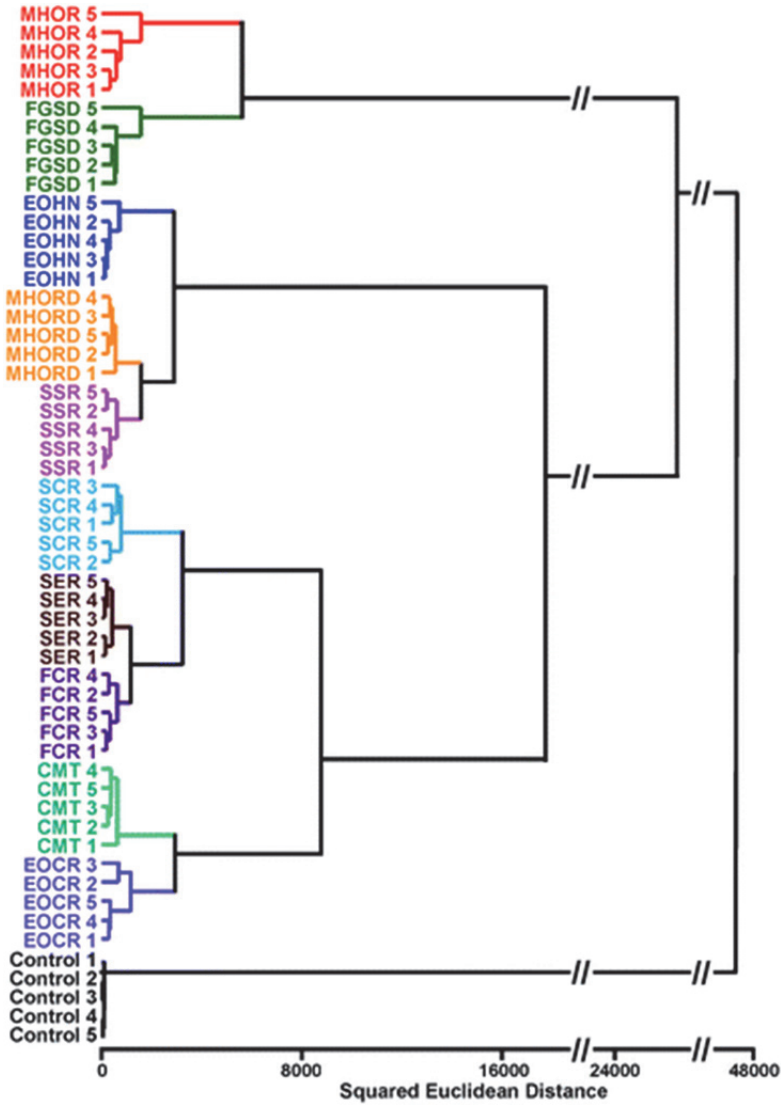

Figure 1.23 HCA for 10 commercially available coffees and a control. All experiments were run in quintuplet trials; no confusions or errors in classification were observed in 55 trials. Abbreviations: Maxwell House Original Roast, MHOR; Folgers Grande Supreme Decaf, FGSD; Eight O'Clock Hazel Nut, EOHN; Maxwell House Original Roast Decaf, MHORD; Starbucks Sumatra Roast, SSR; Starbucks Columbian Roast, SCR; Starbucks Espresso Roast, SER; Folgers Columbian Roast, FCR; Café Mai Traditional, CMT; Eight O'Clock Columbian Roast, EOCR; the number indicates nth trial; Control = no coffee present.[151]

In a solution based colorimetric sensing approach, commercially available soft drinks were analyzed and differentiated with hydrophobic membrane substrates.[152] Fourteen commercial soft drinks were analyzed and facile identification of all of the soft drinks was readily achieved with a misclassification of 2% using HCA. This work demonstrates the potential of colorimetric sensor array technology for quality assurance/control applications of sodas and perhaps other beverages as well. Similar applications have also pursued differentiation of 18 brands of beer. [153] Ales and lagers (**Figure 1.24**) were differentiated without error with <3% error among very similar beers. Moreover, 5 Chinese distilled alcoholic beverage (baijiu) could be differentiated with no misclassification in HCA and LDA.[154]

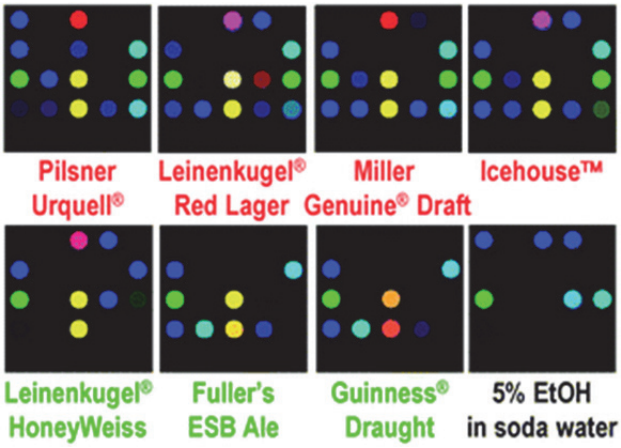

Figure 1.24 Colorimetric array analysis of a complex mixtures: headspace analysis of various beers compared to 5% ethanol in carbonated water. Brands in red are lagers, brands in green are ales.[8]

A third very useful application for colorimetric sensor arrays is food spoilage monitoring, including meat, poultry, and fish freshness. In a report on monitoring fish meat aging, a colorimetric sensor array on a reverse silica plate is used.[155] These arrays were sensitive to the spoilage rate of fish meat with 87.5% accuracy. Recently an optoelectronic nose was also constructed to monitor chicken meat aging in a similar fashion.[156]

1.5.3.2 Detection and Identification of Bacteria

The detection and identification of bacteria is a pressing issue in both medicine and industry.[157-160] Existing methods for identification of pathogenic bacteria are limited by long turnaround times, the need of highly trained laboratory personnel, and the requirement of expensive and high-maintenance equipment.[161-166]

Bacteria stink: that is, they produce volatile organic compounds to which the mammalian olfactory system is highly responsive. Consequently, an experienced microbiologist can readily identify many bacteria by smell. Applications of prior electronic nose technology, however, have been limited by the low dimensionality of traditional sensor arrays (e.g., metal oxides) and have achieved only modest success, even when attempting to classify a small number of bacterial species.[167-169]

Using a disposable colorimetric sensor array, 10 different strains of human pathogenic bacteria were differentiated and identified based on volatile compounds produced during bacterial growth. In 164 trials monitoring bacterial growth as a function of time, the growth profiles of different bacteria were able to identify even by the naked eye. With less than 10 hours of culture time, 98.8% accuracy (evaluated by jackknifed LDA using time stacked data) was achieved.[170] **Figure 1.25** shows the color difference maps and time evolution of the array response to the head-gas mixture produced in sealed Petri dishes.

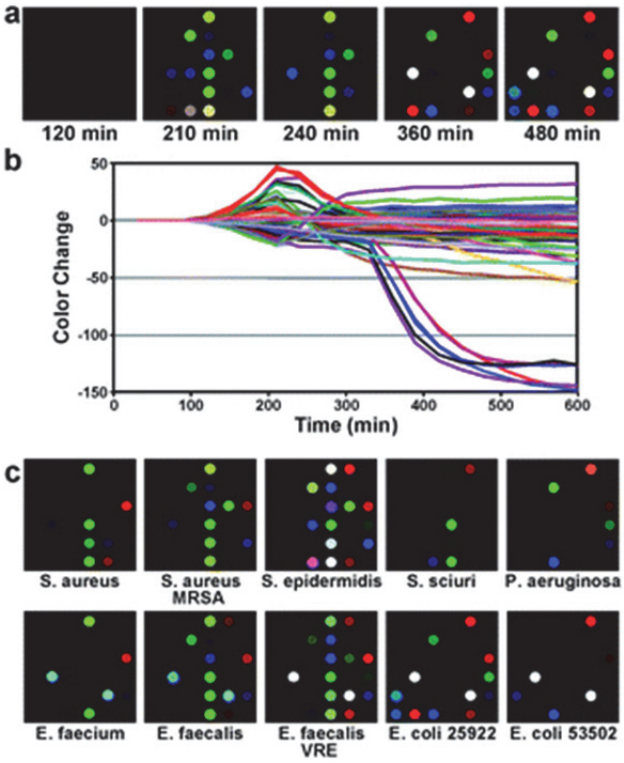

Figure 1.25 (a) Color difference maps and the time response profile resulting from colorimetric sensor array exposure to a growing culture of *E. coli*, American Type Culture Collection (ATCC) #25922. (b) The color change values versus time plotted for all color channels (ΔR, Δ G, and Δ B values for each spot, i.e., 108 color channels) at each time point. (c) Color difference maps for 10 different bacterial strains resulting from colorimetric sensor array exposure to Petri dish-grown cultures after 480 min.[170]

Similar to bacteria, fungi can also be identified and differentiated with a colorimetric sensor array. A detailed description of the identification and detection of fungi (yeast) is in the next chapter.

1.5.3.3 Breath Analysis for Diagnosis

Due to their success with complex mixture differentiation, colorimetric sensor arrays have also been applied to medical diagnosis of disease. This is under the premise that different cell lines (either microorganisms or cancer cells) produce different volatile metabolites during metabolism. As a result, human breath is in principle in equilibrium with the volatiles produced within the body. Breath analysis has a long history as a diagnostic tool[171-173] but due it its low sensitivity and specificity (or sometimes high cost

due to the advanced instrumentation needed) the clinical or hospital applicability is limited. Electronic noses have been explored for breath analysis, especially for diagnosis of lung cancer or respiratory infections but only achieved limited success.[171, 173, 174]

As mentioned earlier, the colorimetric sensor array has been successfully developed for bacterial identification[170] and has also demonstrated some preliminary clinical success for breath diagnosis with an accuracy of 90% in initial studies.[175] Lung cancer screening using breath analysis has also been reported with promising initial results.[174] In a study with 229 subjects (92 with lung cancer), individuals with different histologies were accurately distinguished from one another (86.4% for adeno-carcinoma vs. squamous cell carcinoma), and the accuracy of breath bio-signatures could be optimized by incorporating clinical risk factors.[174]

1.6 Summary and Outlook

In summary, colorimetric sensor arrays have the following advantages:

(1) They give a composite response to not only single component volatiles but also to complex mixtures. The ability to fingerprint complex mixtures is often more facile using such techniques as GC-MS. Although traditionally we are more used to a complete qualitative and quantitative analysis of each analyte, for multi-component analyses sometimes the goal is simply "are those analytes the same" or "is this mixture genuine or not"? In the latter case, colorimetric sensor arrays (or other optoelectronic noses) have their unique niche.

(2) Sensor arrays aim to probe analytes with chemical interactions, rather than physical interactions. And because of this and its ability to interact with volatiles in a cross responsive way, sensor arrays have high sensitivity to those analytes that are chemically reactive, which is often the analytes of concern (e.g., toxic gases).

There are, however, also limitations to sensor arrays:

(1) They can only give a composite response to analytes. Unlike GC-MS or other analytical methods, component by component analysis is generally out of the question. Depending on the goal of the project, one should carefully choose the appropriate analytical tools.

(2) Because they interact quickly with analytes with high chemical reactivity, probing less reactive chemicals could potentially be challenging and sometimes an

enhancement method (e.g., pre-oxidation) could be necessary. Moreover, because of the relatively low S/N ratio from less reactive chemicals, the interference from highly reactive ones could significantly affect the ability of the sensor array to detect these compounds.

(3) Though there was only limited discussion in this chapter, liquid phase sensing has several additional challenges such as dye blooming, dye leaching, change of response due to refractive index, and contamination from the ambient environment. In principle, one way to solve such problems is to immobilize dyes in a sol-gel formulation but in practice immobilization is difficult to achieve in conjunction with other necessary properties.

In the next chapter, an example of the use of a colorimetric sensor array for the identification of fungi is demonstrated. It is the first successful application for sensing eukaryotic cells with a wider and better accuracy than other examples in literature.

1.7 References

(1) Persaud, K.; Dodd, G. Analysis of discrimination mechanisms in the mammalian olfactory system using a model nose. *Nature* **1982,** 299, 352-355.

(2) Hierlemann, A.; Gutierrez-Osuna, R. Higher-order chemical sensing. *Chem. Rev.* **2008,** 108, 563-613.

(3) Suslick, K. S. Synesthesia in science and technology: more than making the unseen visible. *Curr. Opin. Chem. Biol.* **2012,** 16, 557-563.

(4) Stitzel, S. E.; Aernecke, M. J.; Walt, D. R. Artificial Noses. *Annu. Rev. Biomed. Eng.* **2011,** 13, 1-25.

(5) Paolesse, R.; Monti, D.; Dini, F.; Di Natale, C., Fluorescence Based Sensor Arrays. In *Luminescence Applied in Sensor Science*, Prodi, L.; Montalti, M.; Zaccheroni, N., Eds. 2011; Vol. 300, pp 139-174.

(6) Rock, F.; Barsan, N.; Weimar, U. Electronic nose: Current status and future trends. *Chem. Rev.* **2008,** 108, 705-725.

(7) Nakamoto, T.; Ishida, H. Chemical sensing in spatial/temporal domains. *Chem. Rev.* **2008,** 108, 680-704.

(8) Suslick, K. S.; Rakow, N. A.; Sen, A. Colorimetric sensor arrays for molecular recognition. *Tetrahedron* **2004,** 60, 11133-11138.

(9) Turner, A. P. F.; Magan, N. Electronic noses and disease diagnostics. *Nature Reviews Microbiology* **2004,** 2, 161-166.

(10) Lewis, N. S. Comparisons between mammalian and artificial olfaction based on arrays of carbon black-polymer composite vapor detectors. *Acc. Chem. Res.* **2004,** 37, 663-672.

(11) Janata, J., *Principles of Chemical Sensors, Second Edition*. 2009; p 1-373.

(12) Suslick, K. S. An optoelectronic nose: "Seeing" smells by means of colorimetric sensor arrays. *MRS Bull.* **2004,** 29, 720-725.

(13) Anker, J. N.; Hall, W. P.; Lyandres, O.; Shah, N. C.; Zhao, J.; Van Duyne, R. P. Biosensing with plasmonic nanosensors. *Nature Mater.* **2008,** 7, 442-453.

(14) Jeon, S.; Ahn, S. E.; Song, I.; Kim, C. J.; Chung, U. I.; Lee, E.; Yoo, I.; Nathan, A.; Lee, S.; Robertson, J.; Kim, K. Gated three-terminal device architecture to eliminate persistent photoconductivity in oxide semiconductor photosensor arrays. *Nature Mater.* **2012,** 11, 301-305.

(15) Kubo, W.; Fujikawa, S. Au double nanopillars with nanogap for plasmonic sensor. *Nano Lett.* **2011,** 11, 8-15.

(16) Lu, Y.; Peng, S.; Luo, D.; Lal, A. Low-concentration mechanical biosensor based on a photonic crystal nanowire array. *Nature Commun.* **2011,** 2.

(17) Wang, S.; Ota, S.; Guo, B.; Ryu, J.; Rhodes, C.; Xiong, Y.; Kalim, S.; Zeng, L.; Chen, Y.; Teitell, M. A.; Zhang, X. Subcellular resolution mapping of endogenous cytokine secretion by nano-plasmonic-resonator sensor array. *Nano Lett.* **2011,** 11, 3431-3434.

(18) Wang, S.; Pile, D. F. P.; Sun, C.; Zhang, X. Nanopin plasmonic resonator array and its optical properties. *Nano Lett.* **2007,** 7, 1076-1080.

(19) Lim, S. H.; Feng, L.; Kemling, J. W.; Musto, C. J.; Suslick, K. S. An optoelectronic nose for the detection of toxic gases. *Nature Chem.* **2009,** 1, 562-567.

(20) Rakow, N. A.; Suslick, K. S. A colorimetric sensor array for odour visualization. *Nature* **2000,** 406, 710-713.

(21) Lin, H.; Jang, M.; Suslick, K. S. Preoxidation for colorimetric sensor array detection of VOCs. *J. Am. Chem. Soc.* **2011,** 133, 16786-9.

(22) Gründler, P., *Chemical Sensors, An Introduction for Scientists and Engineers*. Springer-Verlag: Berlin Heidelberg, 2007.

(23) Janata, J. Centennial Retrospective on Chemical Sensors. *Anal. Chem.* **2001,** 73, 150 A-153 A.

(24) Stetter, J. R.; Li, J. Amperometric gas sensors - A review. *Chem. Rev.* **2008,** 108, 352-366.

(25) Ahmed, M. U.; Hossain, M. M.; Tamiya, E. Electrochemical biosensors for medical and food applications. *Electroanalysis* **2008,** 20, 616-626.

(26) Tomchenko, A. A.; Harmer, G. P.; Marquis, B. T.; Allen, J. W. Semiconducting metal oxide sensor array for the selective detection of combustion gases. *Sens. Actuators, B* **2003,** 93, 126-134.

(27) Ho, G. W. Gas Sensor with Nanostructured Oxide Semiconductor Materials. *Sci. Adv. Mater.* **2011,** 3, 150-168.

(28) Potyrailo, R. A.; Surman, C.; Nagraj, N.; Burns, A. Materials and Transducers Toward Selective Wireless Gas Sensing. *Chem. Rev.* **2011,** 111, 7315-7354.

(29) James, D.; Scott, S. M.; Ali, Z.; O'Hare, W. T. Chemical Sensors for Electronic Nose Systems. *Microchimica Acta* **2005,** 149, 1-17.

(30) Janata, J.; Josowicz, M. Organic semiconductors in potentiometric gas sensors. *J. Solid State Electrochem.* **2009,** 13, 41-49.

(31) Ronkainen, N. J.; Halsall, H. B.; Heineman, W. R. Electrochemical biosensors. *Chem. Soc. Rev.* **2010,** 39, 1747-1763.

(32) Nambiar, S.; Yeow, J. T. W. Conductive polymer-based sensors for biomedical applications. *Biosensors & Bioelectronics* **2011,** 26, 1825-1832.

(33) Zanardi, C.; Terzi, F.; Seeber, R. Polythiophenes and polythiophene-based composites in amperometric sensing. *Anal. Bioanal. Chem* **2013,** 405, 509-531.

(34) Grate, J. W. Acoustic wave microsensor arrays for vapor sensing. *Chem. Rev.* **2000,** 100, 2627-2647.

(35) Snow, E. S.; Perkins, F. K.; Houser, E. J.; Badescu, S. C.; Reinecke, T. L. Chemical Detection with a Single-Walled Carbon Nanotube Capacitor. *Science* **2005,** 307, 1942-1945.

(36) Park, S.; Vosguerichian, M.; Bao, Z. A. A review of fabrication and applications of carbon nanotube film-based flexible electronics. *Nanoscale* **2013,** 5, 1727-1752.

(37) Cui, Y.; Wei, Q.; Park, H.; Lieber, C. M. Nanowire Nanosensors for Highly Sensitive and Selective Detection of Biological and Chemical Species. *Science* **2001,** 293, 1289-1292.

(38) Patolsky, F.; Zheng, G.; Lieber, C. M. Nanowire sensors for medicine and the life sciences. *Nanomedicine* **2006,** 1, 51-65.

(39) Sharma, S.; Madou, M. A new approach to gas sensing with nanotechnology. *Philosophical Transactions of the Royal Society a-Mathematical Physical and Engineering Sciences* **2012,** 370, 2448-2473.

(40) Zhu, Z. G.; Garcia-Gancedo, L.; Flewitt, A. J.; Xie, H. Q.; Moussy, F.; Milne, W. I. A Critical Review of Glucose Biosensors Based on Carbon Nanomaterials: Carbon Nanotubes and Graphene. *Sensors* **2012,** 12, 5996-6022.

(41) Gan, T.; Hu, S. S. Electrochemical sensors based on graphene materials. *Microchimica Acta* **2011,** 175, 1-19.

(42) Ma, Q.; Su, X. G. Recent advances and applications in QDs-based sensors. *Analyst* **2011,** 136, 4883-4893.

(43) Pumera, M.; Ambrosi, A.; Bonanni, A.; Chng, E. L. K.; Poh, H. L. Graphene for electrochemical sensing and biosensing. *Trac-Trends in Analytical Chemistry* **2010,** 29, 954-965.

(44) Bakker, E.; Qin, Y. Electrochemical Sensors. *Anal. Chem.* **2006,** 78, 3965-3984.

(45) Privett, B. J.; Jae, H. S.; Schoenfisch, M. H. Electrochemical sensors. *Anal. Chem.* **2008,** 80, 4499-4517.

(46) Privett, B. J.; Shin, J. H.; Schoenfisch, M. H. Electrochemical sensors. *Anal. Chem.* **2010,** 82, 4723-4741.

(47) Kimmel, D. W.; LeBlanc, G.; Meschievitz, M. E.; Cliffel, D. E. Electrochemical Sensors and Biosensors. *Anal. Chem.* **2011,** 84, 685-707.

(48) Brett, C. M. A. Novel sensor devices and monitoring strategies for green and sustainable chemistry processes. *Pure Appl. Chem.* **2007,** 79, 1969-1980.

(49) Hanrahan, G.; Patil, D. G.; Wang, J. Electrochemical sensors for environmental monitoring: design, development and applications. *J. Environ. Monit.* **2004,** 6, 657-664.

(50) Campas, M.; Garibo, D.; Prieto-Simon, B. Novel nanobiotechnological concepts in electrochemical biosensors for the analysis of toxins. *Analyst* **2012,** 137, 1055-1067.

(51) Parellada, J.; Narváez, A.; López, M. A.; Domínguez, E.; Fernández, J. J.; Pavlov, V.; Katakis, I. Amperometric immunosensors and enzyme electrodes for environmental applications. *Anal. Chim. Acta* **1998,** 362, 47-57.

(52) Solé, S.; Alegret, S. Environmental toxicity monitoring using electrochemical biosensing systems. *Environ. Sci. Pollut. Res.* **2001,** 8, 256-264.

(53) Dalbasti, T.; Kilinc, E., Microelectrode for in vivo real-time detection of NO. In 2005; Vol. 396, pp 584-592.

(54) Wang, Y.; Xu, H.; Zhang, J.; Li, G. Electrochemical sensors for clinic analysis. *Sensors* **2008,** 8, 2043-2081.

(55) Hahn, C. E. W. Electrochemical analysis of clinical blood-gases, gases and vapours. *Analyst* **1998,** 123, 57R-86R.

(56) Pedrero, M.; Campuzano, S.; Pingarron, J. M. Electrochemical genosensors based on PCR strategies for microorganisms detection and quantification. *Anal. Methods* **2011,** 3, 780-789.

(57) Laschi, S.; Centi, S.; Mascini, M. Electrochemical arrays coupled with magnetic separators for immunochemistry. *Bioanal. Rev.* **2011,** 3, 11-25.

(58) Shiddiky, M. J. A.; Torriero, A. A. J. Application of ionic liquids in electrochemical sensing systems. *Biosens. Bioelectron.* **2011,** 26, 1775-1787.

(59) Song, S.; Xu, H.; Fan, C. Potential diagnostic applications of biosensors: current and future directions. *Int. J. Nanomed.* **2006,** 1, 433-440.

(60) Serra, B.; Reviejo, Á. J.; Pingarrón, J. M., Chapter 13 Application of electrochemical enzyme biosensors for food quality control. In *Comprehensive Analytical Chemistry*, Alegret, S.; Merkoçi, A., Eds. Elsevier: 2007; Vol. Volume 49, pp 255-298.

(61) Pedrero, M.; Campuzano, S.; Pingarrón, J. M. Magnetic Beads-Based Electrochemical Sensors Applied to the Detection and Quantification of Bioterrorism/Biohazard Agents. *Electroanalysis* **2012,** 24, 470-482.

(62) Danielsson, B.; Mosbach, K.; Winquist, F.; Lundström, I. Biosensors based on thermistors and semiconductors and their bioanalytical applications. *Sens. Actuators* **1988,** 13, 139-146.

(63) Barsony, I.; Ducso, C.; Furjes, P., *Thermometric Gas Sensing*. Springer: New York, 2009; p 237-260.

(64) Ramanathan, K.; Jönsson, B. R.; Danielsson, B. Thermometric Sensing of Peroxide in Organic Media. Application To Monitor the Stability of RBP−Retinol−HRP Complex. *Anal. Chem.* **2000,** 72, 3443-3448.

(65) Ramanathan, K.; Jönsson, B. R.; Danielsson, B. Sol–gel based thermal biosensor for glucose. *Anal. Chim. Acta* **2001,** 427, 1-10.

(66) Yakovleva, M.; Bhand, S.; Danielsson, B. The enzyme thermistor-A realistic biosensor concept. A critical review. *Anal. Chim. Acta* **2013,** 766, 1-12.

(67) Mandenius, C. F.; Bülow, L.; Danielsson, B.; Mosbach, K. Monitoring and control of enzymic sucrose hydrolysis using on-line biosensors. *Appl. Microbiol. Biotechnol.* **1985,** 21, 135-142.

(68) Xie, B.; Ramanathan, K.; Danielsson, B. Mini/micro thermal biosensors and other related devices for biochemical/clinical analysis and monitoring. *TrAC, Trends Anal. Chem.* **2000,** 19, 340-349.

(69) Xie, B.; Mecklenburg, M.; Danielsson, B.; Öhman, O.; Winquist, F. Microbiosensor based on an integrated thermopile. *Anal. Chim. Acta* **1994,** 299, 165-170.

(70) Bataillard, P.; Steffgen, E.; Haemmerli, S.; Manz, A.; Widmer, H. M. An integrated silicon thermopile as biosensor for the thermal monitoring of glucose, urea and penicillin. *Biosens. Bioelectron.* **1993,** 8, 89-98.

(71) Zhang, Y.; Tadigadapa, S. Calorimetric biosensors with integrated microfluidic channels. *Biosens. Bioelectron.* **2004,** 19, 1733-1743.

(72) Shimohigoshi, M.; Karube, I. Development of uric acid and oxalic acid sensors using a bio-thermochip. *Sensors and Actuators, B: Chemical* **1996,** 30, 17-21.

(73) Mecklenburg, M.; Lindbladh, C.; Li, H.; Mosbach, K.; Danielsson, B. Enzymatic amplification of a flow-injected thermometric enzyme-linked immunoassay for human insulin. *Anal. Biochem.* **1993,** 212, 388-393.

(74) Scheller, F.; Siegbahn, N.; Danielsson, B.; Mosbach, K. High-sensitivity enzyme thermistor determination of L-lactate by substrate recycling. *Anal. Chem.* **1985,** 57, 1740-1743.

(75) Wolf, A.; Weber, A.; Hüttl, R.; Lerchner, J.; Wolf, G. Sequential flow injection analysis of complex systems using calorimetric detection. *Thermochim. Acta* **2002,** 382, 89-98.

(76) Xie, B.; Mecklenburg, M.; Danielsson, B.; Ohman, O.; Norlin, P.; Winquist, F. Development of an integrated thermal biosensor for the simultaneous determination of multiple analytes. *Analyst* **1995,** 120, 155-160.

(77) Jerónimo, P. C. A.; Araújo, A. N.; Conceição B.S.M. Montenegro, M. Optical sensors and biosensors based on sol–gel films. *Talanta* **2007,** 72, 13-27.

(78) Nassau, K., *The Physics and Chemistry of Color*. Wiley: New York, 2001.

(79) Janzen, M. C.; Ponder, J. B.; Bailey, D. P.; Ingison, C. K.; Suslick, K. S. Colorimetric sensor arrays for volatile organic compounds. *Anal. Chem.* **2006,** 78, 3591-3600.

(80) El-Desouki, M.; Deen, M. J.; Fang, Q. Y.; Liu, L.; Tse, F.; Armstrong, D. CMOS Image Sensors for High Speed Applications. *Sensors* **2009,** 9, 430-444.

(81) Meier, R. J.; Fischer, L. H.; Wolfbeis, O. S.; Schaferling, M. Referenced luminescent sensing and imaging with digital color cameras: A comparative study. *Sens. Actuator B-Chem.* **2013,** 177, 500-506.

(82) Lakowicz, J. R., *Principles of Fluorescence Spectroscopy, 3rd ed.* 4th Printing: New York, 2006.

(83) Podbielska, H.; Ulatowska-Jarza, A.; Muller, G.; Eichler, H. J., Sol-Gels for Optical Sensors. In *Optical Chemical Sensors*, Baldini, F.; Chester, A. N.; Homola, J.; Martellucci, S., Eds. Springer: Erice, Italy, 2006.

(84) Orellana, G., Fluorescence –Based Sensors. In *Optical Chemical Sensors*, Baldini, F.; Chester, A. N.; Homola, J.; Martellucci, S., Eds. 2006; pp 99-116.

(85) Bonacchi, S.; Genovese, D.; Juris, R.; Montalti, M.; Prodi, L.; Rampazzo, E.; Sgarzi, M.; Zaccheroni, N., Luminescent Chemosensors Based on Silica Nanoparticles. In *Topics in Current Chemistry: Luminescence Applied in Sensor Science*, Prodi, L.; Montalti, M.; Zaccheroni, N., Eds. Springer Berlin / Heidelberg: 2011; Vol. 300, pp 93-138.

(86) dos Santos, C. M. G.; Harte, A. J.; Quinn, S. J.; Gunnlaugsson, T. Recent developments in the field of supramolecular lanthanide luminescent sensors and self-assemblies. *Coord. Chem. Rev.* **2008,** 252, 2512-2527.

(87) Thomas, S. W.; Joly, G. D.; Swager, T. M. Chemical Sensors Based on Amplifying Fluorescent Conjugated Polymers. *Chem. Rev.* **2007,** 107, 1339-1386.

(88) de Silva, A. P.; Gunaratne, H. Q. N.; Gunnlaugsson, T.; Huxley, A. J. M.; McCoy, C. P.; Rademacher, J. T.; Rice, T. E. Signaling Recognition Events with Fluorescent Sensors and Switches. *Chem. Rev.* **1997,** 97, 1515-1566.

(89) Newman, R. H.; Fosbrink, M. D.; Zhang, J. Genetically Encodable Fluorescent Biosensors for Tracking Signaling Dynamics in Living Cells. *Chem. Rev.* **2011,** 111, 3614-3666.

(90) Wade, C. R.; Broomsgrove, A. E. J.; Aldridge, S.; Gabbaï, F. o. P. Fluoride Ion Complexation and Sensing Using Organoboron Compounds. *Chem. Rev.* **2010,** 110, 3958-3984.

(91) Lee, J. Y.; Kim, S. K.; Jung, J. H.; Kim, J. S. Bifunctional Fluorescent Calix[4]arene Chemosensor for Both a Cation and an Anion. *J. Org. Chem.* **2005,** 70, 1463-1466.

(92) Turkewitsch, P.; Wandelt, B.; Darling, G. D.; Powell, W. S. Fluorescent Functional Recognition Sites through Molecular Imprinting. A Polymer-Based Fluorescent Chemosensor for Aqueous cAMP. *Anal. Chem.* **1998,** 70, 2025-2030.

(93) Wiskur, S. L.; Ait-Haddou, H.; Lavigne, J. J.; Anslyn, E. V. Teaching Old Indicators New Tricks. *Acc. Chem. Res.* **2001,** 34, 963-972.

(94) Pinalli, R.; Dalcanale, E. Supramolecular Sensing with Phosphonate Cavitands. *Acc. Chem. Res.* **2013,** 46, 399-411.

(95) Nguyen, B. T.; Anslyn, E. V. Indicator-displacement assays. *Coord. Chem. Rev.* **2006,** 250, 3118-3127.

(96) Umali, A. P.; Anslyn, E. V. A general approach to differential sensing using synthetic molecular receptors. *Curr. Opin. Chem. Biol.* **2010,** 14, 685-692.

(97) Wright, A. T.; Anslyn, E. V. Differential receptor arrays and assays for solution-based molecular recognition. *Chem. Soc. Rev.* **2006,** 35, 14-28.

(98) Booksh, K. S.; Kowalski, B. R. Theory of analytical chemistry. *Anal. Chem.* **1994,** 66, 782A-791A.

(99) Hunter, C. A. Quantifying intermolecular interactions: Guidelines for the molecular recognition toolbox. *Angew. Chem.-Int. Edit.* **2004,** 43, 5310-5324.

(100) Rigby, M.; Smith, E. B.; Wakeham, W. A.; Maitland, G. C., *The Forces Between Molecules*. Clarendon: Oxford, 1986.

(101) Müller-Dethlefs, K.; Hobza, P. Noncovalent Interactions: A Challenge for Experiment and Theory. *Chem. Rev.* **1999,** 100, 143-168.

(102) Hsieh, M. D.; Zellers, E. T. Limits of recognition for simple vapor mixtures determined with a microsensor array. *Anal. Chem.* **2004,** 76, 1885.

(103) Healey, B. G.; Walt, D. R. *Anal. Chem.* **1997,** 69, 2213.

(104) Lavigne, J. J.; Anslyn, E. V. Sensing A Paradigm Shift in the Field of Molecular Recognition. From Seeking Selective to Seeking Differential Receptors. *Angew. Chem. Int. Ed.* **2001,** 40, 3118-3130.

(105) Dini, F.; Magna, G.; Martinelli, E.; Paolesse, R.; Filippini, D.; Lundstrcm, I.; Di Natale, C. In *Gas sensitivity of blends of metalloporphyrins and colorimetric acid-base indicators*, Procedia Engineering, 2012; 2012; pp 1413-1416.

(106) Kolthoff, I. M., *Acid Base Indicators*. Macmillan: New York, 1937.

(107) Green, F. J., *The Sigma-Aldrich Handbook of Stains, Dyes and Indicators*. Aldrich Chemical Co., Inc.: Milwaukee, WI, 1990.

(108) Lee, J.-S.; Yoon, N.-R.; Kang, B.-H.; Lee, S.-W.; Gopalan, S.-A.; Jeong, H.-M.; Lee, S.-H.; Kwon, D.-H.; Kang, S.-W. Response Characterization of a Fiber Optic Sensor Array with Dye-Coated Planar Waveguide for Detection of Volatile Organic Compounds. *Sensors* **2014,** 14, 11659-11671.

(109) Reichardt, C.; Welton, T., *Solvents and solvent effects in organic chemistry, 4th ed.* Wiley-VCH: Weinheim, 2010.

(110) Reichardt, C., *Solvent Effects in Organic Chemistry, 2nd ed.* Verlag Chemie: Weinheim, 1988.

(111) Reichardt, C. SOLVATOCHROMIC DYES AS SOLVENT POLARITY INDICATORS. *Chem. Rev.* **1994,** 94, 2319-2358.

(112) Reichardt, C. Polarity of ionic liquids determined empirically by means of solvatochromic pyridinium N-phenolate betaine dyes. *Green Chemistry* **2005,** 7, 339-351.

(113) Reichardt, C. Solvents and solvent effects: An introduction. *Organic Process Research & Development* **2007,** 11, 105-113.

(114) Kamlet, M. J.; Abboud, J. L. M.; Taft, R. W. An examination of linear free energy relationships. *Prog. Phys. Org. Chem.* **1981,** 13, 485-630.

(115) Taft, R. W.; Abboud, J. L. M.; Kamlet, M. J.; Abraham, M. H. LINEAR SOLVATION ENERGY RELATIONS. *J. Solution Chem.* **1985,** 14, 153-186.

(116) Cabot, R.; Hunter, C. A. Molecular probes of solvation phenomena. *Chem. Soc. Rev.* **2012,** 41, 3485-3492.

(117) Mancini, P. M.; Adam, C. G.; Fortunato, G. G.; Vottero, L. R. A comparison of nonspecific solvent scales. Degree of agreement of microscopic polarity values obtained by different measurement methods. *Arkivoc* **2007,** 266-280.

(118) Marini, A.; Muñoz-Losa, A.; Biancardi, A.; Mennucci, B. What is Solvatochromism? *J. Phys. Chem. B* **2010,** 114, 17128-17135.

(119) Matyushov, D. V.; Schmid, R.; Ladanyi, B. M. A thermodynamic analysis of the pi* and E(T)(30) polarity scales. *J. Phys. Chem. B* **1997,** 101, 1035-1050.

(120) Buncel, E.; Rajagopal, S. SOLVATOCHROMISM AND SOLVENT POLARITY SCALES. *Acc. Chem. Res.* **1990,** 23, 226-231.

(121) Katritzky, A. R.; Fara, D. C.; Yang, H. F.; Tamm, K.; Tamm, T.; Karelson, M. Quantitative measures of solvent polarity. *Chem. Rev.* **2004,** 104, 175-198.

(122) Wolfbeis, O. S. Fiber-optic chemical sensors and biosensors. *Anal. Chem.* **2008,** 80, 4269-4283.

(123) Lin, H.; Suslick, K. S. A Colorimetric Sensor Array for Detection of Triacetone Triperoxide Vapor. *J. Am. Chem. Soc.* **2010,** 132, 15519-15521.

(124) Lobnik, A.; Čajlaković, M. Sol–gel based optical sensor for continuous determination of dissolved hydrogen peroxide. *Sens. Actuators, B* **2001,** 74, 194-199.

(125) Long, J.; Xu, J.; Yang, Y.; Wen, J.; Jia, C. A colorimetric array of metalloporphyrin derivatives for the detection of volatile organic compounds. *Mat. Sci. Eng. B* **2011,** 176, 1271-1276.

(126) Rottman, C.; Grader, G.; De Hazan, Y.; Melchior, S.; Avnir, D. Surfactant-induced modification of dopants reactivity in sol-gel matrixes. *J. Am. Chem. Soc.* **1999,** 121, 8533-8543.

(127) Feng, L.; Musto, C. J.; Kemling, J. W.; Lim, S. H.; Zhong, W.; Suslick, K. S. Colorimetric sensor array for determination and identification of toxic industrial chemicals. *Anal. Chem.* **2010,** 82, 9433-9440.

(128) Suslick, K. S.; Bailey, D. P.; Ingison, C. K.; Janzen, M.; Kosal, M. E.; McNamara III, W. B.; Rakow, N. A.; Sen, A.; Weaver, J. J.; Wilson, J. B.; Zhang, C.; Nakagaki, S. Seeing smells: Development of an optoelectronic nose. *Quim. Nova* **2007,** 30, 677-681.

(129) Zhang, C.; Suslick, K. S. A Colorimetric Sensor Array for Organics in Water. *J. Am. Chem. Soc.* **2005,** 127, 11548-11549.

(130) Kemling, J. W.; Suslick, K. S. Nanoscale porosity in pigments for chemical sensing. *Nanoscale* **2011,** 3, 1971-1973.

(131) Lukowiak, A.; Strek, W. Sensing abilities of materials prepared by sol-gel technology. *J. Sol-Gel Sci. Technol.* **2009,** 50, 201-215.

(132) Lim, S. H.; Kemling, J. W.; Feng, L.; Suslick, K. S. A colorimetric sensor array of porous pigments. *Analyst* **2009,** 134, 2453-2457.

(133) Borisov, S. M.; Wolfbeis, O. S. Optical biosensors. *Chem. Rev.* **2008,** 108, 423-461.

(134) Bang, J. H.; Lim, S. H.; Park, E.; Suslick, K. S. Chemically responsive nanoporous pigments: Colorimetric sensor arrays and the identification of aliphatic amines. *Langmuir* **2008,** 24, 13168-13172.

(135) Haswell, S. J., *Practical guide to chemometrics*. CRC Press: 1992.

(136) Johnson, R. A.; Wichern, D. W., *Applied Multivariate Statistical Analysis*. 6th ed.; Prentice Hall: Upper Saddle River, NJ, 2007.

(137) Hair, J. F.; Black, B.; Babin, B.; Anderson, R. E.; Tatham, R. L., *Multivariate data analysis*. 6th ed.; Prentice Hall: Upper Saddle River, NJ, 2005.

(138) Massart, D. L., Kaufman, L., *The Interpretation of Analytical Chemical Data by the Use of Cluster Analysis*. John Wiley & Sons: New York, 1983.

(139) Askim, J. R.; Mahmoudi, M.; Suslick, K. S. Optical sensor arrays for chemical sensing: the optoelectronic nose. *Chem. Soc. Rev.* **2013,** 42, 8649-8682.

(140) Musto, C. J.; Lim, S. H.; Suslick, K. S. Colorimetric detection and identification of natural and artificial sweeteners. *Anal. Chem.* **2009,** 81, 6526-6533.

(141) Li, B.; M.K., K.; Altman, N. On dimension folding of matrix-or-array-valued statistical objects. *Ann. Statist.* **2010,** 38, 1094-1121.

(142) Zeng, P.; Zhong, W. In *Dimension reduction for tensor classification*, Topics in Applied Statistics: 2012 Symposium of the International Chinese Statistical Association (Springer Proceedings in Mathematics & Statistics), New York, 2013, 2013; Hu, M.; Liu, Y.; Lin, J., Eds. Springer: New York, 2013.

(143) Zhong, W.; Suslick, K. Penalized classification for matrix predictors with application to colorimetric sensor arrays. *Technometrics* **2012**.

(144) Zhang, Y.; Askim, J. R.; Zhong, W.; Orlean, P.; Suslick, K. S. Identification of pathogenic fungi with an optoelectronic nose. *Analyst* **2014,** 139, 1922-1928.

(145) Rakow, N. A.; Sen, A.; Janzen, M. C.; Ponder, J. B.; Suslick, K. S. Molecular recognition and discrimination of amines with a colorimetric array. *Angew. Chem. Int. Ed.* **2005,** 44, 4528-4532.

(146) Byrnes, M. E.; King, D. A.; Tierno Jr, P. M., *Nuclear, Chemical, and Biological Terrorism: Emergency Response and Public Protection*. CRC Press: 2003.

(147) Feng, L.; Musto, C. J.; Kemling, J. W.; Lim, S. H.; Suslick, K. S. A colorimetric sensor array for identification of toxic gases below permissible exposure limits. *Chem. Commun.* **2010,** 46, 2037-2039.

(148) Illy, E. The complexity of coffee. *Scientific American* **2002,** 286, 86-91.

(149) Clarke, R. J.; Vitzthum, O. G., *Coffee: Recent Developments*. Blackwell Science: Oxford, 2001.

(150) Flament, I., *Coffee Flavor Chemistry*. J. Wiley & Sons: Chichester, 2002.

(151) Suslick, B. A.; Feng, L.; Suslick, K. S. Discrimination of complex mixtures by a colorimetric sensor array: Coffee aromas. *Anal. Chem.* **2010,** 82, 2067-2073.

(152) Zhang, C.; Suslick, K. S. Colorimetric sensor array for soft drink analysis. *J. Agric. Food. Chem.* **2007,** 55, 237-242.

(153) Zhang, C.; Bailey, D. P.; Suslick, K. S. Colorimetric sensor arrays for the analysis of beers: A feasibility study. *J. Agric. Food. Chem.* **2006,** 54, 4925-4931.

(154) Ya, Z.; He, K.; Lu, Z. M.; Yi, B.; Hou, C. J.; Shan, S.; Huo, D. Q.; Luo, X. G. Colorimetric artificial nose for baijiu identification. *Flavour and Fragrance Journal* **2012,** 27, 165-170.

(155) Huang, X.; Xin, J.; Zhao, J. A novel technique for rapid evaluation of fish freshness using colorimetric sensor array. *J. Food Eng.* **2011,** 105, 632-637.

(156) Salinas, Y.; Ros-Lis, J. V.; Vivancos, J. L.; Martínez-Máñez, R.; Marcos, M. D.; Aucejo, S.; Herranz, N.; Lorente, I. Monitoring of chicken meat freshness by means of a colorimetric sensor array. *Analyst* **2012,** 137, 3635-3643.

(157) Riedel, S.; Carroll, K. C. Blood cultures: key elements for best practices and future directions. *Journal of Infection and Chemotherapy* **2010,** 16, 301-316.

(158) Martin, G. S.; Mannino, D. M.; Eaton, S.; Moss, M. The epidemiology of sepsis in the United States from 1979 through 2000. *New England Journal of Medicine* **2003,** 348, 1546-1554.

(159) Lazcka, O.; Del Campo, F. J.; Munoz, F. X. Pathogen detection: A perspective of traditional methods and biosensors. *Biosensors & Bioelectronics* **2007,** 22, 1205-1217.

(160) Savov, A. V.; Kouzmanov, G. B. FOOD QUALITY AND SAFETY STANDARDS AT A GLANCE. *Biotechnology & Biotechnological Equipment* **2009,** 23, 1462-1468.

(161) Miller, M. B.; Tang, Y. W. Basic Concepts of Microarrays and Potential Applications in Clinical Microbiology. *Clin. Microbiol. Rev.* **2009,** 22, 611-633.

(162) Weile, J.; Knabbe, C. Current applications and future trends of molecular diagnostics in clinical bacteriology. *Anal. Bioanal. Chem* **2009,** 394, 731-742.

(163) Peters, R. P. H.; Savelkoul, P. H. M.; Vandenbroucke-Grauls, C. M. J. E. Future diagnosis of sepsis. *Lancet* **2010,** 375, 1779-1780.

(164) Seng, P.; Drancourt, M.; Gouriet, F.; La Scola, B.; Fournier, P. E.; Rolain, J. M.; Raoult, D. Ongoing Revolution in Bacteriology: Routine Identification of Bacteria by

Matrix-Assisted Laser Desorption Ionization Time-of-Flight Mass Spectrometry. *Clinical Infectious Diseases* **2009,** 49, 543-551.

(165) Klouche, M.; Schroder, U. Rapid methods for diagnosis of bloodstream infections. *Clin. Chem. Lab. Med.* **2008,** 46, 888-908.

(166) Raoult, D.; Fournier, P. E.; Drancourt, M. What does the future hold for clinical microbiology? *Nature Reviews Microbiology* **2004,** 2, 151-159.

(167) Karasinski, J.; Andreescu, S.; Sadik, O. A.; Lavine, B.; Vora, M. N. Multiarray sensors with pattern recognition for the detection, classification, and differentiation of bacteria at subspecies and strain levels. *Anal. Chem.* **2005,** 77, 7941-7949.

(168) Setkus, A.; Kancleris, Z.; Olekas, A.; Rimdeika, R.; Senuliene, D.; Strazdiene, V. Qualitative and quantitative characterization of living bacteria by dynamic response parameters of gas sensor array. *Sens. Actuator B-Chem.* **2008,** 130, 351-358.

(169) Dutta, R.; Das, A.; Stocks, N. G.; Morgan, D. Stochastic resonance-based electronic nose: A novel way to classify bacteria. *Sens. Actuator B-Chem.* **2006,** 115, 17-27.

(170) Carey, J. R.; Suslick, K. S.; Hulkower, K. I.; Imlay, J. A.; Imlay, K. R. C.; Ingison, C. K.; Ponder, J. B.; Sen, A.; Wittrig, A. E. Rapid identification of bacteria with a disposable colorimetric sensing array. *J. Am. Chem. Soc.* **2011,** 133, 7571-7576.

(171) Montuschi, P.; Mores, N.; Trove, A.; Mondino, C.; Barnes, P. J. The Electronic Nose in Respiratory Medicine. *Respiration* **2013,** 85, 72-84.

(172) Amann, A.; Corradi, M.; Mazzone, P.; Mutti, A. Lung cancer biomarkers in exhaled breath. *Expert Rev. Mol. Diagn.* **2011,** 11, 207-217.

(173) Thaler, E. R.; Hanson, C. W. Medical applications of electronic nose technology. *Expert Rev. Med. Devices* **2005,** 2, 559-566.

(174) Mazzone, P. J.; Wang, X. F.; Xu, Y. M.; Mekhail, T.; Beukemann, M. C.; Na, J.; Kemling, J. W.; Suslick, K. S.; Sasidhar, M. Exhaled Breath Analysis with a Colorimetric Sensor Array for the Identification and Characterization of Lung Cancer. *J. Thor. Oncol.* **2012,** 7, 137-142.

(175) Thaler, E. R.; Lee, D. D.; Hanson, C. W. Diagnosis of rhinosinusitis with a colorimetric sensor array. *Journal of Breath Research* **2008,** 2.

CHAPTER 2
DETECTION AND IDENTIFICATION OF FUNGI VIA COLORIMETRIC SENSOR ARRAY

2.1 Introduction

Worldwide mortality from human invasive fungal infections is comparable to those from tuberculosis or malaria, and mortality rates exceed 50%.[1] Fungal infections have received increasing clinical focus,[2-4] and contaminated compounding pharmacies have brought this crisis to widespread public attention.[1, 5] Despite the increasing awareness of the situation's severity, currently available fungal diagnostic methods cannot always meet diagnostic needs, especially for invasive fungal infections. Traditional culturing methods are slow and labor-intensive, immunological tests often suffer from cross contamination, and molecular diagnostic methods lack standard criteria or diagnostic scope.[4, 6, 7] Thus, the development of new techniques for the rapid identification of fungal strains would be highly desirable.

The volatile organic compounds (VOCs) produced by fungi may have great utility as an alternative diagnostic approach. There are approximately 250 fungal VOCs identified (including alcohols, phenols, thiols, sulfides, hydrocarbons and aldehydes) that derive from fungal primary or secondary metabolic pathways.[8] It has been shown that fungal VOC fingerprints can be used to discriminate noninvasively among medically relevant fungi[9-11] and to rapidly screen and monitor the effectiveness of anti-fungal drugs.[12, 13] Previous VOC identification and profiling methods, however, are either not cost-effective or not robust. Gas chromatography-mass spectrometry (GC-MS) is high-maintenance and expensive. Moreover, sample collection methods, such as solid-phase micro-extraction (SPME) (**Figure 2.1**), can have adsorption bias and poor recovery.[8] Conventional electronic nose techniques, another commonly used VOC fingerprint profiling method, rely on weak and non-specific chemical interactions that induce changes in sensors' physical or electrical properties after exposure to VOCs.[8, 14] Such electronic noses, however, are generally sensitive to changes in humidity, require frequent recalibration, and are often limited in their sensitivity.

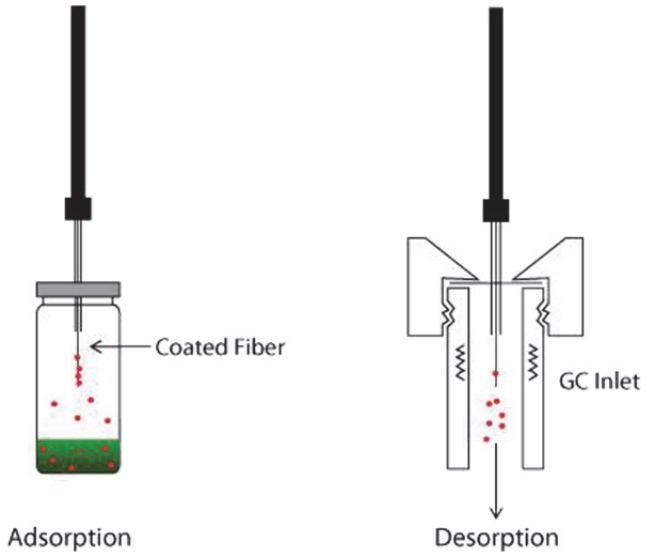

Figure 2.1 Schematic of SPME sampling method.[15, 16]

Previously, we have developed an optoelectronic nose approach using colorimetric sensor arrays for VOC detection and identification.[17-21] The sensor consists of a disposable array of cross-responsive nanoporous pigments whose colours are changed by diverse chemical interactions with analytes and which is unresponsive to changes in humidity. This portable, inexpensive, and highly sensitive optoelectronic nose produces a composite response which generates a unique molecular fingerprint for each analyte or mixture. Colorimetric senor arrays can differentiate and identify single analytes (e.g., toxic industrial gases[19, 22, 23] and explosives[24]) at concentrations well below 1 ppm. We have also successfully demonstrated fingerprinting and identification of complex odorant mixtures, including discrimination of the head gases of beverages,[25-27] the rapid identification of human pathogenic bacteria,[28] and even breath diagnosis of lung cancer.[29]

Herein, we report a colorimetric sensor array system for fungi differentiation and identification by profiling the composite volatile metabolites produced during fungal growth.

2.2 Experimental Procedures

2.2.1 Fungal Cell Strain and Cell Culture Experimental Procedure

12 fungal strains were tested, including *Candida albicans* (CAI-4), *Candida albicans* (B311), *Candida albicans* (1-28), *Candida glabrata*-1, *Candida guilliermondii*, *Candida parapsilosis*, *Trichosporon asahii* 3323, *Debaryomyces hansenii* 3333, *Candida stellatoidea*, *Candida keyfr*, *Saccharomyces cerevisiae* 4742 and *Kluyveromyces lactis* (cf. **Table 2.1**)

Strains were maintained on solid yeast extract-peptone-dextrose (YPD) medium. Fungal cell suspensions were prepared by inoculating 10 mL medium with a single colony, and liquid cultures were incubated overnight for 16 h at 30°C. A subculture was prepared by diluting the overnight culture into 10 mL fresh YPD medium to an optical density (OD_{600}) of 0.1, where 1 OD corresponds to $2.4x10^7$ colony forming units/mL (CFU/mL). After 6 more hours of rotary shaking at 30 °C, after which all strains were in exponential phase, $4.8x10^7$ CFU were harvested and re-suspended in 150 μL sterile water (*i.e.*, 3.13×10^8 CFU/mL) and then uniformly spread on 6 cm diameter plates containing 7 mL of solid YPD medium which had been pre-dried at 37 °C for 1 h. The inoculating suspension was allowed to soak into the agar medium for 10 min, after which the sensor array was exposed to the headspace, at room temperature, of the culture by replacing the original petri dish lid with one containing the sensor array and sealing with parafilm. A control with 150 μL sterile water inoculation was performed in parallel in each trial.

For anti-fungal drug experiments, 20 μL of stock drug solutions in dimethyl sulfoxide (DMSO) were added to 130 μL sterile water-suspended fungal cells. 20 μL DMSO in 130 μL sterile water was used as control.

Table 2.1 Summary of fungal strain information and number of replicate experiments for each strain.

Strain	Strain origin	Replicates
Control	n/a	34
Candida albicans (CAI-4)	Fonzi & Irwin[30]	12
Candida albicans (B311)	ATCC† 32354	11
Candida albicans (1-28)	Wrobel et al.[31]	10
Candida glabrata-1	Hoyer collection§	11
Candida guilliermondii	Hoyer collection§	6
Candida parapsilosis	Hoyer collection§	6
Trichosporon asahii 3323	Domestic pig isolates§	6
Debaryomyces hansenii 3333 (Candida famata)	Domestic pig isolates§	6
Candida stellatoidea	ATCC 36232	13
Candida keyfr	ATCC 46764	10
Saccharomyces cerevisiae 4742	Brachmann et al.[32]	18
Kluyveromyces lactis	New England Biolabs	12

†ATCC: American Type Culture Collection number

§Hoyer, Lois L <lhoyer@illinois.edu>

2.2.2 Colorimetric Sensor Array Detection Procedure

The disposable colorimetric sensor array was prepared by printing a 6x6 matrix of nanoporous dyes onto polyvinylidene fluoride (PVDF) membrane. PVDF was chosen because it is neutral, inert, and hydrophobic. The specific dyes used for this study are listed in **Table 2.2**. In order to support the array in the head space of the culture and to easily conduct the experiments, an engineered petri dish lid was designed. The colorimetric sensor array was attached to a plastic stage via 3M double-sided tape (which showed no effect in controls), which allowed volatiles diffuse and interact with all the dyes. The stage was then secured to the petri dish lid using silicone oil ($2x10^6$ cSt). After the engineered lid was in place, the Petri dish was sealed with parafilm and placed

inverted on a commercially available scanner (**Figure 2.2**) inside an incubator at 30 °C. Data was collected every 15 min using Epson Perfection V600 scanner.

Table 2.2 List of chemically responsive dyes. Spot numbering for the 6x6 as shown in **Figure 2.4** from left to right, top to bottom.

spot #	Name
1	5,10,15,20-tetraphenylporphyrinatozinc(II)
2	5,10,15,20-tetrakis(2,4,6-trimethylphenyl)porphyrinatozinc(II)
3	5,10,15,20-tetrakis(pentafluorophenyl)porphyrinatozinc(II)
4	5,10,15,20-tetrakis(2,4,6-trimethylphenyl)porphyrinatocobalt(II)
5	5,10,15,20-tetraphenylporphyrinatocadmium(II)
6	5,10,15,20-tetraphenylporphyrinatochromium(III) chloride
7	Bromophenol Blue + TBAH
8	Methyl Red + TBAH
9	Chlorophenol Red + TBAH
10	Nitrazine Yellow + TBAH
11	Bromothymol Blue + TBAH
12	Thymol Blue + TBAH
13	m-Cresol Purple + TBAH
14	$Zn(OAc)_2$ + m-Cresol Purple + TBAH
15	$HgCl_2$ + Bromophenol Blue + TBAH
16	$HgCl_2$ + Bromocresol Green + TBAH
17	$Pb(OAc)_2$
18	1-[4-[[4-(dimethylamino)phenyl]azo]phenyl]-2,2,2-trifluoroethanone+TsOH
19	α-Naphthol Red + TsOH
20	Tetraiodophenolsulfonephthalein
21	Fluorescein
22	Bromocresol Green

Table 2.2 (continued)

23	Methyl Red
24	Bromocresol Purple
25	Bromophenol Red
26	Rosolic Acid
27	Bromopyrogallol Red
28	Pyrocatechol Violet
29	Nile Red
30	Disperse Orange #25
31	4-(4-Nitrobenzyl)pyridine + N-Benzylaniline
32	Pyrylium, 4-[2-[4-(dimethylamino)phenyl]ethenyl]-2,6-dimethyl-, tetrafluoroborate
33	$LiNO_3$ + Cresol Red
34	Acridine Orange Base
35	$AgNO_3$ + Bromophenol Blue
36	$AgNO_3$ + Bromocresol Green

TBAH: 1.0 M tetrabutylammonium hydroxide water solution. TsOH: 1.0 M *p*-toluenesulfonic acid in 2-methoxyethanol. Red, green and blue colour channels are defined for each spot (e.g., for spot 3, G values are channel 8).

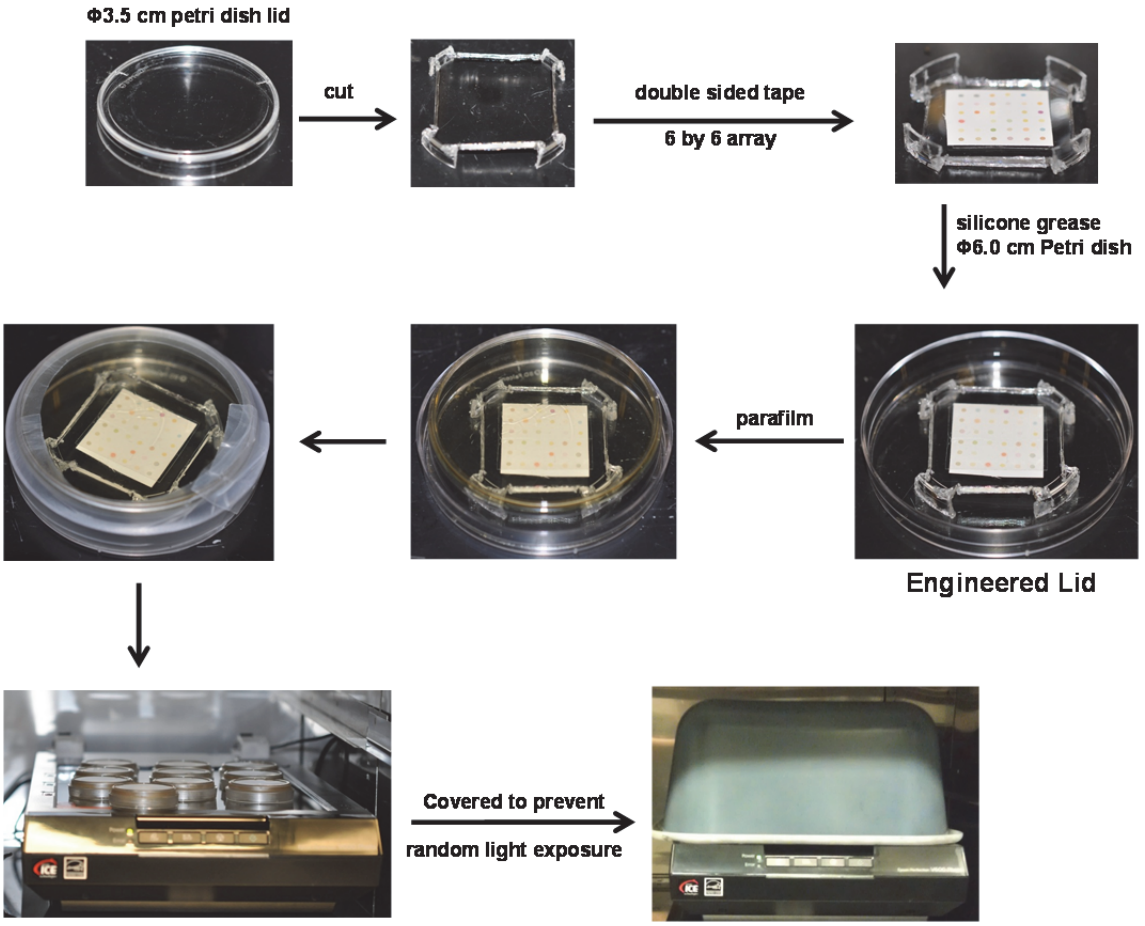

Figure 2.2 Construction of the colorimetric sensor array within Petri dishes and scanner placement within a standard incubator.

2.2.3 Color Change Profiles Generation

Color difference maps were generated by averaging the color value changes of red, green and blue (RGB), at each spot. The baseline values were taken 15 min after sealing the Petri dish. Each strain has a unique color difference map at each specific time point. Time response profiles were obtained by plotting color changes of all 108 channels (*i.e.*, ΔR, ΔG, ΔB values of 36 spots) over time (**Figure 2.3**). The complete database is provided in Database 2.2.3.

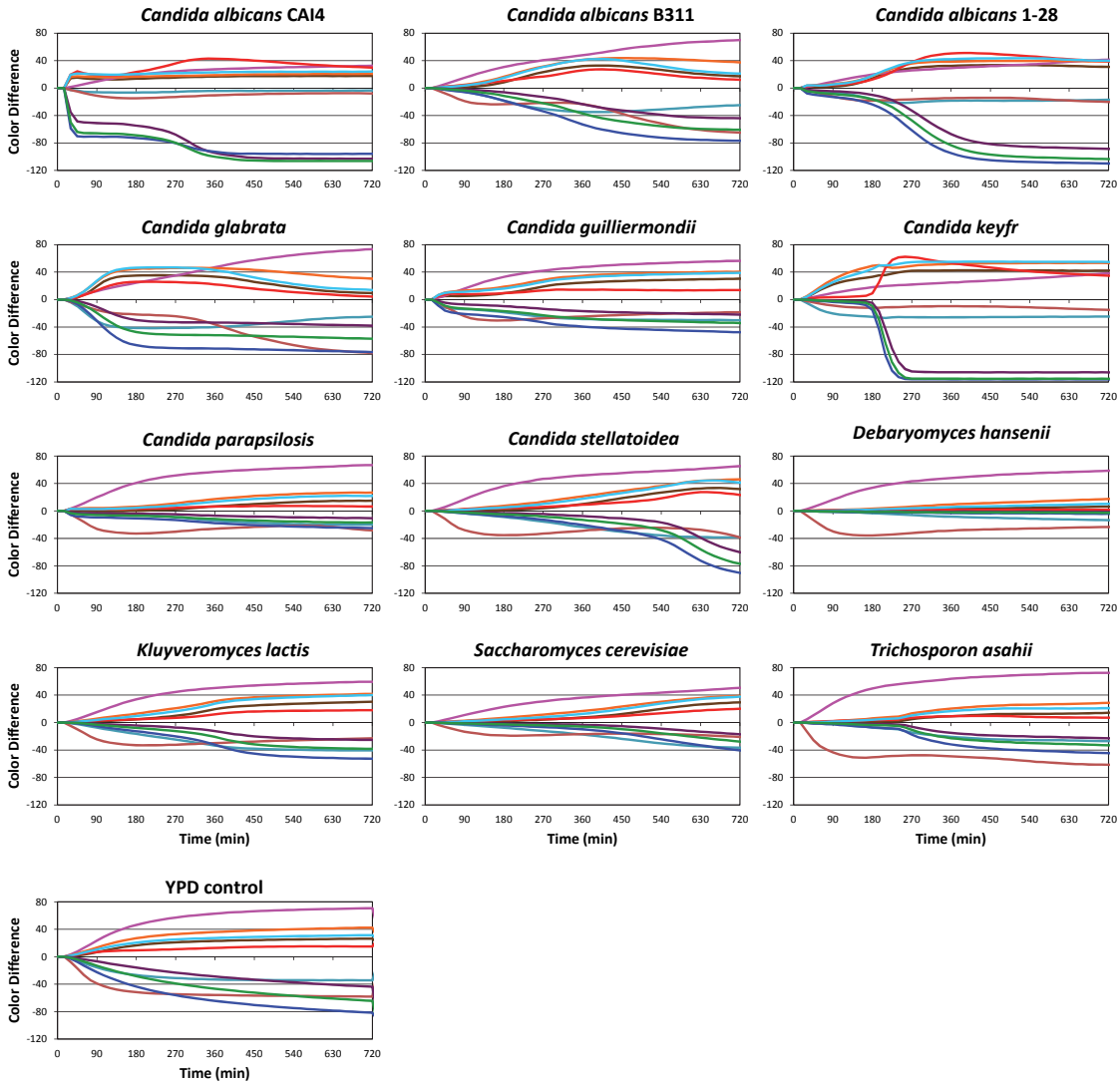

Figure 2.3 Time response profiles for all 12 different fungal strains. For each strain, the colour changes versus time are plotted for all 108 colour channels. For the clarity of the figures, 10 most responsive channels (out of 108 channels) are shown in the figure.

2.2.4 Linear Discriminant Analysis (LDA) and Tensor Discriminant Analysis (TDA)

Linear discriminant analysis[33] was performed using a commercially available program, SYSTAT13 (Systat Software Chicago, Illinois, USA, 2009). The data set consisted of 155 array responses (*i.e.*, observations) at a single time (180 min). In the classification matrix (**Table 2.3**), each observation is classified into the group where the value of its classification function is largest. All 13 classes, including 12 strains and 1 background, were classified 100% correctly. A Jackknifed classification (leave-one-out cross-validation) was used to test the predictability of the sensor array: one observation is left out and the rest of the data are used as a training set to generate the linear discriminant function, the model is then tested with the single left-out observation, and the procedure is then iterated through all of the observations in turn. The accuracy thus determined for the Jackknifed LDA prediction was 94%. The complete Jackknifed classification matrix table is shown in **Table 2.4**.

Table 2.3 Classification Matrix (Cases in row categories classified into columns).

	C.stellatoidea	C.albicans 1-28	C.albicans B311	C.albicans CAI4	C.glabrata	C.guilliermondii	C.keyfr	C.parapsilosis	D.hansenii	K.lactis	Medium (background)	S.cerevisiae	T.asahii	%corr.
C.stellatoidea	13	0	0	0	0	0	0	0	0	0	0	0	0	100
C.albicans 1-28	0	10	0	0	0	0	0	0	0	0	0	0	0	100
C.albicans B311	0	0	11	0	0	0	0	0	0	0	0	0	0	100
C.albicans CAI4	0	0	0	12	0	0	0	0	0	0	0	0	0	100
C.glabrata	0	0	0	0	11	0	0	0	0	0	0	0	0	100
C.guilliermondii	0	0	0	0	0	6	0	0	0	0	0	0	0	100
C.keyfr	0	0	0	0	0	0	10	0	0	0	0	0	0	100
C.parapsilosis	0	0	0	0	0	0	0	6	0	0	0	0	0	100
D.Hansenii	0	0	0	0	0	0	0	0	6	0	0	0	0	100
K.lactis	0	0	0	0	0	0	0	0	0	12	0	0	0	100
Medium (background)	0	0	0	0	0	0	0	0	0	0	34	0	0	100
S.cerevisiae	0	0	0	0	0	0	0	0	0	0	0	18	0	100
T.asahii	0	0	0	0	0	0	0	0	0	0	0	0	6	100
Total	13	10	11	12	11	6	10	6	6	12	34	18	6	100

Table 2.4 Jackknifed Classification Matrix of Linear Discriminant Analysis.

	C.Stellatoidea	C.albicans 1-28	C.albicans B311	C.albicans CAI4	C.glabrata	C.guilliermondii	C.keyfr	C.parapsilosis	D.hansenii	K.lactis	Medium (background)	S.cerevisiae	T.asahii	%corr.
C.stellatoidea	12	0	0	0	0	0	0	0	0	1	0	0	0	92
C.albicans 1-28	0	10	0	0	0	0	0	0	0	0	0	0	0	100
C.albicans B311	0	1	8	0	0	0	0	0	0	0	0	2	0	73
C.albicans CAI4	0	0	0	12	0	0	0	0	0	0	0	0	0	100
C.glabrata	0	0	0	0	11	0	0	0	0	0	0	0	0	100
C.guilliermondii	0	0	0	0	0	5	0	0	0	1	0	0	0	83
C.keyfr.	0	0	0	0	0	0	10	0	0	0	0	0	0	100
C.parapsilosis	0	0	0	0	0	0	0	6	0	0	0	0	0	100
D.hansenii	0	0	0	0	0	0	0	0	6	0	0	0	0	100
K.lactis	0	0	0	0	0	3	0	0	0	9	0	0	0	75
Medium (background)	0	0	0	0	0	0	0	0	0	0	34	0	0	100
S.cerevisiae	0	0	1	0	0	0	0	0	0	0	0	17	0	94
T.asahii	0	0	0	0	0	0	0	0	0	0	0	0	6	100
Total	12	11	9	12	11	8	10	6	6	11	34	19	6	94

For our tensor discriminant analysis (TDA), we used the colour difference changes (ΔR ΔG ΔB) from all 36 dye spots for 9 different times (from 120 min to 360 min in 30 min intervals). TDA is a generalization of LDA to multiway arrays.[34-36] TDA constructs optimal linear classifiers in a trimodal fashion, optimized separately for (1) the combination vector of dye spot, (2) the effects of the three colour factors (ΔR ΔG ΔB) for each dye, and (3) the temporal progression. The general strategy of the TDA algorithm in the colorimetric sensor array classification can be clearly illustrated using the flow chart given below in **Scheme 2.1**.[34]

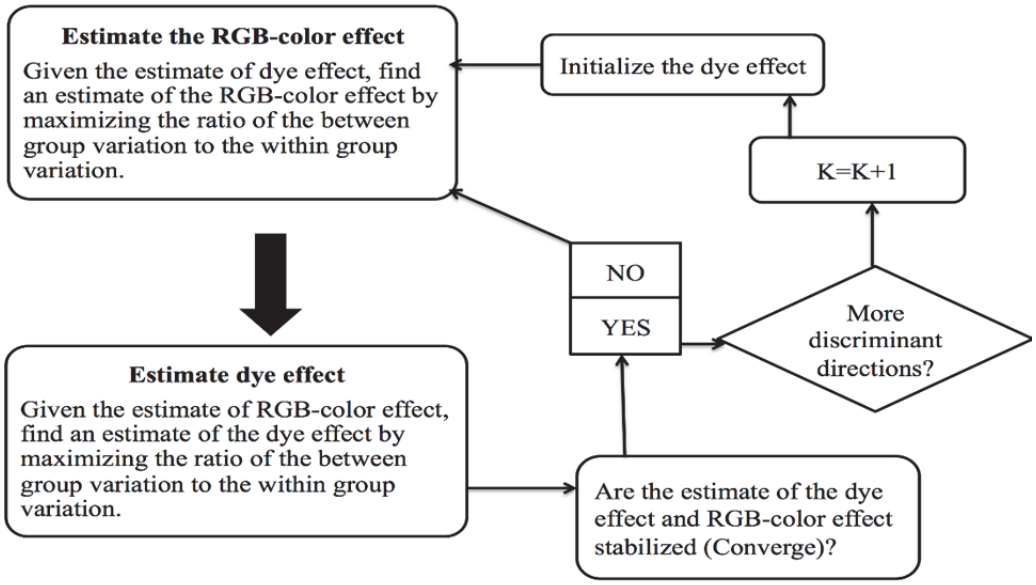

Scheme 2.1 Flow chart of tensor discriminant analysis.

2.3 Results and Discussions

2.3.1 Colorimetric Sensor Arrays

A colorimetric sensor array uses cross-reactive chemoresponsive colorants whose color changes reflect a diverse range of chemical interactions between the analytes and the colorants. We have developed an optimized set of 36 dyes that yield an essentially universal chemical sensor array.[19] The dyes fall into four classes: (1) dyes containing metal ions (e.g., metalloporphyrins) that respond to Lewis basicity (that is, electron-pair donation, metal-ion ligation), (2) pH indicators that respond to Brønsted acidity/basicity (that is, proton acidity and hydrogen bonding), (3) dyes with large permanent dipoles (e.g., vapochromic or solvatochromic dyes) that respond to local polarity, and (4) metal salts that participate in redox and precipatory reactions. This colorimetric sensor array, therefore, is responsive to the chemical reactivity of analytes, rather than to their effects on secondary physical properties (e.g., mass, conductivity, adsorption, etc.). The specific dyes used for this study are given in **Table 2.2**.

We selected twelve clinically and commercially relevant fungal strains to test the CSA's ability to differentiate strains based on their VOC profiles. These twelve strains (**Table 2.1**) were grown on YPD agar (yeast extract, peptone, and dextrose), a commonly used rich growth medium chosen because it accommodates a wide range of fungal strains. It is worth mentioning that YPD medium (control, **Figure 2.3.3**) also gives off volatiles. As a result, the signals obtained from the CSA color changes are from the combined volatiles from the YPD medium and from the fungi.

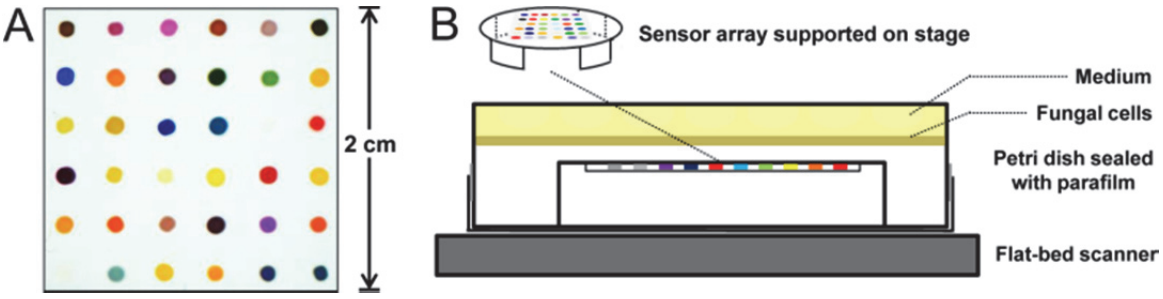

Figure 2.4 Schematic experimental apparatus. (A) An image of the CSA from a flat-bed scanner with different responsive dyes printed on hydrophobic PVDF substrate. For a complete list of dyes used in this research see Supporting Information. (B) Inverted Petri dish showing a colorimetric sensor array supported in a plastic stage in the head gas volume. Fungal cells were uniformly inoculated on YPD agar growth medium and the array digitally imaged with a flatbed scanner inside an incubator at 30 °C. Color changes were obtained as a function of time.

2.3.2 Color Difference Maps and Time Response Profiles

For analysis of the colorimetric sensor arrays, color difference maps were generated from the color values (*i.e.*, red, green and blue (RGB) values) for each spot at any given time by subtracting the baseline values of each spot taken at 15 min after the Petri dish was sealed. Representative difference maps are given for *Candida albicans* (CAI-4) from 15 to 480 min are given in **Figure 2.5**. At any given time, each of the 12 fungal strains shows a unique color difference map; for example, **Figure 2.6** shows the color difference maps of the 12 strains after 180 min growth. The color difference maps of all 12 strains are clearly differentiable by eye, even before any statistical analysis. Qualitatively, one may easily differentiate among the three *Candida albicans* strains, and identify *Debaryomyces hansenii,* which is often misdiagnosed as *Candida guilliermondii*[37].

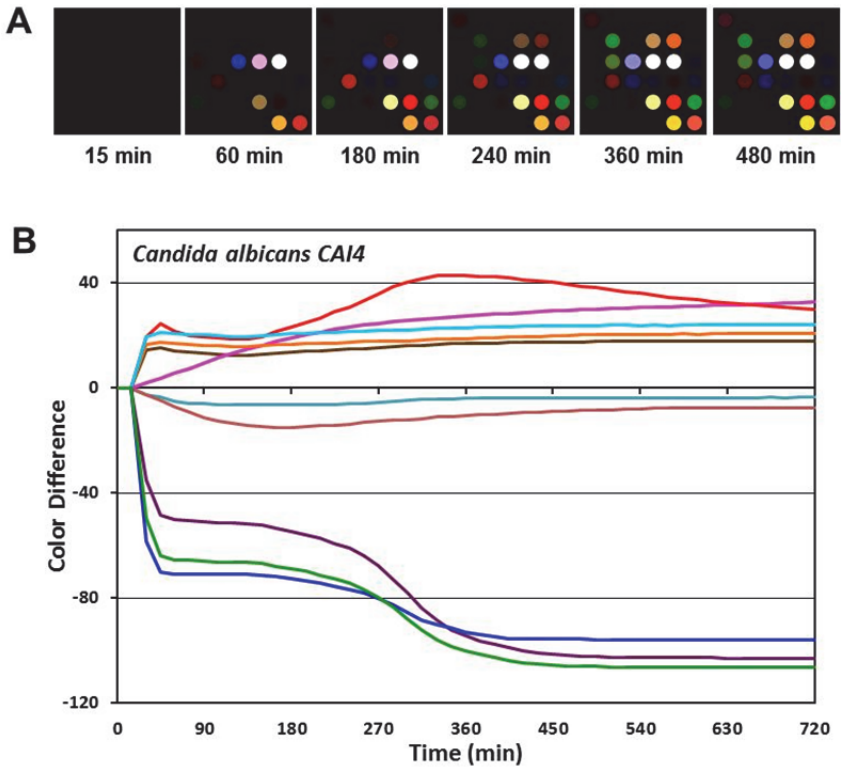

Figure 2.5 Sensor array response to *Candida albicans* (CAI-4) out-gases. (A) Color difference maps (*i.e.*, ΔR, ΔG and ΔB of 36 sensor spots) at different time points were generated by subtracting the RGB values from baseline at 15 minutes after sealing of Petri dish. For visualization in the color difference maps, four bit color was expanded to 8 bit color (*i.e.*, the RGB values of 4-19 were expanded to 0-255). (B) Temporal profile from the 10 most responsive channels vs. time.

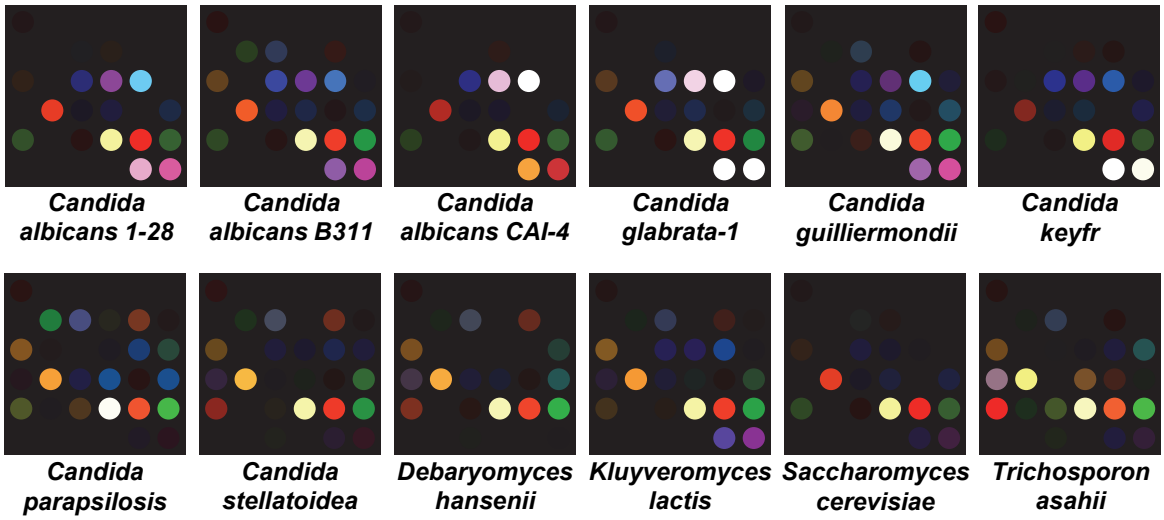

Figure 2.6 Color difference maps for 12 different fungal strains grown on YPD medium at 180 minutes. Each fungal species has a unique pattern.

Time response profiles were obtained by plotting the colour changes of the individual channels (*i.e.*, ΔR, ΔG, ΔB values for 36 spots) vs. time. For clarity of presentation, only the ten most responsive channels are shown in **Figure 2.5** B, again for *C. albicans* as an example. The time response profiles for all 12 strains of fungi are provided as **Figure 2.3**. The differences in the time response provides for each of the fungal strains serve as fingerprints that allow one both to qualitatively differentiate and identify strains even by the naked eye and to provide a quantitative pattern analysis.

The time response profiles for different fungal strains vary both in the intensities of the color changes and in the times at which such response begin to occur. For example, thiols and sulfides are common metabolites among fungi,[38] and the sensor spot that are most responsive to thiols and sulfides (*i.e.*, the blue, green, and purple lines in **Figure 2.5** B and **Figure 2.3**) do indeed undergo large color changes. The timings of these color changes, however, are strain specific: rapid changes occur for *C. albicans* (CAI-4) (even after just 15 min), whereas the changes begin to occur only after 180 min for *C. keyfr*, 450 min for *C. stellatoidea*, and not at all with *D. hansenii*. This thiol and sulfide responding spot has a dye formulation containing $Pb(O_2CCH_3)_2$ (**Table 2.2**).

2.3.3 Pattern Recognition and Statistical Analysis

To provide a statistically meaningful analysis, we utilized a standard chemometric approach, hierarchical cluster analysis (HCA),[33] to discriminate the VOC temporal profiles among the 12 strains and to demonstrate excellent reproducibility among replicates. HCA is a model-free clustering analysis that generates a dendrogram based on the Euclidean distances between the difference maps of each trial using all 108 dimensions. No mis-clusterings were observed for data from 155 trials after 180 min growth (**Figure 2.7**), which demonstrates that the method is reproducible and differentiates among different strains of fungi. It is worth noting that the clustering is not directly related to fungal phylogenetic classifications. This is not surprising as our methodology detects metabolic byproducts and is only indirectly responsive to genomic sequence: we are probing the metabolomics of the microorganisms, not their genomes.

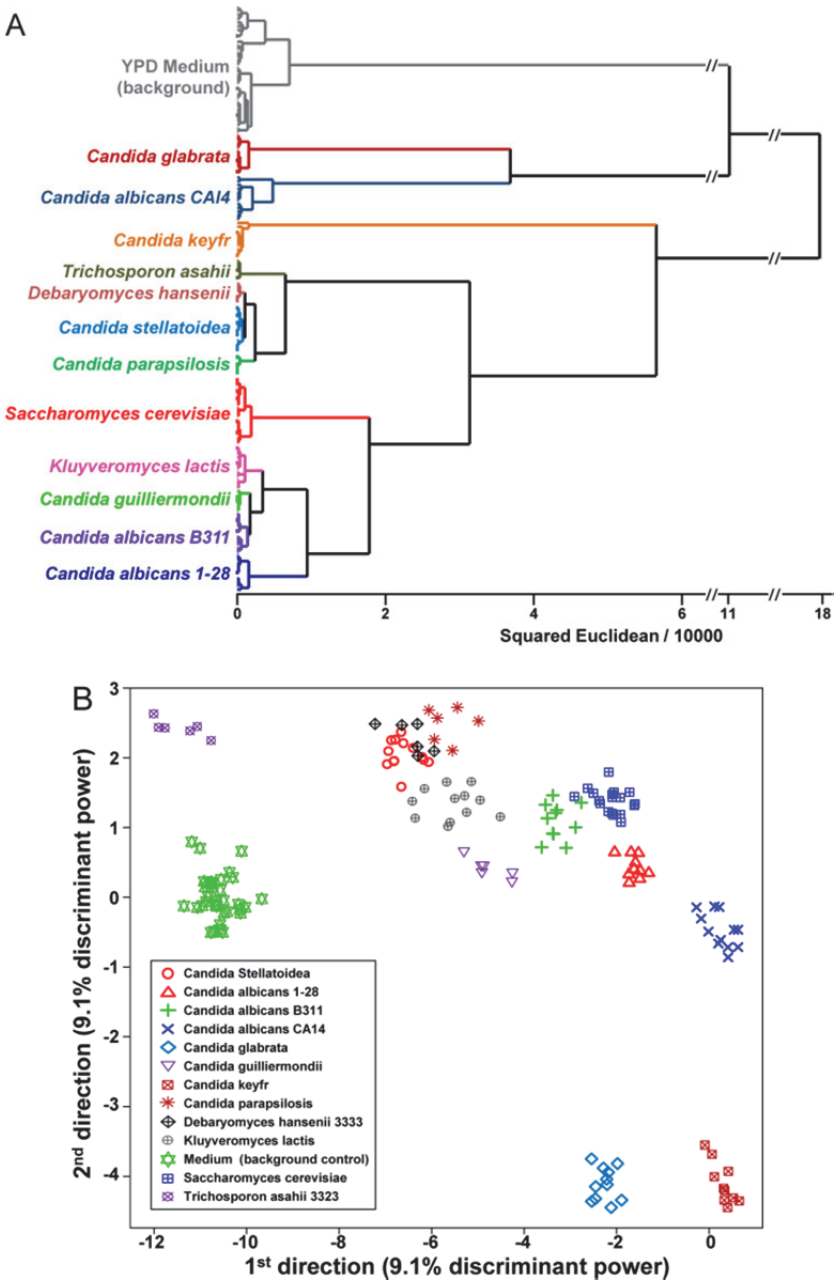

Figure 2.7 Classification analysis. (A) Hierarchical cluster analysis dendrogram (using Ward's method) of 12 fungal strains and YPD medium background at 180 min with 2.4×10^7 colony forming units of inoculation; no errors in clustering were observed among a total of 155 trials. (B) Scatter plot of the first two directions from the tensor discriminant analysis. Surprising good discrimination of the fungal strains is achieved even with only two TDA directions, which account for only 18.2% of the total discriminant power. The accuracy of classification using TDA maximizes at 98.1% using an optimal 10 dimensions.

To provide a quantitative evaluation of the accuracy of classification of the fungal strains by our colorimetric sensor arrays, we first completed a standard linear discriminant analysis (LDA). LDA of the array response (*i.e.*, the RGB color changes of each sensor spot) at 180 min gave a classification matrix with no errors (**Table 2.3**). To quantitatively test the prediction accuracy of a new unknown input using LDA, a standard Jackknifed analysis was performed (leaving out one observation at a time and permuting through the full dataset), giving a prediction accuracy of 94% (**Table 2.4**). Data from these colorimetric sensor arrays have an exceptionally high dimensionality, and LDA does not provide optimal classification with such data due to the "curse of dimensionality" (*i.e.*, the difficulties that a large number of dimensions can create for function approximation, model fitting, information extraction, as well as computation).[39]

Tensor discriminant analysis (TDA) is an array generalization of LDA better able to take advantage of high dimensionality.[35, 36] More precisely, tensor discriminant analysis is used to classify multi-way array measurements (*i.e.*, "tensor measurements"), rather than one-way vector measurements. The data collected using colorimetric sensor arrays can be viewed as a 3-way tensor with the first mode corresponding to choice of the dye, the second mode corresponding to the effects of the color changes (*i.e.*, ΔR, ΔG, ΔB), and the third mode corresponding to the time progression.[34] The general strategy of tensor discriminant analysis is to find orthogonal linear classifiers so as to maximize the ratio of between-class variation to within-class variation (i.e., to maximize discrimination among classes). Those orthogonal linear classifiers are essentially linear combinations of the three-way interactions of (1) the effects of the dye spot choice, (2) the three colour changes of each spot (*i.e.*, ΔR, ΔG, ΔB), and (3) the temporal evolution.

Tensor discriminant analysis can greatly improve the sensitivity, specificity, and computational efficiency of discriminant analysis method.[34-36] LDA and most other existing classification methods largely ignore the array structure of the colorimetric sensor array data: the three color changes for each spot are not fully independent dimensions compared to the three color changes of the other spots. For our array data over time, LDA would simply vectorize each 3-way observation into a vector with 972 dimensions (36×3×9, *i.e.*, where 36 dyes × 3 color factors (ΔR ΔG ΔB) × 9 time points (120 min to 360 min in 30 min intervals)) and find classifiers using 972 parameters. In

contrast, TDA constructs the optimal linear classifiers and estimates them in a trimodal tensor (separating spot choice, color, and time). By separating these three classes of effects, we can (1) keep the original design information and avoid interpretation difficulties, (2) substantially limit the effective dimensionality (we only need 48 parameters (i.e., 36+3+9) for TDA, rather than 972 parameters in LDA or PCA), and (3) improve prediction accuracy.

As a result, the directions created in TDA are not obscured by the noise present in the very large number of additional dimensions in LDA or PCA. As a consequence, excellent discrimination of the fungal strains is achieved even with only two TDA directions, which account for only 18.2% of the total discriminant power (as defined by the ratio of the between-group variation to the within-group variation), as seen in **Figure 2.7**. The prediction accuracy of TDA was assessed quantitatively by using a Jackknifed classification (leave-one-out cross-validation using the rest of the data as a training set and permuting through the full dataset). The prediction accuracy of the tensor discriminant analysis reaches a maximum of 98.1% using an optimal 10 dimensions (**Figure 2.8**, based on 155 trials).

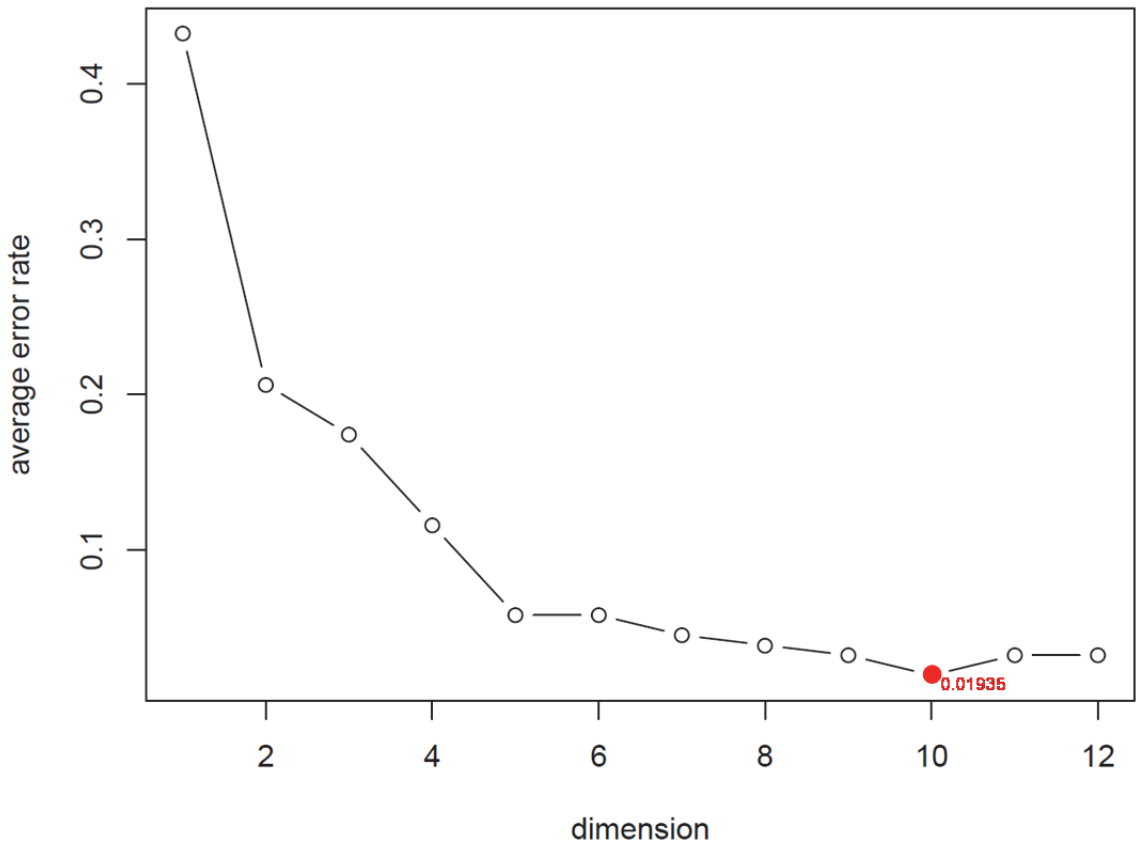

Figure 2.8 Misclassification rate (error rate) results from tensor discriminant analysis. Data between 120 to 360 minutes in 30-minute interval was used. Error rate for each trial was calculated by testing it with the training model built with the rest of the 154 trials. The final error rate was the average of all 155 error rates. The lowest error rate was 0.01935 using 10 dimensions.

2.3.4 Limit of Detection

The limit of detection (LOD) at a given time may be defined as the smallest number of viable fungal cells in the initial inoculum that will give a response from a single channel that is larger than three times the noise at that given time. A more quantitative measure of the LOD at 720 min can be approximated as $3[I]\sigma/C_{max}$ where [I] is the initial inoculum concentration, σ is the standard deviation of the channel with the largest net colour response at 720 min, and C_{max} is that largest net colour response. Time response profiles of the 10 most responsive channels of array response to *Candida albicans* (CAI-4) is shown in **Figure 2.9**. We can interpolate the LOD from the three lowest initial inocula (**Figure 2.10**), and calculate the LOD after 720 min. to be $2x10^4$ CFU for the initial inoculum. One may also define a *time to detection* as the time at which the response of a single channel is larger than three times the noise. Not surprisingly, there is a roughly linear correlation between the time to detection vs. the log of the initial inoculum (**Figure 2.11**); for example, with an initial inoculum of 10^6 CFU, the time to detection is ~400 min.

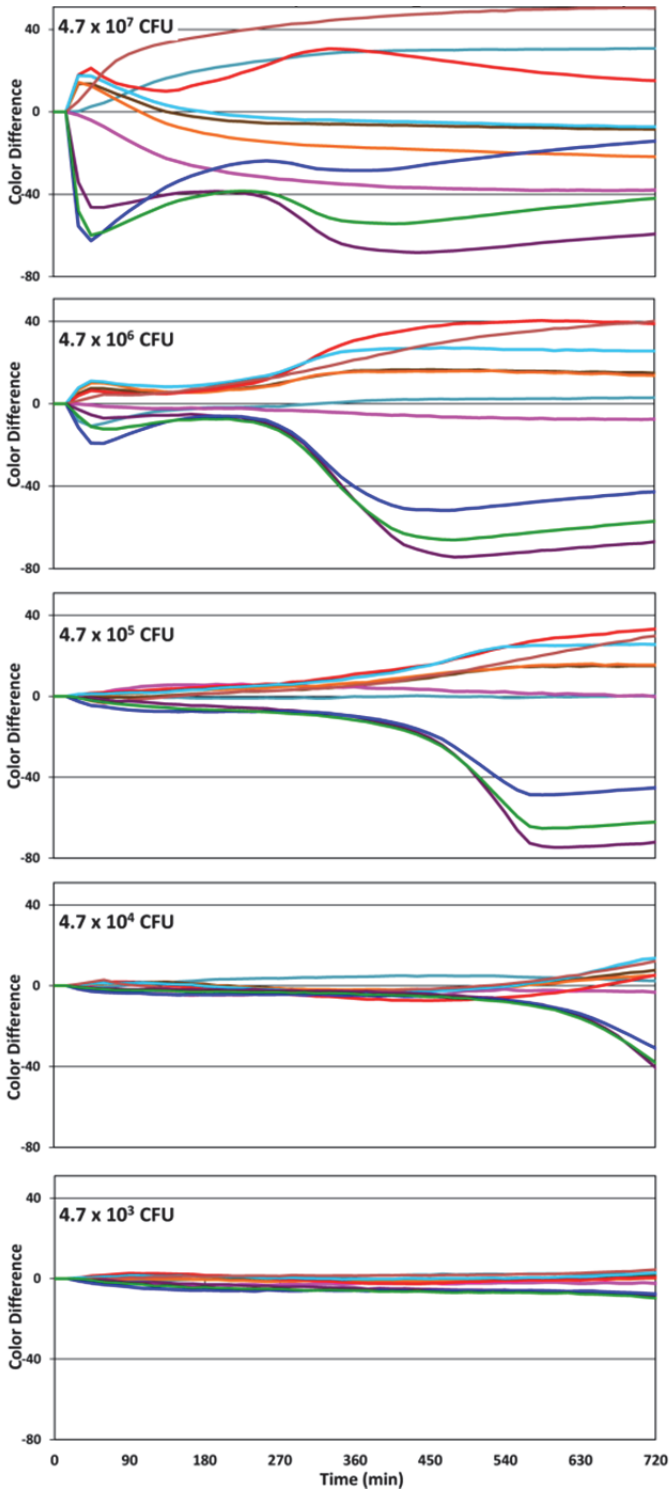

Figure 2.9 Time response profiles of the 10 most responsive channels of array response to *Candida albicans* (CAI-4) after subtraction of the YPD growth medium background. As the initial inoculum is decreased, the time response profiles decrease in intensity. At 720 min, the LOD is approximately $2x10^4$ CFU.

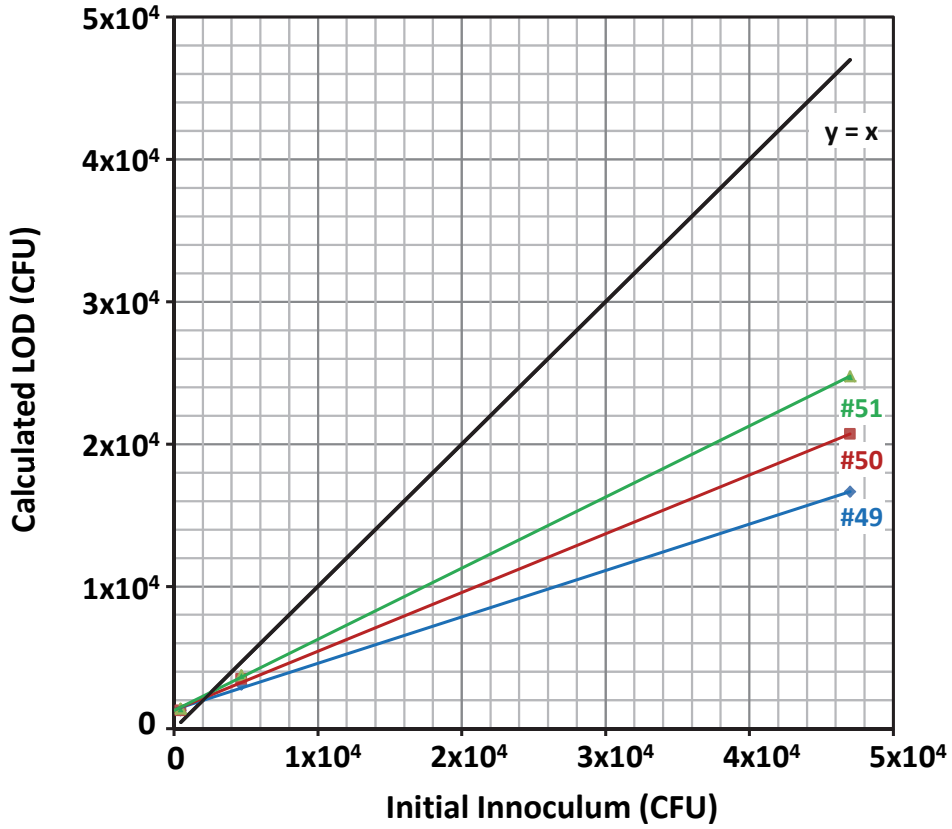

Figure 2.10 Interpolation of the limit of detection (LOD) for *Candida albicans* (CAI-4) for three channels (#49, #50 and #51, which correspond to spot 17, $Pb(O_2CCH_3)_2$). At any given time, the LOD for any given color change (i.e., ΔRGB value) of any given channel of any given spot is defined as the initial inoculum that gives three times the standard deviation of the ΔRGB, which is approximately 8 color difference units (the range of ΔRGB is -255 to +255). The LOD at 720 min was interpolated from the three lowest initial inocula ($4.7x10^3$, $4.7x10^4$ and $4.7x10^5$ CFU) and was determined be $2x10^4$ CFU for the initial inoculum with channel 49, as indicated in the figure. The standard deviation is approximately 8 color difference units (*i.e.*, RGB units ranging from 0 to 255).

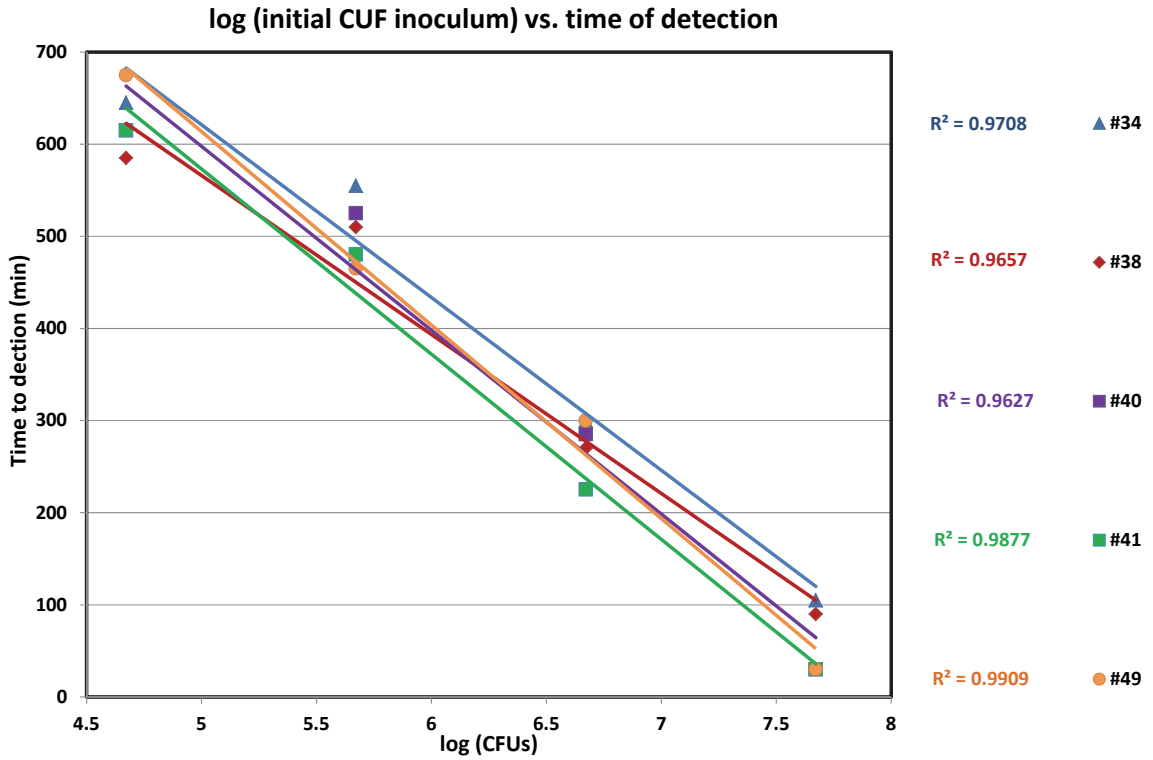

Figure 2.11 Correlation of the time to detection (as determined by the most responsive channel) versus log (initial inoculum in CFU), where the time to detection is defined as the time at which the total signal is greater than three times the standard deviation of the ΔRGB value. The linear regression coefficients are above 0.95.

2.3.5 Effects of Fungicides on Metabolic Patterns

Although chemical profiling at a single time point can be achieved by methods such as GC-MS, monitoring the changing VOC profile continuously during culture growth is challenging. Using this colorimetric sensor array, however, one can monitor cell growth conditions continuously and inexpensively. It is well established that there are changes of metabolic states in response to fungicides[40, 41], and we should expect that the VOCs produced by the fungi should therefore change under drug induced stress. In this manner, the colorimetric sensor array can be used to monitor changes in fungal metabolic states or in response to fungicides during cell growth.

Indeed, the array response (as measured by the total change in the Euclidian distance (ΔED) of all 108 colour channels) of *C. albicans* (CAI-4) is substantially affected by the presence of various concentrations of clotrimazole or miconazole (**Figure**

2.12). The color difference maps (**Figure 2.12 B**) demonstrate the shut-down of VOC production at high concentrations of anti-fungal drugs: volatiles are no longer being released (and the ΔED of the sensor array no longer changes) after roughly 180 min, for clotrimazole at >400 μg/mL and for miconazole at >0.5 μg/mL, which represent the minimum inhibitory concentrations of two drugs. At lower concentrations, the volatile metabolites are clearly changed, relative to untreated fungi, which can lead to either greater or diminished sensor array response (**Figure 2.12 B**). While the colorimetric sensor array does not provide a direct indication of what the changes in the VOCs may be (*i.e.*, the component by component analysis provided by GC-MS, for example), it does yield a rapid and simple indication that significant metabolic changes are occurring. This could prove useful for rapid parallel screening of fungicidal effectiveness.

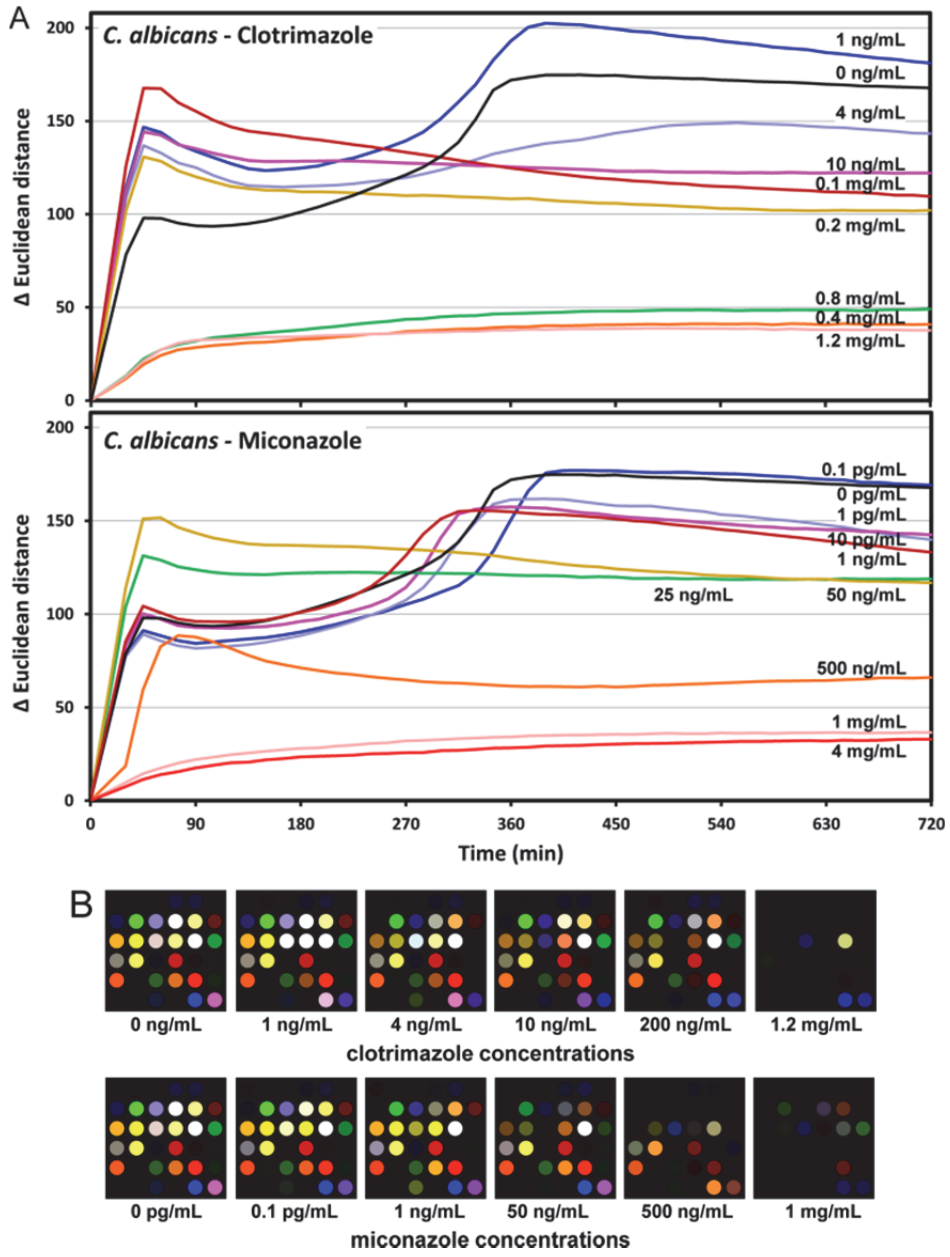

Figure 2.12 Sensor array response to fungal volatiles under the influence of anti-fungal drugs. (A) Total array response (change in Euclidean distance after subtraction of background) under the influence of fungicidal drugs. Significant changes in array response are observed vs. clortrimazole or miconazole concentrations. (B) Color difference maps vs. YPD growth medium control after 400 min as a function of fungicide concentration. Changes in the array response patterns appear to occur at ≥10 ng/mL clotrimazole and at ≥1 ng/mL for miconazole, which are presumably due to changes of metabolic states under the stress of the anti-fungal drug environment. The complete

shutdown of volatile metabolites occurs at >400 μg/mL clotrimazole and at >0.5 μg/mL miconazole.

2.4 Conclusions

In summary, we have used an optoelectronic nose to detect fungal VOCs and generate unique metabolic patterns that differentiate among twelve different fungal strains with high accuracy. The sensor array is also able to observe metabolic changes in growth patterns upon the addition of fungicides, which provides a facile screening tool for determining fungicide efficacy in real time.

2.5 References

(1) Brown, G. D.; Denning, D. W.; Gow, N. A. R.; Levitz, S. M.; Netea, M. G.; White, T. C. Hidden Killers: Human Fungal Infections. *Science Translational Medicine* **2012,** 4, 1-9.

(2) Brown, G. D.; Denning, D. W.; Levitz, S. M. Tackling human fungal infections. *Science* **2012,** 336, 647-647.

(3) Nucci, M.; Marr, K. A. Emerging fungal diseases. *Clin. Infect. Dis.* **2005,** 41, 521-526.

(4) Murray, P. R.; Masur, H. Current approaches to the diagnosis of bacterial and fungal bloodstream infections in the intensive care unit. *Critical care medicine* **2012,** 40, 3277-3282.

(5) Kuehn, B. M. Hospital Faces Uncertainty as It Copes With Surge of Patients With Fungal Meningitis. *JAMA-J. Am. Med. Assoc.* **2013,** 309, 219-221.

(6) Klutts, J. S.; Robinson-Dunn, B. A Critical Appraisal of the Role of the Clinical Microbiology Laboratory in Diagnosis of Invasive Fungal Infections. *J. Clin. Microbiol.* **2011,** 49, S39-S42.

(7) Yeo, S. F.; Wong, B. Current status of nonculture methods for diagnosis of invasive fungal infections. *Clin. Microbiol. Rev.* **2002,** 15, 465-484.

(8) Morath, S. U.; Hung, R.; Bennett, J. W. Fungal volatile organic compounds: A review with emphasis on their biotechnological potential. *Fungal Biol. Rev.* **2012,** 26, 73-83.

(9) Sahgal, N.; Monk, B.; Wasil, M.; Magan, N. *Trichophyton species*: use of volatile fingerprints for rapid identification and discrimination. *Br. J. Dermatol.* **2006,** 155, 1209-1216.

(10) Scotter, J. M.; Langford, V. S.; Wilson, P. F.; McEwan, M. J.; Chambers, S. T. Real-time detection of common microbial volatile organic compounds from medically important fungi by Selected Ion Flow Tube-Mass Spectrometry (SIFT-MS). *J. Microbiol. Methods* **2005,** 63, 127-134.

(11) Sahgal, N.; Magan, N. Fungal volatile fingerprints: discrimination between dermatophyte species and strains by means of an electronic nose. *Sensors Actuators B: Chem.* **2008,** 131, 117-120.

(12) Naraghi, K.; Sahgal, N.; Adriaans, B.; Barr, H.; Magan, N. Use of volatile fingerprints for rapid screening of antifungal agents for efficacy against dermatophyte *Trichophyton* species. *Sensors Actuators B: Chem.* **2010,** 146, 521-526.

(13) Pont, N. P.; Kendall, C. A.; Magan, N. Analysis of Volatile Fingerprints for Monitoring Anti-Fungal Efficacy Against the Primary and Opportunistic Pathogen *Aspergillus fumigatus*. *Mycopathologia* **2012,** 173, 93-101.

(14) Rock, F.; Barsan, N.; Weimar, U. Electronic nose: Current status and future trends. *Chem. Rev.* **2008,** 108, 705-725.

(15) Galipo, R. C.; Canhoto, A. J.; Walla, M. D.; Morgan, S. L. Analysis of volatile fragrance and flavor compounds by headspace solid phase microextraction and GC-MS: an undergraduate instrumental analysis experiment. *J. Chem. Educ.* **1999,** 76, 245.

(16) Randolph, R.; Canhoto, A.; Walla, M.; Morgan, S. Analysis of volatile fragrance and flavor compounds by headspace solid phase microextraction combined with gas chromatography/mass spectrometry. *An instrumental analysis experiment. The Board of Trustees of The University of South Carolina. Columbia, SC* **2002**.

(17) Rakow, N. A.; Suslick, K. S. A colorimetric sensor array for odour visualization. *Nature* **2000,** 406, 710-713.

(18) Suslick, K. S. Synesthesia in science and technology: more than making the unseen visible. *Current Opinion Chem. Biol.* **2012,** 16, 557-563.

(19) Lim, S. H.; Feng, L.; Kemling, J. W.; Musto, C. J.; Suslick, K. S. An optoelectronic nose for the detection of toxic gases. *Nat. Chem.* **2009,** 1, 562-567.

(20) Janzen, M. C.; Ponder, J. B.; Bailey, D. P.; Ingison, C. K.; Suslick, K. S. Colorimetric sensor arrays for volatile organic compounds. *Anal. Chem.* **2006,** 78, 3591-3600.

(21) Suslick, K. S.; Bailey, D. P.; Ingison, C. K.; Janzen, M.; Kosal, M. E.; McNamara III, W. B.; Rakow, N. A.; Sen, A.; Weaver, J. J.; Wilson, J. B.; Zhang, C.; Nakagaki, S. Seeing smells: Development of an optoelectronic nose. *Quim. Nova* **2007,** 30, 677-681.

(22) Feng, L.; Musto, C. J.; Kemling, J. W.; Lim, S. H.; Zhong, W.; Suslick, K. S. Colorimetric sensor array for determination and identification of toxic industrial chemicals. *Anal. Chem.* **2010,** 82, 9433-9440.

(23) Feng, L.; Musto, C. J.; Kemling, J. W.; Lim, S. H.; Suslick, K. S. A colorimetric sensor array for identification of toxic gases below permissible exposure limits. *Chem. Commun.* **2010,** 46, 2037-2039.

(24) Lin, H.; Suslick, K. S. A colorimetric sensor array for detection of triacetone triperoxide vapor. *J. Am. Chem. Soc.* **2010,** 132, 15519-15521.

(25) Suslick, B. A.; Feng, L.; Suslick, K. S. Discrimination of complex mixtures by a colorimetric sensor array: Coffee aromas. *Anal. Chem.* **2010,** 82, 2067-2073.

(26) Zhang, C.; Bailey, D. P.; Suslick, K. S. Colorimetric sensor arrays for the analysis of beers: A feasibility study. *J. Agric. Food Chem.* **2006,** 54, 4925-4931.

(27) Zhang, C.; Suslick, K. S. Colorimetric sensor array for soft drink analysis. *J. Agric. Food Chem.* **2007,** 55, 237-242.

(28) Carey, J. R.; Suslick, K. S.; Hulkower, K. I.; Imlay, J. A.; Imlay, K. R.; Ingison, C. K.; Ponder, J. B.; Sen, A.; Wittrig, A. E. Rapid identification of bacteria with a disposable colorimetric sensing array. *J. Am. Chem. Soc.* **2011,** 133, 7571-7576.

(29) Mazzone, P. J.; Wang, X. F.; Xu, Y. M.; Mekhail, T.; Beukemann, M. C.; Na, J.; Kemling, J. W.; Suslick, K. S.; Sasidhar, M. Exhaled Breath Analysis with a Colorimetric Sensor Array for the Identification and Characterization of Lung Cancer. *Journal of Thoracic Oncology* **2012,** 7, 137-142.

(30) Fonzi, W. A.; Irwin, M. Y. Isogenic strain construction and gene mapping in *Candida albicans*. *Genetics* **1993,** 134, 717-728.

(31) Wrobel, L.; Whittington, J. K.; Pujol, C.; Oh, S.-H.; Ruiz, M. O.; Pfaller, M. A.; Diekema, D. J.; Soll, D. R.; Hoyer, L. L. Molecular phylogenetic analysis of a

geographically and temporally matched set of *Candida albicans* isolates from humans and nonmigratory wildlife in central Illinois. *Eukaryot. Cell* **2008,** 7, 1475-1486.

(32) Brachmann, C. B.; Davies, A.; Cost, G. J.; Caputo, E.; Li, J.; Hieter, P.; Boeke, J. Designer deletion strains derived from *Saccharomyces cerevisiae* S288C: a useful set of strains and plasmids for PCR-mediated gene disruption and other applications. *YEAST-CHICHESTER-* **1998,** 14, 115-132.

(33) Haswell, S. J., *Practical guide to chemometrics*. CRC Press: 1992.

(34) Zhong, W.; Suslick, K. S. Penalized classification for matrix predictors with application to colorimetric sensor arrays. *Technometrics* **2013,** 55, in press. http://publish.illinois.edu/wenxuan/files/2012/12/matrix_clust.pdf

(35) Li, B.; M.K., K.; Altman, N. On dimension folding of matrix-or-array-valued statistical objects. *Ann. Statist.* **2010,** 38, 1094-1121.

(36) Zeng, P.; Zhong, W. In *Dimension reduction for tensor classification*, Topics in Applied Statistics: 2012 Symposium of the International Chinese Statistical Association (Springer Proceedings in Mathematics & Statistics), New York, 2013, 2013; Hu, M.; Liu, Y.; Lin, J., Eds. Springer: New York, 2013.

(37) Desnos-Ollivier, M.; Ragon, M.; Robert, V.; Raoux, D.; Gantier, J.-C.; Dromer, F. *Debaryomyces hansenii* (*Candida famata*), a rare human fungal pathogen often misidentified as *Pichia guilliermondii* (*Candida guilliermondii*). *J. Clin. Microbiol.* **2008,** 46, 3237-3242.

(38) Newton, G. L.; Arnold, K.; Price, M. S.; Sherrill, C.; Delcardayre, S. B.; Aharonowitz, Y.; Cohen, G.; Davies, J.; Fahey, R. C.; Davis, C. Distribution of thiols in microorganisms: mycothiol is a major thiol in most actinomycetes. *J. Bacteriol.* **1996,** 178, 1990-1995.

(39) Donoho, D. L. High-dimensional data analysis: The curses and blessings of dimensionality. *AMS Math Challenges Lecture* **2000,** 1-32 www-stat.stanford.edu/~donoho/Lectures/AMS2000/Curses.pdf.

(40) Belenky, P.; Camacho, D.; Collins, J. J. Fungicidal Drugs Induce a Common Oxidative-Damage Cellular Death Pathway. *Cell Reports* **2013,** 3, 350-358.

(41) Cannon, R. D.; Lamping, E.; Holmes, A. R.; Niimi, K.; Tanabe, K.; Niimi, M.; Monk, B. C. *Candida albicans* drug resistance–another way to cope with stress. *Microbiology* **2007,** 153, 3211-3217.

CHAPTER 3
ULTRASONIC SPRAY TECHNIQUE FOR MATERIALS SYNTHESIS

3.1 Introduction

Spray synthesis, which generally involves thermal decompositions of aerosols (e.g., spray pyrolysis), is a widely used aerosol process for a variety of powders and films.[1-5] In spray pyrolysis, an aerosol of micro-droplets is generated from a liquid precursor (a solution, dispersion, or pure compound) by a nebulizer in a gas flow, which is then carried through a heated zone where physical and chemical reactions occur.

Based on different atomization processes and liquid-gas-particle conversion routes, one can generally classify the technologies into the following categories: flame spraying, laser ablation, aerosol-assisted CVD, and ultrasonic spray techniques.[1] Ultrasonic spray techniques have been intensively investigated over the past few years for the production of microspheres, nanoparticles, powders and composite materials.[1-3]

Spray synthesis has had substantial impact in particle manufacturing and film deposition. Compared to its counterparts (e.g., hydrothermal synthesis, emulsification techniques, laser ablation and milling), it has many advantages with respect to both the process itself and the materials it produces. As a synthetic tool, spray synthesis is an energy-efficient process. It is simple and inexpensive to implement in a one-step, continuous process, and can be easily scaled up. Spray synthesis products are of high purity and have easily-controlled properties; the composition can be controlled by adjusting precursor ratios, the particle size or deposited film thickness can be controlled by adjusting solvent properties and experimental conditions, and particle morphology is tunable using several methods (e.g., porous and hollow structures can be readily produced by adjusting salts dissolved in a precursor solution).

In this chapter, an overview of spray techniques is described with an emphasis on ultrasonic spray pyrolysis (USP).

3.2 Spray Techniques

For spray techniques, the size of the particles is directly related to the size of the droplets in the aerosol; thus, the method used for nebulization is important. To be more specific, the average particle diameter can be calculated from equation (3.1)

$$D_p = \left(\frac{M D_d^{\,3} C}{1000 \rho_p} \right)^{1/3} \tag{3.1}$$

where D_p is the average particle diameter (μm), M is the molecular weight of the precursor in solution, D_d is the average droplet diameter (μm), C is the molar concentration of the precursor in solution, and ρ_p is the product density (g/cm^3).

Several common nebulization techniques are discussed below, and their advantages and disadvantages are summarized in **Table 3.1**.

Table 3.1 Summary and Comparison of Nebulization Techniques.[1]

Nebulization Method	**Average Droplet Size (μm)**	**Droplet Size Distribution**	**Gas Flow Rate**	**Droplet Delivery Rate**
Pressure	10-1000	Broad	Low	High
Air-assisted	<1000	Broad	High	High
Rotary	10-1000	Broad	Low	High
Electrospray	0.01-1000	Very Narrow	Low	Low to high
Ultrasonic (Nozzle)	10-1000	Medium	Low	Medium
Ultrasonic (Submerged)	1-10	Narrow	Low	Medium

3.2.1 Pressure, Air-assisted, and Rotary Atomizers

Pressure (jet), air-assisted, and rotary atomizers are common industrial tools for fine powder production. This is because of their high throughput and relatively simple processing. Large particle sizes and polydispersity, however, still limit their applications in some sophisticated synthesis and processing. Pressure atomizers are operated by forcing liquid at high pressure through a narrow aperture/nozzle.[1, 6] The kinetic energy of the liquid forces it to break apart into many droplets after exiting the nozzle. This technique has the advantage of high precursor delivery rates and does not require gas flow. Also, this method allows for high-throughput of droplets and better control of the

droplet size than pressure atomizers. However, the aerosol droplets they produce are usually in high-micron range (10-1000 μm in diameter) with some polydispersity. Air-assisted atomizers, also known as pneumatic atomizers, use the energy of a pressured carrier gas to force apart liquid stream into aerosol droplets and they can produce droplet sizes <1000 μm.[1, 6] Rotary atomizers create an aerosol by directing a liquid onto a rotating disk. The kinetic energy transferred from the rotating disk causes the liquid to break apart, producing aerosol droplets.[1, 6] Both high precursor feeds and narrower droplet size distributions make rotary atomizer an attractive technique, but large droplets are still produced.

3.2.2 Electrostatic Atomizers

Electrostatic atomizers use electrostatic forces to create an aerosol.[1, 7] A liquid stream is charged by passing through an electric charge field. Upon exiting a capillary, the stream breaks into many droplets due to the repulsions of built-charges.

By varying the diameter of the capillary and the strength of the electric field, sub-micron to micron size droplets (0.01-1000 μm) can be produced. The aerosols are generally monodisperse with a geometric standard deviation of ~1.1, an advantage of this type of atomizer over other systems. While large particles produced via electrostatic atomization can be made at high scale, smaller droplets (e.g., sub-micron droplets) can only formed at very low concentrations and are not as suitable for mass production compared to other atomization methods. Another limitation is that, due to the aerosol-generating mechanism, electrostatic atomizers also require the use of a conductive or semi-conductive liquid.

3.2.3 Vibrating Orifice Aerosol Generators

In vibrating orifice aerosol generators, a liquid is forced through a small nozzle.[8, 9] The jet produced is broken up by vibrating the plate containing the hole or holes at a specific frequency (1-1000 kHz) using a piezoelectric transducer. The droplets produced are relatively large (20-400 μm) and surprisingly monodisperse, with a geometric distribution of ~1.02. A limitation, though, is that the small orifices can easily get clogged, so only solutions (i.e., no suspensions) can be nebulized.

3.2.4 Ultrasonic Atomizers

In general, Ultrasonic atomizers use piezoelectric transducers that vibrate at a frequency of 50 kHz to 2.4 MHz to produce micro-droplets. Typically, there are two types of ultrasonic atomizers: ultrasonic nozzle atomizers[1, 10] and submerged ultrasonic atomizers.[1, 11] Both types of ultrasonic atomizers have the advantage of requiring low gas and liquid flow rates required. The submerged ultrasonic transducer in particular is a very simple system, though care must be taken to maintain a consistent level of fluid above the piezoelectric transducer so as to keep the size distribution and concentration of nebulized droplets consistent.

Ultrasonic nozzle atomizers forces the liquid through an ultrasonically vibrating nozzle to cause droplet formation.[2, 12] An example of a commercially available ultrasonic nozzle atomizer is shown in **Figure 3.1**.This method can produce droplets with average diameters of 10-1000 μm and medium polydispersity, with a geometric deviation of ~1.5. As for mass production rate, this type of vibrational spraying systems is capable of handling liquid flow rates from a few mL/h to tens of L/h.

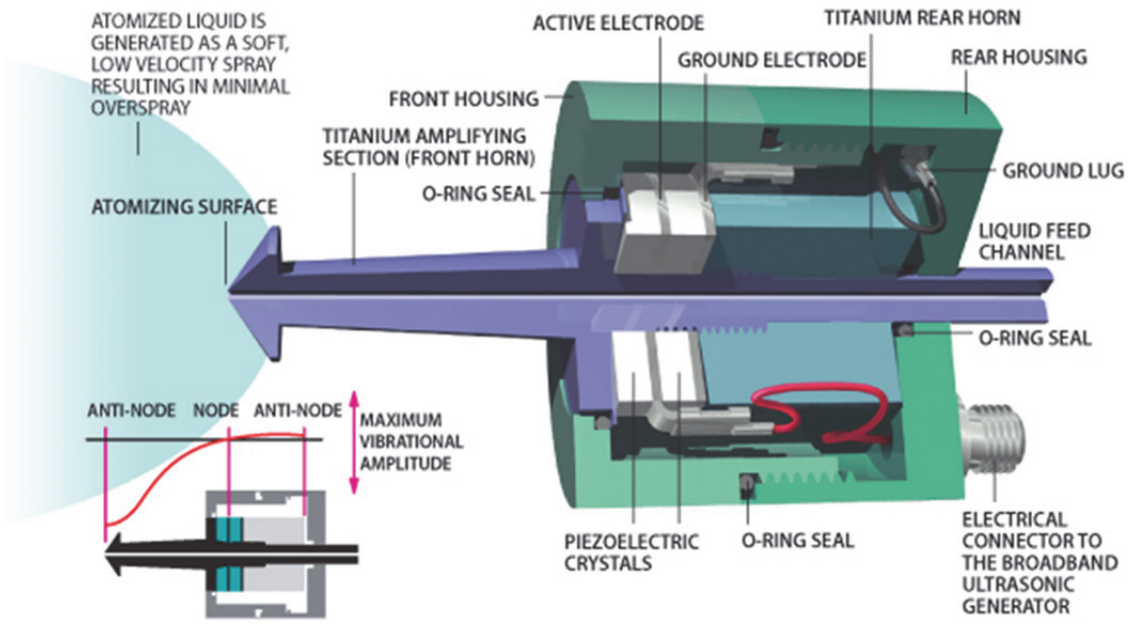

Figure 3.1 Schematic illustration of a commercially available ultrasonic atomizing nozzle system (Sono-Tek).[13]

The second type of ultrasonic atomizer involves a submerged ultrasonic piezoelectric transducer.[1, 11] An example of submerged ultrasonic atomizer in a spray pyrolysis system is shown in **Figure 3.2**. Ultrasonic nebulization by submerged ultrasonic atomizer is the result of momentum transfer. The ultrasound wave is carried via water, and the energy passes through a membrane to the precursor solution. When the ultrasonic wave reaches the air/liquid interface a standing wave (consists of crests and troughs) is produced. When the amplitude of the surface capillary waves is sufficiently high, the crests of the waves are torn away from the bulk liquid, and microdroplets are produced (**Figure 3.3**). Empirically, the diameter of produced droplets can be described by Lang's equation (3.2)[11]

$$D_d = 0.34\left(\frac{8\pi\gamma}{\rho f^2}\right)^{1/3} \tag{3.2}$$

where D_d is the average droplet diameter (cm), γ is the surface tension of the liquid (d/cm), ρ is the liquid density (g/cm^3), and f is the frequency of the piezoelectric transducer (cps).

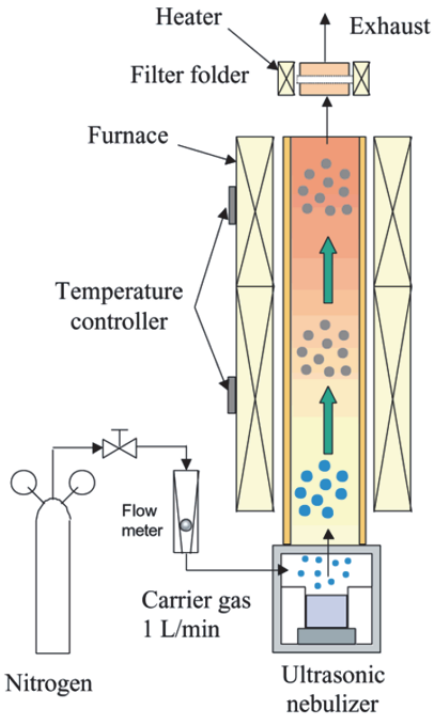

Figure 3.2 Schematic of submerged ultrasonic atomizer for materials synthesis.[14]

Figure 3.3 A photographic image of a nebulized fountain produced by a submerged 1.65 MHz piezoelectric transducer.[15]

Standard operating frequencies for commercially available submerged transducers range from 1.6-2.4 MHz and produce droplets with median diameters of 2-3 μm. Depending on precursor concentration, normally nano-sized materials ara produced at high frequencies (> 1 MHz) while commercial large-scale nebulizers are also available in 25 kHz region for spray drying and painting. The choice of precursor can be a homogeneous liquid or colloidal suspensions as long as the colloidal particles are less than approximately one tenth the size of the overall droplet (generally around 50 nm or less).[5]

Compared with ultrasonic nozzle, submerged ultrasonic atomizers can produce smaller droplet sizes with relatively narrow droplet size distribution while allowing for moderate throughput.[1, 11] And given the fact that the whole process is continuous, this synthetic system is readily scalable. Moreover, by tuning the precursor solutions, various products and morphologies can be controlled. A submerged ultrasonic transducer with a frequency of 1.7 MHz is used in the following chapters for metal oxide and conductive polymer microsphere synthesis.

3.3 Reaction Pathway and Commonly Used Methods for Morphology Control

3.3.1 Aerosol Routes to Particles

In the ultrasonic spray nebulization process, a mist containing the precursor solution is generated, and each micron-droplet acts as a micro-reactor (i.e., the contents of each individual droplet are isolated and separate from other droplets). These micro-droplets are then transported by a carrier gas through a heated zone (usually a furnace). The carrier gas be either be inert (e.g. Ar, N_2) or reactive (e.g., air, O_2).[16] Due to small size of the micro-droplets (e.g. usually less than 5 μm), heat and mass transfer throughout the whole droplet is very efficient.

In the heated zone is where products are formed, several processes occur, including the evaporation of solvents, diffusion of solutes, precipitation, precursor decomposition and densification. The entire pyrolysis process, however, is more complicated, with many possible reaction pathways and possibly different events occurring at the same time. A simplified schematic of processes in furnace is depicted in **Figure 3.4**. The various reactions which can occur (such as pyrolysis, decomposition, and polymerization) can be controlled by adjusting the system parameters. Moreover, the morphologies (such as dense solid particles versus hollow shells) can be tuned by solvent evaporation rates and solubility of precursors.[1, 2, 10] These factors can affect the degree of supersaturation, which significantly influences the morphology of final products.

For particle collection, a bubbler, filter, or electrostatic precipitator could be installed after the furnace, whereas for film deposition, a heated substrate (e.g., silicon or glass) is placed inside the furnace chamber[1] or, a spraying tube could be connected after the heated zone to directly spray the products onto a substrate.[17] The final product size can be theoretically calculated based on micro-droplet size, as shown in equation 3.2

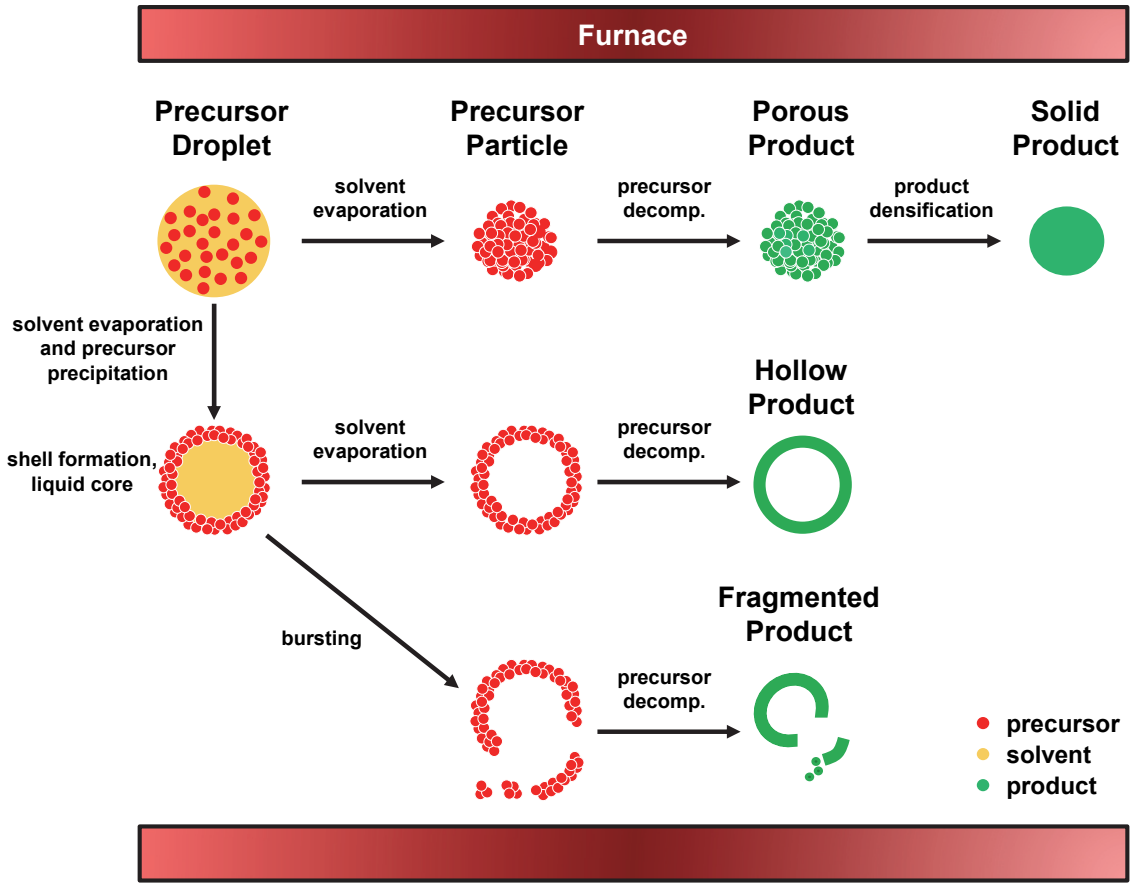

Figure 3.4 Illustration of some possible aerosol pathways during ultrasonic spray product formation.[1]

3.3.2 Template-Based Synthesis

Templates can be introduced to control the morphologies available for spray pyrolysis products. The templates can be formed either *ex situ* or *in situ*.

Here the *ex situ* templates refer to inert solid materials (added intentionally) embedded in the final products, such as silica[18, 19] or polystyrene[14, 20], which is incorporated during the nebulization process. Upon heating, the precursors react as described in section 3.3.1, and products and templates together form a single microsphere. These templates can then be burned out, washed away, or etched.

For carbon-based templates, such as polystyrene microspheres, the template removal can be performed in line with a second furnace tube, burning out the template at a higher temperature. Similarly, surfactants and block copolymers (which are commonly

used to facilitated the self-assembly during nebulization) can also be removed in this manner, giving porous structures in the final products.[21]

Inert salts or their eutectic mixtures can also serve as templating agents.[22-24] When compared to the other *ex situ* templating methods, there are two major advantages: most inert salts are inexpensive and readily washable (removable) and thus are environmentally friendly compared to some etching processes. Also, there are a wide variety of salts or salt mixtures to choose from. The choice of salt or salt mixture dictates the phase of the template, which can greatly impact the final morphology of the particle. A schematic of the salt-templating method is shown in **Figure 3.5**.

A third method is etching away the scaffold templated formed or doped during nebulization process. A typical example of such template is colloidal silica. This templating method has been used widely to provide microspheres with high porosity and layered structures.[19]

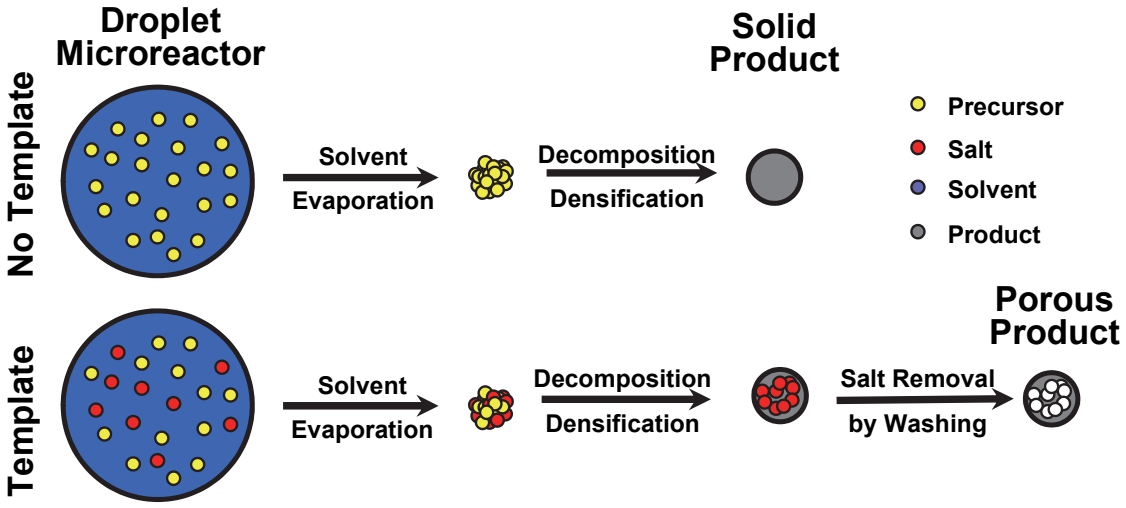

Figure 3.5 Schematic of ultrasonic spray technique with salt-templating method

In situ templates here refer to gases formed during the spray synthesis process. Many precursors or template precursors (e.g., gas produced during decomposition processes such as NO_x gases produced by nitrate salts) produce gases under reaction, which can break/open particles, providing hollow structures or porosity.

Some templating materials have dual functions during pyrolysis process. Nitrate salts are a typical example. First, they melt and form a liquid salt. Second, they decompose and form NO_x gases which provides an *in situ* template. Third, after decomposition they leave behind sodium hydroxide (solid or liquid depending on the furnace temperature) which can interact further to promote base-catalyzed reactions.[25, 26] Another example is the decomposition of permanganic acid which will be discussed in detail in the next chapter.

3.3.3 Aerosol Routes to Films

Film deposition processes with spray pyrolysis generally involve evaporation of solvents, precursor decomposition, and deposition on the substrate (and further surface reactions on the substrate may occur). Similar to particle production, there also could be many different reaction pathways during the process and proper precursor or substrate should be used. These various film deposition processes are depicted in **Figure 3.6**.

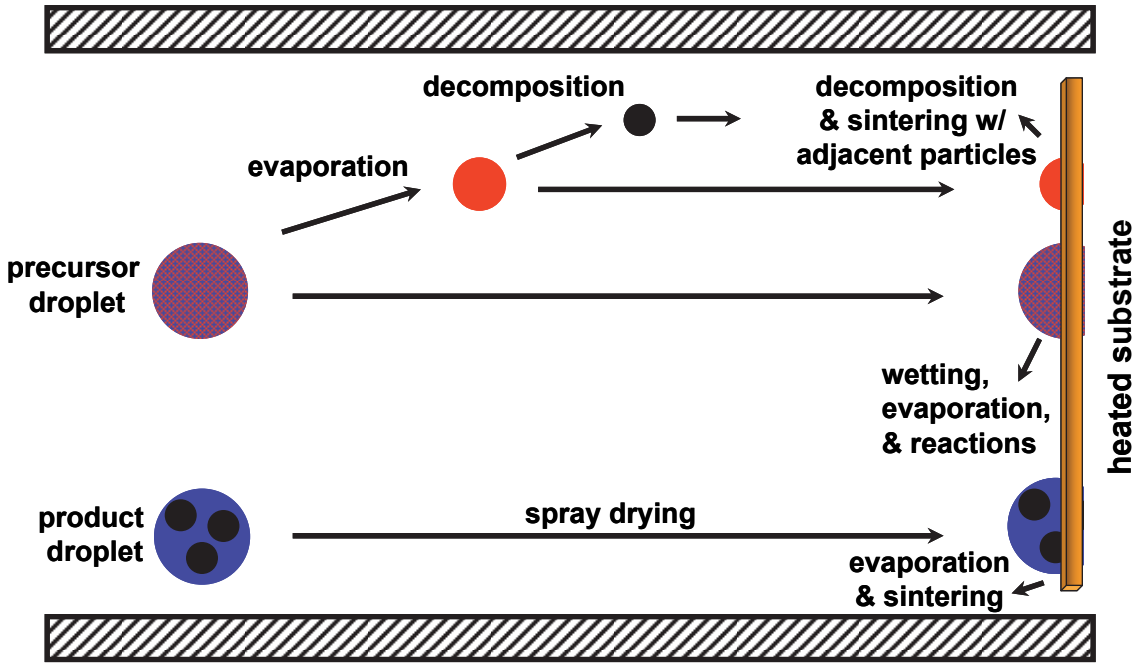

Figure 3.6 Methods of film deposition using aerosol techniques.[1]

Depending on the applications of the desired film, the criteria for film quality may include porosity, microstructure, uniformity, and smoothness. Spray drying is generally used to produce a dense film with solid product particles,[27] whereas porous films can be produced with an ultrasonic spray synthesis technique, taking advantage of its ability to produce particles with various sizes and porosities. Such porosities. i.e., with high surface area, are especially desirable for sensor applications,[15, 28] Particle smoothness/roughness could be a potential bottle-neck for its application in film deposition due to the polydispersity of the droplets produced during the process, unless the droplet sized can be carefully controlled within specs.

Despite some potential problems with aerosol deposition techniques, they still provide numerous advantages over other preparatory methods, particularly in their continuousness, low cost, and the wide choice of precursor materials (solutions or suspensions). In addition, aerosol-assisted CVD expanded the product variety zone for aerosol spray synthesis.

3.4 Examples of Products Prepared by Ultrasonic Spray Technique

3.4.1 Metal and Metal Oxide Microspheres

Ultrasonic Spray pyrolysis has been frequently used to prepare micro-structured fine powders. So far, a number of metals (or metal alloys) have been synthesized, including Au, Ag, Pd, Cu, Ni, bimetallic Au/Ag and Ag/Pd.[29-39] Typically, a single metal salt or metal salt mixture is used as the precursor, and metal products are produced by thermal decomposition under inert atmosphere (e.g. Ar and N_2). A reductive environment, i.e., using H_2, is also sometimes applied for more reactive materials (e.g., Cu, Ni or Co).[40] In additional, reducing reagents such as ethanol, which produce CO, CH_4, and H_2, are also used as co-solvent in precursors.[37, 41]

Numerous metal oxide powders have also been prepared via spray pyrolysis, including mono-metallic oxides (e.g. Fe_2O_3, Fe_3O_4, SnO_2, ZnO, TiO_2, V_2O_5 and Co_3O_4),[42-56] multi-component oxides (e.g. $NiFe_3O_4$, $LaCoO_3$, $BaTiO_3$, and $SiTiO_3$) and binary metal oxides (e.g. Al_2O_3-SiO_2).[57-63] Generally, metal salts, such as metal nitrates, chlorates and acetates are employed as precursors to produce metal oxide powders in an oxidizing environment (e.g., air and H_2O). It should be noted that metal chalogenides,

such as MoS_2, has also been synthesized with USP, and microsphere porosity could be tuned by addition of sacrificial templates.[19]

3.4.2 Nanoparticles

Nanoparticles can be produced using ultrasonic spray techniques. The limitation, however, is the practical application of these techniques given the fact that the precursor concentration needs to be significantly reduced, resulting in a production rate much lower than other spraying processes. To overcome this shortcoming, two methods have been developed to produce multiple nanoparticles per droplet during spray pyrolysis: salt-assisted aerosol decomposition (SAAD) and chemical aerosol flow synthesis (CAFS).[16, 64, 65]

In the SAAD process, instead of using a highly diluted solution, a large concentration of salt (e.g., KCl, NaCl, and LiCl, or their eutectic mixtures) is added to the precursor solution. This salt, which then melts upon heating, acts as a high temperature solvent that prevents the agglomeration and densification of the nanoparticles nucleated in the micro-droplet After the reaction, the excess salt "solvent" is washed away, leaving nanoparticle products in the collecting bubblers.[66] For comparison, traditional spray pyrolysis synthesis of Y_2O_3-ZrO_2 yields particles with an average diameter of 660 nm. Using the SAAD method, the products are about 12.8 nm in size (**Figure 3.7**).[67] Nanoparticles that have been prepared using this method include Ag/Pd[67], ZnS[67], CeO_2[68], NiO[69], $BaTiO_3$[70], ZnO[71], hydroxyapatite[72], CuO[73] , Co_3O_4[74], Ga_2O_3[75] , and $LaMnO_3$[76].

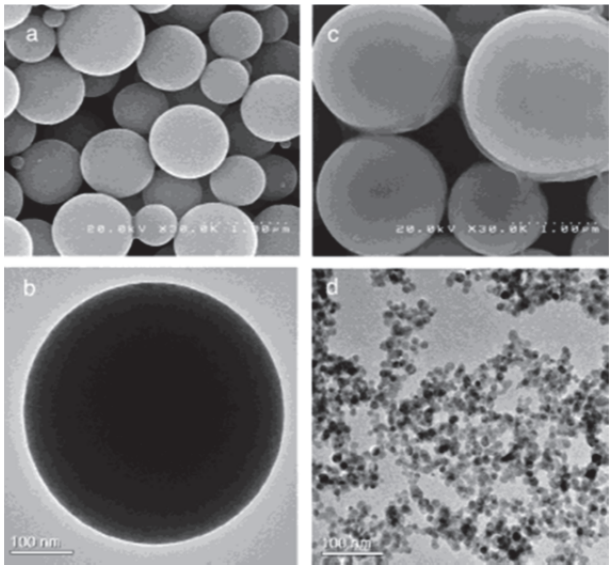

Figure 3.7 SEM and TEM images of Y_2O_3-ZrO_2 products produced with (a and b) conventional spray pyrolysis, and (c and d) with SAAD method. (c) Unwashed and (d) washed SAAD products. Note that the conventional aerosol decomposition technique leads to large spheres while SAAD templating method gives nanoparticles.[76]

Chemical aerosol flow synthesis (CAFS) synthesis uses high temperature solvent during spray pyrolysis. In CAFS two solvents, one with high boiling point and one with low boiling point are used, so that when the reaction happens below the boiling point of the higher one, there is still some solvents remaining in the droplets. In this case, similar to SAAD, no densification occurs after product nucleation process happens. Many semiconductor materials have been produced using this method, including CdS, CdSe, and CdTe quantum dots with narrow size distributions.[64] The size, fluorescence, and band gaps of these nano-dots are also tunable by controlling the concentrations of the reagents in the precursor solution, the reaction temperatures (**Figure 3.8**).

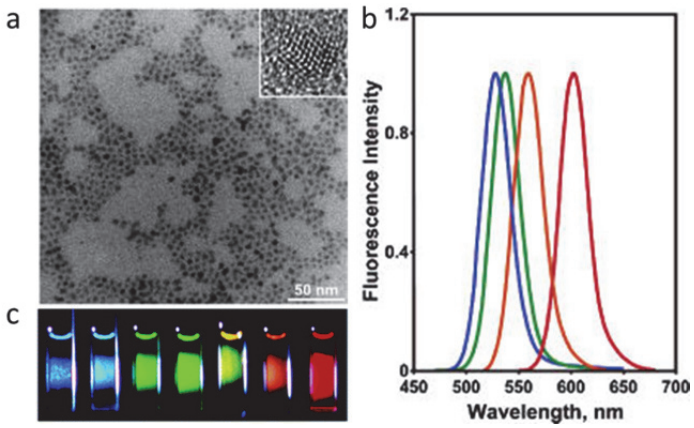

Figure 3.8 (a) TEM and (inset) high resolution TEM of CdSe quantum nanoparticles synthesized via CAFS method. (b) Fluorescence spectra of CdTe quantum dots with increasing Cd concentration from left to right. (c) Photoluminescence photos of CdSe nanoparticles in toluene synthesized using different furnace temperatures (from left to right: 180 °C, 220°C, 240 °C, 260 °C, 280 °C, 300 °C, 320 °C).[64]

3.4.3 Nano-Structured Microsphere Products

Apart from the previously described micron-sized powders, ultrasonic spray techniques can also produce products with a wide variety of nanostructures.

One way to achieve that, as previously stated is, is to use sacrificial templates such as silica nanoparticles, polymers, and metal salts. Upon removal of the template via washing, etching, or burning out, porous products are subsequently recovered. Another way is to take advantage of self-assembly processes which occur during nebulization and heating processes.

3.4.3.1 Self-Assembly

A simple example of nano-structured self-assembly is to use nanoparticles in the precursor. SiO_2 nanoparticles have been used in this manner to assemble well-structured microspheres via the spray drying method (**Figure 3.9**).[77] It was found that both the SiO_2 nanoparticle size and the process temperature affected the morphology of the hierarchical structures produced.

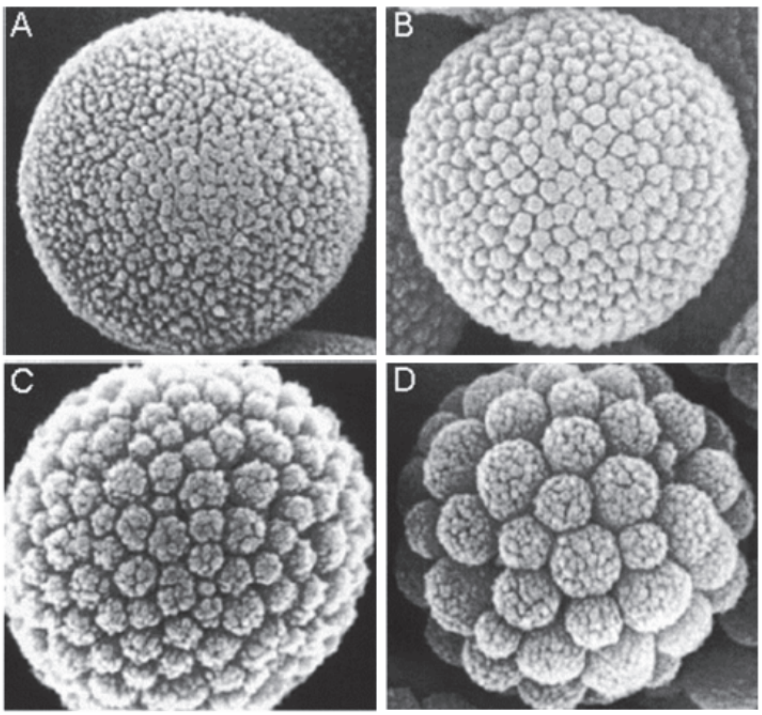

Figure 3.9 SEM images (Magnification of 150 K) of nanostructured SiO_2 spheres prepared by spray drying of colloidal SiO_2 suspensions at 200 °C. The sizes of SiO_2 nanoparticles are (A) 4 to 6 nm, (B) 10 to 20 nm, (C) 40 to 60 nm and (D) 80 to 100 nm.[77]

Surfactant or block-co-polymers can also facilitate the formation of hierarchically structured microspheres. An example of SiO_2 microspheres is illustrated in **Figure 3.10,** in which self-assembly results from using silica nanoparticles and a surfactant in the ethanol/water homogenized precursor.[78, 79] Upon heating and densification, the nanoparticles are remained in the micelle-formed, organized structures. The final morphologies can be controlled via solvent evaporation rate and precursor concentrations.

.

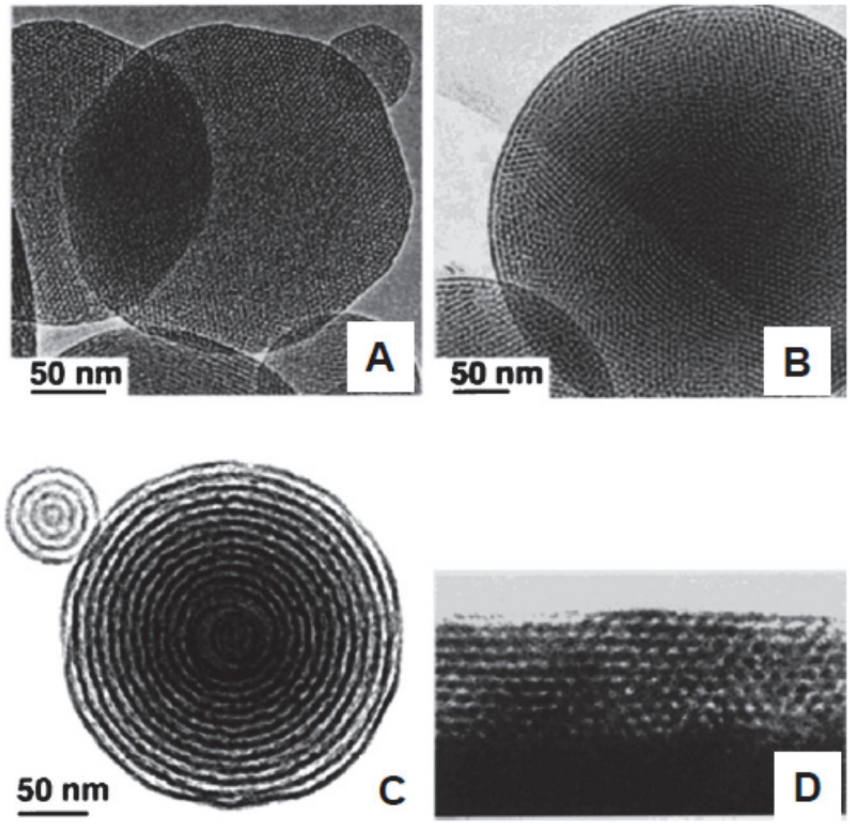

Figure 3.10 TEM images of porous and well-organized silica spheres prepared by evaporation-induced self-assembly showing (A) faceted, (B) cubic, (C) vesicular meso-structure. (D) Cross-section of a porous silica film deposited on a silicon substrate.[63]

Another classic example of self-assembly during the spray drying process is the synthesis of hollow metal-organic framework (MOF) microspheres using MOF nanoparticles as the precursor (e.g., HKUST-1, MIL-88A, ZIF-8, and MOF-5) (**Figure 3.11**). There are no further chemical reactions during the spraying and densification processes, as these hollow spheres will disassemble under sonication, producing well-dispersed, discrete MOF nanoparticles.[80]

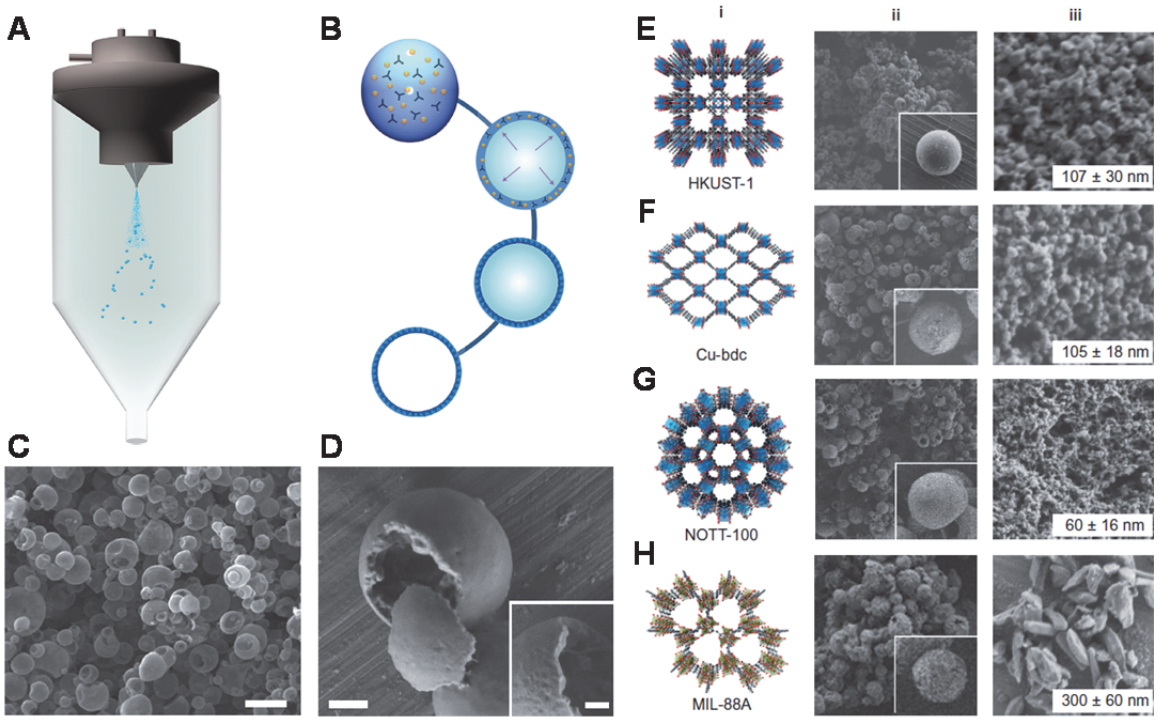

Figure 3.11 (A) illustration of spray drying process for the synthesis of HKUST-1 microspheres. Blue dots, sprayed solution; blue spheres, resulting spherical particles. (B) Proposed spherical superstructure formation process. FESEM images of (C) the HKUST-1 superstructures and (D) a mechanically broken hollow superstructure. Series of MOF superstructures synthesized by spray-drying: (E) HKUST-1, (F) Cu-bdc, (G) NOTT-100, and (H) MIL-88A with (ii) SEM, and (iii) TEM images.[80]

3.4.3.2 Nanostructured Materials via Templating Strategy

Briefly mentioned previously, colloidal SiO_2 nanoparticles can be used as sacrificial templates to produce microspheres with high surface areas. Porous MoS_2 microspheres are synthesized in this manner with ultrasonic spray pyrolysis (**Figure 3.12**).[19] SiO_2/MoS_2 composite particles are first formed by $(NH4)_2MoS_4$ in the presence of SiO_2 nanoparticles. Following HF etching, which selectively leaches out SiO_2, porous MoS_2 microspheres are left behind. The porosity of MoS_2 microspheres can tuned by SiO_2 nanoparticle size. These porous MoS_2 microspheres were proven to have high catalytic activity for thiophene hydrodesulfurization compared to conventional nonporous MoS_2 particles. Moreover, by doping with cobalt, these microspheres exhibit better

activity than RuS_2, which was previously the most active catalyst known for hydrodesulfurization.[19]

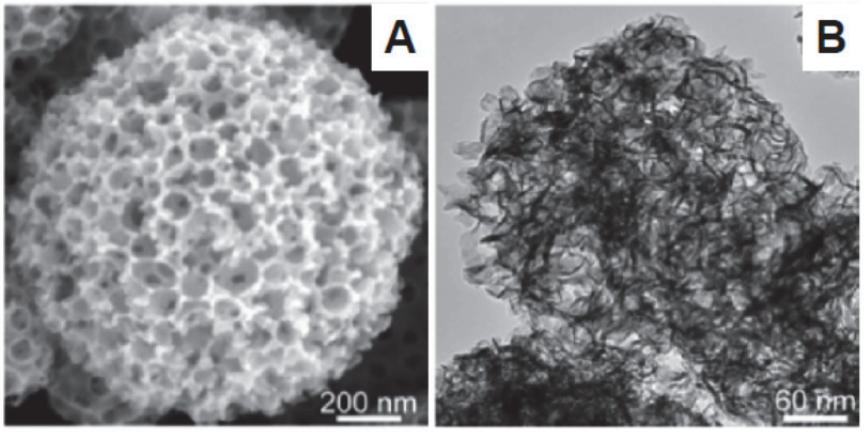

Figure 3.12 (A) An SEM image and (B) TEM image of porous MoS_2 prepared by ultrasonic spray pyrolysis using silica nanoparticles as sacrificial template.[19]

A second example using SiO_2 colloidal templating during USP is in the synthesis of ZnS:Ni^{2+} nanostructured doped composite microspheres. In this example, ZnS:Ni^{2+} hollow microspheres and ZnS nanoparticles were synthesized, with the obtained product depending on the reaction temperature (**Figure 3.13**).[81] At lower temperature, hollow and mesoporous ZnS:Ni^{2+} were obtained after silica template removal, whereas at a higher temperature (~1000 °C), ZnS:Ni^{2+} nanoparticles were produced. The reason for obtaining nanoparticles instead of microspheres is due to rapid ZnS growth, resulting in larger ZnS nanocrystals. As the silica template is removed, the microsphere structure tends to lose its stability and collapse, resulting in individual ZnS nanocrystals. The USP-synthesized ZnS:Ni^{2+} nanoparticles exhibited higher photocatalytic activity compared to ZnS:Ni^{2+} powders prepared by a conventional approaches.

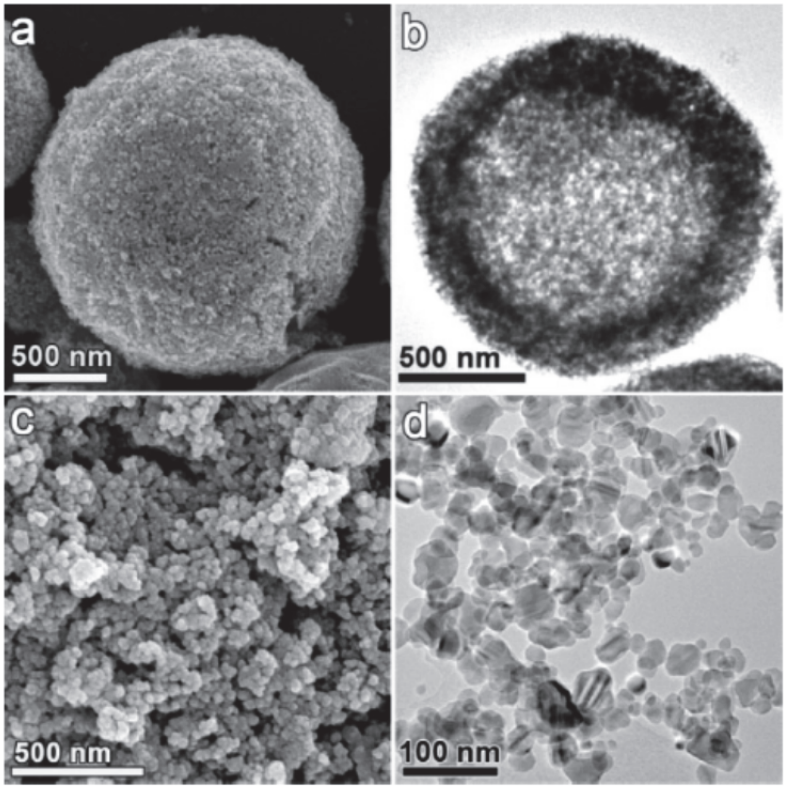

Figure 3.13 SEM and TEM images of ZnS:Ni^{2+} hollow microspheres (a, b), and nanoparticles (c, d) prepared with a silica template by ultrasonic spray pyrolysis.[81]

Another example of using a silica template is the production of nanostructured titania microspheres. Porous, hollow, and ball-in-ball nanostructures of titania were successfully synthesized via USP (**Figure 3.14**).[82] In this case, titania-silica composite microspheres with a ball-in-ball structure were first produced as the reaction occurs in the furnace. After silica is removed with HF etching, nanostructured titania remains, whose drug loading efficiency was superior than that of other reported counterparts.

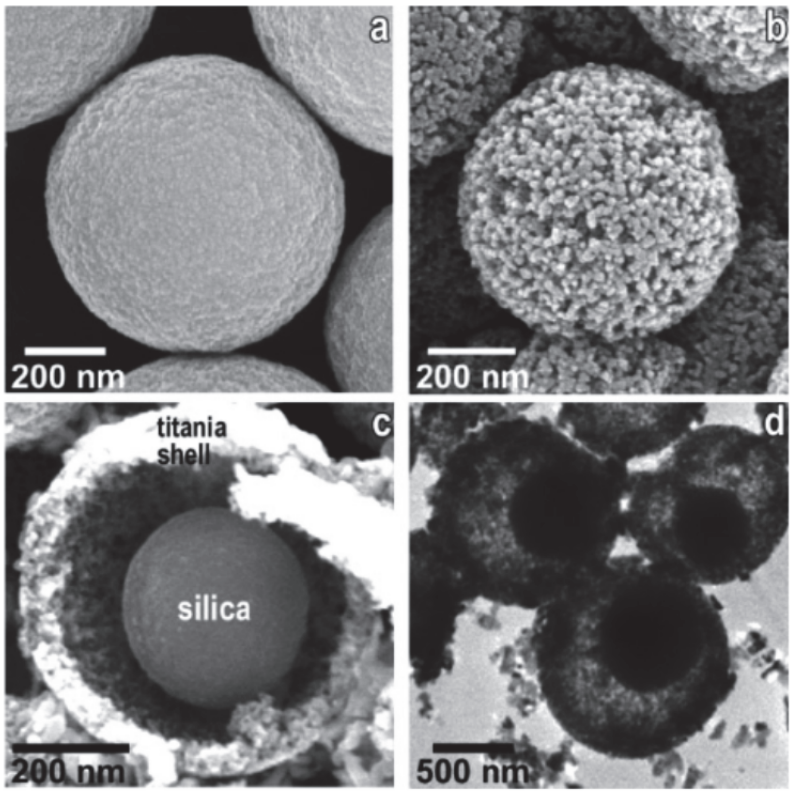

Figure 3.14 SEM and TEM images of (a) silica-titania composite microspheres and (b) porous titania microspheres after HF etching; (c) SEM and (d) TEM images of ball-in-ball silica-titania composite microspheres doped with Co oxide nanoparticles.[82]

Colloidal polymer can also be used as templates during USP to produce nanostructured materials. Similar to sacrificial silica templates, sacrificial latex templates have been used to synthesize ordered mesoporous silica microspheres (**Figure 3.15**).[9] In this case, instead of etching, two furnace were used in serial, with a higher temperature in the second. After the composite microspheres were formed (at 200 °C) using 5 nm SiO_2 nanoparticles and 70 nm polystyrene latex nanoparticles, the higher temperature of the second furnace (at 450 °C) burns away the polystyrene, leaving porous silica structures.

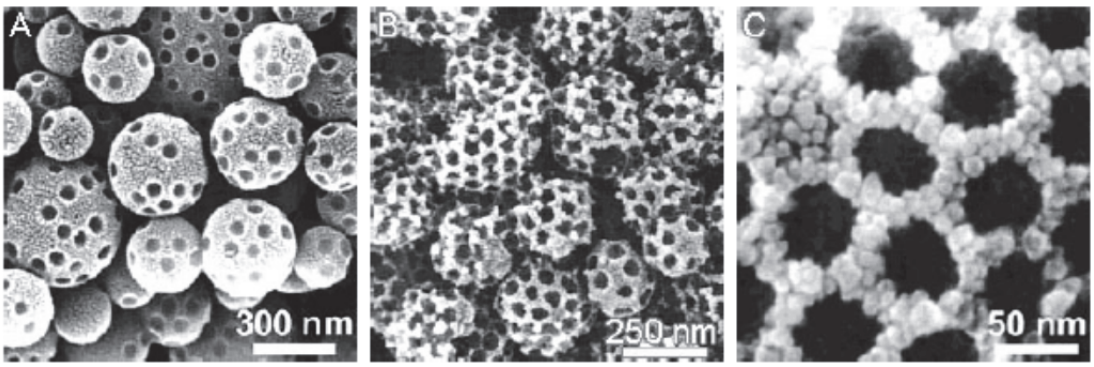

Figure 3.15 SEM images of SiO_2 spheres with organized mesopores prepared by spray pyrolysis of SiO_2/polystyrene colloidal mixtures. The composition of the precursor mixture is (A) 10 mL SiO_2 colloids with 0.5 mL polystyrene colloids and (B) 1.0 mL polystyrene colloids 1.0 mL polystyrene colloids. (C) A high magnification SEM image of the porous SiO_2 matrix.[9]

In another polymer template example, instead of using polystyrene colloids, styrene was used, which polymerized *in situ* after nebulization and heating. This *in situ* polymerization was used in the production of magnetic, metal-doped macroporous silica microspheres (**Figure 3.16**).[8] Again, the synthesized polystyrene template was pyrolyzed out in a subsequent hotter furnace.

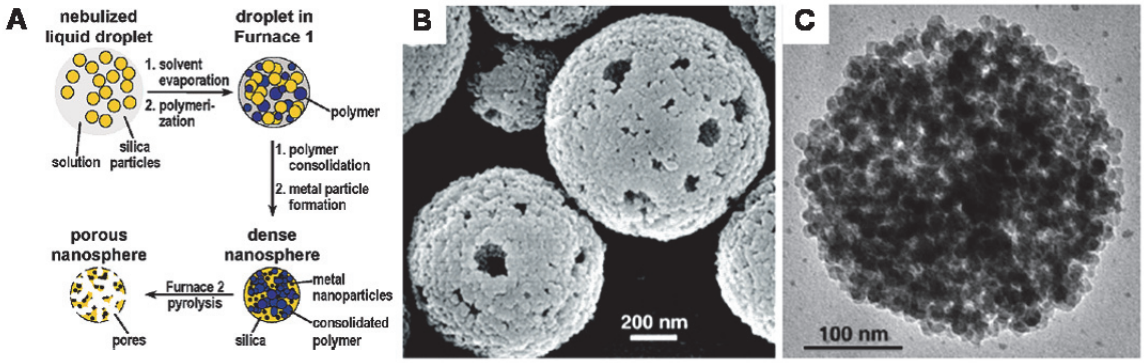

Figure 3.16 (A) Schematic of the synthetic route for porous silica spheres. (B) An SEM image of macroporous silica spheres produced via USP. (C) A TEM image of Co-doped porous magnetic silica sphere.[8]

Salt templates are also used to prepare nanostructured materials with USP process. Metal salts can be intentionally added into the precursor solution or generated *in situ* during the chemical reaction in the furnace (the later case is fairly common and neat in that no additional template is used). The advantage of using a salt template is that it can easily be washed away after spray pyrolysis, leaving the resulted nanostructured particles; thus, the time-consuming and usually dangerous etching process to remove silica template can also be avoided. By utilizing rationally designed organic salts with easily dissociated leaving groups (e.g. CO_2, H_2O, and HCl), porous carbon spheres with high surface area and unique structures have been synthesized via ultrasonic spray pyrolysis.[22, 26, 83, 84]

A one-step synthesic route for the production of porous carbon microspheres from organic salts (e.g., sodium chloroacetate) was developed (**Figure 3.17**).[83] Additionally, different morphologies and surface areas were achieved using different alkali salts, depending on the melting points and decomposition pathways of precursors. Later, a more cost-effective and environmentally benign precursor, sucrose, was used to produce porous carbon microspheres via USP (**Figure 3.18**).[26] Na_2CO_3 or $NaHCO_3$ was added to the aqueous sucrose solution as both a catalyst for sucrose decomposition and a porogen by producing gaseous products. The resulting carbon microspheres have hierarchically porous structures with microporous shells and macroporous cores. In another report, energetic carbon precursors were used—specifically alkali propiolate salts—to produce porous carbons with unique and unprecedented structures (**Figure 3.19** and **3.20**).[84] More importantly, the morphology and surface area of the porous carbon spheres can be readily controlled by using different single alkali propiolate salts or salt mixtures. These porous carbon spheres can be used as catalyst supports and absorbents for environmental pollutants. The Suslick group has further expanded the synthesis of porous carbon to include nanoparticles composites, including gold, silver and iron oxide in porous carbon.[85, 86]

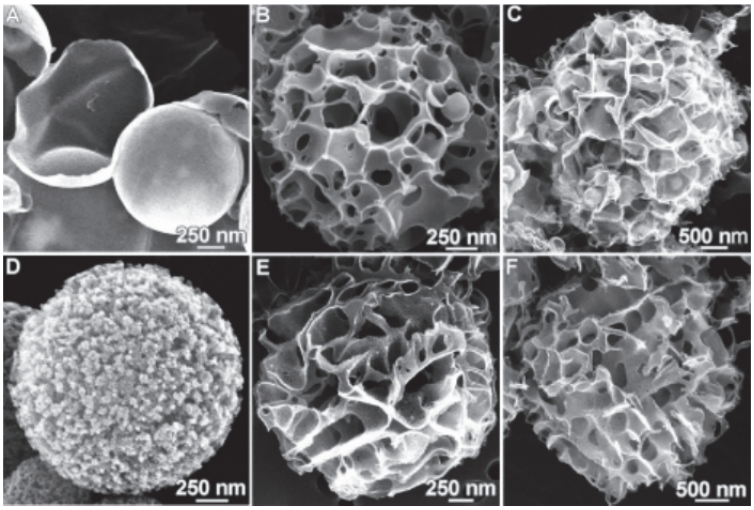

Figure 3.17 SEM images of porous carbon microspheres via USP from different precursors: (A) lithium chloroacetate, (B) sodium chloroacetate, (C) potassium chloroacetate, (D) lithium dichloroacetate, (E) sodium dichloroacetate, and (F) potassium dichloroacetate.[83]

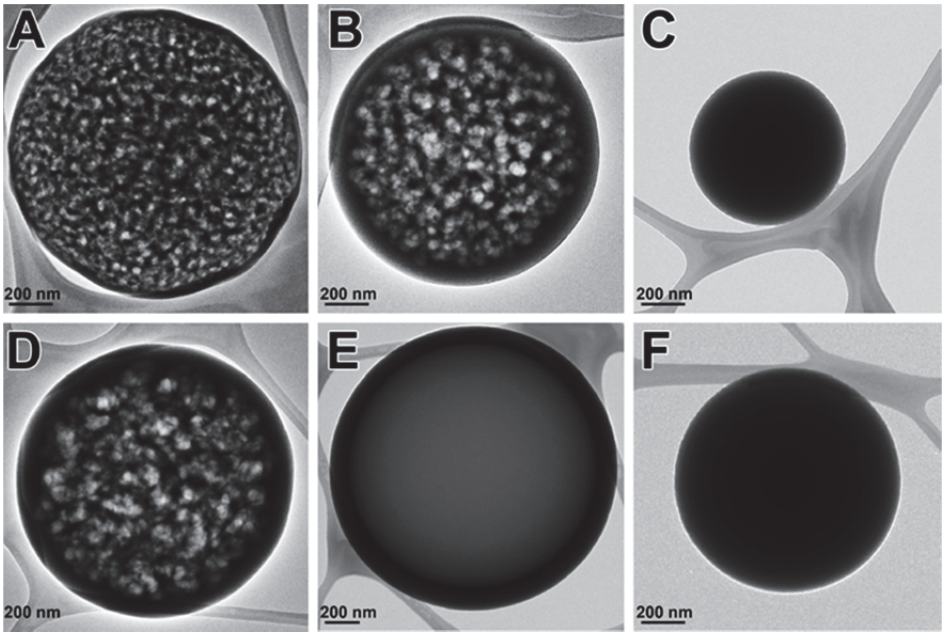

Figure 3.18 TEM images of porous carbons produced from aqueous solutions of 0.5 M sucrose and (A) 1.0 M sodium carbonate, (B) 0.5 M sodium carbonate, (C) 0.1 M sodium carbonate, (D) 1.0 M sodium bicarbonate, (E) 0.5 M sodium bicarbonate, and (F) 0.1 M sodium bicarbonate pyrolyzed at 800 °C.[26]

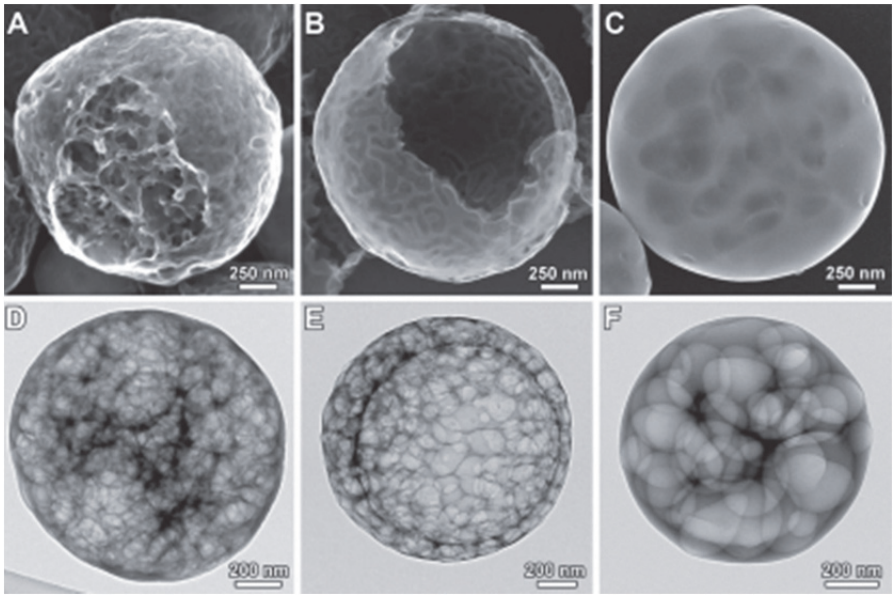

Figure 3.19 SEM and TEM images of porous carbons produced from 1.0 M aqueous solutions of (A and D) lithium propiolate, (B and E) sodium propiolate, and (D and F) potassium propiolate pyrolyzed at 700 °C.[84]

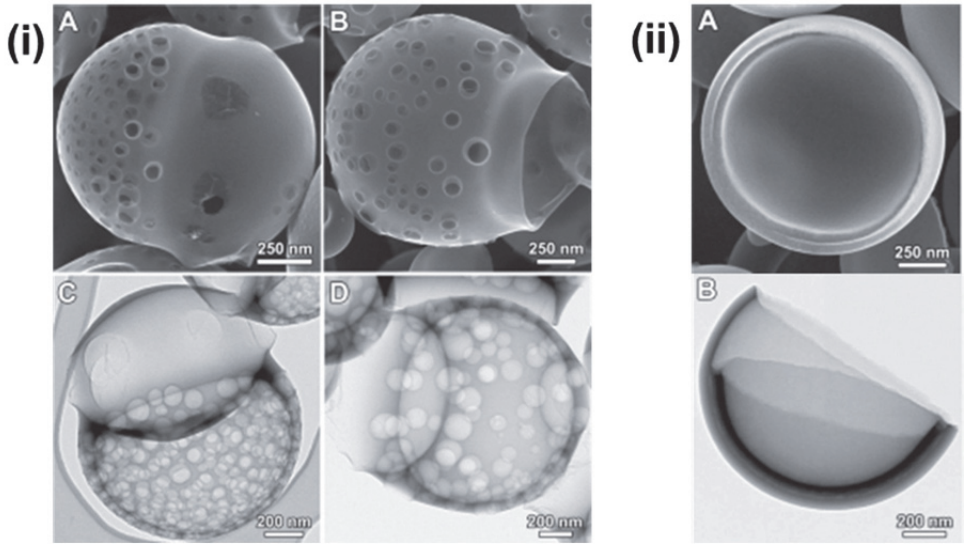

Figure 3.20 SEM and TEM images of porous carbons produced from 1.0 M aqueous solutions of mixtures of propiolate salts: (i) lithium propiolate and sodium propiolate in a (A and C) 1:3 ratio and (B and D) 3:1 ratio; (ii) lithium propiolate and potassium propiolate in a 3:1 ratio.[84]

Interesting morphologies other than spheres have also been achieved with spray pyrolysis including nanoplates and nanowires.[23, 87] single-crystalline Bi_2WO_6 nanoplates were synthesized by combing solid-state metathesis reactions with ultrasonic spray pyrolysis (**Figure 3.21**).[85] In this case, colloidal BiOCl (from the hydrolysis of $BiCl_3$ and Na_2WO_4) was used as precursor material. Since only Bi_2WO_6 microspheres can be produced by traditional USP, it was proposed that the non-transient byproduct and the heat produced are crucial for nanocrystal growth, which facilitates the formation of single-crystalline Bi_2WO_6 nanoplates.

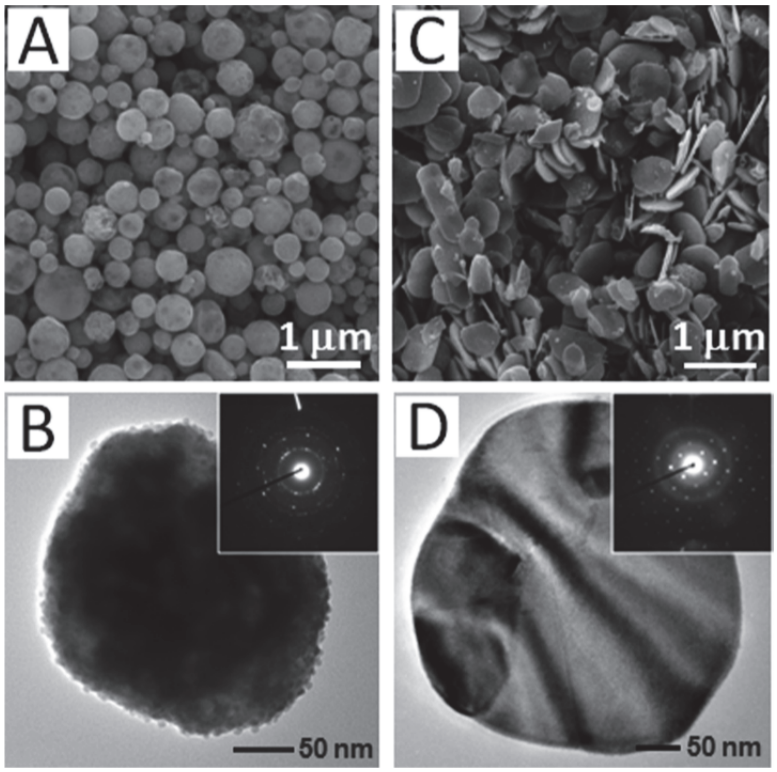

Figure 3.21 (A) SEM and (B) TEM images of Bi_2WO_6 microsphere. Inset: electro diffraction pattern of a Bi_2WO_6 microsphere. (C) SEM and (D) TEM images of Bi_2WO_6 nanoplates. Inset: electro diffraction pattern of a Bi_2WO_6 nanoplate.[85]

3.5 Summary and Outlook

As discussed in this chapter, ultrasonic spray techniques have been used extensively in the preparation of materials with various morphologies. A diverse set of

materials have been synthesized, ranging from simple metals or metal oxides to more complex carbon, MOF, and even composite materials. The morphologies can be controlled by properly choosing the appropriate precursors, templates, solvents, and furnace temperature. Ultrasonic spray techniques are a powerful synthetic tool, especially for application-based materials due to the scalability of the techniques and the environmentally friendly nature of many of the common precursors and templating methods. The following two chapters focus on using ultrasonic spray techniques for the synthesis of supercapacitor electrode materials. Chapter 4 is a thorough study of synthesis of manganese dioxide. Chapter 5 presents the synthesis of conductive polymer, which is by far the most facile way of synthesizing solid, hollow, and porous Poly(3,4-ethylenedioxythiophene) microspheres. All synthesized materials were tested for supercapacitive performance and show superior abilities in comparison to reported counterparts.

3.6 References

(1) Kodas, T. T.; Hampden-Smith, M. J., *Aerosol Processing of Materials*. Wiley-VCH: New York, 1999; p 680.

(2) Messing, G. L.; Zhang, S.-C.; Jayanthi, G. V. Ceramic Powder Synthesis by Spray Pyrolysis. *J. Am. Ceram. Soc.* **1993,** 76, 2707-2726.

(3) Patil, P. S. Versatility of chemical spray pyrolysis technique. *Mater. Chem. Phys.* **1999,** 59, 185-198.

(4) Bang, J.; Didenko, Y.; Helmich, R.; Suslick, K. Nanostructured materials through ultrasonic spray pyrolysis. *Aldrich Materials Matter* **2012,** 7, 15-18.

(5) Xu, H.; Zeiger, B. W.; Suslick, K. S. Sonochemical synthesis of nanomaterials. *Chem. Soc. Rev.* **2013,** 42, 2555-2567.

(6) Nasr, G. G.; Yule, A. J.; Bendig, L., *Industrial Sprays and Atomization*. Springer-Verlag: London, 2002.

(7) Rosell-Llompart, J.; Fernandez, d. l. M. J. Generation of monodisperse droplets 0.3 to 4 μm in diameter from electrified cone-jets of highly conducting and viscous liquids. *J. Aerosol Sci.* **1994,** 25, 1093-1119.

(8) Suh, W. H.; Suslick, K. S. Magnetic and Porous Nanospheres from Ultrasonic Spray Pyrolysis. *J. Am. Chem. Soc.* **2005,** 127, 12007-12010.
(9) Iskandar, F.; Mikrajuddin; Okuyama, K. In Situ production of spherical silica particles containing self-organized mesopores. *Nano Lett.* **2001,** 1, 231-234.
(10) Topp, M. N. Ultrasonic atomization-a photographic study of the mechanism of disintegration. *J. Aerosol Sci* **1973,** 4, 17-25.
(11) Lang, R. J. Ultrasonic Atomization of Liquids. *The Journal of the Acoustical Society of America* **1962,** 34, 6-8.
(12) Lenggoro, I. W.; Hata, T.; Iskandar, F.; Lunden, M. M.; Okuyama, K. An experimental and modeling investigation of particle production by spray pyrolysis using a laminar flow aerosol reactor. *J. Mater. Res.* **2000,** 15, 733-743.
(13) commercially available ultrasonic atomizing nozzle system. http://www.sono-tek.com/how-ultrasonic-nozzles-work/.
(14) Iskandar, F.; Mikrajuddin; Okuyama, K. Controllability of Pore Size and Porosity on Self-Organized Porous Silica Particles. *Nano Lett.* **2002,** 2, 389-392.
(15) Mädler, L.; Roessler, A.; Pratsinis, S. E.; Sahm, T.; Gurlo, A.; Barsan, N.; Weimar, U. Direct formation of highly porous gas-sensing films by in situ thermophoretic deposition of flame-made Pt/SnO 2 nanoparticles. *Sensors and Actuators B: Chemical* **2006,** 114, 283-295.
(16) Helmich, R. J.; Suslick, K. S. Chemical Aerosol Flow Synthesis of Hollow Metallic Aluminum Particles. *Chem. Mater.* **2010,** 22, 4835-4837.
(17) Zhang, Y.; Huff, L. A.; Gewirth, A. A.; Suslick, K. S. Synthesis of Manganese Oxide Microspheres by Ultrasonic Spray Pyrolysis and Their Application as Supercapacitors. *Particle & Particle Systems Characterization* **2015,** 32, 899-906.
(18) Kim, H. Ultrasonic Synthesis of Materials for Energy Conversion Devices. Dissertation, University of Illinois at Urbana-Champaign, Urbana, IL, 2012.
(19) Skrabalak, S. E.; Suslick, K. S. Porous MoS2 Synthesized by Ultrasonic Spray Pyrolysis. *J. Am. Chem. Soc.* **2005,** 127, 9990-9991.
(20) Abdullah, M.; Iskandar, F.; Shibamoto, S.; Ogi, T.; Okuyama, K. Preparation of oxide particles with ordered macropores by colloidal templating and spray pyrolysis. *Acta Mater.* **2004,** 52, 5151-5156.

(21) Fan, H.; Van Swol, F.; Lu, Y.; Brinker, C. J. Multiphased assembly of nanoporous silica particles. *J. Non-Cryst. Solids* **2001,** 285, 71-78.
(22) Skrabalak, S. E.; Suslick, K. S. Carbon powders prepared by ultrasonic spray pyrolysis of substituted alkali benzoates. *The Journal of Physical Chemistry C* **2007,** 111, 17807-17811.
(23) Mann, A. K. P.; Skrabalak, S. E. Synthesis of Single-Crystalline Nanoplates by Spray Pyrolysis: A Metathesis Route to Bi2WO6. *Chem. Mater.* **2011,** 23, 1017-1022.
(24) Peterson, A. K.; Morgan, D. G.; Skrabalak, S. E. Aerosol Synthesis of Porous Particles Using Simple Salts as a Pore Template. *Langmuir* **2010,** 26, 8804-8809.
(25) Atkinson, J. D.; Fortunato, M. E.; Dastgheib, S. A.; Rostam-Abadi, M.; Rood, M. J.; Suslick, K. S. Synthesis and characterization of iron-impregnated porous carbon spheres prepared by ultrasonic spray pyrolysis. *Carbon* **2010,** 49, 587-598.
(26) Fortunato, M. E.; Rostam-Abadi, M.; Suslick, K. S. Nanostructured Carbons Prepared by Ultrasonic Spray Pyrolysis. *Chem. Mater.* **2010,** 22, 1610-1612.
(27) Arun, M., Principles, Classification, and Selection of Dryers. In *Handbook of Industrial Drying, Third Edition*, CRC Press: 2006.
(28) Brousse, T.; Schleich, D. Sprayed and thermally evaporated SnO 2 thin films for ethanol sensors. *Sensors and Actuators B: Chemical* **1996,** 31, 77-79.
(29) Xia, B.; Lenggoro, I. W.; Okuyama, K. Preparation of Nickel Powders by Spray Pyrolysis of Nickel Formate. *J. Am. Ceram. Soc.* **2001,** 84, 1425-1432.
(30) Xia, B.; Lenggoro, I. W.; Okuyama, K. Preparation of Ni particles by ultrasonic spray pyrolysis of NiCl2·6H2O precursor containing ammonia. *Journal of Materials Science* **2001,** 36, 1701-1705.
(31) Kieda, N.; Messing, G. L. Preparation of silver particles by spray pyrolysis of silver-diammine complex solutions. *J. Mater. Res.* **1998,** 13, 1660-1665.
(32) Pluym, T. C.; Powell, Q. H.; Gurav, A. S.; Ward, T. L.; Kodas, T. T.; Wang, L. M.; Glicksman, H. D. Solid silver particle production by spray pyrolysis. *J. Aerosol Sci.* **1993,** 24, 383-92.
(33) Majumdar, D.; Kodas, T. T.; Glicksman, H. D. Gold particle generation by spray pyrolysis. *Adv. Mater. (Weinheim, Ger.)* **1996,** 8, 1020-1022.

(34) Guermen, S.; Stopic, S.; Friedrich, B. Synthesis of nanosized spherical cobalt powder by ultrasonic spray pyrolysis. *Mater. Res. Bull.* **2006,** 41, 1882-1890.
(35) Zheng, R.; Guo, X.; Fu, H. One-step, template-free route to silver porous hollow spheres and their optical property. *Appl. Surf. Sci.* **2010,** 257, 2367-2370.
(36) Iida, N.; Naito, H.; Ito, H.; Nakayama, K.; Lenggoro, I. W.; Okuyama, K. Spray pyrolysis synthesis and evaluation of fine bimetallic Au-Pd particles. *J. Ceram. Soc. Jpn.* **2004,** 112, 405-408.
(37) Kim, J. H.; Babushok, V. I.; Germer, T. A.; Mulholland, G. W.; Ehrman, S. H. Cosolvent-assisted spray pyrolysis for the generation of metal particles. *J. Mater. Res.* **2003,** 18, 1614-1622.
(38) Kodera, T.; Myojin, K.; Ogihara, T. Preparation and characterization of spherical metal particles by spray pyrolysis. *Key Eng. Mater.* **2010,** 421-422, 558-561.
(39) Iida, N.; Nakayama, K.; Okuyama, K.; Lenggoro, I. W. Preparation of Au/Ag Alloy Particles by Spray Pyrolysis and Its Applications. *Journal of the Society of Powder Technology, Japan* **2004,** 41, 246-251.
(40) Bang, J. H.; Suslick, K. S. Applications of ultrasound to the synthesis of nanostructured materials. *Adv. Mater.* **2010,** 22, 1039-1059.
(41) Kim, J. H.; Germer, T. A.; Mulholland, G. W.; Ehrman, S. H. Size-monodisperse metal nanoparticles via hydrogen-free spray pyrolysis. *Adv. Mater.* **2002,** 14, 518.
(42) Basak, S.; Rane, K. S.; Biswas, P. Hydrazine-assisted, low-temperature aerosol pyrolysis method to synthesize γ-Fe2O3. *Chem. Mater.* **2008,** 20, 4906-4914.
(43) Chou, S.-L.; Wang, J.-Z.; Wexler, D.; Konstantinov, K.; Zhong, C.; Liu, H.-K.; Dou, S.-X. High-surface-area α-Fe2O3/carbon nanocomposite: one-step synthesis and its highly reversible and enhanced high-rate lithium storage properties. *J. Mater. Chem.* **2010,** 20, 2092-2098.
(44) Kim, D.-H.; Kim, K.-N.; Kim, K.-M.; Shim, I.-B.; Lee, M.-H.; Lee, Y.-K. Tuning of magnetite nanoparticles to hyperthermic thermoseed by controlled spray method. *Journal of materials science* **2006,** 41, 7279-7282.
(45) Xu, X. L.; Guo, J. D.; Wang, Y. Z. A novel technique by the citrate pyrolysis for preparation of iron oxide nanoparticles. *Mater. Sci. Eng., B* **2000,** B77, 207-209.

(46) Cabanas, M. v.; Vallet-Reg, M.; Labeau, M.; Gonzalez, C. Spherical iron oxide particles synthesized by an aerosol technique. *J. Mater. Res.* **1993,** 8, 2694-701.
(47) Lee, J. H.; Park, S. J. Preparation of spherical SnO2 powders by ultrasonic spray pyrolysis. *J. Am. Ceram. Soc.* **1993,** 76, 777-780.
(48) Milosevic, O.; Jordovic, B.; Uskokovic, D. Preparation of fine spherical ZnO powders by an ultrasonic spray pyrolysis method. *Mater. Lett.* **1994,** 19, 165-70.
(49) Liu, T.-Q.; Sakurai, O.; Mizutani, N.; Kato, M. Preparation of spherical fine ZnO particles by the spray pyrolysis method using ultrasonic atomization techniques. *Journal of Materials science* **1986,** 21, 3698-3702.
(50) Tani, T.; Maedler, L.; Pratsinis, S. E. Homogeneous ZnO Nanoparticles by Flame Spray Pyrolysis. *J. Nanopart. Res.* **2002,** 4, 337-343.
(51) Murugavel, P.; Kalaiselvam, M.; Raju, A. R.; Rao, C. N. R. Sub-micrometer spherical particles of TiO2, ZrO2 and PZT by nebulized spray pyrolysis of metal-organic precursors. *J. Mater. Chem.* **1997,** 7, 1433-1438.
(52) Lee, J. H.; Cho, H. J.; Park, S. J. Preparation of spherical titania particles by ultrasonic spray pyrolysis. *Ceram. Trans.* **1991,** 22, 39-44.
(53) Ahonen, P.; Kauppinen, E.; Joubert, J.; Deschanvres, J.; Tendeloo, G. V. Preparation of nanocrystalline titania powder via aerosol pyrolysis of titanium tetrabutoxide. *J. Mater. Res.* **1999,** 14, 3938-3948.
(54) Xiong, Y.; Lyons, S. W.; Kodas, T. T.; Pratsinis, S. E. Volatile metal oxide evaporation during aerosol decomposition. *J. Am. Ceram. Soc.* **1995,** 78, 2490-6.
(55) Kim, D. Y.; Ju, S. H.; Koo, H. Y.; Hong, S. K.; Kang, Y. C. Synthesis of nanosized Co3O4 particles by spray pyrolysis. *J. Alloys Compd.* **2006,** 417, 254-258.
(56) Zhao, Z. W.; Konstantinov, K.; Yuan, L.; Liu, H. K.; Dou, S. X. In-situ fabrication of nanostructured cobalt oxide powders by spray pyrolysis technique. *J. Nanosci. Nanotechnol.* **2004,** 4, 861-866.
(57) Yu, H.-F.; Gadalla, A. M. Preparation of NiFe2O4 powder by spray pyrolysis of nitrate aerosols in NH3. *J. Mater. Res.* **1996,** 11, 663-70.
(58) Chiarello, G. L.; Grunwaldt, J.-D.; Ferri, D.; Krumeich, F.; Oliva, C.; Forni, L.; Baiker, A. Flame-synthesized LaCoO3-supported Pd. 1. Structure, thermal stability and reducibility. *J. Catal.* **2007,** 252, 127-136.

(59) Chiarello, G. L.; Rossetti, I.; Forni, L. Flame-spray pyrolysis preparation of perovskites for methane catalytic combustion. *J. Catal.* **2005,** 236, 251-261.
(60) Huang, C. S.; Tao, C. S.; Lee, C. H. Nebulized spray deposition of Pb(Zr, Ti)O3 thin films. *J. Electrochem. Soc.* **1997,** 144, 3556-3561.
(61) Nimmo, W.; Ali, N. J.; Brydson, R. M.; Calvert, C.; Hampartsoumian, E.; Hind, D.; Milne, S. J. Formation of lead zirconate titanate powders by spray pyrolysis. *J. Am. Ceram. Soc.* **2003,** 86, 1474-1480.
(62) Nimmo, W.; Ali, N. J.; Brydson, R.; Calvert, C.; Milne, S. J. Particle formation during spray pyrolysis of lead zirconate titanate. *J. Am. Ceram. Soc.* **2005,** 88, 839-844.
(63) Laine, R. M.; Baranwal, R.; Hinklin, T.; Treadwell, D.; Sutorik, A.; Bickmore, C.; Waldner, K.; Neo, S. S. Making nanosized oxide powders from precursors by flame spray pyrolysis. *Key Eng. Mater.* **1999,** 159-160, 17-24.
(64) Didenko, Y. T.; Suslick, K. S. Chemical Aerosol Flow Synthesis of Semiconductor Nanoparticles. *J. Am. Chem. Soc.* **2005,** 127, 12196-12197.
(65) Bang, J. H.; Suh, W. H.; Suslick, K. S. Quantum Dots from Chemical Aerosol Flow Synthesis: Preparation, Characterization, and Cellular Imaging. *Chem. Mater.* **2008,** 20, 4033-4038.
(66) Kim, S. H.; Liu, B. Y. H.; Zachariah, M. R. Synthesis of Nanoporous Metal Oxide Particles by a New Inorganic Matrix Spray Pyrolysis Method. *Chem. Mater.* **2002,** 14, 2889-2899.
(67) Xia, B.; Lenggoro, I. W.; Okuyama, K. Novel route to nanoparticle synthesis by salt-assisted aerosol decomposition. *Adv. Mater. (Weinheim, Ger.)* **2001,** 13, 1579-1582.
(68) Xia, B.; Lenggoro, I. W.; Okuyama, K. Synthesis of CeO2 nanoparticles by salt-assisted ultrasonic aerosol decomposition. *J. Mater. Chem.* **2001,** 11, 2925-2927.
(69) Xia, B.; Lenggoro, I. W.; Okuyama, K. Nanoparticle separation in salted droplet microreactors. *Chem. Mater.* **2002,** 14, 2623-2627.
(70) Itoh, Y.; Lenggoro, I. W. Agglomerate-free BaTiO3 particles by salt-assisted spray pyrolysis. *J. Mater. Res.* **2002,** 17, 3222-3229.
(71) Panatarani, C.; Lenggoro, I. W.; Okuyama, K. Synthesis of Single Crystalline ZnO Nanoparticles by Salt-Assisted Spray Pyrolysis. *J. Nanopart. Res.* **2003,** 5, 47-53.

(72) An, G. H.; Wang, H. J.; Kim, B. H.; Jeong, Y. G.; Choa, Y. H. Fabrication and characterization of a hydroxyapatite nanopowder by ultrasonic spray pyrolysis with salt-assisted decomposition. *Mater. Sci. Eng., A* **2007,** A449-A451, 821-824.
(73) Lee, S. G.; Choi, S. M.; Lee, D. The role of salt in nanoparticle generation by salt-assisted aerosol method: Microstructural changes. *Thermochim. Acta* **2007,** 455, 138-147.
(74) Ran, S.; Gao, L. Preparation of α-MnO2 nanorods and Co3O4 submicrooctahedrons by molten salt route. *Chem. Lett.* **2007,** 36, 688-689.
(75) Ogi, T.; Kaihatsu, Y.; Iskandar, F.; Tanabe, E.; Okuyama, K. Synthesis of nanocrystalline GaN from Ga2O3 nanoparticles derived from salt-assisted spray pyrolysis. *Adv. Powder Technol.* **2009,** 20, 29-34.
(76) Chen, W.; Hong, J.; Li, Y. Facile fabrication of perovskite single-crystalline LaMnO3 nanocubes via a salt-assisted solution combustion process. *J. Alloys Compd.* **2009,** 484, 846-850.
(77) Iskandar, F.; Lenggoro, I. W.; Xia, B.; Okuyama, K. Functional nanostructured silica powders derived from colloidal suspensions by sol spraying. *J. Nanopart. Res.* **2001,** 3, 263-270.
(78) Lu, Y.; Fan, H.; Stump, A.; Ward, T. L.; Rieker, T.; Brinker, C. J. Aerosol-assisted self-assembly of mesostructured spherical nanoparticles. *Nature (London)* **1999,** 398, 223-226.
(79) Ji, X.; Hu, Q.; Hampsey, J. E.; Qiu, X.; Gao, L.; He, J.; Lu, Y. Synthesis and characterization of functionalized mesoporous silica by aerosol-assisted self-assembly. *Chem. Mater.* **2006,** 18, 2265-2274.
(80) Carné-Sánchez, A.; Imaz, I.; Cano-Sarabia, M.; Maspoch, D. A spray-drying strategy for synthesis of nanoscale metal–organic frameworks and their assembly into hollow superstructures. *Nature chemistry* **2013,** 5, 203-211.
(81) Bang, J. H.; Helmich, R. J.; Suslick, K. S. Nanostructured ZnS: Ni2+ photocatalysts prepared by ultrasonic spray pyrolysis. *Adv. Mater.* **2008,** 20, 2599-2603.
(82) Suh, W. H.; Jang, A. R.; Suh, Y.-H.; Suslick, K. S. Porous, hollow, and ball-in-ball metal oxide microspheres: preparation, endocytosis, and cytotoxicity. *Adv. Mater. (Weinheim, Ger.)* **2006,** 18, 1832-1837.

(83) Skrabalak, S. E.; Suslick, K. S. Porous Carbon Powders Prepared by Ultrasonic Spray Pyrolysis. *J. Am. Chem. Soc.* **2006,** 128, 12642-12643.
(84) Xu, H.; Guo, J.; Suslick, K. S. Porous Carbon Spheres from Energetic Carbon Precursors using Ultrasonic Spray Pyrolysis. *Adv. Mater. (Weinheim, Ger.)* **2012,** 24, 6028-6033.
(85) Atkinson, J. D.; Fortunato, M. E.; Dastgheib, S. A.; Rostam-Abadi, M.; Rood, M. J.; Suslick, K. S. Synthesis and characterization of iron-impregnated porous carbon spheres prepared by ultrasonic spray pyrolysis. *Carbon* **2011,** 49, 587-598.
(86) Guo, J.; Suslick, K. S. Gold nanoparticles encapsulated in porous carbon. *Chem. Commun. (Cambridge, U. K.)* **2012,** 48, 11094-11096.
(87) Vivekchand, S.; Gundiah, G.; Govindaraj, A.; Rao, C. A new method for the preparation of metal nanowires by the nebulized spray pyrolysis of precursors. *Adv. Mater.* **2004,** 16, 1842-1845.

CHAPTER 4
ULTRASONIC SPRAY SYNTHESIS FOR MNO_2 MICROSPHERES AS SUPERCAPACITOR ELECTRODE MATERIALS

4.1 Introduction to Supercapacitors

Supercapacitors, also known as electrochemical capacitors (EC), have attracted tremendous attention due to their ability to store energy quickly and efficiently.[1-11] As illustrated in the Ragone Plot (**Figure 4.1**),[2, 12] in which different types of energy storage methods are compared, electrochemical capacitors fill the gap between batteries and conventional solid state and electrolytic capacitors. Although their energy density is generally lower than that of batteries, they can be fully charged or discharged within seconds and can deliver or uptake a much higher energy within a short time frame.[6] Supercapacitors have already been widely used in consumer electronics, memory back-up systems, un-interruptible power supplies (back-up supplies used to protect against power disruption) and load leveling. Another recent exciting application is their use in airplane emergency doors (16 per plane) on the Airbus380, which highlight their safety and reliability. In short, supercapacitors are demonstrating their importance in a variety of innovative technologies.[6]

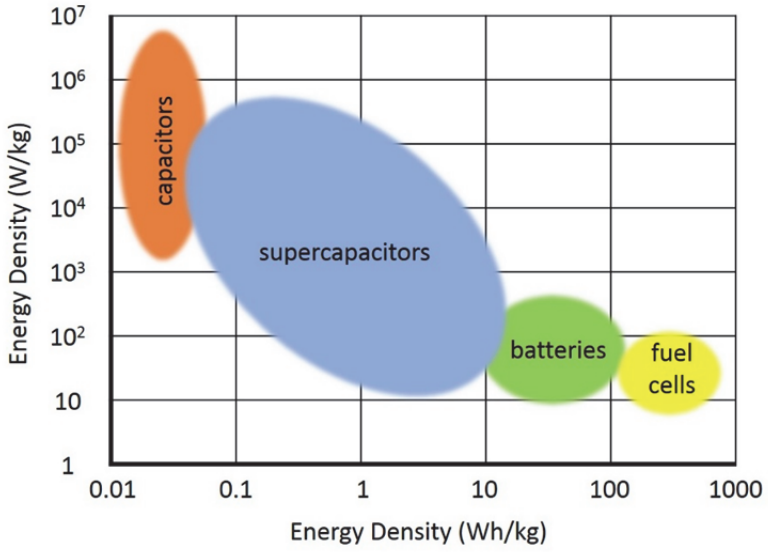

Figure 4.1 Ragone plot of the electrochemical energy storage system.[12]

Based on different energy storage mechanisms, supercapacitors can be classified into two categories: electrical double layer capacitors (EDLC) and pseudocapacitors (**Figure 4.2**).[13] EDLC relies on the capacitance of electrostatic charge accumulation at the interface of electrode and electrolyte. As a result, capacity is determined by the available surface area on the electrode to the electrolyte ions. Currently, such EDLC materials are generally carbon-based structures with high surface area.[7, 14-18] Pseudocapacitors, on the other hand, use fast and reversible surface or near-surface faradic process charge storage. In this sense, electro-active materials/chemical groups are essential to its performance. Transition metal oxides[19, 20] as well as electrically conducting polymers[21, 22] are examples of pseudo-capacitive active materials. While pseudo-capacitance can be higher than EDL capacitance, it usually suffers from low power density (due to poor electrical conductivity) and a lack of stability during cycling. Hybrid capacitors are a third type of supercapacitor which combine a capacitive or pseudo-capacitive electrode with a battery electrode and benefit from both the capacitor and the battery properties.[6, 23]

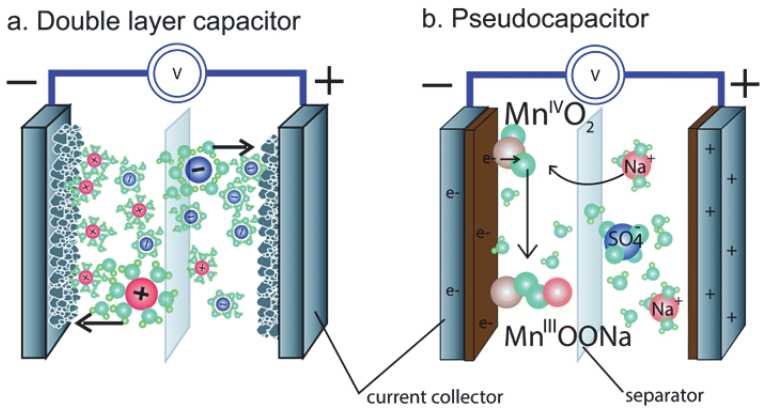

Figure 4.2 Basic schematics for (a) carbon EDLC and (b) pseudocapacitor (MnO_2 based).[13]

4.2 Electrochemical Double Layer Capacitors (EDLC)

The first patent describing the concept of an electrochemical capacitor was filed in 1957 by Becker[24]. In 1971, NEC developed aqueous-electrolyte capacitors for power-saving units in electronics; this application can be considered as the first application for electrochemical capacitor use in commercial devices.[6, 24]

EDLCs are electrochemical capacitors that store the charge electrostatically using reversible adsorption of electrolyte ion onto electrochemically stable materials which have high accessible surface area. In 1853, Helmholtz described the double layer capacitance C, which occurs due to charge separation on the polarized electrode–electrolyte interface, with Equation 4.1.[6]

$$C = \frac{\varepsilon_r \varepsilon_0 A}{d} \tag{4.1}$$

Here, ε_r is the electrolyte dielectric constant, ε_0 is the dielectric constant of the vacuum, *d* is the effective thickness of the double layer (charge separation distance) and *A* is the electrode surface area.[6, 25]

This capacitance model was then revised by the Stern model (**Figure 4.3**).[25] The Stern model contains the inner Helmholtz plane (IHP) and the outer Helmholtz plane (OHP). The IHP refers to the distance of closest packed monolayer of adsorbed counter-charged ions or dipoles (usually polarized solvent), and the OHP refers to that of the non-specifically adsorbed ions outside the IHP (which usually contains solvated ions). The OHP is also the plane where the diffuse layer begins.

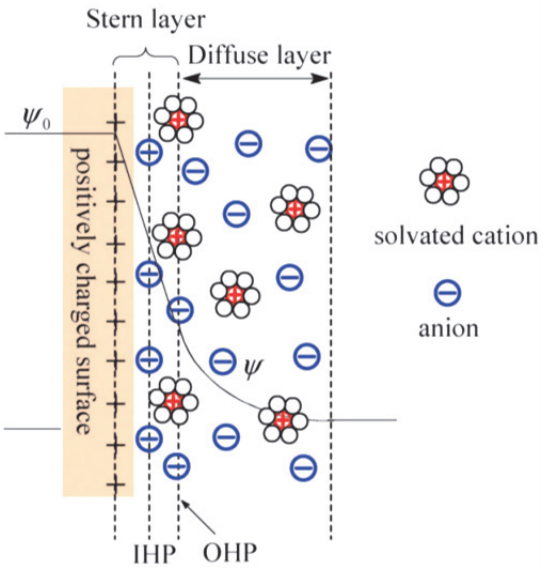

Figure 4.3 For the double layer charge, charge separation occurs when the electrode–electrolyte interfaces polarized, which in turn induces the double layer supercapacitance. This is referred to Stern model, showing the inner Helmholtz plane (IHP) and outer Helmholtz plane (OHP).[6, 25] The IHP refers to the distance of closest approach of specifically adsorbed ions (generally anions) and OHP refers to that of the non-specifically adsorbed ions. The OHP is also the plane where the diffuse layer begins. D is the double layer distance described by the Helmholtz model. Ψ_0 and Ψ are the potentials at the electrode surface and the electrode/electrolyte interface, respectively.

The double layer capacitance is usually between 5 and 20 μF/cm^2 depending on the electrolyte used.[7] Specific capacitance achieved with aqueous alkaline or acid solutions is generally higher than in organic electrolytes, but organic electrolytes are more widely used as they can sustain a higher operation voltage (up to 2.7 V in symmetric systems). The energy stored is proportional to voltage squared according to Equation 4.2.[6]

$$E = \tfrac{1}{2} CV^2 \qquad (4.2)$$

Where V is voltage, C is capacitance, E is stored energy. A three-fold increase in voltage would result in about an order of magnitude increase of excess capacitance.

Since no redox reactions occur during energy storage at EDLC electrodes, the major difference compared to batteries is that there is no charge/discharge rate limitation due to electrochemical kinetics. This surface storage mechanism of electro-energy on EDLC allows fast energy uptake and delivery, thus allowing better power performance. The absence of redox reactions also eliminates swelling of the active material that batteries show during charge/discharge cycles.[6] EDLCs can sustain millions of cycles whereas batteries survive several thousand at best. Moreover, since the electrolyte in the solvent is not involved during charge/discharge process (unlike in Li-ion batteries), there is no limit in solvent choice and no contribution to any sort of solid–electrolyte interphase. In addition, electrolytes with high power performances at low temperatures (down to -40 °C) have been achieved for EDLCs.[6]

As a consequence of redox-free electrostatic surface charging mechanism, however, EDLC suffers from a limited energy density. This explains why today's EDLC research is largely focused on stretching their temperature limits to where batteries cannot operate.[24]

4.3 Pseudocapacitor (Redox-Based) Capacitors

In contrast to EDLC, pseudo-capacitors use fast and reversible redox reactions (Faradaic process) between species in electrolyte and electro-active chemicals on the surface. As shown in the **Figure 4.4**, the electrons travel through the electrode materials to the current collector (and vice versa, depending on the charge/discharge process) and induce redox reactions on electrode surfaces. Meanwhile, the charged ions, such as protons, metal ions, or hydroxide are incorporated into/excluded from electrodes during faradic processes. The capacitance is $C = d(\Delta q)/(d\Delta V)$, where Δq is accepted charge and ΔV is the change in potential.

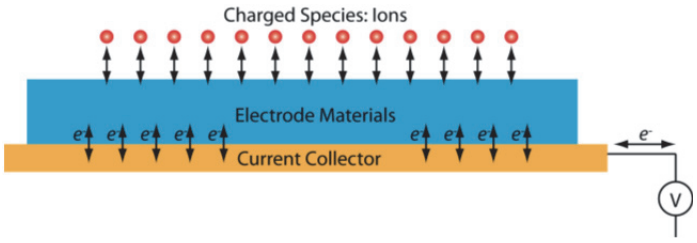

Figure 4.4 Schematic diagram of working mechanism of pseudocapacitive charge and discharge.[12]

Metal oxides such as RuO_2,[26, 27] Fe_3O_4,[28] or MnO_2,[29-31] as well as electronically conducting polymers, have been extensively studied in past years. In general, the specific pseudo-capacitance of these materials exceeds that of carbon materials using merely double layer charge storage, justifying the importance of these systems. But because redox reactions are used, pseudo-capacitors, like batteries, often suffer from a lack of stability during cycling.

A well-known material exhibiting good pseudocapacitance is Ruthenium oxide, RuO_2.[6, 26, 27] It has been widely studied because it is conductive, and has three distinct oxidation states accessible within 1.2 V working window. The pseudo-capacitive behavior of RuO_2 in acidic solutions has been the focus of research in the past 30 years.[32] In detail, it can be described as a fast, reversible electron transfer together with an electro-adsorption of protons on the surface of RuO_2 particles, where Ru oxidation states can change from (II) up to (IV): $RuO_2 + xH^+ + xe^- \leftrightarrow RuO_{2-x}(OH)_x$, where $0 \leq x \leq 2$. The continuous change of x during proton insertion and extrusion occurs over a window of about 1.2 V through the redox transitions of oxyruthenium groups (i.e., Ru(IV)/Ru(III) and Ru(III)/Ru(II)). Specific capacitance of as high as 720 F/g has been achieved.[30] There are some drawbacks to Ru-based aqueous electrochemical capacitors that limit their applications to small electronic devices, however, due to their extremely high cost and 1-V voltage window in aqueous solutions.

Some other less expensive oxides of iron, vanadium, nickel and cobalt have been tested in aqueous electrolytes, but none of them has been investigated as much as manganese dioxide. The charge storage mechanism is based on surface adsorption of electrolyte cations M^+ (e.g., Li^+, Na^+, K^+) as well as proton incorporation according to the reaction: $MnO_2 + xM^+ + yH^+ + (x+y)e^- \leftrightarrow MnOOM_xH_y$ MnO_2 is generally characterized in the neutral aqueous electrolytes within a voltage window of <1 V. Other transition metal oxides with various oxidation degrees, such as molybdenum oxides, should also be explored as active materials for pseudo-capacitors.

A second type of materials, conducting polymers (polyaniline[33], polypyrrole[33, 34], polythiophene[35]) have been tested in EC applications as pseudo-capacitive materials, and have shown high gravimetric and volumetric pseudo-capacitance in various non-aqueous electrolytes at operating voltages as high as 3 V. When used as bulk materials, however,

conducting polymers suffer from a limited stability during cycling (i.e., reduction from initial performance).

4.4 Current MnO_2 Materials for Supercapacitors

Manganese oxide (MnO_2)[23, 36-39] has been widely studied as a promising supercapacitor[19, 32, 40-43] material because it has a high theoretical specific capacitance, low cost, high natural abundance and is environmentally benign. Substantial efforts have been undertaken to synthesize MnO_2 based nanomaterials with very high surface area in order to maximize the capacitance with high charge/discharge rates. MnO_2 nanomaterials that have been synthesized include nanorods/nanowires,[44, 45] nanostructured films[46] and composite nanomaterials (e.g., CNT[47]/graphene[48, 49]/conductive polymer[50-52]/metal[53, 54]).

Other studies report on the synthesis of MnO_2 microspheres and their composites via a wet chemical process at room temperature or hydrothermal process at high temperature.[55-63] Controlling the size and morphology of these MnO_2 microspheres, however, presents a dilemma: control of morphology is difficult without the use of structure-directing agents, but on the other hand, additives such as surfactants may harm the electrochemical properties of the final products. Sub-micron-sized spheres are an important class of materials due to their high surface area, ability to retain high dispersity (i.e., limited aggregation), and excellent processability even without the use of surfactants. MnO_2 microspheres of micron or submicron size, however, have been explored only to a limited extent, and only rarely reported as supercapacitor electrode materials.[36, 62]

4.5 Ultrasonic Spray Pyrolysis for MnO_2 Microspheres

Ultrasonic spray pyrolysis (USP) has been used to prepare a variety of materials including carbon, metal, metal oxides and semiconductors.[64-69] Carbon microspheres specifically prepared by USP have found several applications for energy storage materials, including supercapacitors and lithium ion batteries.[70-76] Spray processing has also been widely used in industry for fine powder production and thin film deposition because the process is simple and can easily be scaled-up for mass production.[64]

4.5.1 Ultrasonic Spray Pyrolysis Apparatus

All Ultrasonic Spray Pyrolysis (or Polymerization) process in this thesis used an ultrasonic nebulizer built in-house at the Chemical Sciences Electronic Shop at University of Illinois (**Figure 4.5**). The nebulizer consists of a board (APC International,

Inc., #50-1011) of a piezoelectric transducer which operates at 1.65 MHz (**Figure 4.5**). The base also has an internal variable AC transformer to control the power going to the piezoelectric transducer and thus controlling the intensity of the ultrasonic wave generated. All syntheses were performed using the maximum power of the nebulizer. The top portion of the nebulizer is a water bath which is in contact with the piezoelectric, filling the medium between nebulizer and membrane (on which is the precursor solution).

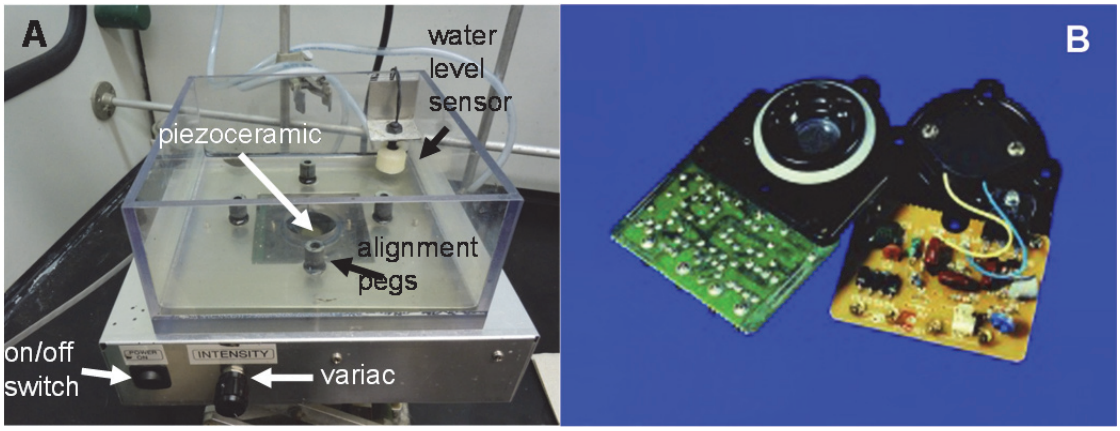

Figure 4.5 Photographs of (A) the home-built nebulizer and (B) the front and back of the piezoceramic nebulizer board.[77]

The custom nebulization cell consists of a 57 mm O-ring flat flange (Chemglass, #CG-138-02) fused to the bottom of a 1 L, 3-necked round bottom flask with 24/40 ground glass joints. A custom clamp (made by the Chemical Sciences Machine Shop at University of Illinois) is used to secure a polyethylene membrane to the flange of the cell. The membrane separates the precursor solution in the nebulization cell from water in the nebulizer, and allows ultrasound transduces from the water bath to the precursor solution. The clamp has a structure as follows: a brass ring (9 cm outer diameter, 6 cm inner diameter, 2 mm thick) with six equally spaced holes (1/4 inch diameter), a Teflon ring of similar dimensions, a second Teflon ring (5.6 cm outer diameter, 2.8 cm inner diameter, 7 mm thick) with an O-ring groove (4 mm wide, 1.5 mm deep) and a corresponding O-ring (which comes with the flat flange), the plastic film, the nebulization cell flange, two half-moon Teflon rings, and two half-moon brass rings (with

the same dimensions as the first brass and Teflon rings). This assembly is held together with six socket head cap screws (1/4 inch outer diameter, 2 inch in length) which are threaded through the six holes and secured with appropriate nuts and washers (**Figure 4.6** and **4.7**). The assembled cell is placed into the water bath, and any air bubble trapped between the membrane and the water bath is removed (with a syringe) to minimize impedance mismatch so as to maximize ultrasound transduction efficiency to the precursor solution.

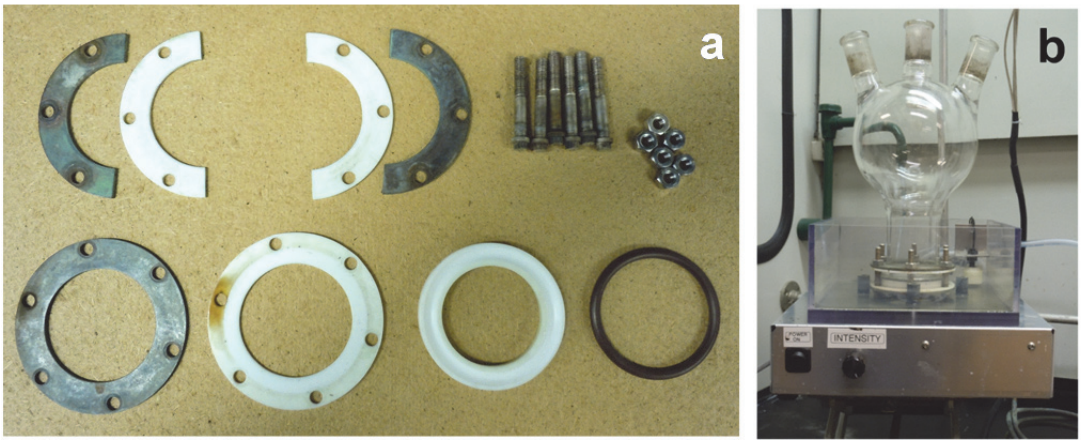

Figure 4.6 (a) Photograph of the custom nebulization cell clamp parts. (b) Photograph of the custom nebulization cell with clamp in the nebulizer base.

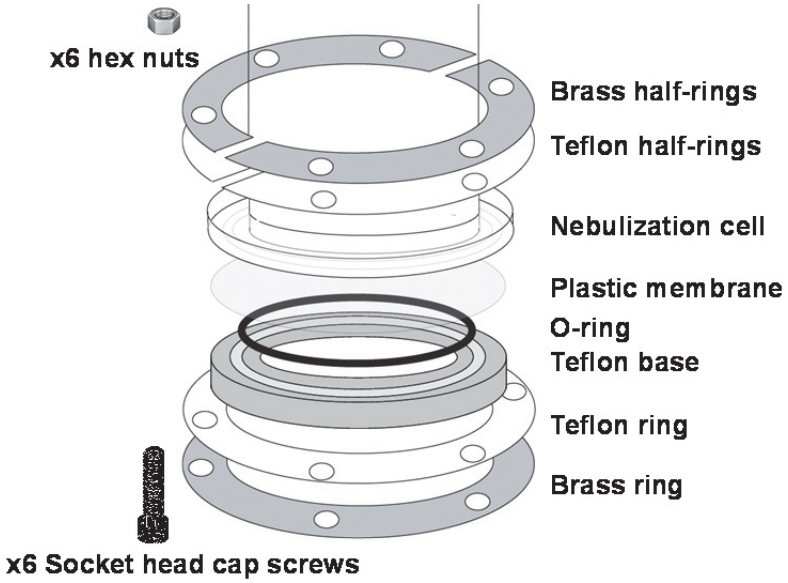

Figure 4.7 Illustration of nebulizer cell base clamp part assembly showing the order of the different parts, as well as location of the membrane and nebulization cell.

A custom carrier gas inlet (**Figure 4.8**) is used at a side neck of the nebulization cell to allow the carrier gas to pass mist sol through the furnace tube. This inlet has a male 24/40 ground glass hose connection joint with a tube that extends into the center of the nebulization cell (7 mm outer diameter, 5 mm inner diameter, ~3 inch in length). The flow rate of the carrier gas is controlled by a rotameter. The other side neck of the nebulization cell is sealed (normally with a rubber septum). This allows further precursor solution refilling without exposing the inner environment to the outside.

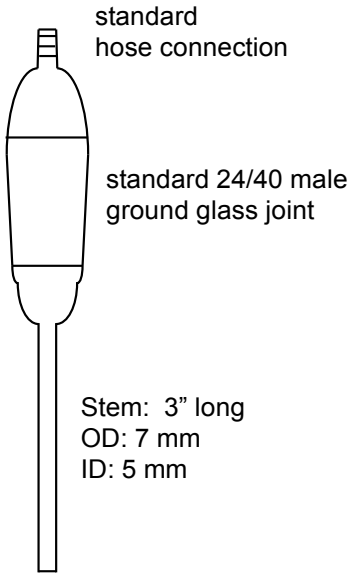

Figure 4.8 Schematic of the custom carrier gas inlet with some specifications.

A standard glass rotary evaporator trap (with a 24/40 ground joint) is used in the center neck of the nebulization cell to prevent large splashes fall from furnace tube, which may contaminate the precursor solution. A quartz furnace tube (35 mm outer diameter, 32 mm inner diameter ~40 cm long, made by Quartz Scientific, Inc., **Figure 4.9**) with a 24/40 male ground glass joint at one end and a 35/25 ground glass ball joint at the top is inserted through a horizontally oriented radiant heating furnace (Omega CRFC-212/120-C-A) and connected to the bump trap via the 24/40 joint.[78] The furnace (**Figure 4.10**) is controlled by a variable AC transformer and can reach temperatures as high as 1100 °C. The temperature is monitored by a K-type thermocouple inserted between the

furnace and the furnace tube. The tip of the thermocouple is placed approximately one-fourth of the way down the tube.

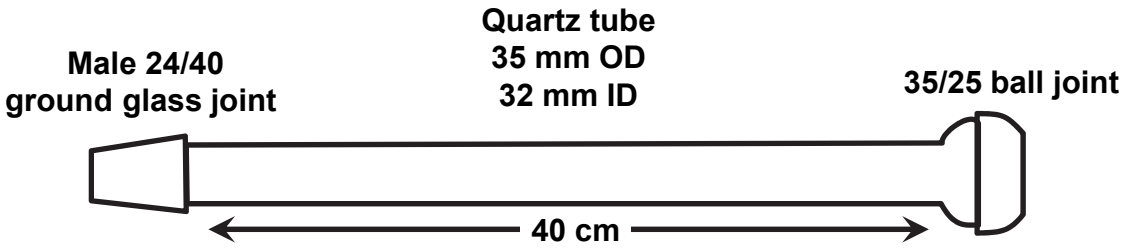

Figure 4.9 Schematic of the specification of quartz furnace tube.

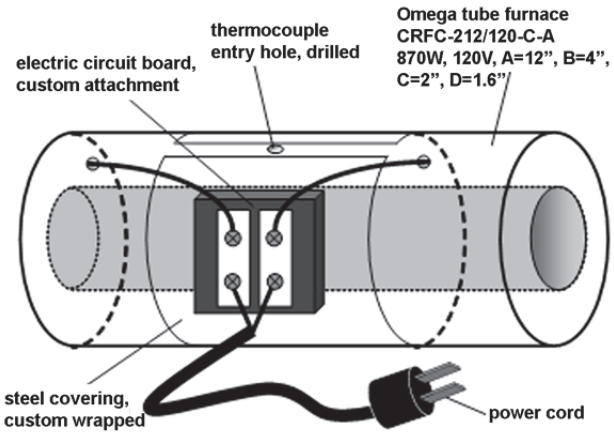

Figure 4.10 Illustration of cylindrical furnace.[78]

The last part of the system is a couple of bubblers for product collection (e.g., Chemglass #CG-4515, containing ~50 mL of collection liquid). A glass adapter with a 35/25 ground glass socket joint (secured with a c-clamp) is used to connect bubblers and the tube furnace. All the rest of the glass joints are connected with a Tygon tubing (5/16 inch inner diameter, 7/16 inch outer diameter).

4.5.2 Preparation of MnO_2 Microspheres

The USP set-up illustration is shown in **Figure 4.11**. The operating frequency of the water nebulizer is 1.7 MHz. The furnace was preheated to the desired temperature

(e.g., 150 °C). Air was used as the carrier gas at a flow rate of 0.5 L/min. The precursor solution (100 mM $KMnO_4$ and 500mM HCl) was prepared and then immediately added to the nebulizing chamber. The black-brown powders were collected in bubblers containing water and subsequently washed and centrifuged with deionized water a minimum of 4 times. The final products were dried overnight in a vacuum oven at 100 °C. The as-prepared powders were then used for further characterization.

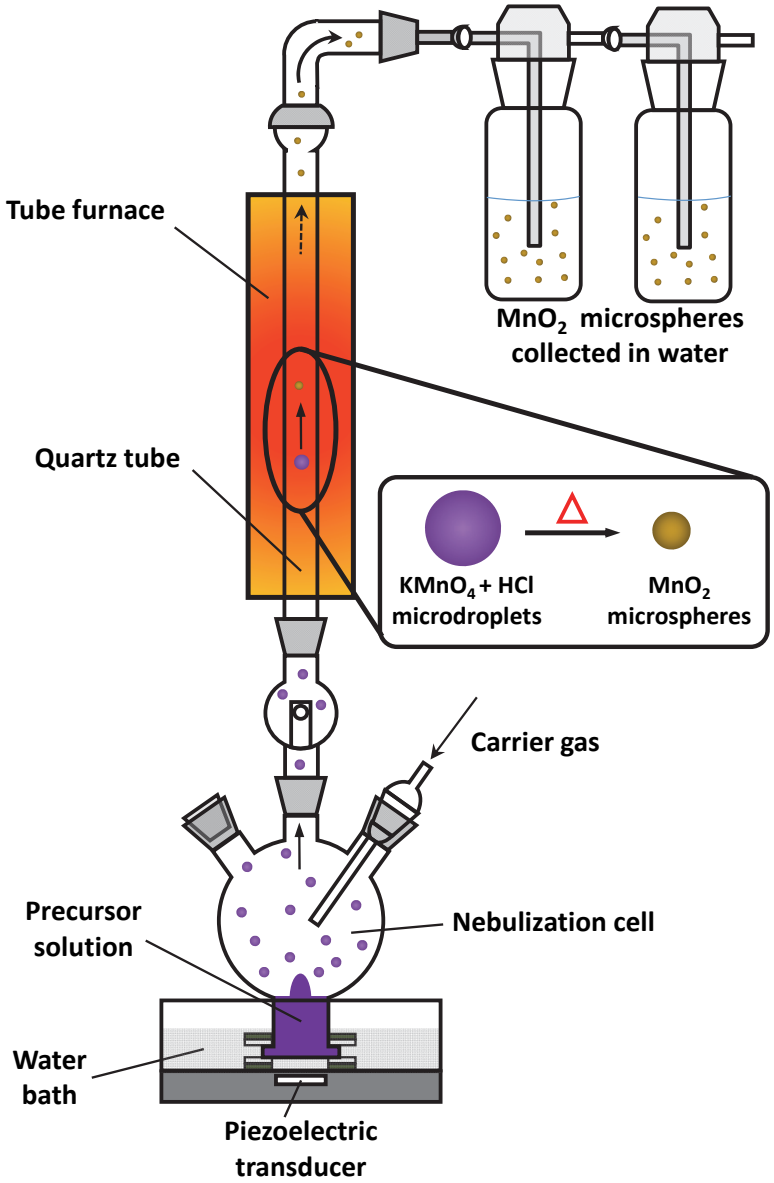

Figure 4.11 USP apparatus for the synthesis of MnO_2 microspheres.

4.5.3 Synthesis of PEDOT Coated MnO_2 Microspheres

50 μL of 100 mM SDS solution was added to 5 mL of 14.8 mM EDOT solution. This mixture was then added to 5 mL of 0.25 mg/mL MnO_2 dispersant (prepared by sonicating as prepared MnO_2 powder in deionized water for 2 minutes). Next, 25 μL of 1 M H_2SO_4 solution was added to this solution under stirring. The mixture was kept at 80 °C in a water bath under stirring at 500 rpm until its color changed from brown to blue-brown. The reaction was then quenched with ice and the product was collected by centrifugation and washed three times. The product was then drop-cast onto pre-weighed carbon paper, which was then thoroughly dried under vacuum at room temperature. This coated carbon paper then served as working electrode for electrochemical studies.

4.5.4 Material Characterizations Instruments

Scanning electron micrographs (SEMs) were taken using a JEOL 7000F field emission (FE)-SEM instrument operated at 10 kV. Energy-dispersive X-ray spectroscopy (EDX) is coupled with the 7000F-SEM instrument using a Thermo Electron EDX microanalysis system. Transmission electron microscopy (TEM) was conducted using a JEOL 2100 Cryo instrument operated at 200 kV. Raman spectroscopy was collected by a Nanophoton RAMAN 11 laser Raman microscope a frequency-doubled Nd:YAG 532-nm laser (laser power 0.267 mW). The Brunauer-Emmitt-Teller (BET) specific surface area was measured using a Quantachrome Nova 2200e system. X-ray photoelectron spectra (XPS) were collected on a Kratos Axis ULTRA instrument (Al Kα radiation). Powder X-ray diffraction (XRD) patterns were obtained on a Siemens-Bruker D-5000 XRD instrument operated at 40 kV and 30 mA (Cu Kα radiation). Zeta potential was measured using zetaPALS zeta potential analyzer.

4.5.5 Electrochemical Experiments

Working electrodes were prepared by directly spraying MnO_2 microspheres onto pre-weighed carbon paper. The spray-coated carbon paper was then washed thoroughly with deionized water to remove any unreacted precursor species. The spray-coated carbon paper was then dried thoroughly under vacuum, baked at 120 °C, and weighed. The amount of deposited material was then calculated from this weight. The MnO_2 coatings are well-adhered to the carbon paper, and exhaustive washing does not lead to

any significant loss of deposited material; similarly after 1000 charge/discharge cycles no significant loss of material is observed.

The cyclic voltammetry (CV) and galvanostatic charge/discharge based on chronopotentiometry (CP) were conducted using a CH Instruments Electrochemical Workstation (potentiostat/galvanostat) with a platinum mesh counter electrode and a silver/silver chloride (Ag/AgCl) reference electrode. The measurements were made at five different scan rates (50, 100, 250, 500, and 1000 mV/s), and at five different current densities (2.5, 5, 10, 25, 50 mA/cm^2), respectively. All electrochemical experiments were conducted in 1M $LiClO_4$ aqueous solution. Reference electrode: The reference electrode used in this thesis is Ag/AgCl electrode, which has a standard potential of 0.197 V (v.s. standard hydrogen electrode) if the electrode are stored in saturated KCl solution. Counter electrode: The counter electrodes in this thesis are simply made by stripes of platinum foil, which is chemical inert. The working, reference, and counter electrode are subsequently immersed in a beaker that is filled in the electrolyte to compose a three electrode electrochemical cell.

4.6 Results and Discussion

4.6.1 MnO_2 Microsphere Formation Mechanism and Morphologies

Figure 4.11 depicts a typical USP apparatus for the synthesis of MnO_2 microspheres. The precursor aqueous solution contains $KMnO_4$ and HCl at different concentrations, which is nebulized into micron-sized droplets and carried by an air flow through the furnace tube. Each droplet serves as a single micro-reactor, and upon heating, the precursors in the droplet decompose into MnO_2 microspheres. These microspheres are then collected in bubblers as a suspension in water.

The morphology of the MnO_2 microspheres can be controlled by varying the ratios of $KMnO_4$: HCl, as well as by tuning the furnace temperature (**Figure 4.12**). In a typical synthesis, a mixture of 100 mM $KMnO_4$ and 500 mM HCl is nebulized into micro-droplets and heated to 150 °C in the cylindrical furnace. The decomposition of MnO_4^- in acidic media is shown in **Equation 4.3** below.[79] The reaction is self-catalytic, i.e., MnO_2 seeds initially formed in the droplet will further catalyze additional acidic MnO_4^- to decompose.[60, 80-82]

$$4KMnO_4 + 4HCl \rightarrow 4KCl + 4MnO_2 + 3O_2 + 2H_2O \quad (4.3)$$

As illustrated in **Figure 4.12 (a),** the formation of MnO_2 microspheres involves the concentration of the acidic $KMnO_4$ solution as water evaporation occurs, followed by MnO_2 formation upon permanganate decomposition. The spherical shape of MnO_2 microspheres results from the initially isotropic water droplet generated by the ultrasonic nebulization. SEM, TEM and high resolution TEM images are given in **Figure 4.12 (b)** and **Figure 4.12 (c),** and **Figure 4.12 (d)**, respectively. Electron beam diffraction indicates a partially amorphous state, as seen in **Figure 4.12 (e).**

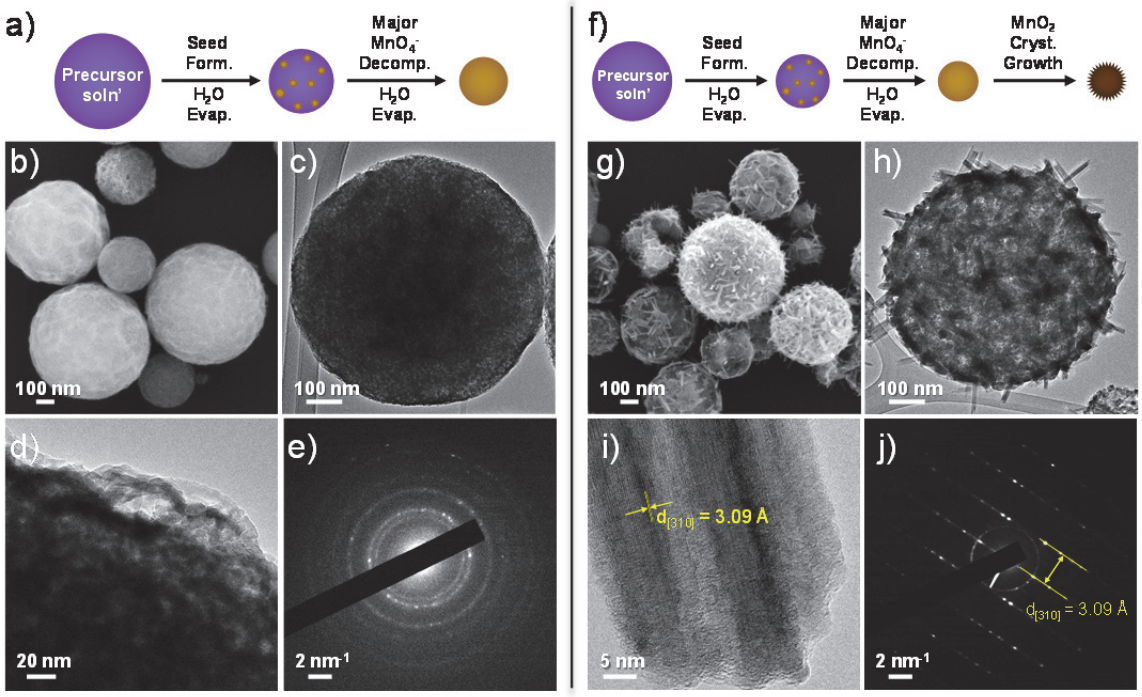

Figure 4.12 MnO_2 microsphere (synthesized with 100 mM $KMnO_4$ and 500 mM HCl) formation mechanisms at 150 °C (a) and 500 °C (f). SEM images of purified MnO_2 microspheres synthesized at 150 °C (b) and 500 °C (g). TEM images of purified MnO_2 microspheres synthesized at 150 °C (c, d) and 500 °C (h, i). Electron diffraction patterns of products from 150 °C (e) and 500 °C (j).

In contrast, the reaction pathway of $KMnO_4$ and HCl at 500 °C, shown in **Figure 4.12 (f)-(j)**, produces microspheres made up of MnO_2 nano-needles that grow on the surface and inside the sphere. The high resolution TEM (**Figure 4.12** (i) and electron diffraction pattern from the tip of a nano-needle (**Figure 4.12** (j)) demonstrate that the microspheres are now highly crystalline. The lattice spacing found in the diffraction pattern of 3.09 Å matches with the x-ray powder pattern (d- spacing) of α-MnO_2 with a [310] Miller index (**Figure 4.13**). The crystallinity of MnO_2 increases with increasing temperature during USP synthesis (from 150 to 300 to 500 °C, **Figure 4.13**). The peaks in the MnO_2 Raman spectra (**Figure 4.14**) match well with previous studies of α-MnO_2.[83, 84]

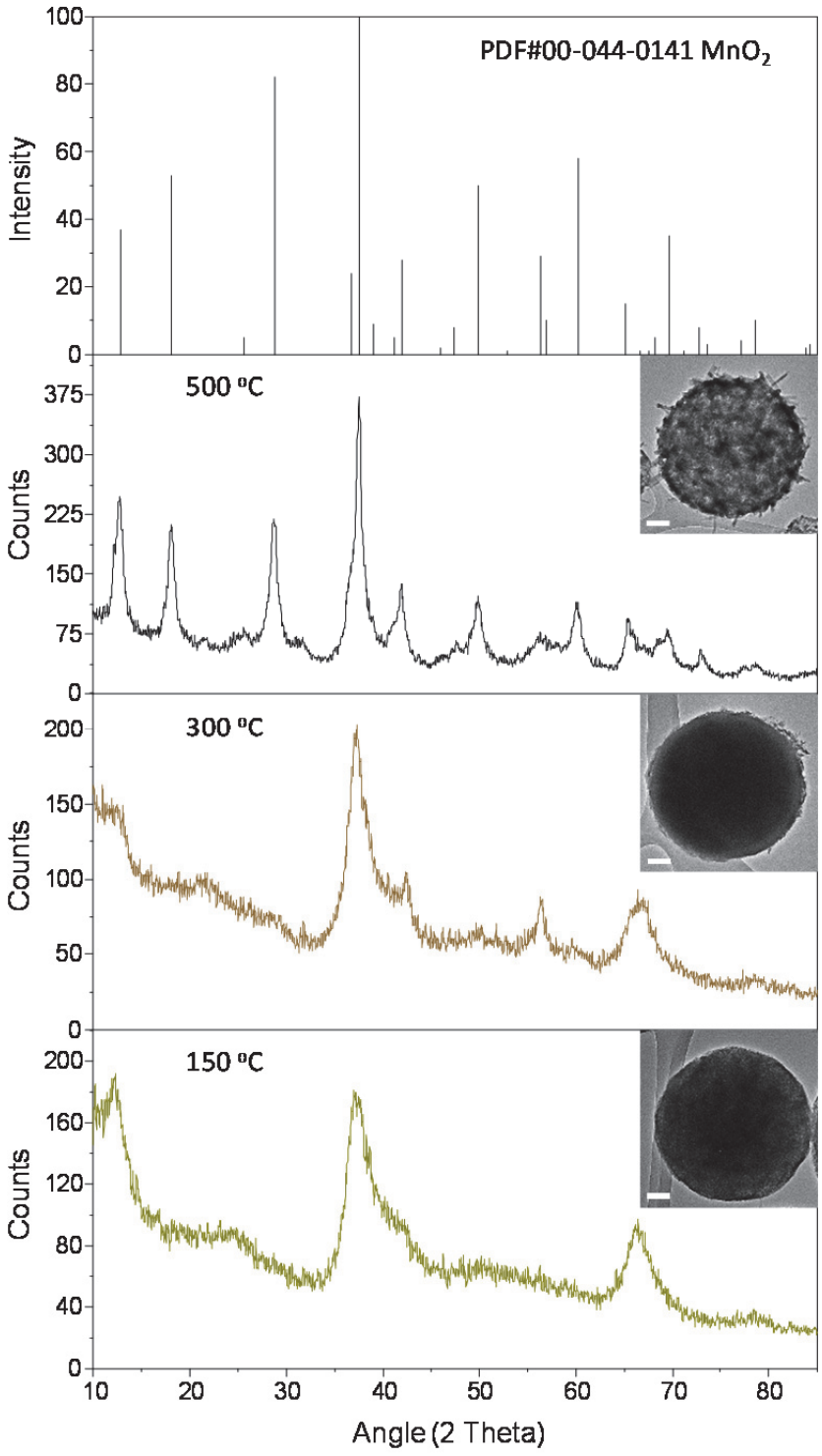

Figure 4.13 XRD data of MnO_2 microspheres synthesized by USP at different temperatures from an aqueous solution that is 100 mM $KMnO_4$ and 500 mM HCl. The scale bar is 100 nm.

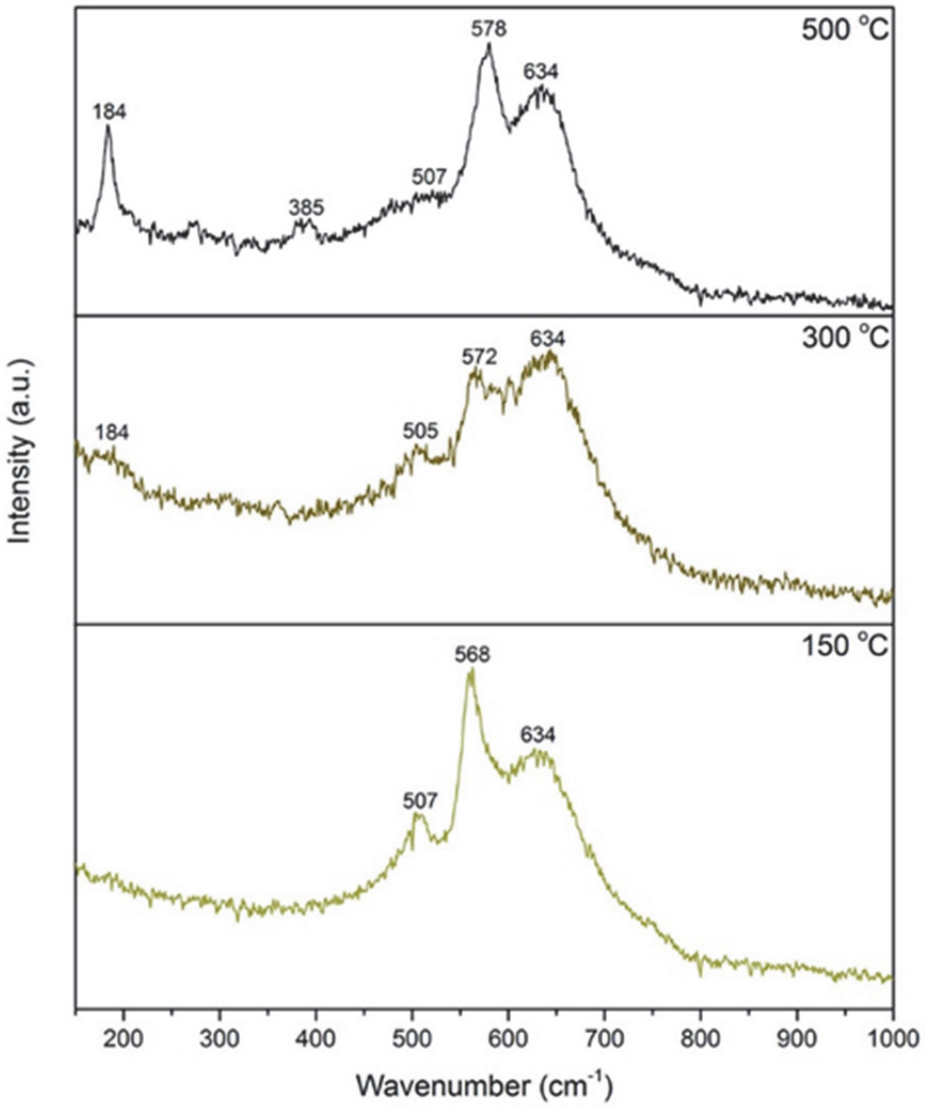

Figure 4.14 Raman spectra of MnO_2 microspheres synthesized at different temperatures.

The chemical states and composition of the microspheres' surface were probed by XPS analysis (**Figure 4.15**). The Mn peaks, $2p_{3/2}$ (centered at 642 eV) and $2p_{1/2}$ (centered at 653.8 eV), show a spin energy separation of 11.8 eV, which is in good agreement with previously reported MnO_2 data.[47] The Mn to O ratio from the XPS was determined to be 0.5.

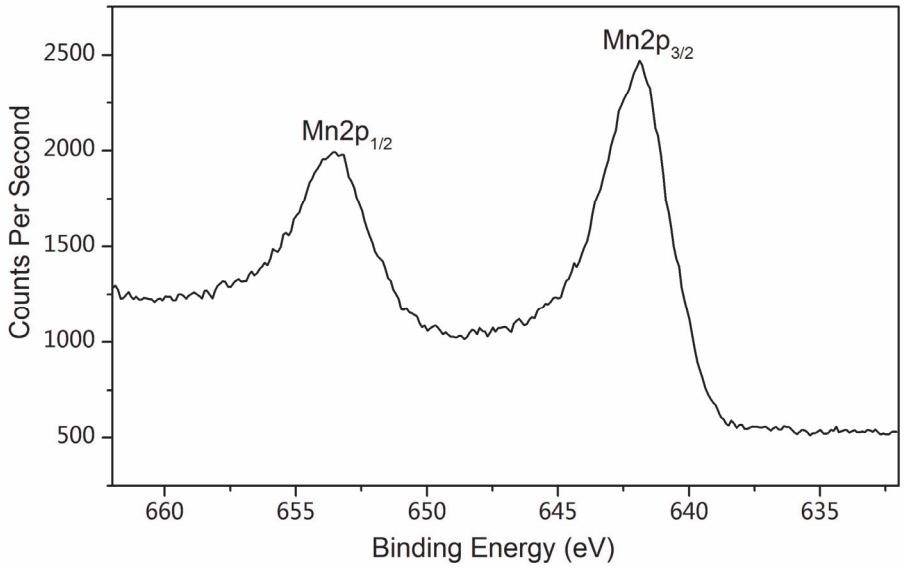

Figure 4.15 XPS analysis of MnO_2 microspheres synthesized from the mixture of 100 mM $KMnO_4$ and 500 mM HCl at 150 °C. The Mn peaks, $2p_{3/2}$ (642 eV) and $2p_{1/2}$ (653.8 eV), gives a spin energy separation of 11.8 eV.

When the hydrochloric acid concentration is kept low (between 0-50 mM), the MnO_4^- (100 mM) does not decompose during USP at either 150 or 300 °C. At low HCl concentrations, a higher temperature is required to trigger the decomposition of permanganate. Indeed, in the absence of added HCl, a temperature of 500 °C is required to form products. The SEM and TEM images of these products are shown in **Figure 4.16**. Under USP at 500 °C without added acid, the MnO_2 microspheres are irregular ovals in shape, which implies that the decomposition reaction must occur in the solid state after evaporation of the water (**Equation 4.4**).[85, 86] The TEM images (Figure S3b) show that the MnO_2 crystals grow anisotropically during this process. Upon addition of 50 mM

HCl, decomposition will occur at 300 °C (and at 500 °C), but again the irregular, non-spherical shape of the products (**Figure 4.17**) shows that the decomposition during USP is still occurring in the solid state.

$$4\ KMnO_{4\ (s)} \rightarrow 2\ K_2O\ +\ 4\ MnO_{2(s)}\ +\ 3\ O_2 \qquad (4.4)$$

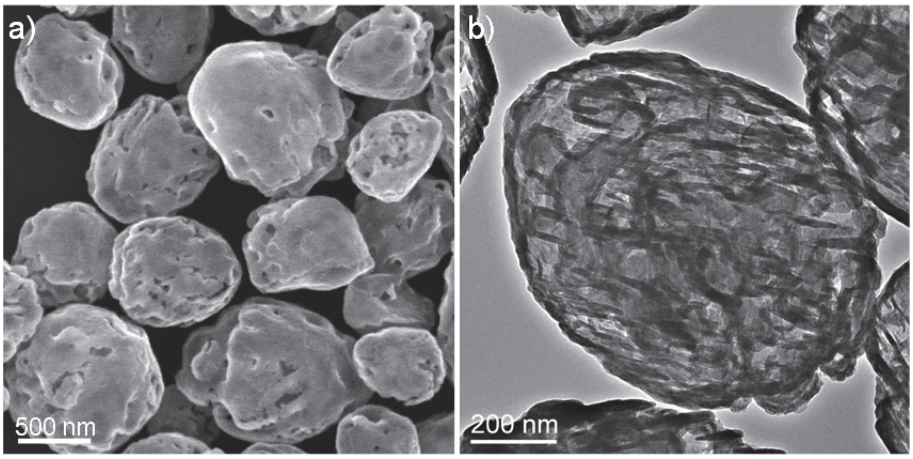

Figure 4.16 Product formation mechanism illustration, SEM (a) and TEM (b) images of $KMnO_4$ decomposition (100 mM $KMnO_4$ and no HCl) at 500 °C.

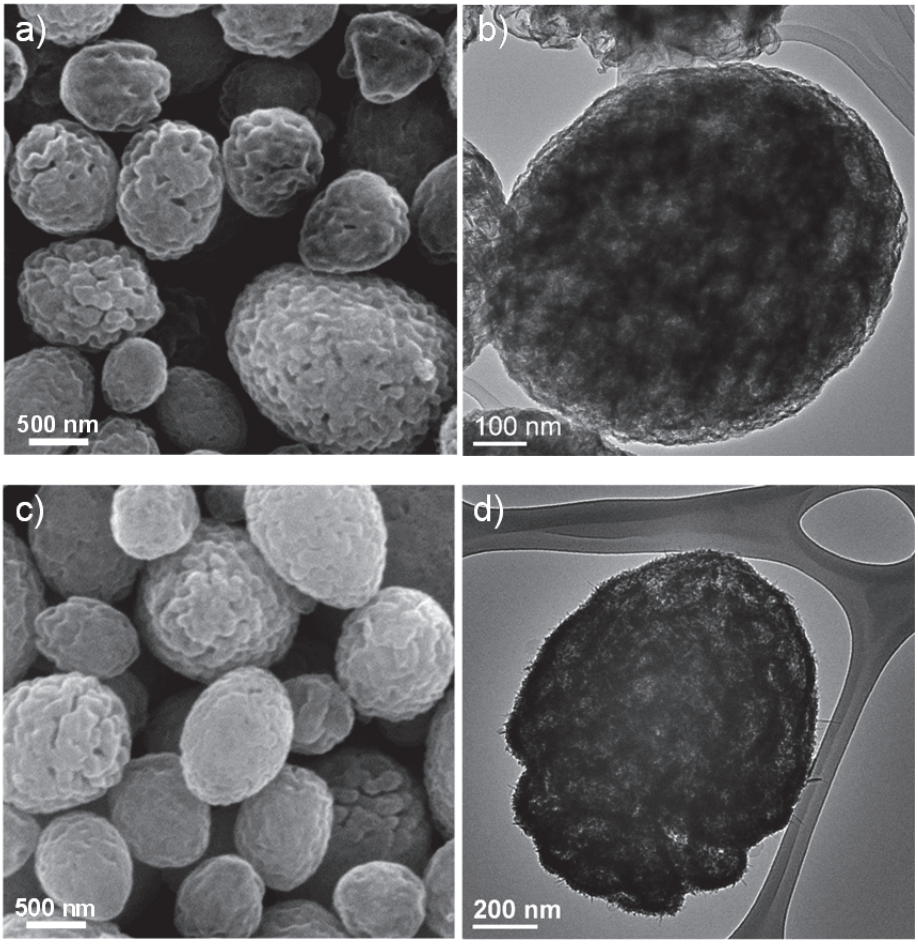

Figure 4.17 SEM images of products synthesized with 100 mM $KMnO_4$ and 50 mM HCl precursor at 300 °C (a-b) and 500 °C (c-d).

When the precursors are present at higher concentrations (500 to 1000 mM $HCl_{(aq)}$ and 100 to 400 mM MnO_4^-), the acidified MnO_4^- becomes unstable even at room temperature and spontaneously form seeds of MnO_2 (**Equation 4.5**).[87] Under these conditions, large numbers of MnO_2 seeds form in the solution even before nebulization. Morphologies of MnO_2 microspheres produced under these high concentrations are shown in **Figure 4.18**. Under high concentration conditions, the MnO_2 microspheres are less porous than those synthesized with lower HCl concentrations, as shown in the TEM images (**Figure 4.18** (a-b)). At 300 °C, the microspheres begin to collapse and shrink as the amorphous material becomes crystalline. During this process, the MnO_2 surface begins to be decorated by small nanocrystals (**Figure 4.18** (c-d)). At even higher temperature (500 °C), longer MnO_2 needles grow out from the surface in abundance (**Figure 4.18** (e-f)).

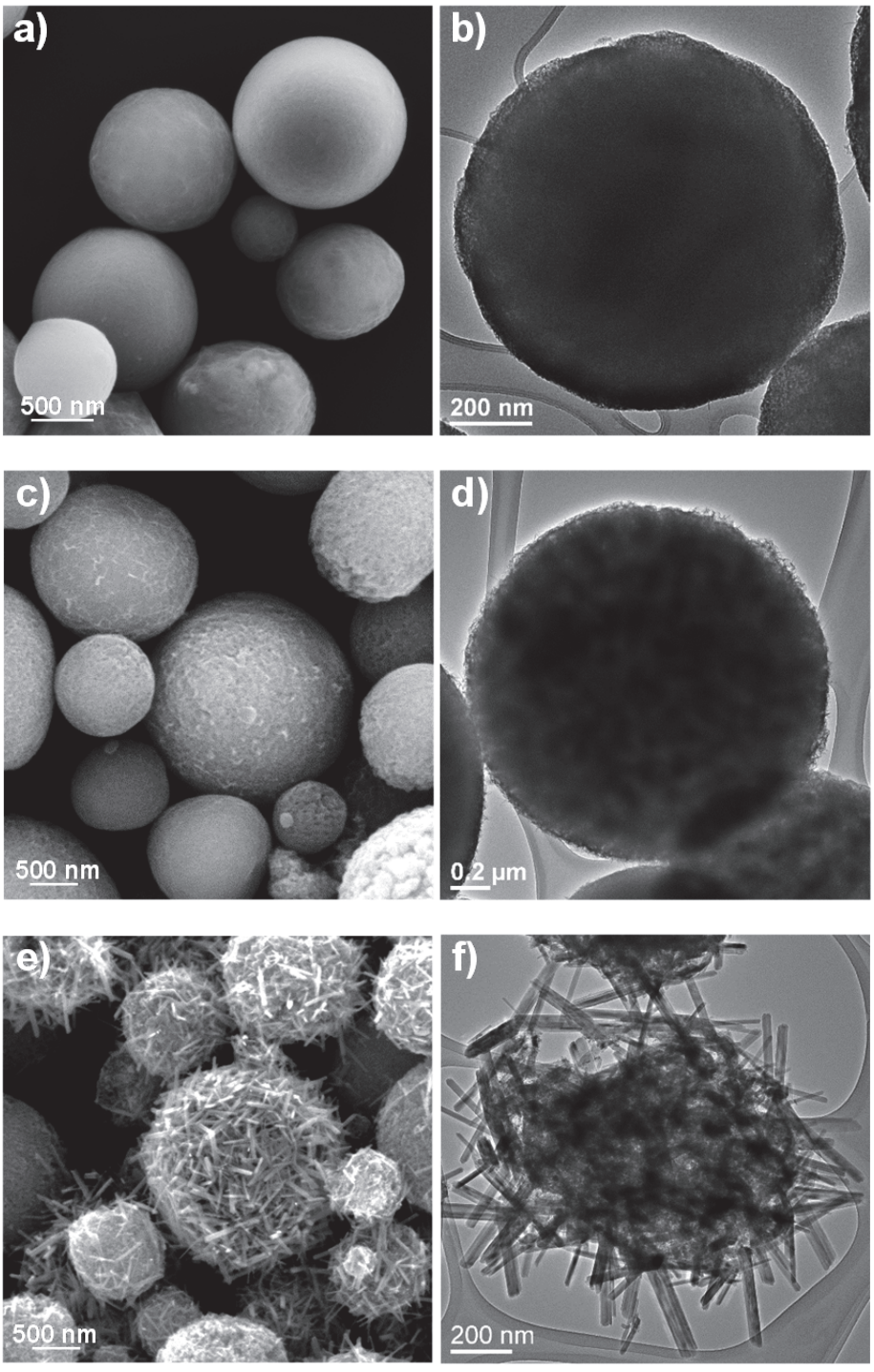

Figure 4.18 SEM and TEM images, respectively, of MnO_2 microspheres synthesized with high concentrations (400 mM $KMnO_4$ and 1000 mM HCl); (a-b) at 150 °C; (c-d) 300 °C; (e-f) 500 °C.

$$2\,KMnO_4 + 16\,HCl \rightleftharpoons 2\,KCl + 2\,MnCl_2 + 8\,H_2O + 5\,Cl_2 \quad (4.5)$$

4.6.2 Direct Spray of MnO_2 on Electrodes and Electrochemical Characterizations

MnO_2 microspheres formed in the tube furnace are carried forward by the air flow and collected in water inside bubblers for further washing and processing. One may also spray the air-carried MnO_2 microspheres directly onto conductive substrates to form a uniform MnO_2 microsphere coating. **Figure 4.19 (a)** illustrates the set-up of the spray nozzle over a carbon fiber surface (Spectracarb 2050A-0850, graphitized resin-bonded carbon fiber paper). MnO_2 microspheres are released from the nozzle and sprayed onto the carbon fibers. The coated carbon fibers are allowed to air-dry and subsequently rinsed three times with water to remove any residual impurities. An SEM image taken of uniformly coated carbon paper (**Figure 4.19 (b)**) shows fiber-like fine structure thoroughly coated with MnO_2 microspheres. We presume that the adhesion of the MnO_2 microspheres to the carbon fibers is due in part to van der Waals attractions between the microspheres and the fibers and in part to more specific interactions between surface functionality on the carbon (e.g., carboxylates, carbonyls, and alcohol groups) and the MnO_2 surface. In a similar fashion, we have also examined deposition of the MnO_2 microspheres on flat substrates. **Figure 4.20** provides an SEM of a flat Si wafer coated with MnO_2 microspheres; the MnO_2 microspheres provide a well-adhered, dense coating to the Si surface.

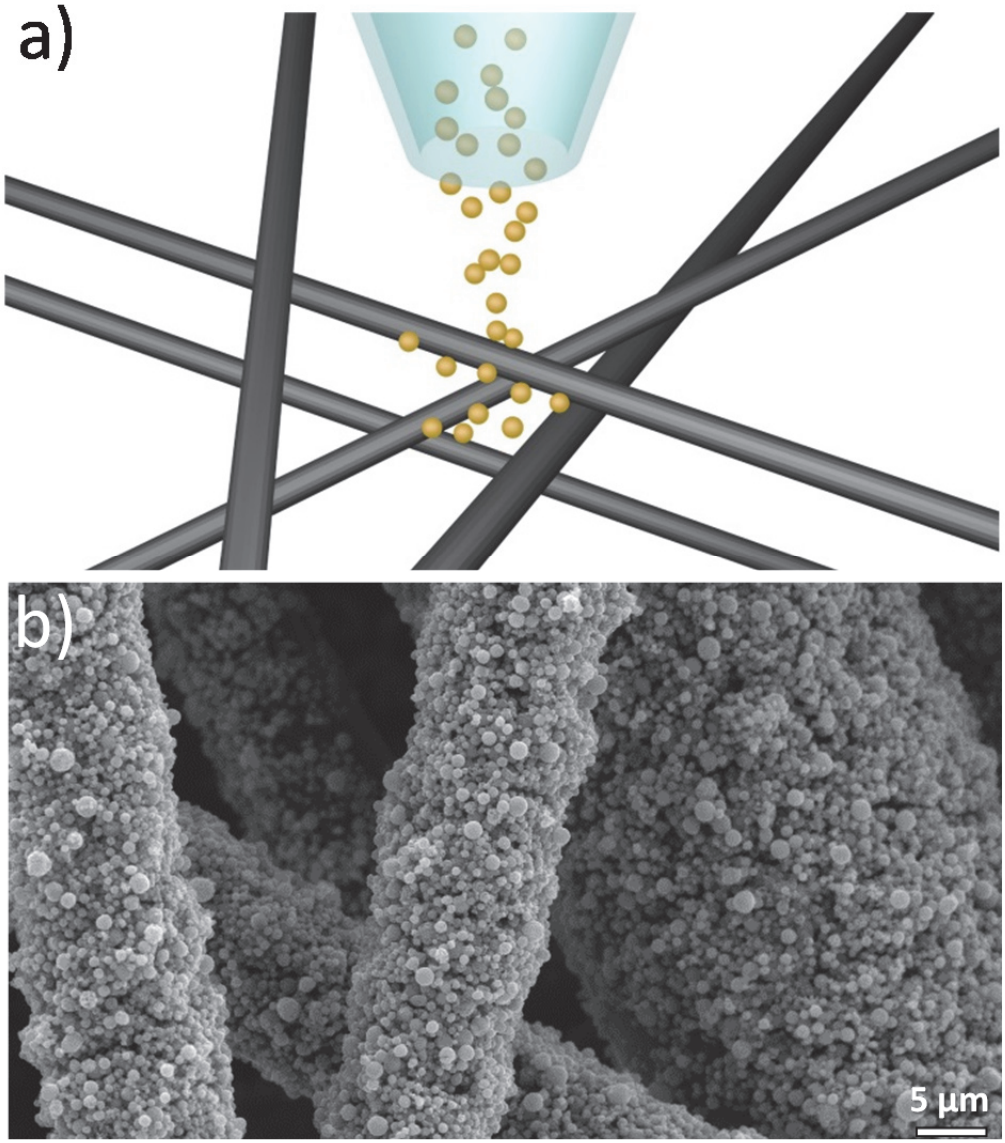

Figure 4.19 (a) Illustration of direct spray of MnO_2 microspheres on carbon fiber paper and (b) SEM image of direct spray of MnO_2 microspheres on carbon fiber paper. The MnO_2 microspheres are synthesized from the mixture of 100 mM $KMnO_4$ and 500 mM HCl at 150 °C.

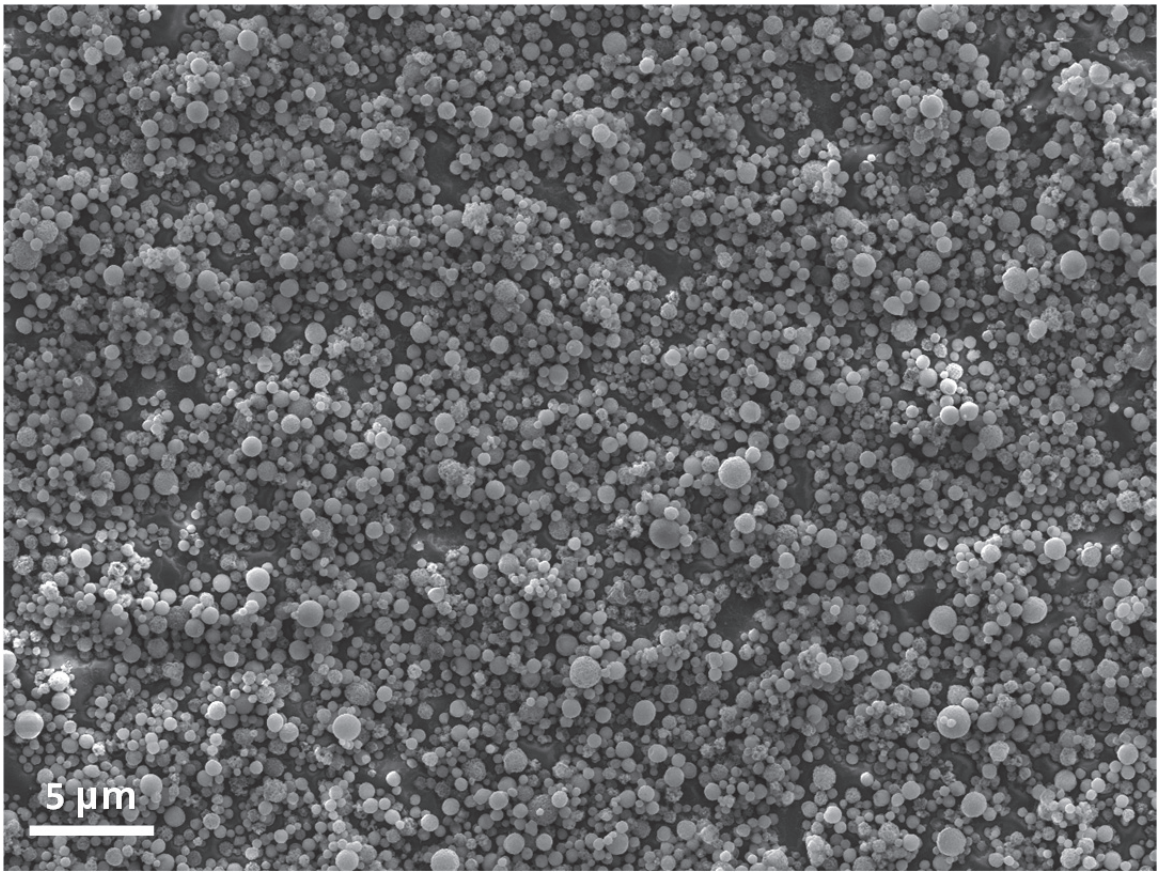

Figure 4.20 SEM image of a silicon waver coated with MnO_2 microspheres. The coated substrate was soaked in water, rinsed three times to remove any residual impurities, and dried under air.

4.6.3 Electrochemical Studies of MnO_2 Microspheres

Electrochemical studies were performed on working electrodes prepared by spray-coating conductive carbon fiber paper with MnO_2 microspheres. Cyclic voltammetry (CV) and galvanostatic charge-discharge curves were used to evaluate the supercapacitive properties of MnO_2 microspheres. The MnO_2 microspheres exhibit square shaped CV scans at low scan rates and symmetrical triangular shapes in galvanostatic curves that are indicative of nearly ideal capacitive behavior (**Figure 4.21** and Figure 4.6.3b)]. At high scan rates (>250 mV/s), however, the CV deviates from the ideal square shape and the specific capacitance drops significantly (**Figure 4.22** and **Figure 4.23**). The specific capacitance can be derived from (**Equation 4.6**)[88], where I is the charge/discharge current, m is the loading mass of the materials, dV/dt is the slope of

galvanostatic charge discharge curves (based on chronopotentiometry method). The energy density and power density at different current densities are also calculated[89], which is shown in **Figure 4.24** (Ragone plot). These MnO_2 microsphere supercapacitors can maintain at least 65% of their energy densities (7.3 Wh/kg) and specific capacitance (210 F/g) as the power density is increased from 0.3 to 6.1 kW/kg. Moreover, the materials demonstrated excellent cyclability by maintaining shapes of both cyclic voltammagrams and galvanostatic charge/discharge curves even after 1000 cycles (**Figure 4.25 (a)** and (**b)**) with 92% retention of capacity after 1000 cycles.

$$C_{spec} = \frac{I}{\mathrm{m}\frac{dV}{dt}} \tag{4.6}$$

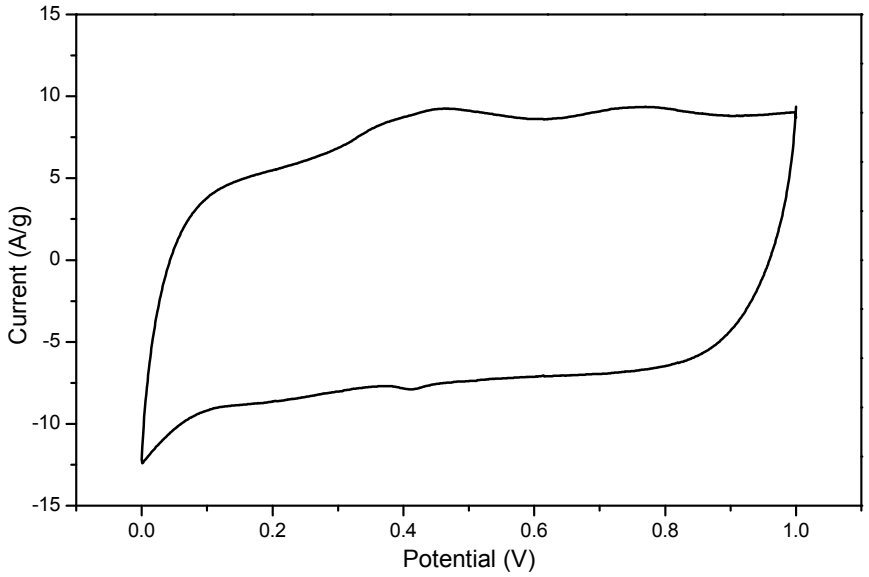

Figure 4.21 Cyclic voltammetry of products from the reaction of 100 mM $KMnO_4$ and 500 mM HCl at 150 °C at a scan rate of 25 mV/s. The electrolyte is 1 M $LiClO_4$ aqueous solution.

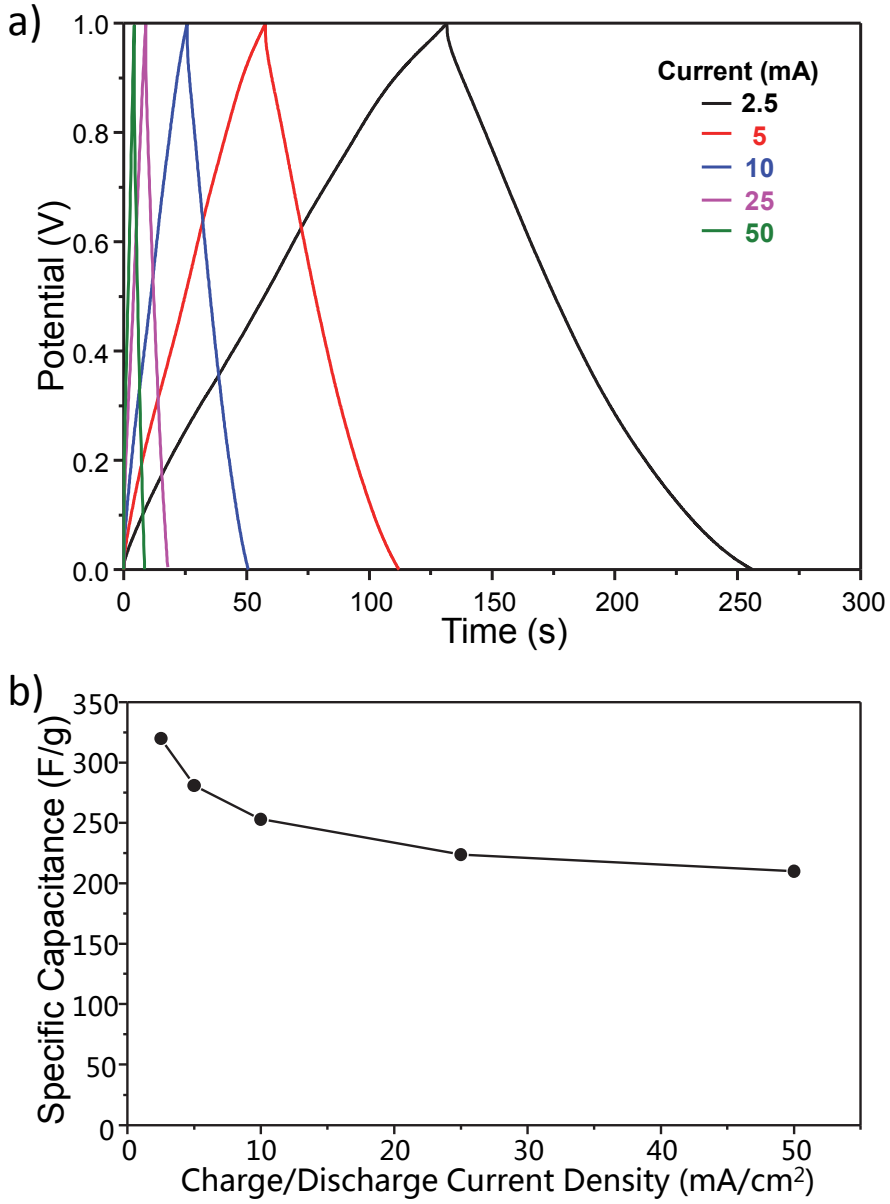

Figure 4.22 (a) Galvanostatic charge and discharge curves (based on chronopotentiometry method) at different charge/discharge current densities of MnO_2 products formed from the reaction of 100 mM $KMnO_4$ and 500 mM HCl at 150 °C. Potentials were cycled from 0 to 1 V at a current density of 5 mA/cm^2 in 1 M $LiClO_4$ aqueous solution. (b) Calculated specific capacitance vs. charge/discharge current density from galvanostatic charge/discharge measurements. The MnO_2 microspheres were USP synthesized from a nebulized solution (100 mM $KMnO_4$ and 500 mM HCl) heated to 150 °C. The electrolyte used was 1M $LiClO_4$ aqueous solution.

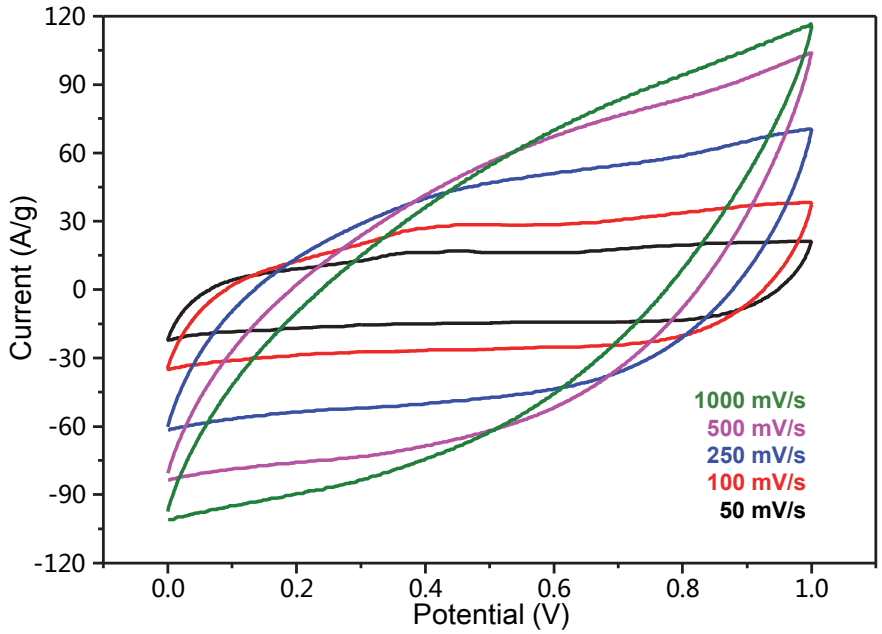

Figure 4.23 Cyclic voltammetry (CV) as a function of scan rate. The CVs exhibit non-ideal capacitive behavior (i.e., deviation from a square shape) at scan rates greater than 250 mV/s.

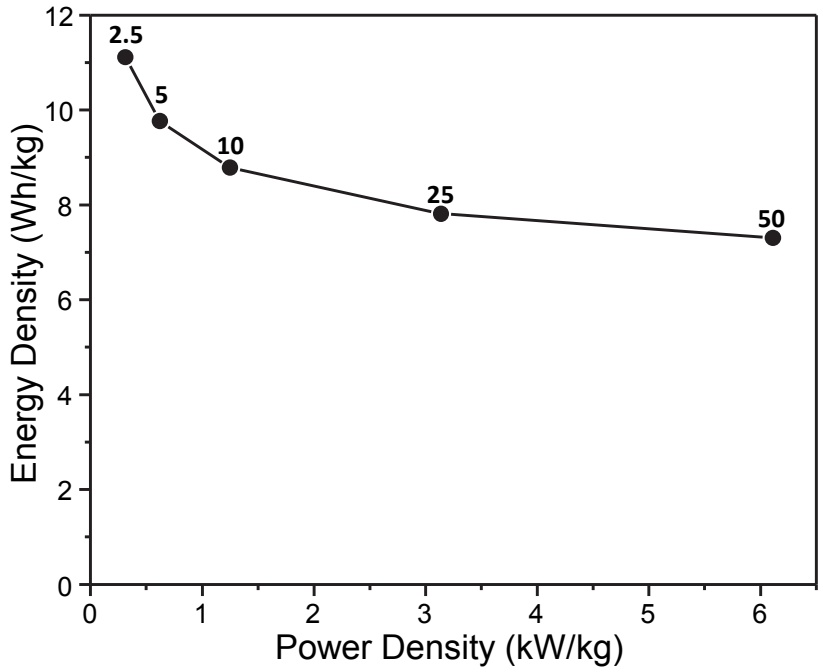

Figure 4.24 The plot of energy density versus power density (Ragone plot) for MnO_2 microspheres synthesized from 100 mM $KMnO_4$ and 500 mM HCl at 150 °C. The inserted numbers represent the current densities (mA/cm^2) for the charge and discharge.

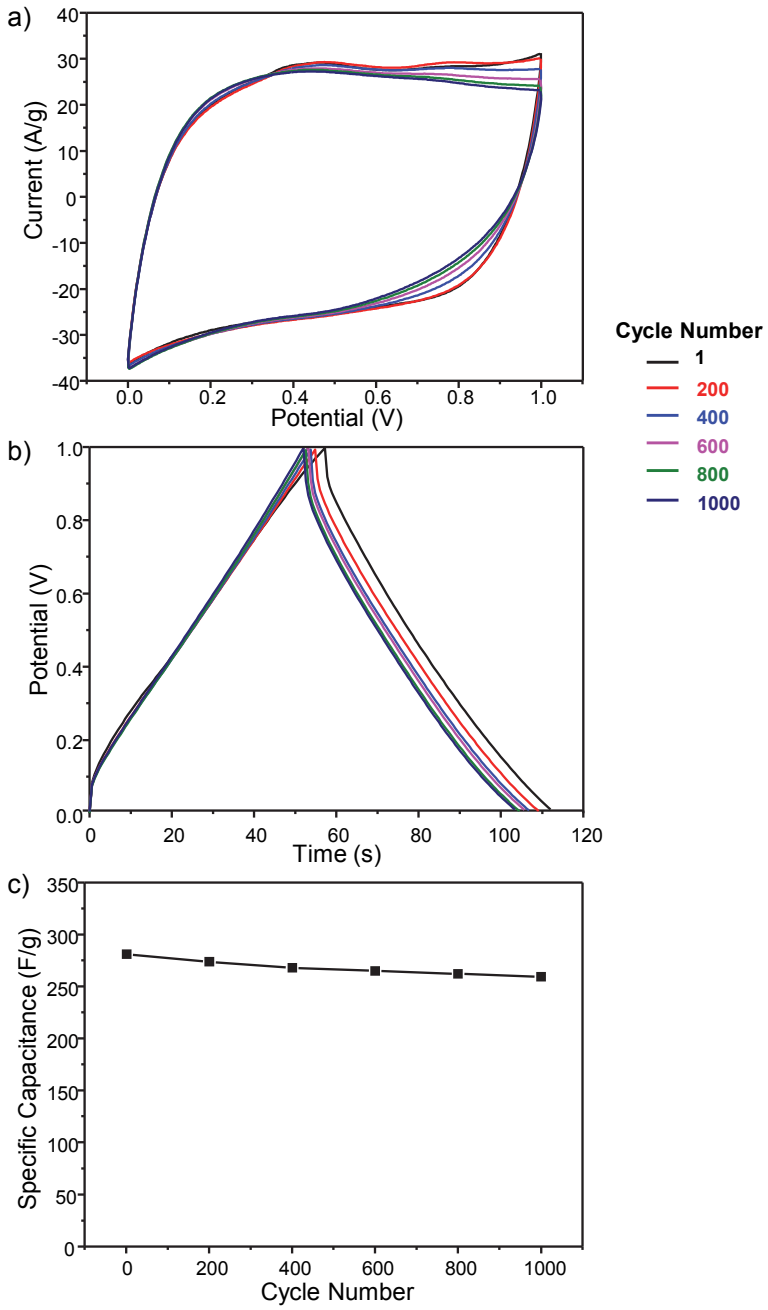

Figure 4.25 (a) Cyclic voltammegrams with a scan rate of 100 mV/s and (b) galvanostatic charge/discharge curves at the current density of 5mA/cm^2 of at different cycles from 1st to 1000th, from MnO_2 microspheres synthesized from 100 mM $KMnO_4$ and 500 mM HCl at 150 °C. The electrolyte used is 1M $LiClO_4$ aqueous solution. (c) The calculated specific capacitance, based on galvanostatic charge/discharge measurements in (b), as a function of cycle number. The curves show excellent capacity retention 92% after 1000 cycles.

The non-ideal capacitive behavior at high scan rates originates from inefficient charge/discharge of the MnO_2 materials, which is attributed to two main reasons. First, the MnO_2 microspheres are densely packed and this limits the amount of surface area available on which redox reactions may occur. Second, the low conductivity of MnO_2 impedes electron transfer between the MnO_2 surface (i.e., redox species at the surface) and the conductive substrate.[90]

To improve the supercapacitive performance of MnO_2 at high charge/discharge rates, we have taken two different approaches: increasing the porosity of the MnO_2 and coating the MnO_2 with highly conductive polymer. The first approach is meant to increase electrolyte access area per unit weigh and the second approach is intended to enhance the MnO_2 utilization per unit area. Previously studies show that thin layers of MnO_2 coated onto conductive substrates permit increases in the specific capacitance to as high as 1380 F/g, which is close to theoretical specific capacitance value of MnO_2 expected for a redox process involving one electron per manganese atom.[91] Such extremely thin films, however, have limited practical applications since the electrode surface must be prohibitively large. This problem can be solved with a three–dimensional, high-surface-area conductive substrate coated with a very thin layer of MnO_2. Indeed, recent work by Chen *et al.* has demonstrated that thin layer of MnO_2 coated on nanoporous gold can reach specific capacitance of 1145 F/g at a decent charge/discharge rate[92]. The gold electrodes used in that study, however, are prohibitively expensive.

4.6.4 Size and Porosity Control and their Effects on Electrochemical Properties

Since changes in both density and surface tension are negligible as the precursor ($KMnO_4$) concentration is increased from 50 to 100 mM, the particle size is dependent primarily on the precursor concentration. The average diameter of the microsphere obtained from 100 mM $KMnO_4$ is 700±100nm, and average diameter of the microsphere from 50 mM $KMnO_4$ is 430±85 nm, as determined from the SEM images (**Figure 4.26**). The microspheres synthesized at lower concentrations of $KMnO_4$ are smaller and more porous, and are therefore less stable when dispersed as colloidal solution; the zeta potential of the microspheres synthesized from 50 mM $KMnO_4$ is -23.3 mV, while that obtained from 100 mM $KMnO_4$ is -33.75 mV. The importance of the large magnitude of

the zeta potential is that it imparts excellent stability to suspensions of the MnO_2 microspheres.

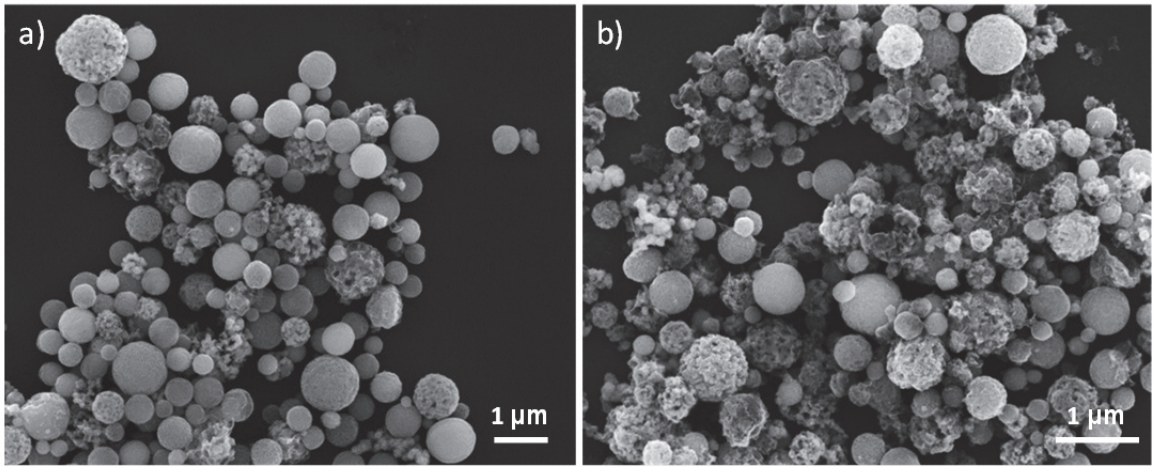

Figure 4.26 SEM images of microsphere products synthesized from the reaction of (a) 100 mM and (b) 50 mM $KMnO_4$ with 500 mM HCl at 150 °C.

The high porosity of the MnO_2 microspheres is electrochemically advantageous since a greater MnO_2 surface area per unit weight may be accessed by the electrolyte. Both the cyclic voltammetry (**Figure 4.27**) and specific capacitance of particles formed in 50 mM $KMnO_4$ precursor (430 nm, BET surface area 284 m^2/g) demonstrate increased capacitance compared to those formed in 100 mM $KMnO_4$ precursor (700 nm, BET surface area 228 m^2/g). These are mesoporous materials, with an average pore dimension of ~2.0 nm). As expected, the specific capacitance of porous MnO_2 microspheres are also better maintained at high charge discharge rates than less porous microspheres (**Figure 4.28**).

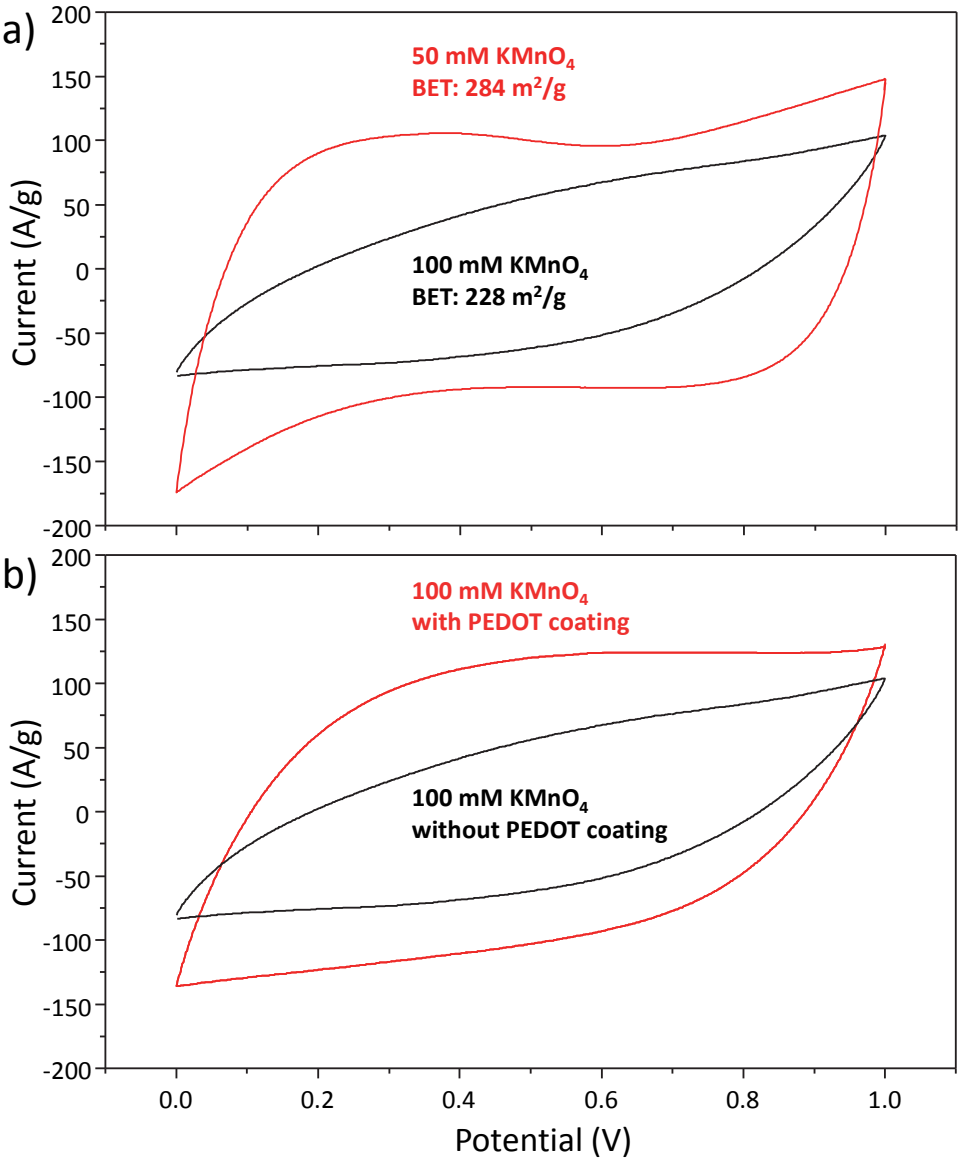

Figure 4.27 (a) Cyclic voltammograms (500 mV/s) of MnO_2 microspheres synthesized from 100 mM and 50 mM $KMnO_4$ in 500 mM HCl at 150 °C, giving microspheres with different porosity. (b) Cyclic voltammograms (500 mV/s) comparison of MnO_2 microspheres (synthesized from 100 mM $KMnO_4$ and 500 mM HCl at 150 °C) with and without PEDOT coating.

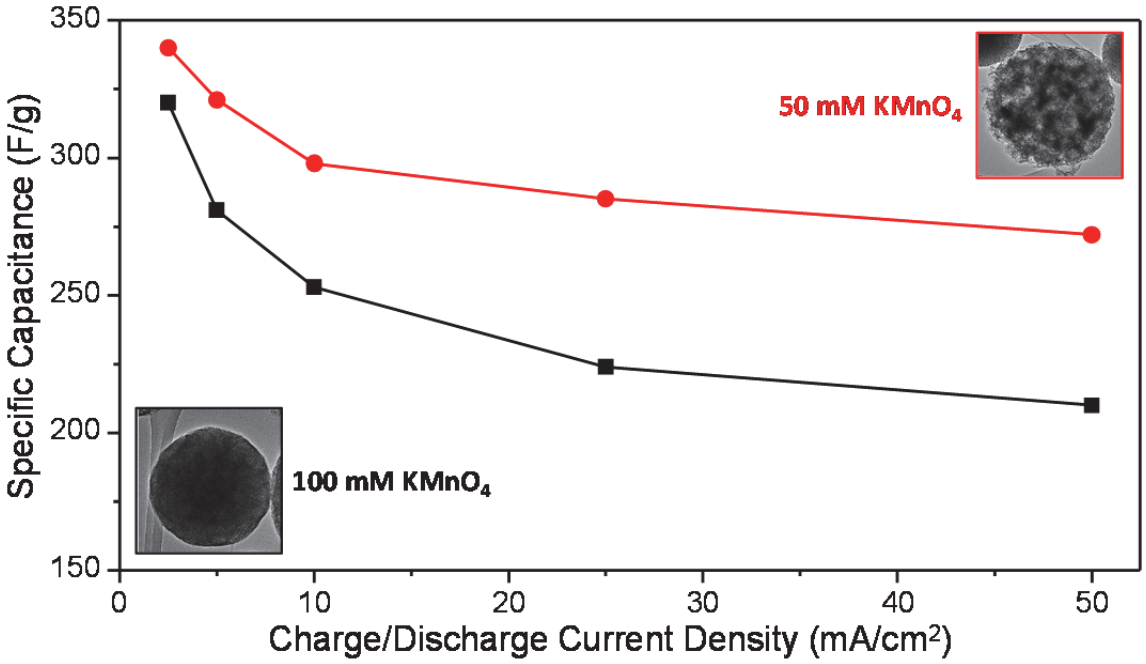

Figure 4.28 Specific capacitance vs. charge/discharge current densities for the MnO_2 microsphere with different porosities (red line: porous MnO_2 microspheres synthesized from 50 mM $KMnO_4$ and 500 mM HCl at 150 °C. black line: porous MnO_2 microspheres synthesized from 100 mM $KMnO_4$ and 500 mM HCl at 150 °C.)

4.6.5 PEDOT Coating of MnO_2 with Enhanced Electrochemical Properties

As noted above, the problem with MnO_2 is the low conductance that impedes the electrolytes from transporting during realistic charge/discharge rates. Another method to increase capacitance is to coat MnO_2 nanomaterials with a thin layer of highly conductive polymer.[51, 52] To this end, we have examined PEDOT as a conductive coating for the MnO_2 microspheres. An SEM image of the PEDOT-coated MnO_2 microspheres is shown in **Figure 4.29 (a)**, and EDS mappings of the S and Mn elements, respectively, are shown in **Figure 4.29 (b)** and **Figure 4.29 (c)**. The EDS mapping indicates that the polymer coats evenly on the MnO_2 microsphere surfaces.

Figure 4.27 (b) shows cyclic voltammograms at a scan rate of 500 mV/s of MnO_2 microspheres before and after PEDOT coating. As expected, the specific capacitance of PEDOT-coated MnO_2 microspheres is greater than un-coated MnO_2 microspheres at high charge and discharge rates. (**Figure 4.30**). The coating clearly increases the electrochemical kinetics of the MnO_2 microsphere electron transfer due to the high conductivity of the PEDOT coating, which facilitates electron transfer between the shell and MnO_2 core. The PEDOT coating therefore increases the reaction rate per unit area of the MnO_2 microspheres. As a polymer, PEDOT can also improve the mechanical properties of MnO_2, which is normally brittle and fragile, causing the MnO_2 to be more flexible and more easily processed.[51] This is, of course, a compromise: PEDOT has a maximum theoretical supercapacitance of only ~200 F/g, which is much lower than that of MnO_2. As a result, the maximum supercapacitance of any composite is inherently lower than pure MnO_2 at infinitely slow scan rates.

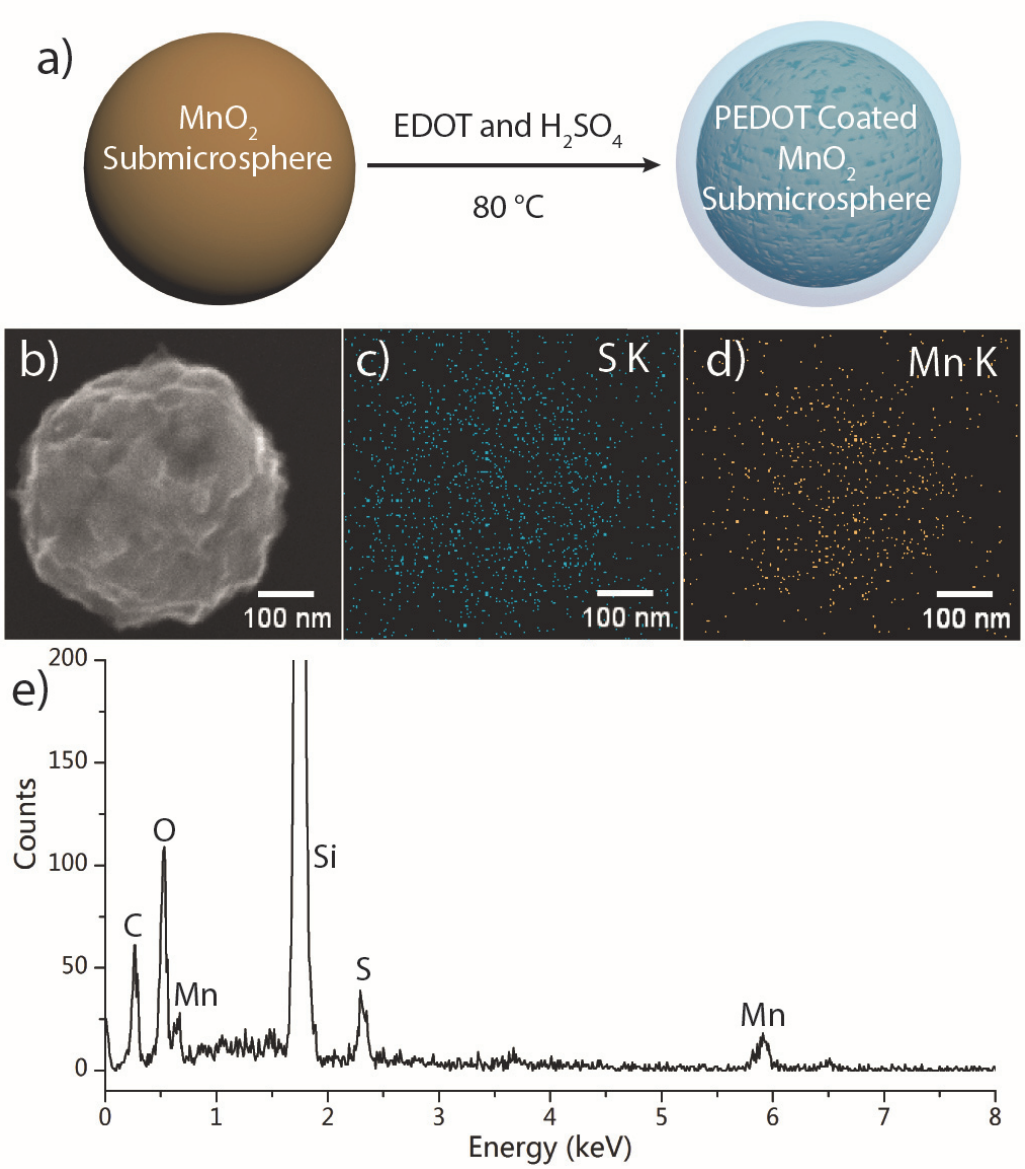

Figure 4.29 (a) Scheme depicting the coating of MnO_2 with PEDOT and (b) SEM image of PEDOT coated MnO_2 microsphere composite. The microsphere here is synthesized via the condition of 100 mM $KMnO_4$ and 500 mM HCl at 150 °C. (c-d) EDX elemental mapping of Sulfur and Manganese, respectively, of the microsphere composite shown in (b). (e) EDX spectra of the whole MnO_2 composite microsphere shown in (b).

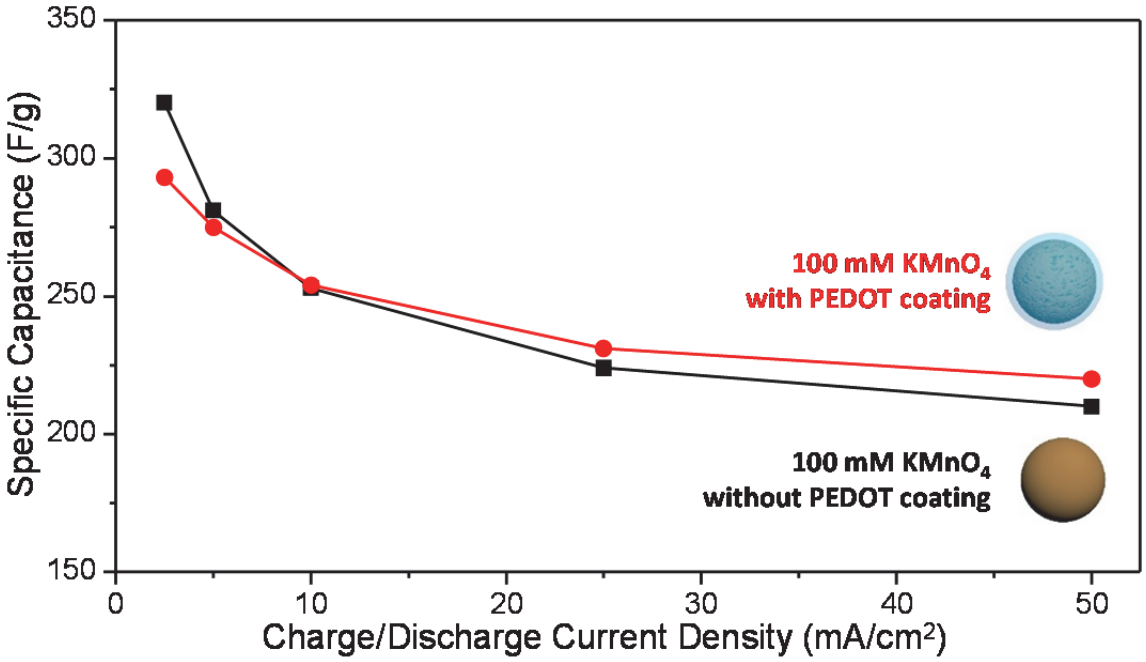

Figure 4.30 Specific capacitance vs. charge/discharge current densities of the MnO_2 microsphere with and without PEDOT coating. MnO_2 microspheres here are synthesized via 100 mM $KMnO_4$ and 500 HCl at 150 °C condition.

4.7 Conclusions

We have successfully synthesized manganese oxide (MnO_2) microspheres using ultrasonic spray pyrolysis (USP). This process involves thermal decomposition of acidified potassium permanganate in a nebulized micron-sized droplet. The MnO_2 microspheres were thoroughly characterized (SEM, TEM, powder-XRD, Raman spectroscopy, and XPS). The morphology and crystallinity of the MnO_2 micropheres can be controlled by tuning precursor concentrations (ratios) and tube furnace temperatures. We also investigate the capacitive properties of MnO_2 microspheres and demonstrate that they are a promising electrode material with applications for supercapacitors since they exhibit a specific capacitance of 320 F/g. Finally, we have successfully improved the capacitive properties of MnO_2 particles at high charge and discharge rates by increasing the effective surface area and coating with a thin layer of conductive polymer.

This microsphere synthesis method is facile and can easily be scaled up. Importantly, the microspheres can be sprayed directly from the USP apparatus onto a

conductive substrate (i.e., conductive carbon fiber paper). This gas-phase spray-coating provides for an easy method of fabrication of supercapacitor electrode materials with high specific capacitances and excellent cyclability.

4.8 References

(1) Romm, J. The car and fuel of the future. *Energy Policy* **2006,** 34, 2609-2614.

(2) Service, R. F. Materials science. New'supercapacitor'promises to pack more electrical punch. *Science (New York, NY)* **2006,** 313, 902.

(3) Brodd, R. J.; Bullock, K. R.; Leising, R. A.; Middaugh, R. L.; Miller, J. R.; Takeuchi, E. Batteries, 1977 to 2002. *Journal of the Electrochemical Society* **2004,** 151, K1-K11.

(4) Armand, M.; Tarascon, J.-M. Building better batteries. *Nature* **2008,** 451, 652-657.

(5) Miller, J. R.; Simon, P. Electrochemical capacitors for energy management. *Science Magazine* **2008,** 321, 651-652.

(6) Conway, B. E., *Electrochemical supercapacitors: scientific fundamentals and technological applications*. Springer Science & Business Media: 2013.

(7) Pandolfo, A.; Hollenkamp, A. Carbon properties and their role in supercapacitors. *Journal of power sources* **2006,** 157, 11-27.

(8) Dubal, D. P.; Kim, J. G.; Kim, Y.; Holze, R.; Lokhande, C. D.; Kim, W. B. Supercapacitors based on flexible substrates: An overview. *Energy Technology* **2014,** 2, 325-341.

(9) Yan, J.; Wang, Q.; Wei, T.; Fan, Z. Recent advances in design and fabrication of electrochemical supercapacitors with high energy densities. *Advanced Energy Materials* **2014,** 4.

(10) Peng, X.; Peng, L.; Wu, C.; Xie, Y. Two dimensional nanomaterials for flexible supercapacitors. *Chemical Society reviews* **2014,** 43, 3303-3323.

(11) Naoi, K.; Naoi, W.; Aoyagi, S.; Miyamoto, J.-i.; Kamino, T. New generation "nanohybrid supercapacitor". *Accounts of chemical research* **2012,** 46, 1075-1083.

(12) Winter, M.; Brodd, R. J. What are batteries, fuel cells, and supercapacitors? *Chemical reviews* **2004,** 104, 4245-4270.

(13) Jost, K.; Dion, G.; Gogotsi, Y. Textile energy storage in perspective. *Journal of Materials Chemistry A* **2014,** 2, 10776-10787.

(14) Frackowiak, E.; Metenier, K.; Bertagna, V.; Beguin, F. Supercapacitor electrodes from multiwalled carbon nanotubes. *Applied Physics Letters* **2000,** 77, 2421-2423.
(15) Frackowiak, E.; Beguin, F. Carbon materials for the electrochemical storage of energy in capacitors. *Carbon* **2001,** 39, 937-950.
(16) Vix-Guterl, C.; Frackowiak, E.; Jurewicz, K.; Friebe, M.; Parmentier, J.; Béguin, F. Electrochemical energy storage in ordered porous carbon materials. *Carbon* **2005,** 43, 1293-1302.
(17) Yoon, B.-J.; Jeong, S.-H.; Lee, K.-H.; Kim, H. S.; Park, C. G.; Han, J. H. Electrical properties of electrical double layer capacitors with integrated carbon nanotube electrodes. *Chemical Physics Letters* **2004,** 388, 170-174.
(18) Fuertes, A.; Lota, G.; Centeno, T.; Frackowiak, E. Templated mesoporous carbons for supercapacitor application. *Electrochimica Acta* **2005,** 50, 2799-2805.
(19) Conway, B. E. TRANSITION FROM SUPERCAPACITOR TO BATTERY BEHAVIOR IN ELECTROCHEMICAL ENERGY-STORAGE. *Journal of the Electrochemical Society* **1991,** 138, 1539-1548.
(20) Raymundo-Pinero, E.; Khomenko, V.; Frackowiak, E.; Beguin, F. Performance of manganese oxide/CNTs composites as electrode materials for electrochemical capacitors. *Journal of the Electrochemical Society* **2005,** 152, A229-A235.
(21) Arbizzani, C.; Mastragostino, M.; Meneghello, L. Polymer-based redox supercapacitors: A comparative study. *Electrochimica Acta* **1996,** 41, 21-26.
(22) Ryu, K. S.; Kim, K. M.; Park, N.-G.; Park, Y. J.; Chang, S. H. Symmetric redox supercapacitor with conducting polyaniline electrodes. *Journal of Power Sources* **2002,** 103, 305-309.
(23) Wang, G.; Zhang, L.; Zhang, J. A review of electrode materials for electrochemical supercapacitors. *Chemical Society reviews* **2012,** 41, 797-828.
(24) Kötz, R.; Carlen, M. Principles and applications of electrochemical capacitors. *Electrochimica Acta* **2000,** 45, 2483-2498.
(25) Stern, O. 30, 508; DC Grahame. *Chem. Rev* **1947,** 41, 441.
(26) Zheng, J. P. Ruthenium Oxide-Carbon Composite Electrodes for Electrochemical Capacitors. *Electrochemical and Solid-State Letters* **1999,** 2, 359-361.

(27) Zheng, J.; Cygan, P.; Jow, T. Hydrous ruthenium oxide as an electrode material for electrochemical capacitors. *Journal of the Electrochemical Society* **1995,** 142, 2699-2703.
(28) Cottineau, T.; Toupin, M.; Delahaye, T.; Brousse, T.; Belanger, D. Nanostructured transition metal oxides for aqueous hybrid electrochemical supercapacitors. *Applied Physics A* **2006,** 82, 599-606.
(29) Toupin, M.; Brousse, T.; Bélanger, D. Influence of microstucture on the charge storage properties of chemically synthesized manganese dioxide. *Chemistry of Materials* **2002,** 14, 3946-3952.
(30) Hu, C.-C.; Tsou, T.-W. Ideal capacitive behavior of hydrous manganese oxide prepared by anodic deposition. *Electrochemistry Communications* **2002,** 4, 105-109.
(31) Jiang, J.; Kucernak, A. Electrochemical supercapacitor material based on manganese oxide: preparation and characterization. *Electrochimica Acta* **2002,** 47, 2381-2386.
(32) Augustyn, V.; Simon, P.; Dunn, B. Pseudocapacitive oxide materials for high-rate electrochemical energy storage. *Energy & Environmental Science* **2014,** 7, 1597.
(33) Fusalba, F.; Gouérec, P.; Villers, D.; Bélanger, D. Electrochemical characterization of polyaniline in nonaqueous electrolyte and its evaluation as electrode material for electrochemical supercapacitors. *Journal of the Electrochemical Society* **2001,** 148, A1-A6.
(34) An, K. H.; Jeon, K. K.; Heo, J. K.; Lim, S. C.; Bae, D. J.; Lee, Y. H. High-capacitance supercapacitor using a nanocomposite electrode of single-walled carbon nanotube and polypyrrole. *Journal of the Electrochemical Society* **2002,** 149, A1058-A1062.
(35) Fonseca, C. P.; Benedetti, J. E.; Neves, S. Poly (3-methyl thiophene)/PVDF composite as an electrode for supercapacitors. *Journal of power sources* **2006,** 158, 789-794.
(36) Wei, W.; Cui, X.; Chen, W.; Ivey, D. G. Manganese oxide-based materials as electrochemical supercapacitor electrodes. *Chemical Society reviews* **2011,** 40, 1697-721.
(37) Hu, C. C.; Tsou, T. W. Ideal capacitive behavior of hydrous manganese oxide prepared by anodic deposition. *Electrochemistry Communications* **2002,** 4, 105-109.

(38) Toupin, M.; Brousse, T.; Belanger, D. Influence of microstucture on the charge storage properties of chemically synthesized manganese dioxide. *Chemistry of Materials* **2002,** 14, 3946-3952.
(39) Reddy, R. N.; Reddy, R. G. Sol-gel MnO2 as an electrode material for electrochemical capacitors. *Journal of Power Sources* **2003,** 124, 330-337.
(40) Kotz, R.; Carlen, M. Principles and applications of electrochemical capacitors. *Electrochimica Acta* **2000,** 45, 2483-2498.
(41) Arico, A. S.; Bruce, P.; Scrosati, B.; Tarascon, J. M.; Van Schalkwijk, W. Nanostructured materials for advanced energy conversion and storage devices. *Nature Materials* **2005,** 4, 366-377.
(42) Simon, P.; Gogotsi, Y. Materials for electrochemical capacitors. *Nature Materials* **2008,** 7, 845-854.
(43) Wang, J.; Xin, H. L.; Wang, D. Recent progress on mesoporous carbon materials for advanced energy conversion and storage. *Particle & Particle Systems Characterization* **2014,** 31, 515-539.
(44) Subramanian, V.; Zhu, H. W.; Vajtai, R.; Ajayan, P. M.; Wei, B. Q. Hydrothermal synthesis and pseudocapacitance properties of MnO2 nanostructures. *J. Phys. Chem. B* **2005,** 109, 20207-20214.
(45) Wang, X.; Li, Y. D. Selected-control hydrothermal synthesis of alpha- and beta-MnO2 single crystal nanowires. *J. Am. Chem. Soc.* **2002,** 124, 2880-2881.
(46) Omomo, Y.; Sasaki, T.; Wang, L. Z.; Watanabe, M. Redoxable nanosheet crystallites of MnO2 derived via delamination of a layered manganese oxide. *J. Am. Chem. Soc.* **2003,** 125, 3568-3575.
(47) Reddy, A. L. M.; Shaijumon, M. M.; Gowda, S. R.; Ajayan, P. M. Coaxial MnO2/Carbon Nanotube Array Electrodes for High-Performance Lithium Batteries. *Nano Lett.* **2009,** 9, 1002-1006.
(48) Chen, S.; Zhu, J. W.; Wu, X. D.; Han, Q. F.; Wang, X. Graphene Oxide-MnO2 Nanocomposites for Supercapacitors. *ACS Nano* **2010,** 4, 2822-2830.
(49) Wu, Z. S.; Ren, W. C.; Wang, D. W.; Li, F.; Liu, B. L.; Cheng, H. M. High-Energy MnO2 Nanowire/Graphene and Graphene Asymmetric Electrochemical Capacitors. *ACS Nano* **2010,** 4, 5835-5842.

(50) Hou, Y.; Cheng, Y. W.; Hobson, T.; Liu, J. Design and Synthesis of Hierarchical MnO2 Nanospheres/Carbon Nanotubes/Conducting Polymer Ternary Composite for High Performance Electrochemical Electrodes. *Nano Lett.* **2010,** 10, 2727-2733.
(51) Liu, R.; Lee, S. B. MnO2/Poly(3,4-ethylenedioxythiophene) coaxial nanowires by one-step coelectrodeposition for electrochemical energy storage. *Journal of the American Chemical Society* **2008,** 130, 2942-2943.
(52) Liu, R.; Duay, J.; Lee, S. B. Redox Exchange Induced MnO2 Nanoparticle Enrichment in Poly(3,4-ethylenedioxythiophene) Nanowires for Electrochemical Energy Storage. *ACS Nano* **2010,** 4, 4299-4307.
(53) Pang, H.; Wang, S.; Li, G.; Ma, Y.; Li, J.; Li, X.; Zhang, L.; Zhang, J.; Zheng, H. Cu superstructures fabricated using tree leaves and Cu–MnO 2 superstructures for high performance supercapacitors. *J. Mater. Chem. A* **2013,** 1, 5053-5060.
(54) Yuan, C.; Zhang, L.; Hou, L.; Pang, G.; Zhang, X. Green Template-Free Synthesis of Mesoporous Ternary CoNi–Mn Oxide Nanowires Towards High-Performance Electrochemical Capacitors. *Particle & Particle Systems Characterization* **2014,** 31, 778-787.
(55) Sun, Y.; Wang, L.; Liu, Y.; Ren, Y. Birnessite-Type MnO2 Nanosheets with Layered Structures Under High Pressure: Elimination of Crystalline Stacking Faults and Oriented Laminar Assembly. *Small* **2015,** 11, 300-305.
(56) Liu, M.; Gan, L.; Xiong, W.; Xu, Z.; Zhu, D.; Chen, L. Development of MnO2/porous carbon microspheres with a partially graphitic structure for high performance supercapacitor electrodes. *Journal of Materials Chemistry A* **2014,** 2, 2555.
(57) Kim, M.; Kim, J. Redox deposition of birnessite-type manganese oxide on silicon carbide microspheres for use as supercapacitor electrodes. *ACS applied materials & interfaces* **2014,** 6, 9036-45.
(58) Kim, M.; Kim, J. Development of high power and energy density microsphere silicon carbide-MnO2 nanoneedles and thermally oxidized activated carbon asymmetric electrochemical supercapacitors. *Physical chemistry chemical physics : PCCP* **2014,** 16, 11323-36.

(59) Lu, Q.; Zhou, Y. Synthesis of mesoporous polythiophene/MnO2 nanocomposite and its enhanced pseudocapacitive properties. *Journal of Power Sources* **2011,** 196, 4088-4094.
(60) Chen, R.; Yu, J.; Xiao, W. Hierarchically porous MnO2 microspheres with enhanced adsorption performance. *Journal of Materials Chemistry A* **2013,** 1, 11682.
(61) Zhou, X.; Chen, S.; Zhang, D.; Guo, X.; Ding, W.; Chen, Y. Microsphere organization of nanorods directed by PEG linear polymer. *Langmuir* **2006,** 22, 1383-1387.
(62) Ghodbane, O.; Pascal, J. L.; Favier, F. Microstructural effects on charge-storage properties in MnO2-based electrochemical supercapacitors. *ACS applied materials & interfaces* **2009,** 1, 1130-9.
(63) Ko, W.-Y.; Chen, L.-J.; Chen, Y.-H.; Chen, W.-H.; Lu, K.-M.; Yang, J.-R.; Yen, Y.-C.; Lin, K.-J. One-Step Solvothermal-Processed 3D Spinel-Type Manganese Oxide Microspheres and Their Improved Supercapacitive Properties. *The Journal of Physical Chemistry C* **2013,** 117, 16290-16296.
(64) Toivo T. Kodas, M. J. H.-S., *Aerosol Processing of Materials*. Wiley: 1998.
(65) Bang, J. H.; Suslick, K. S. Applications of Ultrasound to the Synthesis of Nanostructured Materials. *Adv. Mater.* **2010,** 22, 1039-1059.
(66) Xu, H.; Zeiger, B. W.; Suslick, K. S. Sonochemical synthesis of nanomaterials. *Chem. Soc. Rev.* **2013,** 42, 2555-2567.
(67) Messing, G. L.; Zhang, S.-C.; Jayanthi, G. V. Ceramic Powder Synthesis by Spray Pyrolysis. *J. Am. Ceram. Soc.* **1993,** 76, 2707-2726.
(68) Okuyama, K.; Wuled Lenggoro, I. Preparation of nanoparticles via spray route. *Chem. Eng. Sci.* **2003,** 58, 537-547.
(69) Jain, S.; Skamser, D. J.; Kodas, T. T. Morphology of Single-Component Particles Produced by Spray Pyrolysis. *Aerosol Sci. Technol.* **1997,** 27, 575-590.
(70) Kim, H.; Fortunato, M. E.; Xu, H.; Bang, J. H.; Suslick, K. S. Carbon Microspheres as Supercapacitors. *The Journal of Physical Chemistry C* **2011,** 115, 20481-20486.
(71) Xu, H.; Guo, J.; Suslick, K. S. Porous carbon spheres from energetic carbon precursors using ultrasonic spray pyrolysis. *Adv Mater* **2012,** 24, 6028-33.

(72) Jokić, B.; Drmanić, S.; Radetic, T.; Krstić, J.; Petrović, R.; Orlović, A.; Janaćković, D. Synthesis of submicron carbon spheres by the ultrasonic spray pyrolysis method. *Mater. Lett.* **2010,** 64, 2173-2176.
(73) Skrabalak, S. E. Ultrasound-assisted synthesis of carbon materials. *Phys. Chem. Chem. Phys.* **2009,** 11, 4930-42.
(74) Jung, D. S.; Hwang, T. H.; Lee, J. H.; Koo, H. Y.; Shakoor, R. A.; Kahraman, R.; Jo, Y. N.; Park, M. S.; Choi, J. W. Hierarchical porous carbon by ultrasonic spray pyrolysis yields stable cycling in lithium-sulfur battery. *Nano Lett.* **2014,** 14, 4418-25.
(75) Mai, L. Q.; Minhas-Khan, A.; Tian, X.; Hercule, K. M.; Zhao, Y. L.; Lin, X.; Xu, X. Synergistic interaction between redox-active electrolyte and binder-free functionalized carbon for ultrahigh supercapacitor performance. *Nat. Commun.* **2013,** 4, 2923.
(76) Ko, Y. N.; Park, S. B.; Jung, K. Y.; Kang, Y. C. One-pot facile synthesis of ant-cave-structured metal oxide-carbon microballs by continuous process for use as anode materials in Li-ion batteries. *Nano Lett.* **2013,** 13, 5462-6.
(77) USP nebulizer pictures.
(78) USP furnace tube.
(79) Li, D. Y.; Chen, Y. F. Facile Controlled Synthesis of Manganese Oxide Hierarchical Microspheres by Hydrothermal Method. *Materials Science Forum* **2011,** 688, 107-115.
(80) Wang, J.; Liu, J.; Zhou, Y.; Hodgson, P.; Li, Y. One-pot facile synthesis of hierarchical hollow microspheres constructed with MnO2 nanotubes and their application in lithium storage and water treatment. *RSC Advances* **2013,** 3, 25937.
(81) Xiao, W.; Wang, D.; Lou, X. W. Shape-controlled synthesis of MnO2 nanostructures with enhanced electrocatalytic activity for oxygen reduction. *The Journal of Physical Chemistry C* **2009,** 114, 1694-1700.
(82) Byers, H. G., *A study of the reduction of permanganic acid by manganese dioxide*. The Chemical Publishing Company: 1899.
(83) Gao, T.; Fjellvåg, H.; Norby, P. A comparison study on Raman scattering properties of α-and β-MnO< sub> 2</sub>. *Analytica chimica acta* **2009,** 648, 235-239.
(84) Julien, C. Raman spectra of birnessite manganese dioxides. *Solid State Ionics* **2003,** 159, 345-356.

(85) Herbstein, F.; Ron, G.; Weissman, A. The thermal decomposition of potassium permanganate and related substances. Part I. Chemical aspects. *Journal of the Chemical Society A: Inorganic, Physical, Theoretical* **1971,** 1821-1826.
(86) Herbstein, F.; Kapon, M.; Weissman, A. Old and new studies of the thermal decomposition of potassium permanganate. *Journal of thermal analysis* **1994,** 41, 303-322.
(87) Venable, F.; Jackson, D. THE REACTION BETWEEN HYDROCHLORIC ACID AND POTASSIUM PERMANGANATE. *Journal of the American Chemical Society* **1920,** 42, 237-239.
(88) SuongáOu, F. Synthesis of hybrid nanowire arrays and their application as high power supercapacitor electrodes. *Chemical Communications* **2008,** 2373-2375.
(89) Zheng, J. P. Theoretical energy density for electrochemical capacitors with intercalation electrodes. *Journal of the Electrochemical Society* **2005,** 152, A1864-A1869.
(90) Chang, J. K.; Tsai, W. T. Material characterization and electrochemical performance of hydrous manganese oxide electrodes for use in electrochemical pseudocapacitors. *Journal of the Electrochemical Society* **2003,** 150, A1333-A1338.
(91) Toupin, M.; Brousse, T.; Bélanger, D. Charge Storage Mechanism of MnO2 Electrode Used in Aqueous Electrochemical Capacitor. *Chemistry of Materials* **2004,** 16, 3184-3190.
(92) Lang, X.; Hirata, A.; Fujita, T.; Chen, M. Nanoporous metal/oxide hybrid electrodes for electrochemical supercapacitors. *Nat Nano* **2011,** 6, 232-236.

CHAPTER 5
ULTRASONIC SPRAY POLYMERIZATION FOR PEDOT MICROSPHERES AS SUPERCAPACITOR ELECTRODE MATERIALS

5.1 Introduction

5.1.1 Conductive Polymer PEDOT as Supercapacitor Materials

Conductive polymers are another important class of material for redox supercapacitor materials, [1-3] because of their excellent electrochemical reversibility, fast switching between redox states, high conductivity in a doped state, mechanical flexibility, low toxicity, and low cost.[4, 5] Among those conductive polymers, Poly(3,4-ethylenedioxythiophene), PEDOT, is an attractive conjugated polymer that can be tailored to exhibit different electronic properties (i.e., insulating, semiconducting, metallic, semi-metallic)[6, 7], and is useful for various applications such as energy storage, photovoltaics, and LEDs.[1, 8] Its use as an energy storage material, supercapacitor, is based on an ability to store charge in the electrical double layer and throughout the body of the polymer by rapid faradaic charge transfer (pseudocapacitance, **Figure 5.1**). PEDOT is generally considered a superior supercapacitor within the field of conjugated polymers (e.g., polyaniline and polypyrrole) due to its chemical and thermal stability, despite the fact that it has a lower theoretical capacitance.[1] A list of common conducting polymers is shown in **Figure 5.2**.

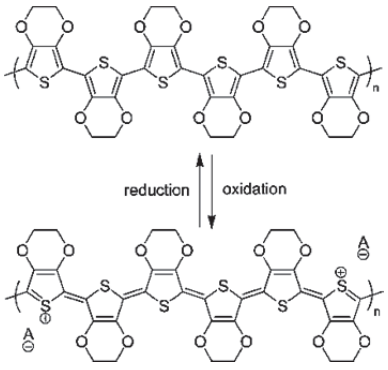

Figure 5.1 Molecular structures of oxidized (charge) and reduced (discharge) forms of PEDOT.

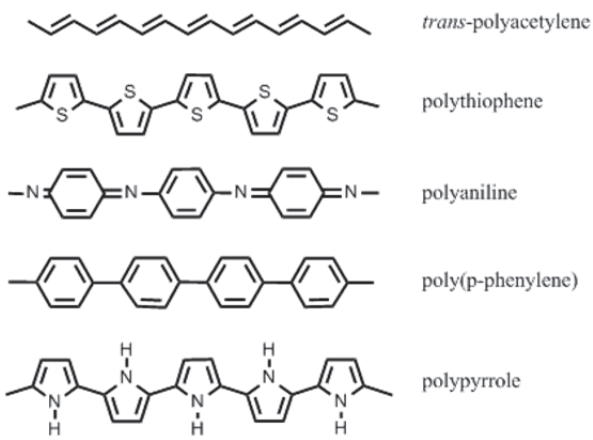

Figure 5.2 Some common conjugated conductive polymers.

5.1.2 Current Materials and Synthetic Methods

Since the charging and discharging of PEDOT involves mass transport of counter ions into and out of the polymer structure, slow ion diffusion is often the limiting factor in the efficiency of PEDOT-based supercapacitors (especially at high charge/discharge rates). One solution to this problem is to fabricate PEDOT electrodes with high surface areas via template-assisted approaches. Using templates such as surfactant micelles (**Figure 5.3**),[9-19] mesoporous silica (**Figure 5.4**),[20, 21] silica microspheres,[22, 23] or polystyrene,[24, 25] a number of research groups have prepared PEDOT with nano/micron-sized structured features. PEDOT nanotubes have also been prepared by sacrificial growth within anodized alumina pores and extensively investigated as supercapacitor materials (**Figure 5.5**);[26-28] the thinness of nanowires permits rapid ion diffusion, resulting in both high energy and power density. Sacrificial templates, however, are cumbersome and expensive. The ability to synthesize PEDOT micro/nano structures in a template-free fashion could reduce synthetic steps and cost; so far, however, there are only a few reports on template-free morphologically control of PEDOT with only limited supercapacitive properties.[29-32]

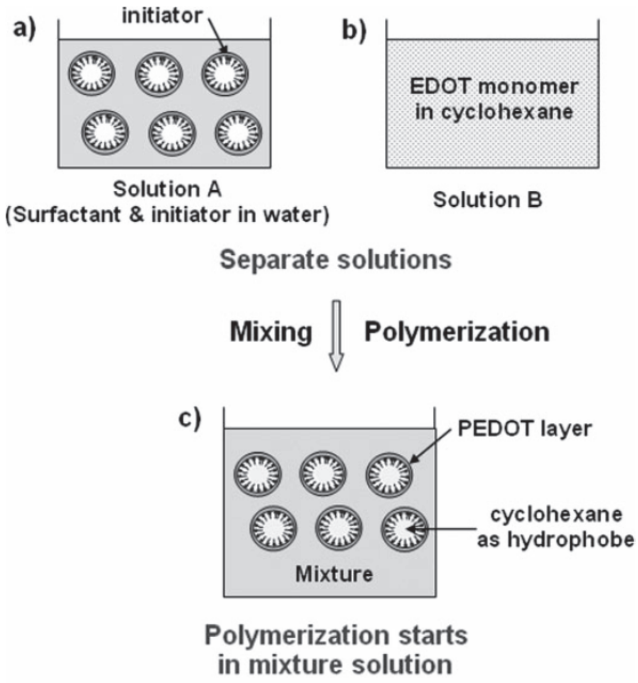

Figure 5.3 The schematic procedure for PEDOT nanocapsules and mesocellular foams using surfactant-mediated interfacial polymerization.[21]

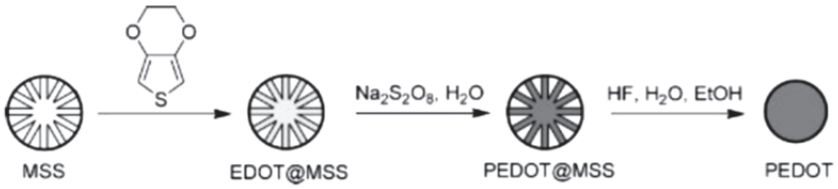

Figure 5.4 Templating methods for PEDOT microsphere synthesis. Here mesoporous silica spheres (MSS) are used as sacrificial template. After EDOT monomer filled in the pores and polymerized, silica is etched away and PEDOT microspheres remain as the final products.[13]

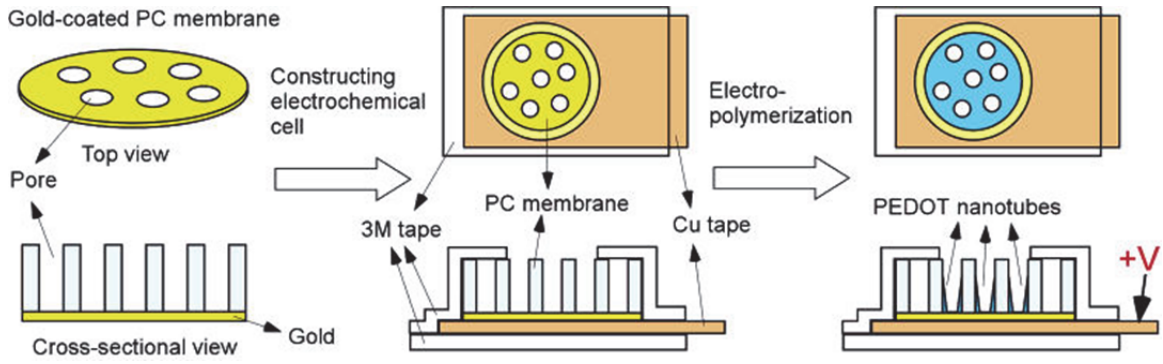

Figure 5.5 Schematic of fabricating PEDOT nanotubes on a flexible template using electrodeposition.[33]

5.2 Ultrasonic Spray Polymerization for PEDOT Microspheres

Ultrasonic spray assisted materials synthesis is a one-step and continuous synthetic process. Ultrasonic nebulization produces micron-sized droplets that function as isolated microreactors.[34-37] To date, ultrasonic spray synthesis has been used to synthesize a diverse range of materials including metals[38], ceramics[39], metal oxides[40], metal sulfides[41], semiconductors[42], and high-surface-area carbons[43, 44] with control over various particle morphologies. Ultrasonic nebulization has had very limited use, however, for the synthesis of polymeric microspheres from monomers.[45]

In this project, we report an ultrasonic spray polymerization (USPo) for PEDOT microspheres. These microspheres were formed by polymerization of nebulized microdroplets of solutions containing monomer 3,4-ethylenedioxythiophene (EDOT) and oxidant (Fe^{III} salts or sodium persulfate) that were then passed through a heated tube (150 – 170 °C). This process is free of template or added surfactant. Three types of PEDOT morphologies (porous, solid, and hollow) can be obtained by using different precursors and solvents (**Figure 5.6**). This ultrasonic spray polymerization of PEDOT is, to our knowledge, the first reported process that can continuously produce PEDOT microspheres with controlled morphologies. Due to the fact that the USPo process is facile, continuous, and single-step, this synthetic process is ultimately scalable for bulk synthesis and large rigs (2.5 m length, 150 kg/day) for ultrasonic spray pyrolysis have been constructed.[46] The synthesized microspheres are tested for their supercapacitance (160 F/g), which is among the highest reported for PEDOT based materials.

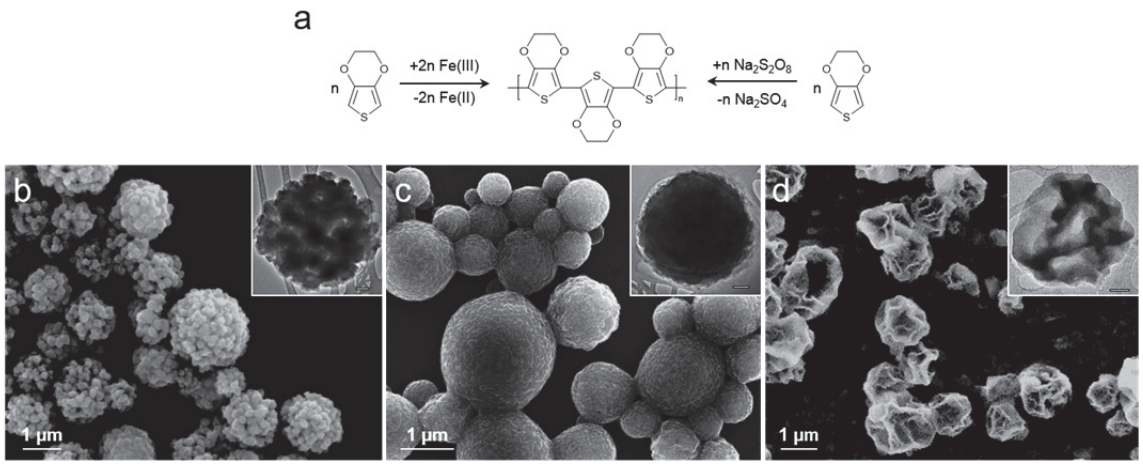

Figure 5.6 (a) PEDOT synthesis scheme illustrating oxidation with either Fe(III) or persulfate salts. SEM images and TEM images of (b) solid, (b) porous, and (c) hollow PEDOT microspheres with $Fe(TsO)_3$, $FeCl_3$ and $Na_2S_2O_8$ oxidation conditions, respectively. The scale bars in the inserts represent 100 nm.

5.2.1 Ultrasonic Spray Polymerization Set-Up of PEDOT Microspheres

A typical USP apparatus for the synthesis of PEDOT microspheres is depicted in **Figure 5.7**. The precursor solution containing EDOT and oxidant (e.g., 200 mM EDOT and 250 mM $FeCl_3$) was nebulized into micron-sized droplets and carried by nitrogen flow through the furnace tube that was preheated to the desired temperature (e.g., 150 °C). The operating frequency of the water nebulizer used was 1.7 MHz. Nitrogen was used as the carrier gas at a flow rate of 1 L/min. The monomer EDOT in each droplet polymerized upon heating. This radical cationic polymerization yields a conjugated backbone chain, polythiophene, with a dark-blue color.[1] The products are then collected in bubblers as a suspension in ethanol and subsequently washed with 50% ethanol/water and centrifuged for a minimum of 4 times. The final products were dried overnight in a vacuum oven at 100 °C for further characterizations. The synthesized PEDOT microspheres have good dispersibility, with a zeta potential of +16 mV. No surfactants or template directing agents (which may affect PEDOT properties either by introducing impurities or damaging PEDOT structures) were used.

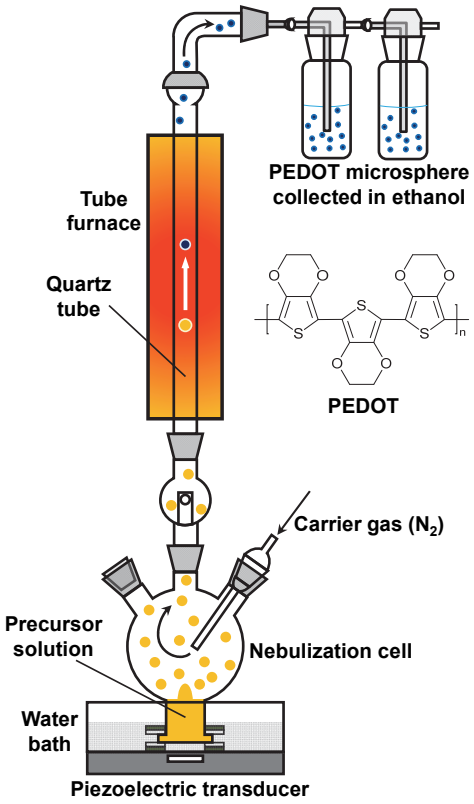

Figure 5.7 Ultrasonic spray polymerization (USPo) apparatus for the synthesis of PEDOT microspheres. The yellow precursor solution here illustrates a solution containing Fe^{3+} ions as oxidant with 3,4-ethylenedioxythiophene monomers.

5.2.2 Reagents and Instrumental Information

Materials and reagents: 3,4-ethylenedioxythiophene, iron(III) p-toluenesulfonate hexahydrate, iron(III) chloride hexahydrate, sodium persulfate, propylene carbonate, poly(methylmethacrylate) (PMMA, Mw ~120,000), and lithium perchlorate were purchased from Sigma Aldrich. Pressure sensitive polypropylene tape (Scotch tape), and copper electrical tape were from 3M Corporation. All the chemicals were used as received without further purification. Carbon paper was purchased from Fuel Cell Store (2050-A).

Material characterizations: Scanning electron micrographs (SEMs) were taken using a JEOL 7000F field emission (FE)-SEM instrument operated at 10 kV. Energy-dispersive X-ray spectroscopy (EDX) was available on the 7000F-SEM instrument by use of a Thermo Electron EDX microanalysis system. Transmission electron microscopy

(TEM) was conducted using a JEOL 2100 Cryo instrument operated at 200 kV. The Brunauer-Emmitt-Teller (BET) specific surface area was measured using a Quantachrome Nova 2200e system. Powder X-ray diffraction (PXRD) patterns were obtained on a Siemens-Bruker D-5000 XRD instrument operated at 40 kV and 30 mA (Cu Kα radiation). Elemental analysis was performed using a CE 440 CHN Analyzer and inductively coupled plasma mass spectrometer (ICP-MS) by the Microanalysis Lab of the School of Chemical Sciences. Thermal gravimetric analysis (TGA) was conducted using a Mettler-Toledo TGA/DSC1 LF. Scans were collected in the range of 25 °C to 660 °C with a ramping rate of 10 °C/min under a dry nitrogen atmosphere.

Electrochemical experiments: Working electrodes were prepared by directly spraying PEDOT microspheres onto pre-weighed carbon paper. The spray-coated carbon paper was then washed thoroughly with deionized water and ethanol to remove any unreacted precursor species. The PEDOT spray-coated carbon paper was then dried thoroughly under vacuum and weighed to calculate the amount of PEDOT deposited. The cyclic voltammetry was conducted using a CH Instruments Electrochemical Workstation (potentiostat/galvanostat) with a platinum mesh counter electrode and a silver/silver chloride (Ag/AgCl) reference electrode. The measurements were made at five different scan rates (50, 100, 250, 500, and 1000 mV/s) in 1M $LiClO_4$ acetonitrile solution. All galvanostatic measurements were performed at a current of 1 mA/cm^2.

PEDOT supercapacitor device fabrication: The electrolyte is made by dissolving 8 g PMMA in 42 mL of 1M $LiClO_4$ acetonitrile/propylene carbonate solution (5:2 v/v). The mixture was heated at 100 °C, with vigorous stirring until the solution begins to gel. This electrolyte is then sandwiched between symmetrical PEDOT electrodes. The system is then sealed with polypropylene tape.

5.3 Results and Discussions

5.3.1 Morphological Control

In general, there are only three morphologies possible for microspheres: solid, porous, and hollow. By controlling the choice of oxidants, we were able to produce examples of each of these morphologies. Oxidation of EDOT with iron(III) p-toluenesulfonate, $FeCl_3$, or sodium persulfate yielded solid, porous, and hollow micro-

spheres, respectively (**Figure 5.6**, **5.8**, and **5.9**). During oxidation, EDOT forms linear polymers of PEDOT,[47] and polymerization induced by oxidation by Fe^{III} is much faster than by persulfate. Fe^{III} oxidants therefore form nanoparticles of PEDOT that aggregate, either nearly completely (which forms solid microspheres) or incompletely (which forms porous microspheres). In the presence of tosylate anions (which appears to act as a plasticizer), the nanoparticle aggregates of linear polymer intermingle during the USPo heating, resulting in relatively smooth, solid microspheres (**Figure 5.3.1a** and **5.3.1b**). When $FeCl_3$ is used, however, the blending of nanoparticles is incomplete and the resulting microspheres are porous aggregates of few nanometer-sized particles (**Figure 5.3.1a** and **5.3.1b**) with a BET surface area of 49 m^2/g, which is comparable to the surface area reported[19] of a nanoporous PEDOT film. In contrast to Fe^{III} oxidants, when sodium persulfate is used as oxidant, the polymerization is slower and as the polymer is formed, it is excluded from the 50% ethanol/water core, forming an outer polymeric surface on the droplet (thus creating hollow microspheres, **Figure 5.3.1a** and **5.3.1b**). By comparison, $FeCl_3$ oxidation in ethanol/water (vs. ethanol only) still produces porous microspheres like those in **Figure 5.3.1a**. In all cases, the overall size of the microspheres is controlled by the precursor concentrations in the nebulized solution and the droplet size during nebulization (which is controlled by the ultrasonic frequency and the liquid surface tension[35, 41-46])

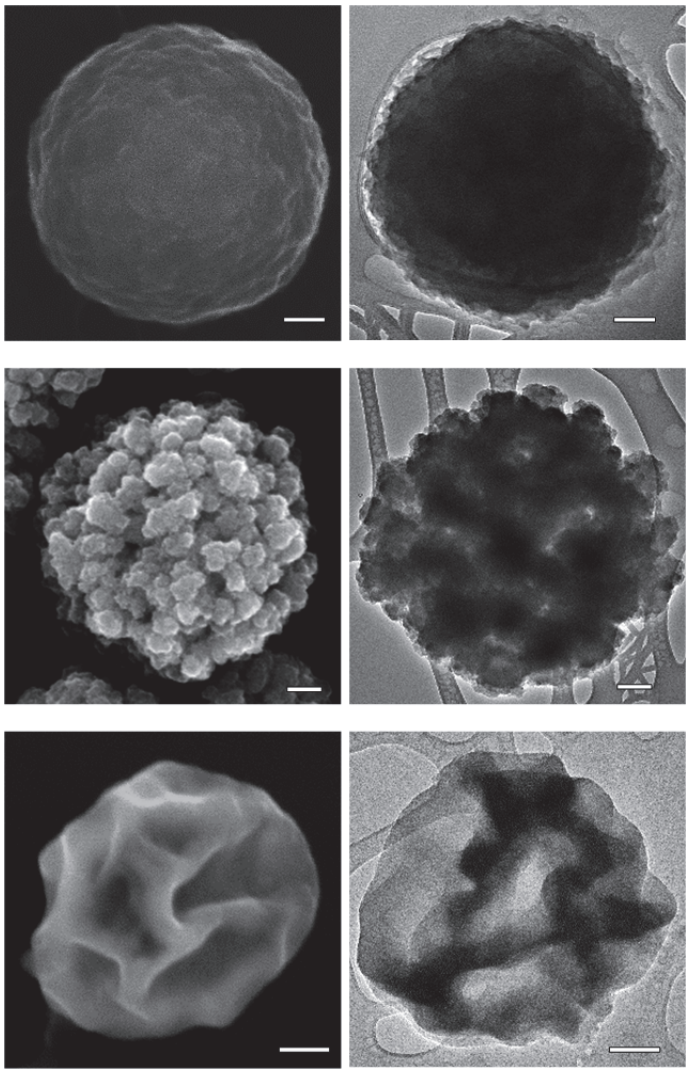

Figure 5.8 SEM (a, c, e) and TEM (b, d, f) of three different morphologies of PEDOT microspheres: (a, b) solid microspheres from $Fe(TsO)_3$ oxidation of 3,4-ethylenedioxythiophene in ethanol, (c, d) porous microspheres from FeCl3 oxidation in ethanol, and (e, f) hollow microsphere from sodium persulfate oxidation in 50% ethanol/water. Scale bars represent 200 nm.

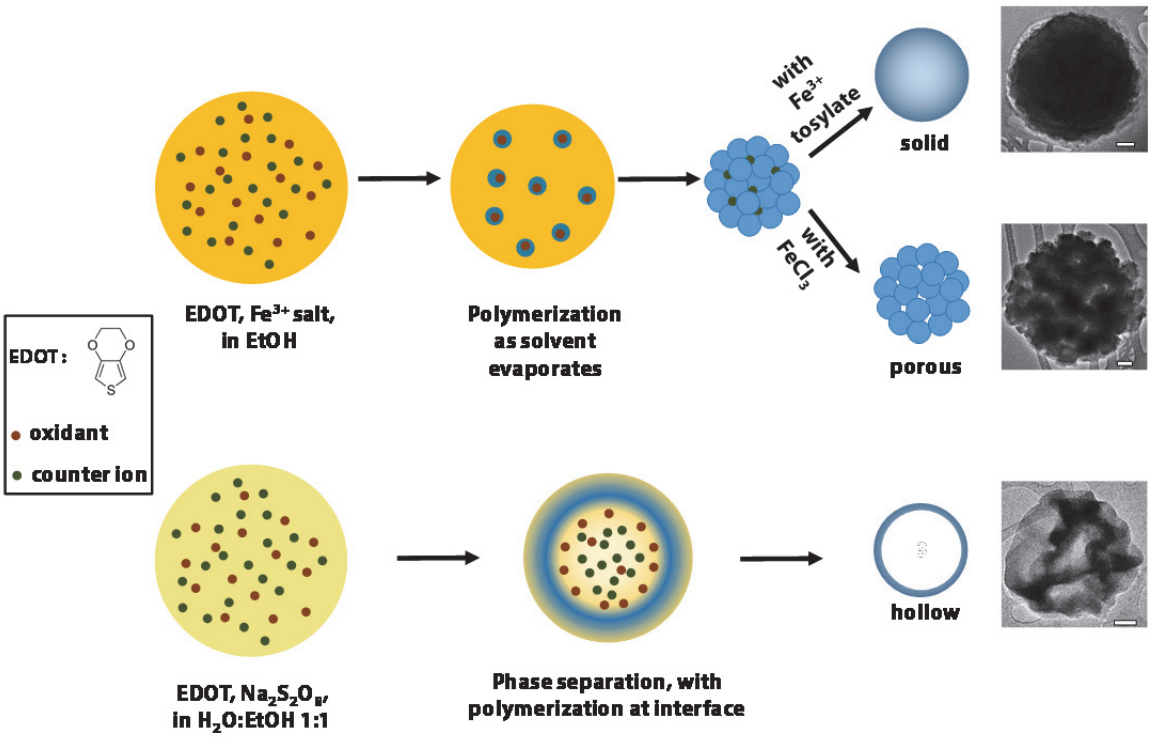

Figure 5.9 Illustration of hypothetical mechanisms behind the formation of solid, porous, and hollow PEDOT micro-sphere. Scale bars represent 200 nm.

5.3.2 Chemical and Structural Properties of the Products

The chemical structure of the PEDOT microspheres was confirmed by FTIR (**Figure 5.10**), which is fully consistent with previously reported data.[48] Thermostability is confirmed with TGA analysis (**Figure 5.11**), showing that the major decomposition occurs around 300 °C.[1] In addition, these PEDOT microspheres are mostly amorphous polymeric material based on the absence of a characteristic peaks in powder XRD data (**Figure 5.12**).[49, 50] Elemental analysis confirms the appropriate composition for PEDOT: C 50.5% (51.0 theor.), H 2.9% (2.9% theor.), and S 22.2% (22.8% theor.). Energy-dispersive X-ray spectroscopy (EDX) (**Figure 5.13**) also confirmed negligible presence of impurities (e.g., less than 0.5% Fe or Na).

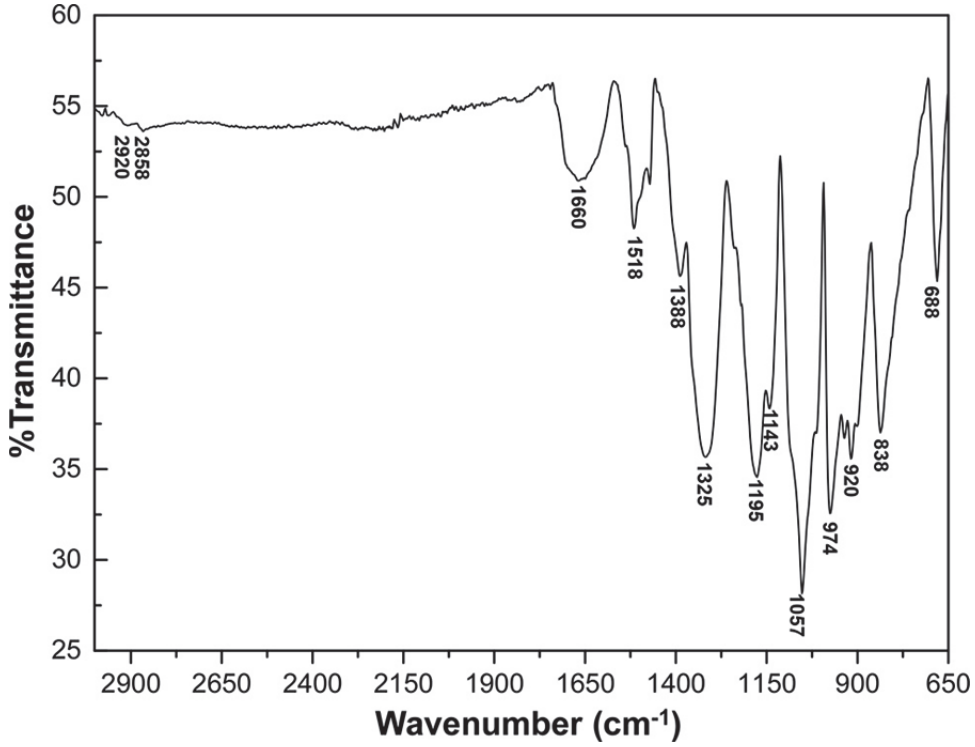

Figure 5.10 FTIR spectrum of PEDOT microspheres.

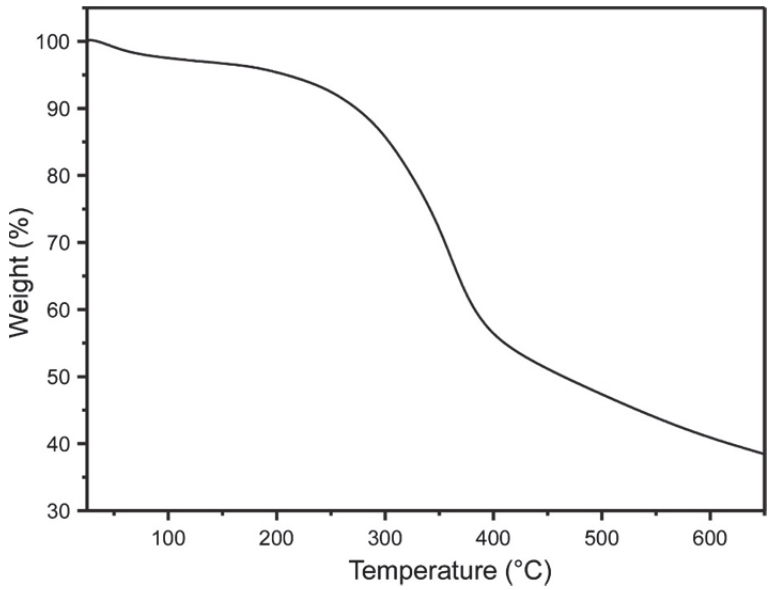

Figure 5.11 TGA data of PEDOT microspheres showing their thermostability; major decomposition begins its onset around 300 °C.

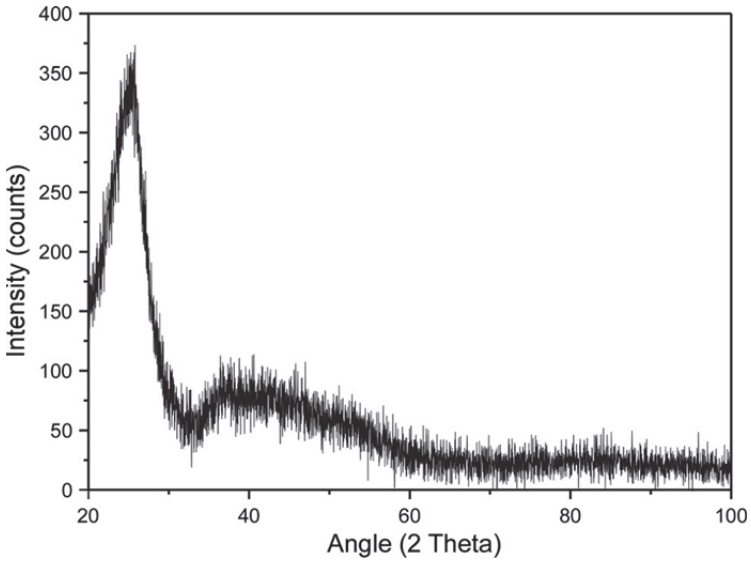

Figure 5.12 PXRD of PEDOT microspheres. The amorphous polymer gives broad peaks at ~25° and ~40°.

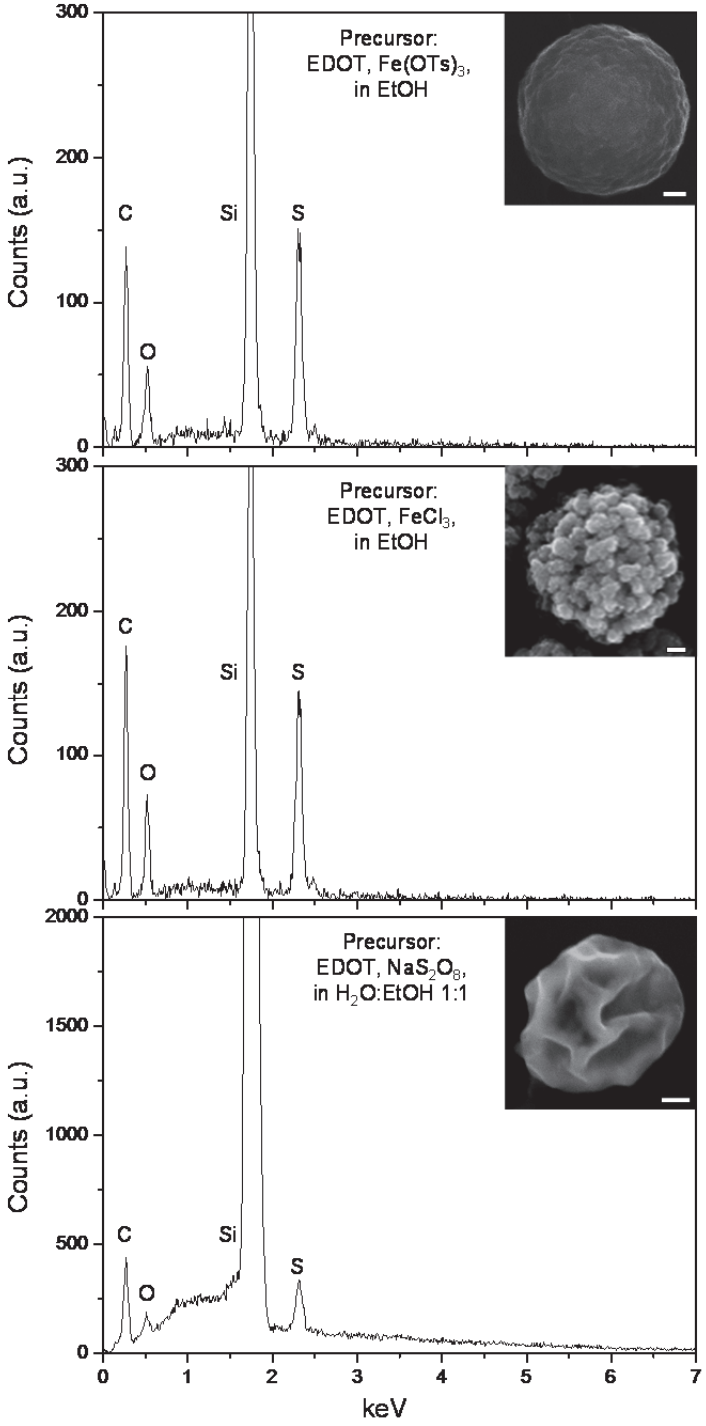

Figure 5.13 EDX spectra of PEDOT microspheres synthesized from three different conditions. It is clearly that after thorough wash, there is negligible impurities (such as Fe^{3+} or Na^{+}) in the final products. Scale bars are each 200 nm.

5.3.3 Spray Coating of PEDOT Microspheres on Conductive Substrates

Formation of PEDOT coatings has remained an interesting challenge.[51-54] The majority of existing approaches are electrochemical deposition or oxidative chemical deposition, which prove difficult to scale-up. We have found that one may readily convert the USPo process into a spray-coating technique simply by diverting the product gas flow to a direct exit through a nozzle (e.g., a pipette tip) onto ones substrate of choice (e.g., silicon wafer, glass coated with FTO, or conductive fibrous carbon paper). We used this spray-coating method to fabricate electrodes by spraying PEDOT microsphere onto fibrous carbon papers (**Figure 5.14 a**). The coated substrates are followed by subsequent rinse and drying steps to remove residual impurities. Given the hydrophobicity of both PEDOT and carbon paper, the microspheres are well attached to the surface. One may also spray-coat flat surfaces in a controlled manner: **Figure 5.14 b** is an enlarged image of spray coating of a flat surface (Si wafer), and **Figure 5.14 c** shows a photo image of a masked spray pattern on colored glass.

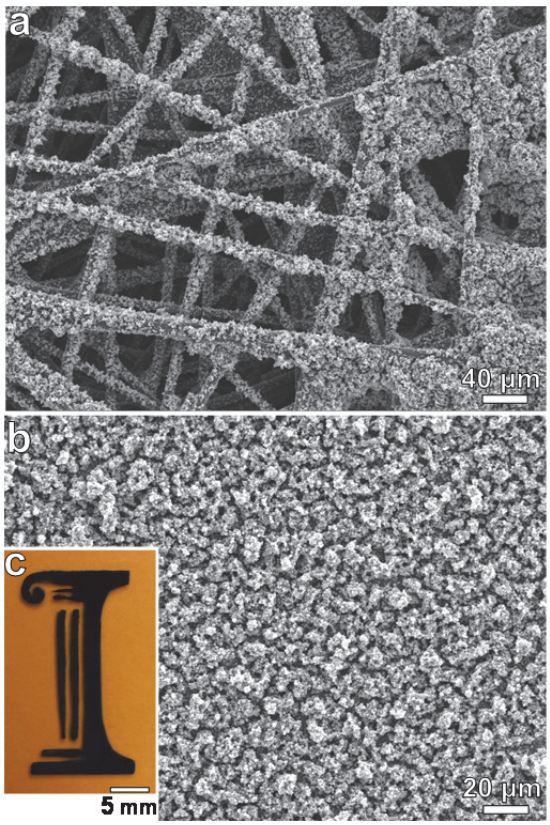

Figure 5.14 (a) SEM image of direct spray of PEDOT microspheres (from $FeCl_3$ oxidation) on carbon fiber paper, and (b) on silicon wafer. Both images are taken after the substrates are coated, washed, and dried under air. (c) Photo images of PEDOT patterning from masked spray coating.

5.3.4 Supercapacitive Performance

The supercapacitor properties of PEDOT microspheres were evaluated by cyclic voltammetry (CV) and galvanostatic charge-discharge curves (with Ag/AgCl reference electrode and in 1M $LiClO_4$ acetonitrile solution). The PEDOT microspheres exhibit CV scans with excellent supercapacitance even at very high sweep rates (**Figures 5.15** and **5.16**). The 10% decrease in the fill factor (from 50 mV/s to 1000 mV/s) is comparable to that observed with electrochemically deposited PEDOT films (**Figures 5.17**).[55] Symmetrical triangular shapes in galvanostatic curves (**Figures 5.18** a) are indicative of ideal capacitive behavior. The highest specific capacitance observed, 160 F/g, is obtained with PEDOT synthesized from $Fe(TsO)_3$ oxidation; this is compares very well with prior supercapacitance measurements on PEDOT prepared using various templated methods.[56]

Finally, a supercapacitor device was fabricated with symmetric PEDOT electrodes.[57] The specific capacitance of the observed with the symmetric PEDOT electrodes was half of the single electrode (measured by galvanostatic charge/discharge experiment, **Figures 5.18** b), as expected.

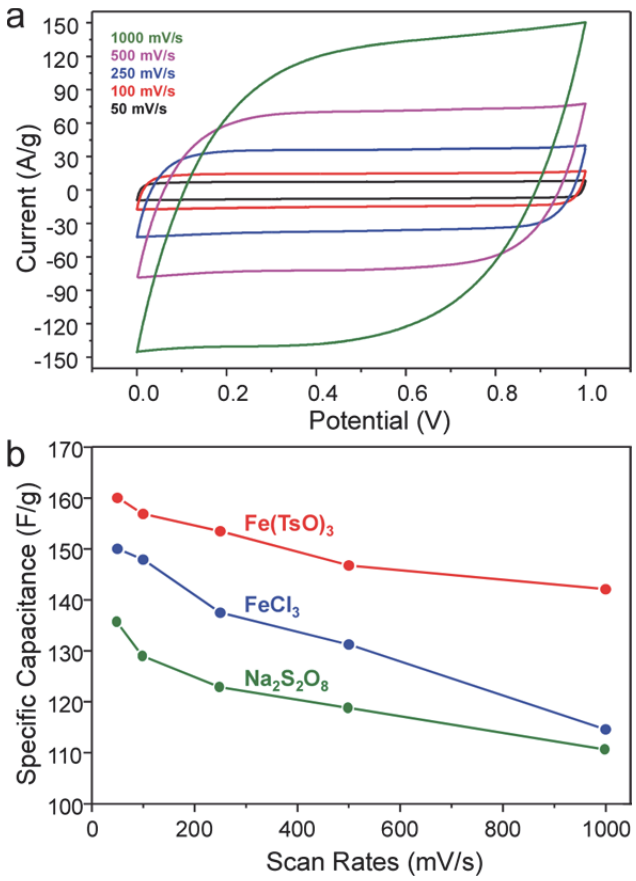

Figures 5.15 (a) Cyclic voltammagram of PEDOT microspheres synthesized from $Fe(TsO)_3$ oxidation. (b) Specific capacitance as a function of scan rate of PEDOT synthesized from $Fe(TsO)_3$, $FeCl_3$, and $Na_2S_2O_8$ oxidation, as labeled. The highest specific capacitance, 160 F/g, is observed with PEDOT synthesized from $Fe(TsO)_3$ oxidation.

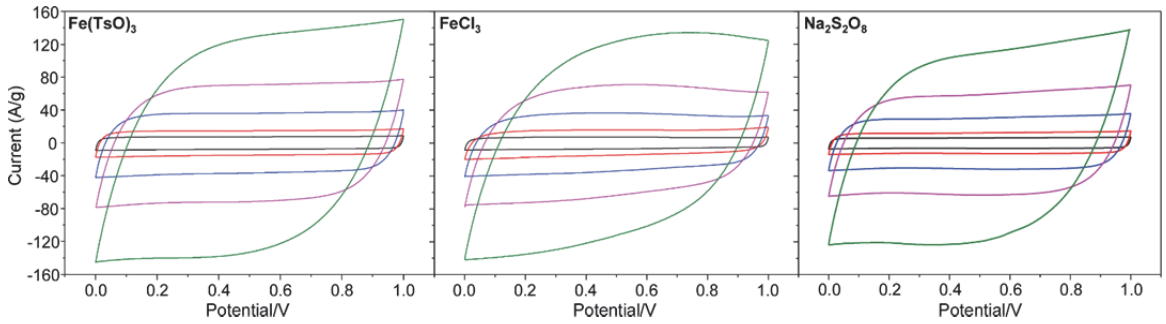

Figures 5.16 Cyclic voltammogram of PEDOT microspheres synthesized from $Fe(TsO)_3$, $FeCl_3$, and $Na_2S_2O_8$ oxidation, as labeled. All products show near ideal charge/discharge cycles for rates as high as 500 mV/s, but with some deviation from ideality at 1000 mV/s.

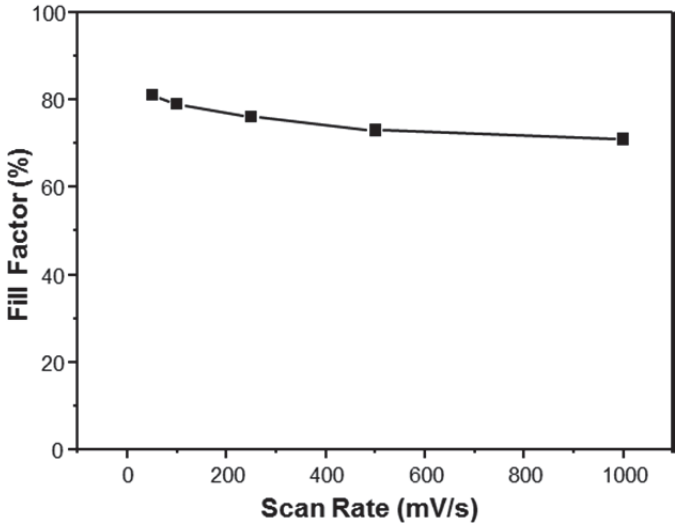

Figures 5.17 Fill factor calculated from Figure 4(a). The highest fill factor is 81% at 50 mV/s and lowest is 71% at 1000 mV/s.

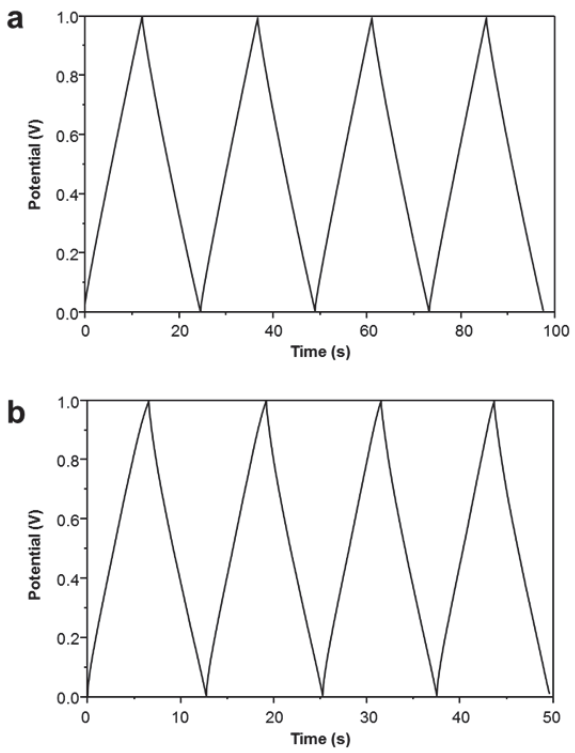

Figures 5.18 Galvanostatic charge-discharge curves (GV) showing excellent reversibility. (a) GV of three electrode system with PEDOT materials as working electrode, with the reference of Ag/AgCl. (b) GV of supercapacitor device with symmetric PEDOT electrodes.

The supercapacitor properties at high scan rates (> 500 mV/s) of previously reported PEDOT microspheres generally suffer loss of ideality due to surfactant impurities or poorly conductive substrate coatings (such as SiO_2).[20] In comparison, PEDOT nanotubes have excellent supercapacitance even at high scan rates(e.g., 140 F/g with ideal charge/discharge behavior at 1000 mV/s), but are exceedingly difficult to prepare in quantity due to the prohibitive costs of the sacrificial alumina templates.[56] In our work here, USPo synthesized PEDOT possesses comparable specific capacitance (160 F/g) and good charge/discharge abilities and can be easily scaled up without templates or additional etching steps.

5.4 Conclusions

In summary, we reported the synthesis of PEDOT microspheres by restricting the oxidative polymerization of EDOT inside micron-sized droplets formed by ultrasonic nebulization. This method provides a facile, one-step, scalable process for bulk PEDOT synthesis.[46] We have successfully controlled microsphere morphologies (porous, solid, and hollow) by choice of oxidant and solvent in the precursor solutions. The microspheres were characterized with electron microscopies, FTIR, TGA, BET, and XRD. These PEDOT microspheres is potentially useful as supercapacitor materials by determining their specific capacitance of 160 F/g, which is among the highest yet reported. This synthetic method is amenable to facile spray-coating of conductive substrates (even textured substrates) and may potentially prove useful in the preparation of composite PEDOT microspheres, e.g., PEDOT-coated metal oxides, to increase the total specific capacitance.

5.5 References

(1) Kirchmeyer, S.; Elschner, A.; Reuter, K.; Lovenich, W.; Merker, U., PEDOT: principles and applications of an intrinsically conductive polymer. In CRC Press, New York: 2011.

(2) Martin, C. R. Membrane-based synthesis of nanomaterials. *Chem. Mater.* **1996,** 8, 1739-1746.

(3) Lakshmi, B. B.; Dorhout, P. K.; Martin, C. R. Sol-gel template synthesis of semiconductor nanostructures. *Chem. Mater.* **1997,** 9, 857-862.

(4) Klein, J. D.; Herrick, R. D.; Palmer, D.; Sailor, M. J.; Brumlik, C. J.; Martin, C. R. Electrochemical fabrication of cadmium chalcogenide microdiode arrays. *Chem. Mater.* **1993,** 5, 902-904.

(5) Bao, J.; Tie, C.; Xu, Z.; Zhou, Q.; Shen, D.; Ma, Q. Template synthesis of an array of nickel nanotubules and its magnetic behavior. *Adv. Mater.* **2001,** 13, 1631.

(6) Bubnova, O.; Khan, Z. U.; Wang, H.; Braun, S.; Evans, D. R.; Fabretto, M.; Hojati-Talemi, P.; Dagnelund, D.; Arlin, J.-B.; Geerts, Y. H. Semi-metallic polymers. *Nat. Mater.* **2014,** 13, 190-194.

(7) Chabinyc, M. Thermoelectric polymers: Behind organics' thermopower. *Nat. Mater.* **2014,** 13, 119-21.

(8) Carlberg, J.; Inganäs, O. Poly (3, 4-ethylenedioxythiophene) as Electrode Material in Electrochemical Capacitors. *J. Electrochem. Soc.* **1997,** 144, L61-L64.

(9) Ghosh, S.; Remita, H.; Ramos, L.; Dazzi, A.; Deniset-Besseau, A.; Beaunier, P.; Goubard, F.; Aubert, P.-H.; Brisset, F.; Remita, S. PEDOT nanostructures synthesized in hexagonal mesophases. *New J. Chem.* **2014,** 38, 1106.

(10) Xu, Y.; Sui, Z.; Xu, B.; Duan, H.; Zhang, X. Emulsion template synthesis of all conducting polymer aerogels with superb adsorption capacity and enhanced electrochemical capacitance. *J. Mater. Chem.* **2012,** 22, 8579-8584.

(11) Ni, X.; Hu, X.; Zhou, S.; Sun, C.; Bai, X.; Chen, P. Synthesis and microwave absorbing properties of poly(3,4-ethylenedioxythiophene) (PEDOT) microspheres. *Polym. Adv. Technol.* **2011,** 22, 532-537.

(12) Müller, K.; Klapper, M.; Müllen, K. Synthesis of conjugated polymer nanoparticles in non-aqueous emulsions. *Macromol. Rapid Commun.* **2006,** 27, 586-593.

(13) Jang, J.; Bae, J.; Park, E. Selective fabrication of poly(3,4-ethylenedioxythiophene) nanocapsules and mesocellular foams using surfactant-mediated interfacial polymerization. *Adv. Mater.* **2006,** 18, 354-358.

(14) Han, J.; Song, G.; Guo, R. A facile solution route for polymeric hollow spheres with controllable size. *Adv. Mater.* **2006,** 18, 3140-3144.

(15) Landfester, K.; Montenegro, R.; Scherf, U.; GüNTNER, R.; Asawapirom, U.; Patil, S.; Neher, D.; Kietzke, T. Semiconducting polymer nanospheres in aqueous dispersion prepared by a miniemulsion process. *Adv. Mater.* **2002,** 14, 651-655.

(16) Henderson, A. M. J.; Saunders, J. M.; Mrkic, J.; Kent, P.; Gore, J.; Saunders, B. R. A new method for stabilising conducting polymer latices using short chain alcohol ethoxylate surfactants. *J. Mater. Chem.* **2001,** 11, 3037-3042.

(17) Morvant, M. C.; Reynolds, J. R. In situ conductivity studies of poly (3, 4-ethylenedioxythiophene). *Synth. Met.* **1998,** 92, 57-61.

(18) Huchet, L.; Akoudad, S.; Roncali, J. Electrosynthesis of highly electroactive tetrathiafulvalene-derivatized polythiophenes. *Adv. Mater.* **1998,** 10, 541-545.

(19) Jones, B. H.; Cheng, K.-Y.; Holmes, R. J.; Lodge, T. P. Nanoporous poly(3,4-ethylenedioxythiophene) derived from polymeric bicontinuous microemulsion templates. *Macromolecules* **2012,** 45, 599-601.

(20) Kelly, T. L.; Yano, K.; Wolf, M. O. Supercapacitive properties of PEDOT and carbon colloidal microspheres. *ACS Appl Mater Interfaces* **2009,** 1, 2536-2543.

(21) Kelly, T. L.; Yamada, Y.; Che, S. P. Y.; Yano, K.; Wolf, M. O. Monodisperse poly(3,4-ethylenedioxythiophene)–silica microspheres: synthesis and assembly into crystalline colloidal arrays. *Adv. Mater.* **2008,** 20, 2616-2621.

(22) GyuáHan, M. Preparation of poly(3,4-ethylenedioxythiophene) (PEDOT) coated silica core–shell particles and PEDOT hollow particles. *Chem. Commun.* **2004,** 2154-2155.

(23) Han, M. G.; Foulger, S. H. Crystalline colloidal arrays composed of poly (3, 4-ethylenedioxythiophene)-coated polystyrene particles with a stop band in the visible regime. *Adv. Mater.* **2004,** 16, 231-234.

(24) Luo, S. C.; Yu, H. h.; Wan, A. C.; Han, Y.; Ying, J. Y. A general synthesis for pedot-coated nonconductive materials and pedot hollow particles by aqueous chemical polymerization. *Small* **2008,** 4, 2051-2058.

(25) Khan, M.; Armes, S. Synthesis and characterization of micrometer-sized poly (3, 4-ethylenedioxythiophene)-coated polystyrene latexes. *Langmuir* **1999,** 15, 3469-3475.

(26) Xiao, R.; Cho, S. I.; Liu, R.; Lee, S. B. Controlled electrochemical synthesis of conductive polymer nanotube structures. *J. Am. Chem. Soc.* **2007,** 129, 4483-4489.

(27) Han, M. G.; Foulger, S. H. 1-Dimensional structures of poly (3, 4-ethylenedioxythiophene)(PEDOT): a chemical route to tubes, rods, thimbles, and belts. *Chem. Commun.* **2005,** 3092-3094.

(28) Cho, S. I.; Kwon, W. J.; Choi, S. J.; Kim, P.; Park, S. A.; Kim, J.; Son, S. J.; Xiao, R.; Kim, S. H.; Lee, S. B. Nanotube-based ultrafast electrochromic display. *Adv. Mater.* **2005,** 17, 171-175.

(29) D'Arcy, J. M.; El-Kady, M. F.; Khine, P. P.; Zhang, L.; Lee, S. H.; Davis, N. R.; Liu, D. S.; Yeung, M. T.; Kim, S. Y.; Turner, C. L. Vapor-phase polymerization of nanofibrillar poly (3, 4-ethylenedioxythiophene) for supercapacitors. *ACS nano* **2014,** 8, 1500-1510.

(30) Du, X.-S.; Zhou, C.-F.; Mai, Y.-W. Novel synthesis of poly (3, 4-ethylenedioxythiophene) nanotubes and hollow micro-spheres. *Mater. Lett.* **2009,** 63, 1590-1593.

(31) Mao, H.; Lu, X.; Chao, D.; Cui, L.; Zhang, W. Self-assembly synthesis of hollow, core–shell and solid soluble oligo(3,4-ethylenedioxythiophene)s microspheres in a mixed solvent. *Mater. Lett.* **2008,** 62, 2543-2546.

(32) Wu, J.; Li, Y.; Feng, W. A novel method to form hollow spheres of poly (3, 4-ethylenedioxythiophene): Growth from a self-assemble membrane synthesized by aqueous chemical polymerization. *Synth. Met.* **2007,** 157, 1013-1018.

(33) Cho, S. I.; Choi, D. H.; Kim, S.-H.; Lee, S. B. Electrochemical synthesis and fast electrochromics of poly (3, 4-ethylenedioxythiophene) nanotubes in flexible substrate. *Chem. Mater.* **2005,** 17, 4564-4566.

(34) Kodas, T. T. T.; Hampden-Smith, M. J., *Aerosol processing of materials*. Wiley-Vch: 1999.

(35) Bang, J. H.; Suslick, K. S. Applications of ultrasound to the synthesis of nanostructured materials. *Adv. Mater.* **2010,** 22, 1039-1059.

(36) Xu, H.; Zeiger, B. W.; Suslick, K. S. Sonochemical synthesis of nanomaterials. *Chem. Soc. Rev.* **2013,** 42, 2555-2567.

(37) Okuyama, K.; Lenggoro, I. W. Preparation of nanoparticles via spray route. *Chem. Eng. Sci.* **2003,** 58, 537-547.

(38) Xia, B.; Lenggoro, I. W.; Okuyama, K. Preparation of nickel powders by spray pyrolysis of nickel formate. *J. Am. Ceram. Soc.* **2001,** 84, 1425-1432.

(39) Messing, G. L.; Zhang, S. C.; Jayanthi, G. V. Ceramic powder synthesis by spray pyrolysis. *J. Am. Ceram. Soc.* **1993,** 76, 2707-2726.

(40) Suh, W. H.; Jang, A. R.; Suh, Y. H.; Suslick, K. S. Porous, hollow, and ball-in-ball metal oxide microspheres: preparation, endocytosis, and cytotoxicity. *Adv. Mater.* **2006,** 18, 1832-1837.

(41) Skrabalak, S. E.; Suslick, K. S. Porous MoS_2 synthesized by ultrasonic spray pyrolysis. *J. Am. Chem. Soc.* **2005,** 127, 9990-9991.

(42) Didenko, Y. T.; Suslick, K. S. Chemical aerosol flow synthesis of semiconductor nanoparticles. *J. Am. Chem. Soc.* **2005,** 127, 12196-12197.

(43) Skrabalak, S. E.; Suslick, K. S. Porous carbon powders prepared by ultrasonic spray pyrolysis. *J. Am. Chem. Soc.* **2006,** 128, 12642-12643.

(44) Xu, H.; Guo, J.; Suslick, K. S. Porous carbon spheres from energetic carbon precursors using ultrasonic spray pyrolysis. *Adv. Mater.* **2012,** 24, 6028-6033.

(45) Suh, W. H.; Suslick, K. S. Magnetic and porous nanospheres from ultrasonic spray pyrolysis. *J. Am. Chem. Soc.* **2005,** 127, 12007-12010.

(46) Bang, J.; Didenko, Y.; Helmich, R.; Suslick, K. Nanostructured materials through ultrasonic spray pyrolysis. *Aldrich Materials Matter* **2012,** 7, 15-18.

(47) Roncali, J. Conjugated poly (thiophenes): synthesis, functionalization, and applications. *Chem. Rev.* **1992,** 92, 711-738.

(48) Meng, H.; Perepichka, D. F.; Bendikov, M.; Wudl, F.; Pan, G. Z.; Yu, W.; Dong, W.; Brown, S. Solid-state synthesis of a conducting polythiophene via an unprecedented heterocyclic coupling reaction. *J. Am. Chem. Soc.* **2003,** 125, 15151-15162.

(49) Selvaganesh, S. V.; Mathiyarasu, J.; Phani, K. L. N.; Yegnaraman, V. Chemical Synthesis of PEDOT–Au Nanocomposite. *Nanoscale Res. Lett.* **2007,** 2, 546-549.

(50) Martin, D. C.; Wu, J.; Shaw, C. M.; King, Z.; Spanninga, S. A.; Richardson-Burns, S.; Hendricks, J.; Yang, J. The Morphology of Poly(3,4-Ethylenedioxythiophene). *Polym. Rev.* **2010,** 50, 340-384.

(51) Pringle, J. M.; Armel, V.; MacFarlane, D. R. Electrodeposited PEDOT-on-plastic cathodes for dye-sensitized solar cells. *Chem. Commun.* **2010,** 46, 5367-5369.

(52) Wood, T. J.; Brown, P. S.; Badyal, J. P. S. Oxidative atomized spray deposition of electrically conductive poly (3, 4-ethylenedioxythiophene). *Chem. Commun.* **2013,** 49, 7741-7743.

(53) Lock, J. P.; Im, S. G.; Gleason, K. K. Oxidative chemical vapor deposition of electrically conducting poly (3, 4-ethylenedioxythiophene) films. *Macromolecules* **2006,** 39, 5326-5329.

(54) Winther-Jensen, B.; Winther-Jensen, O.; Forsyth, M.; MacFarlane, D. R. High rates of oxygen reduction over a vapor phase–polymerized PEDOT electrode. *Science* **2008,** 321, 671-674.

(55) Österholm, A. M.; Shen, D. E.; Dyer, A. L.; Reynolds, J. R. Optimization of PEDOT films in ionic liquid supercapacitors: demonstration as a power source for polymer electrochromic devices. *ACS Appl. Mater. Interfaces* **2013,** 5, 13432-13440.

(56) Liu, R.; Cho, S. I.; Lee, S. B. Poly (3, 4-ethylenedioxythiophene) nanotubes as electrode materials for a high-powered supercapacitor. *Nanotechnology* **2008,** 19, 215710.

(57) Duay, J.; Gillette, E.; Liu, R.; Lee, S. B. Highly flexible pseudocapacitor based on freestanding heterogeneous MnO 2/conductive polymer nanowire arrays. *PCCP* **2012,** 14, 3329-3337.